# Synthesis and Characterization of Ion Conducting Solid Polyelectrolytes and Alkali Fluorooxoborates

Von der Fakultät Chemie der Universität Stuttgart
zur Erlangung der Würde eines Doktors der
Naturwissenschaften (Dr. rer. nat.) genehmigte Abhandlung

Vorgelegt von

Güliz Cakmak

aus Ankara

Hauptbericter: Prof. Dr. Dr. h. c. Martin Jansen
Mitberichter: Prof. Dr. Thomas Schleid

Tag der mündlichen Prüfung: 27.07.2009
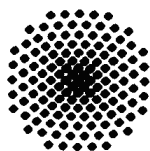
Max-Planck-Institut für Festkörperforschung, Stuttgart

2009

This thesis is dedicated
to Hasan and to my family,
Hasan'a ve aileme,

Acknowledgement

Contents

Part I

Introduction

Both organic and inorganic solid polymeric electrolytes continue to attract significant attention due to their conduction of electricity by the migration of ions, which endows the window for potential applications in batteries and fuel cells. The majority of these materials, the polymer-salt complexes, consists of a salt dissolved in a polymer matrix, in which both cations and anions contribute to the overall conductivity [1]. In such bi-ionic conductors, not only cations but also its counter anions migrate and a main contribution to ion transport is due to the anions as the transference numbers of cations are often as low as 0.2 [2, 3, 4, 5, 6]. Realizing the importance of cationic transport number, attempts have been undertaken in order to reduce the anions mobility and thus increase the contributions from the cations [7], and thus polyelectrolytes have been developed which possess ionic centers as part of their constitutional repeating units [8]. In batteries, they do not cause leakage problems in contrast to polymer gel electrolytes, and they have a high transference number for one of the ionic species present, the mobile ions, which make them single ion conductors. Hence, such a polyelectrolyte appears to be the best system to cover the requirements for a battery electrolyte. Various polyelectrolytes in which anions are covalently bound to the polymer chains have been developed. However, these materials have exhibited but very low conductivities at room temperature ($\sim 10^{-7}$ S cm^{-1}) [9]. Obviously, it is very urgent to provide a better performing polyelectrolyte with a high transference number, a high charge carrier concentration, short hopping distances, and no strong ion pairing.

In order to achieve these aims, the first part of this thesis is devoted to develop several solid polyelectrolytes bearing alkylborate units, such that the anions are immobilized on the chain. For this purpose, two main types of novel polyelectrolytes have been synthesized based on poly(lithium tetrakis(ethyleneborylborates) and poly[tris(tetraethylenesilyl)boranes]. Each of these representative polymers were synthesized by utilizing the hydroboration reaction. These polymers were modified subsequently via incorporating several organyl lithium reagents, where organyl denotes for phenyl, methyl, n-butyl and t-butyl, generating various poly(lithium organylborylborates) and poly[lithium tris(tetraethylenesilyl)organylborates] as novel polyelectrolytes. The effect of these reagents on conductivity was investigated as an effort to

develop better ion conductive polyelectrolytes with a high transference number. Furthermore, poly(lithium organylborylborates) polymers were annealed, and then the effect of annealing on ionic conductivity as well as structural characterizations were investigated. The solid polyelectrolytes were characterized mainly by powder XRD, FT-IR, DTA/TG/MS, solid-state NMR, elemental analysis and impedance spectroscopy techniques. In addition, the electrochemical properties of these polyelectrolytes were determined with ac conductivity and direct current measurements.

Another very challenging topic is crystalline solid alkali ion conductors. Thus, in the second part of this thesis, investigations have been focused on alkali fluorooxoborate materials. Since solid alkali ion conductors are constitutional components of all solid state electric batteries, they thus crucially determine the overall performance of the respective configurations. The structural and compositional preconditions for high electric conductivity, exclusively based on ions as charge carriers, are well understood [10]. However, in spite of lasting efforts in ever better understanding the microscopic mechanisms [11], and in discovering superior materials, no significant progress in providing solid electrolytes with improved pertinent properties has been achieved. The top performing sodium and lithium ion conductors are still Na-β-Alumina [12] and LISICON [13] types, respectively.

Against this background, it appeared to us appropriate, even necessary, to commence systematic and basic studies aiming at identifying additional structural and bonding features that would facilitate migration of alkali metal ions on periodic lattices. We decided to disregard glasses because of the notorious inhomogeneous spread of all relevant attributes on a microscopic level, and to focus on Li$^+$ and Na$^+$, since systems based on those charge carriers are most promising with respect to achieving good weight capacities. Also for the latter reason we have chosen borate based anionic matrices.

The fundamental prerequisites for high conductivity are high concentration and high long range mobility of charge carriers. In order to allow for good long range mobility of cations, the anionic matrix needs to provide two, or better three, dimensionally branched migration paths along which the ions experience but a flat electrostatic potential profile. Therefore, one has to avoid accumulations of negative charges on the walls of the pathways that might act as traps for the moving cations. In oxoanionic matrices, oxygen atoms in terminal position are notorious for trapping cations. Avoiding such terminal oxygen atoms, formally bearing a charge of -1, thus appears to be a promising measure for improving cationic conductivity. One of the unique features of the oxoborate chemistry is providing an option for achieving this goal: boron coordinated by three oxygen atoms is showing significant Lewis-acidity, allowing for adding

a fluoride anion. As a result, a formal charge of -1 can be attributed to the respective boron atom which is reflected by a decrease in the effective negative charge of fluorine. Another aspect favouring borates for the purpose discussed is their structural richness and adaptability, which has been extensively analyzed with a number of classification schemes [14, 15, 16].

Based on these facts, alkali fluorooxoborates have been considered as auspicious materials. Therefore, in the second part, various alkali fluorooxoborates including lithium flurooxoborate (LiB_6O_9F), sodium fluorooxoborate ($Na_3B_3O_3F_6$) and potassium fluorooxoborate ($K_3B_3O_3F_6$) have been synthesized in solid state reactions and characterized. Out of them, the structures of LiB_6O_9F and $Na_3B_3O_3F_6$ have been determined, for the first time, by single crystal analysis. Moreover, the structure of $K_3B_3O_3F_6$ is also revealed by considering the analogy with the $Na_3B_3O_3F_6$. All of these compounds have additionally been characterized via FT-IR, Raman, DSC, DTA/TG/MS, impedance spectroscopy and direct current measurement techniques.

Part II

GENERAL PART

1   Preparative Working Methods

Most of the substances studied in this work are air sensitive. Therefore, handling of air sensitive substances and the reactions were carried out in a highly purified argon atmosphere using standard Schlenk techniques or glove boxes, and with rigorously dried reaction apparatus and solvents.

1.1   Vacuum and Inert Gas Apparatus

The inert conditions were achieved by using a vacuum and inert gas system which is known as Schlenk line. It was constructed from Duran glass, and vacuum and inert gas connections were tightened via specially prepared bended stopcocks or teflon valves (Young valves). Argon flow and vacuum control were adjusted by the help of these teflon valves. The Schlenk line set up, which is schematically shown in Figure 1, was composed of a dual manifold having a number of ports. One line of the manifold was connected to a high vacuum pump and the second line was connected to the argon source. Silicone grease (Wacker Chemie AG, Munich, Germany) was utilized in order to connect the glasswares to the Schlenk line by joints. The connections to the equipments were performed by glass spirals or angled glasses, which were dried by flaming under vacuum and filled with argon by using the concerned valves. The inert gas was selected as argon (purity grade 4.8, Messer-Griesheim, Krefeld, Germany) and it was supplied by the low temperature service department (Max Planck Institute, Stuttgart, Germany) through copper lines. Argon gas was further purified before usage. A trap cooled with liquid nitrogen was connected to the line to prevent the vacuum line from solvent vapours or gaseous products.

The apparatus shown in Figure 2 was employed to handle substances under inert conditions. The construction provides filling the substances in glass capillaries within

a range of diameters under argon flow, and to be sealed inside glass ampoules for long term storage.
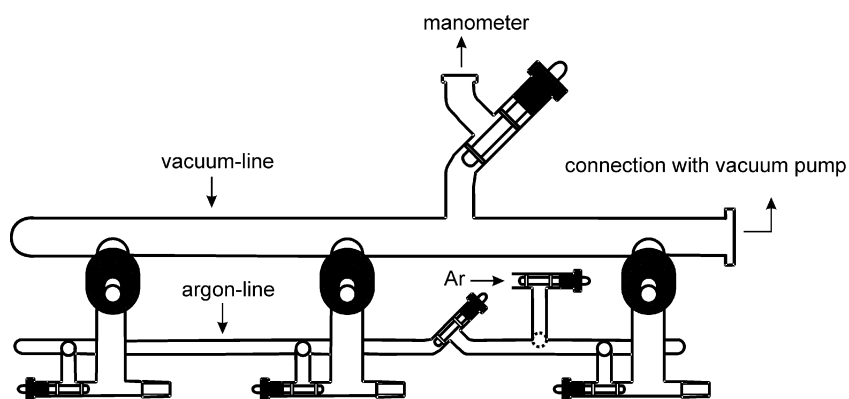
Figure 1: Schematic view of the argon and vacuum line (Schlenk system).
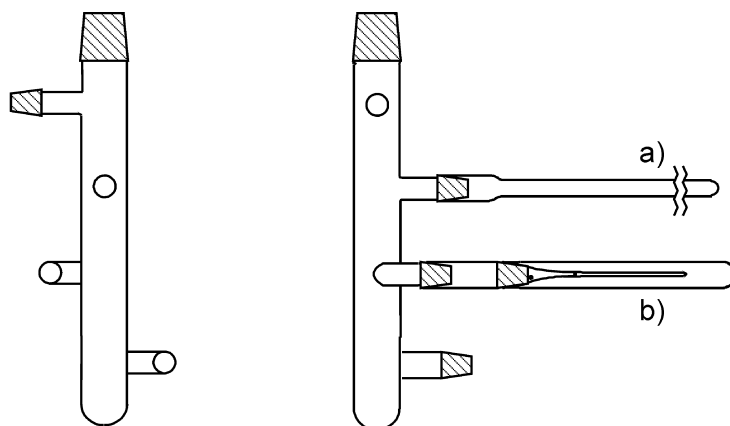
Figure 2: Schlenk apparatus which has LV 29 in the upper part and LV 14 in the remaining connections for (a) sealing of ampoules, and (b) filling of capillaries.

1.2   Vacuum Devices

A fine vacuum level was supplied by employing a rotary vane vacuum pump (Trivac D 4B, Oerlikon Leybod Vacuum GmbH, Köln, Germany). The connection of the pump to the vacuum and inert gas apparatus was achieved by means of a trap cooled with liquid nitrogen through a flexible metal tube. Grease-free teflon valves were utilized in the ports. The vacuum range between 10^{-3} - 10^3 mbar was continuosly monitored with the help of an electronic gauge apparatus (Pirani VAP 5, Vacuubrand GmbH & CoKG, Wertheim, Germany) mounted to the vacuum line.

1.3   Purification of the Solvents and Argon Gas

The drying of the common solvents like hexane and ether was carried out by refluxing the solvents over sodium metal in the presence of benzophenone until receiving a blue color. Afterwards, they were distilled to an other flask to obtain the purified solvents. The distilled solvents were stored in the presence of sodium wires under argon atmosphere.

The prepurified argon, which was received from the common lines, was furher subjected to a set of purification steps in order to remove any traces of oxygen and water impurities (Figure 3). For further purification, the gas was allowed to pass through a set of succesive drying towers. The drying towers were columns filled with "blue gel", potassium hydroxide, molecular sieves (with 3Å mesh size) and phosphorus pentoxide on an inert substrate (Sicapent, Merck, Germany). The drying towers were followed with a pressure regulator (mercury bubblier) in order to release the overpressure. After that, the final purification step was passage of the gas through titanium sponge (Sigma Aldrich, USA) which was filled in a quartz tube located in a horizontal furnace (Loba, HTM Reetz GmbH, Berlin, Germany) at 700 °C. An oil bubbler filled with silicon oil was used to check and monitor the rate of argon gas flow.

1.4   Manipulation of Air and Moisture Sensitive Substances

The handlings and synthetic procedures for all air and moisture sensitive substances were achieved via standard Schlenk techniques [17]. The Schlenk line including all the glassware was flame dried with a high vacuum (10^{-3} mbar) by using a Bunsen burner
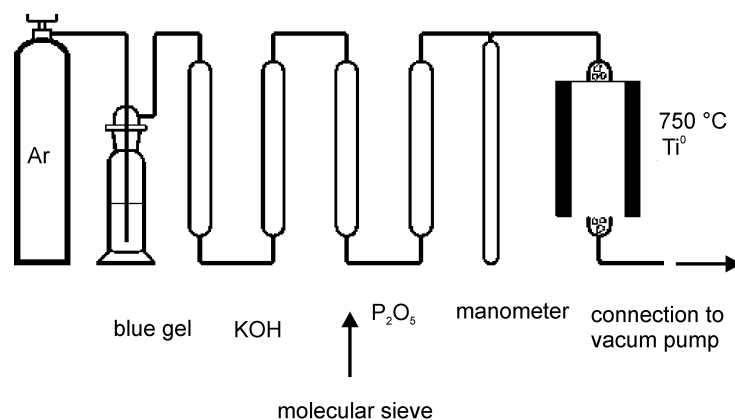
Figure 3: Schematic set up for the argon purification.

and cooled in a stream of argon flow. In order to ensure that the apparatus was completely dry and clean, this process was followed at least three times. All manipulations, such as filling and extracting of substances, were performed under continuos argon flow.

The liquid transfer was performed by the help of disposable syringes (Norm-Ject, Henke Sass Wolf GmbH, Tuttlingen, Germany) connected with a single use needle (Supra, Ehrhardt Medizinprodukte, Geislingen, Germany). These syringes were purged several times with argon gas before usage.

1.5 Glove Box

The preparative works, which could not be performed in the Schlenk line, were facilitated in argon filled glove boxes (MB 200 or MB 150 types, M. Braun, USA) under strict exclusion of air and moisture. Some illustrative manipulations in glove boxes were pressing pellets for both reactions and FT-IR measurements, as well as preparing impedance cells. The purification of the argon gas was performed via molecular sieves (pore diameter 300 pm) and copper contact filters (BTS-catalyst, Sigma-Aldrich, Taufkirschen, Germany). The purity of the argon gas was controlled by gas analyzers. Both water and oxygen levels of the glove boxes were maintained below 0.1 ppm, and continiuos monitoring of the atmosphere was performed by detectors. All apparatus

and samples were transported in and outside of the glove box through air-tight evacuation chambers. Before any manipulation, chambers were evacuated three times (each 15 min) and refilled with argon.

2   Characterization Techniques

2.1   Thermal Analyses

2.1.1   Simultaneous Thermal Analysis (DTA/TG/MS)

Simultaneous thermal investigations of the samples were achieved by means of differential thermal analysis (DTA) and thermogravimetric analysis (TG) with a STA 409 thermal analyzer (Netzsch, Selb, Germany). The measurements were performed with a heating rate of $10\,°C\,min^{-1}$ under argon flow. In order to monitor the atomic/molecular masses of volatile decomposition products, the instrument was equipped with a quadrupole mass spectrometer (QMS 421, Balzers, Hudson, NH, USA) having a Skimmer coupling. 10-20 mg of samples were placed in a corundum crucible for the measurements. Air sensitive samples were transferred via a special Schlenk apparatus.

The measurements and evaluation of the results were performed with special program packages maintaned by Netsch [18, 19].

2.1.2   Differential Scanning Calorimeter (DSC)

Differential scanning calorimeter measurements were performed by using a DSC 404 (Netzsch, Selb, Germany) equipped with a NiCr/NiCu thermocouple (Type E) under argon atmosphere. A cylindrical platinum crucible (outer diameter 7 mm, height 2.5 mm) with a cap was used as a sample holder. For each measurement, approximately 10 mg substances were introduced into the crucibles.

2.2   Quantitative Chemical Elemental Analysis

2.2.1   Hot Gas Extraction

Quantitative analyses of carbon in solid samples were performed in a hot gas extraction analyzer (C-200, Leco, St Joseph, MI, USA). 10-20 mg of samples were placed in a

tin crucible together with a metal accelerator (0.8 g iron, 1.0 g cupper) and heated inductively (T > 2500 K) with an oxygen flow. Entire carbon was oxidized to CO_2 by the combustion and the quantitative determination of carbon was carried out with the help of infrared absorption. SiC was used as a calibration standard during the combustion.

2.2.2 Atomic Emission Spectroscopy with Inductively Coupled Plasma

Boron, lithium and silicon were quantified by means of inductively coupled plasma atomic emission spectroscopy (ICP-AES) with a model ARL 3580 B (ARL, EcuBlens, Switzerland). The multi channel instrument was equipped with a conventional grating monochromator as a vacuum spectrometer in a Paschen-Runge mounting. The equipment provides both to record the emission lines sequentially, and also to measure simultaneously the light intensities of up to 50 elements within the wavelength range of 170-810 nm. A low energy plasma chamber was equipped as a plasma source, and the elements were quantified and analyzed with the generated argon plasma. Standard addition method was used to calibrate Si and B. ICP Expert Software was used to analyze the data [20].

For the ICP analysis, digestion was performed by dissolving the samples in a mixture of HNO_3 and HF at elevated temperatues under pressure for 20 hours in a steel pressure digestion vessel of type DAB 1 (Berghof, Eningen, Germany) having a 10 ml PTFE compartment [21].

2.3 X-ray Diffraction Techniques

2.3.1 Powder X-ray Diffraction

Powder X-ray diffraction of the samples were collected by employing a Stadi-P (Stoe & Cie, Darmstadt) or a D8-Advance (Bruker AXS, USA) type diffractometers at ambient conditions.

Stoe Stadi-P diffractometer was equipped with a curved germanium (111) type monochromator and a copper anode with Cu-$K_{\alpha1}$ (λ = 1.540598 Å) radiation. The routine measurements were performed with a position sensitive detector (PSD 1 - Position Sensitive Detector) having a large angle and a low resolution (angle range 35 ° and $\Delta 2\theta$ resolution = 0.15 °). Higher resolutions in the measurements were obtained with a high resolution detector having an effective range of 6 ° and a resolution of 0.06 ° (PSD 2). The external standard for calibration was elementary silicon. Air

sensitive samples, which were placed in a glass capillary ($\o$ = 0.1 - 0.7 mm, Hilgenberg, Germany) and sealed under argon atmosphere, were measured with the Debye-Scherrer geometry. On the other hand, air insensitive samples were measured in transmission geometry with flat sample holders having the powder samples distributed with silicon grease between X-ray amorphous polyethylene foils. The powder X-ray patterns were analyzed via WinXPow [22] software. In order to identify the substances, the measured diffractograms were compared with the diffractograms of already explored substances stored in data bases such as ICSD [23] and JCPDS [24].

High resolution laboratory D8-Advance X-ray powder diffractometers were utilized to collect diffraction patterns of the high resolution measurements. The diffraction patterns of the samples were collected by using the radiation of Cu-K$_{\alpha 1}$ from a primary Ge(111)-Johansson type monochromator in conjunction with a Vantag-1 position sensitive detector (PSD) with an opening angle of 6 °. The measurements of air sensitive samples were carried out with glass capillaries sealed under argon atmosphere. Concerning non-air sensitive samples, powders were distributed with ethanol on a silicon mirror of the flat sample holder and the measurements were allowed in transmission geometry.

2.3.2   Single Crystal Diffraction

The measurements of single crystals were carried out with two different single crystal diffractometers. The first one is the AXS Smart APEX three circle single crystal diffractometer (Bruker, Karlsruhe) equipped with a fine focus tube with Mo anode (MoK$_\alpha$ radiation, λ = 0.71073 Å) which was used as X-ray source. The X-ray beam was monochromatized by using a graphite single crystal monochromator. The data were collected by using a CCD detector (AXS, Bruker, Karlsruhe, Germany).

Alternatively, the experimental intensity data of the single crystals were collected with a dual wavelength diffractometer system: Smart APEX II three circle single crystal diffractometer (Bruker AXS, Karlsruhe, Germany) equipped with a CCD-detector, a Siemens X-ray sealed tube (MoK$_\alpha$ radiation, λ = 0.71073 Å), an Incoatec (Geestacht, Germany) microfocus X-ray source IμS (CuK$_\alpha$ radiation, λ = 1.54178 Å) and a N-Helix low temperature device (Oxford Cryosystems, Oxford, United Kingdom (28−300 K)), see Figure 4. The copper source was used for compounds containing the light elements. The X-ray beam was generated with Incoatec IG150 and monochromotized by using a Montel optic monochromator (Incoatec, Geestacht, Germany).

The crystal structures were solved by using the program package SHELXS-97 with direct methods [25]. The initial structure models were refined with full-matrix least

-square refinement procedure with the help of SHELXL-97 [26] program package, which was implemented in the WinGX Software [27]. Further details on crystallographic data, measurements and the final structure models are given in the corresponding chapters.
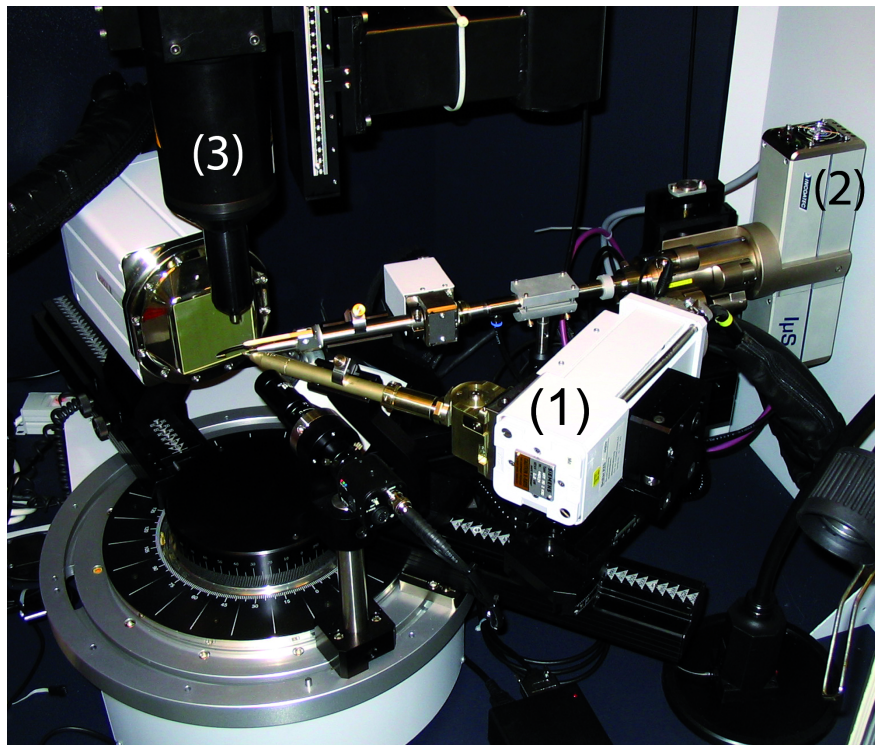
Figure 4: Dual wavelength diffractometer system: (1) sealed tube (Mo), (2) IμS microfocus source (Cu), (3) N-Helix cooling device.

2.4   Infrared Spectroscopy

Infrared spectroscopy measurements were performed with a FT-IR spectrometer (Fourier-Transform, IFS 113v, Bruker, Karlsruhe) accompanied with vacuum optics and a Genzel interferometer. The spectrometer was equipped with a DTGS (deuterated triglycine sulphate) detector and a silicon carbide globar for radiation source. The measurements were performed over a wavenumber range of $400\,cm^{-1}$ to $4000\,cm^{-1}$ with a resolution of $2\,cm^{-1}$. Air sensitive samples were prepared in a glove box and transferred inside a desiccator for measurements. Samples were prepared by grinding 1-2 mg material together with a 300 mg KBr (99+%, Aldrich, further dried in vacuum at 200 °C) matrix in an agate mortar, and then the pellets were pressed in a hydrolytic press at 0.8 GPa for 10 minutes.

2.5   Raman Spectroscopy

Raman spectra were recorded with a microscope laser Raman spectrometer (LabRAM system, Co. : Jobin-Yvon, USA) functioning at the Helium-Neon (632.8 nm) and Diode-Laser (784.7 nm) laser lines at 20 mW. The instrument was operating by irradiation of a micrometer size (10-20 µm) sample with focusing the laser and by detection of the scattered light with a multi channel CCD (charge coupled device) detector. The powder samples were placed in glass capillaries (ø = 1 mm). Air sensitive samples were prepared and sealed under argon atmosphere. The measurements were performed at room temperature.

2.6   NMR Spectroscopy

Both solid state and liquid NMR spectra were recorded with pulse fourier transform NMR spectrometers. The XWin-NMR program [28] was used for the analysis of the data and XWin-plot program [29] was utilized to draw the spectra. Matlab [30] was used to process solid state NMR data. The raw data of the MQMAS experiment were processed with the matNMR toolbox [31]. ^{1}H, ^{7}Li, ^{11}B and ^{13}C nuclei were measured in this thesis. The measurement frequencies and the standard solutions used to calibrate the chemical shift axis are given in Table 1.

Table 1: NMR active nuclei with corresponding Larmor frequencies and reference solutions.

Nuclei	Larmor frequency /MHz		Standard substance
	9.4 T	7.05 T	
^{1}H	400.00	300.13	Tetramethylsilane, $Si(CH_3)_4$
^{7}Li	155.45	116.6	1 M aqueous LiCl solution
^{11}B	128.34	96.25	Borontrifluoride diethylether, $BF_3.O(CH_2CH_3)_2$
^{13}C	100.57	75.46	Tetramethylsilane, $Si(CH_3)_4$

2.6.1   Solid-State NMR Spectroscopy

Solid state NMR experiments were carried out on a 400 MHz Spectrometer (DSX-400 WB, Bruker Analytic, Karlsruhe) with a 9.4 Tesla magnet. Zirconium dioxide rotors were used as the sample holders. ^{11}B, ^{13}C and ^{1}H solid state NMR were performed with a 2.5 mm double resonance Magic Angle Spinning (MAS) probe (Bruker Analytic, Karlsruhe; Germany). These experiments were all performed with a MAS frequency of 25 kHz.

^{13}C spectra were obtained by using an adiabatic-passage Hartmann-Hahn cross-polarization (APHH-CP) with a contact time of 1 ms [32]. The RF amplitudes for the CP pulses were 80 kHz and 55 kHz for ^{13}C and ^{1}H, respectively.

For ^{11}B, the Multiple-Quantum Magic Angle Spinning (MQMAS) technique was applied [33]. To achieve a pure-phase 2D spectrum, MQMAS was combined with a Z-filter [34]. The raw data of the MQMAS experiments were processed with the matNMR toolbox [31].

For ^{7}Li Variable Temperature NMR (VT-NMR), a 7 mm WVT (Wide Range Variable Temperature) probe (Bruker Analytic, Karlsruhe) was used under static conditions. The RF field for ^{7}Li was 50 kHz. The line width of the ^{7}Li peak was estimated by taking the full width at half maximum.

Air sensitive samples were sealed in glass ampoules by a natural gas-oxygen hand burner and they were placed inside the 7 mm zirconium dioxide rotors for measurements. 2.5 mm rotors were too small to place glass ampoules, but they were sufficiently airtight to hold air sensitive samples.

2.6.2   Liquid NMR Spectroscopy

NMR spectra of the dissolved samples were recorded by using a 300 MHz spectrometer (Avance DPX 300 SB, Bruker Analytic, Karlsruhe, Germany) operating at 7.05 Tesla. The samples were dissolved in deuterated solvents (i.e. d^{8}-THF) in NMR tubes (WG-5-mm-Economy-8, Co.: RototecSpintec Gmbh, Biebesheim, Germany). Air sensitive samples were prepared by using the standard Sclenk techniques under a purified argon atmosphere. Some samples were prepared and measured at low temperatures, which can be followed in the related chapters. The measurements were performed with a 5 mm broad band probe head (^{1}H; ^{109}Ag -^{31}P). ^{13}C NMR spectra were recorded with ^{1}H broad band coupling.

2.7   Impedance Spectroscopy

2.7.1   Overview of Impedance Spectroscopy

Impedance spectroscopy is a powerful method for electrochemical characterization of various materials. It is also capable to determine the contributions of individual electrode or electrolyte processes [35, 36]. Electrical response of a system can be determined by several single processes in solid state electrochemistry. The key property of the impedance spectroscopy is its unique capability to distinguish the different steps in an electrochemical process including the detailed information about the surface and bulk properties. To illustrate, the resistance in ion conducting materials is caused not only by bulk but also sometimes by grain boundary contributions. In a conventional direct current (dc) measurement only the overall sample resistance, which is the sum over all individual processes, is measured. In contrast to dc measurements, frequency dependent alternating current (ac) resistance measurements generally give more detailed information on the electrical properties of a system. Electrochemical impedance measurements are performed by applying a small sinusoidal potential or current to an electrochemical cell and measuring its current or potential response over a wide range of frequencies. Individual resistive processes can usually be distinguished via varying the frequency by several orders of magnitude.

In 1969, Bauerle was the first researcher who realized the potential of the impedance spectroscopy and applied the technique for ion conducting materials to differentiate between bulk, grain boundary and electrode resistances [37]. After this pioneering work, impedance spectroscopy has gained a great attention and become the most powerful tool to investigate a wide range of ionic conductors such as polymers, ceramics and glasses.

The excitation signal of a sinusoidal voltage as a function of time is represented by:

$$E \ = \ E_0 \, cos(\omega t)$$

E : The sinusoidal potential
E_0: The amplitude of the signal
ω : The radial frequency
t : Time

or

$$E \quad = \quad E_0 \, cos(\omega t) \ + \ E_0 \, i \, sin(\omega t) \quad = \quad E_0 \, e^{i\omega t}$$

where $\omega = 2\pi f$ is the relationship between radial frequency ω (in radians/second) and

frequency f (in Hertz).

The response to the applied perturbation is a sinusoidal signal of the current, which is shifted in phase and amplitude from the applied signal, and expressed by:

$$ I \quad = \quad I_0\,cos(\omega t + \theta) \quad + \quad I_0\,i\;sin(\omega t + \theta) \quad = \quad I_0\,e^{i(\omega t + \theta)} $$

where θ is the phase shift.

It is possible to evaluate the impedance of a system by using an analogous equation to the Ohms law. When the equation for the frequency independent dc resistance is replaced with the frequency dependent ac version, impedance (Z) can be derived as:

$$ Z \quad = \quad \frac{E}{I} \quad = \quad \frac{E_0\,e^{i\omega t}}{I_0\,e^{i(\omega t + \theta)}} \quad = \quad \frac{E_0}{I_0}\,e^{-i\theta} $$

The impedance can be transformed from the complex notation to the Cartesian coordinate by using the Euler transformation, which is $e^{ix} = \cos x + i \sin x$. When further replacement of E_0/I_0 with $|Z|$ is applied, the representation of impedance appears in the form of:

$$ Z \quad = \quad \frac{E_0}{I_0}\,e^{-i\theta} \quad = \quad |Z|\,cos\theta \; - \; i\,|Z|\,sin\theta $$

The impedance can be separated into real and imaginary parts,

$$ Z \quad = \quad Z\,' \; - \; i\,Z\,'' $$

$$ \Rightarrow \quad \text{Impedance Z} \quad = \quad \text{Real part Z}\,' \; - \; i\,\text{Imaginary part Z}\,'' $$

The real and imaginary parts of impedance are described by Z $'$ = Re (Z) = $|Z|$ cos θ and Z $''$ = Im (Z) = $|Z|$ sin θ, respectively. The modulus (represented by $|Z|$) and phase angle, θ, can be derived with the following equations:

$$ |Z| \quad = \quad (\text{Re}^2 + i\,\text{Im}^2)^{1/2} $$

$$ \theta \quad = \quad \text{Arc tan (Im/Re)} $$

The measured resistance can be simplified into the ohmic resistance in the impedance equation given above if the phase angle is equal to 0, where there is no phase difference between potential and current:

$$\theta \quad = \quad 0 \qquad \Rightarrow \quad Z \quad = \quad \frac{E_0}{I_0} \quad = \quad R$$

The current lags behind the potential by $\pi/2$ in the case of pure capacitor with a capacitance of C and the capacitive resistance is given as:

$$\frac{E_0}{I_0} \quad = \quad \frac{1}{\omega C} \qquad \text{and} \qquad \theta \quad = \frac{\pi}{2} \qquad \Rightarrow \quad Z \quad = \quad -i\,\frac{1}{\omega C}$$

Two methods of graphical representation are mostly applied for the complex function, Z, in order to analyze the impedance measurements. The first one is the Nyquist plot or the Argand plot, where the real and imaginary parts are plotted on linear axis against one another in one plane, as shown in the Figure 5. The impedance can be represented as a vector having $|Z|$ as the length, and θ as the angle between this vector and the x-axis. Lower frequency data are represented on higher values in x axis of the Nyquist plot. This representation is widely used for the interpretation of the ion conducting materials. The second way of data representation is called as the Bode diagram. It is represented by plotting plane diagram of two components, which are complex logarithm (log $|Z|$) and phase angle (θ), against logarithm of frequency (log $|\omega|$).

2.7.2 Equivalent Circuit Elements

In order to interpret the measured impedance spectra, the most popular approach is based on to construct an electrical network representation, so-called an equivalent circuit. Optimisation of impedance analysis via equivalent circuit simulation has the basis to regard the measured impedances as a network of impedance elements [38, 39]. This network model has to approximate the measured impedance well over the whole frequency range and it can consist of resistors (R), capacitors (C), inductors (L), Warburg impedance (W) and constant phase element (CPE). Each of these elements can be characterized in Nyquist as well as in Bode plots (Table 2). Serial or parallel combinations of these elements produce the impedance plots.
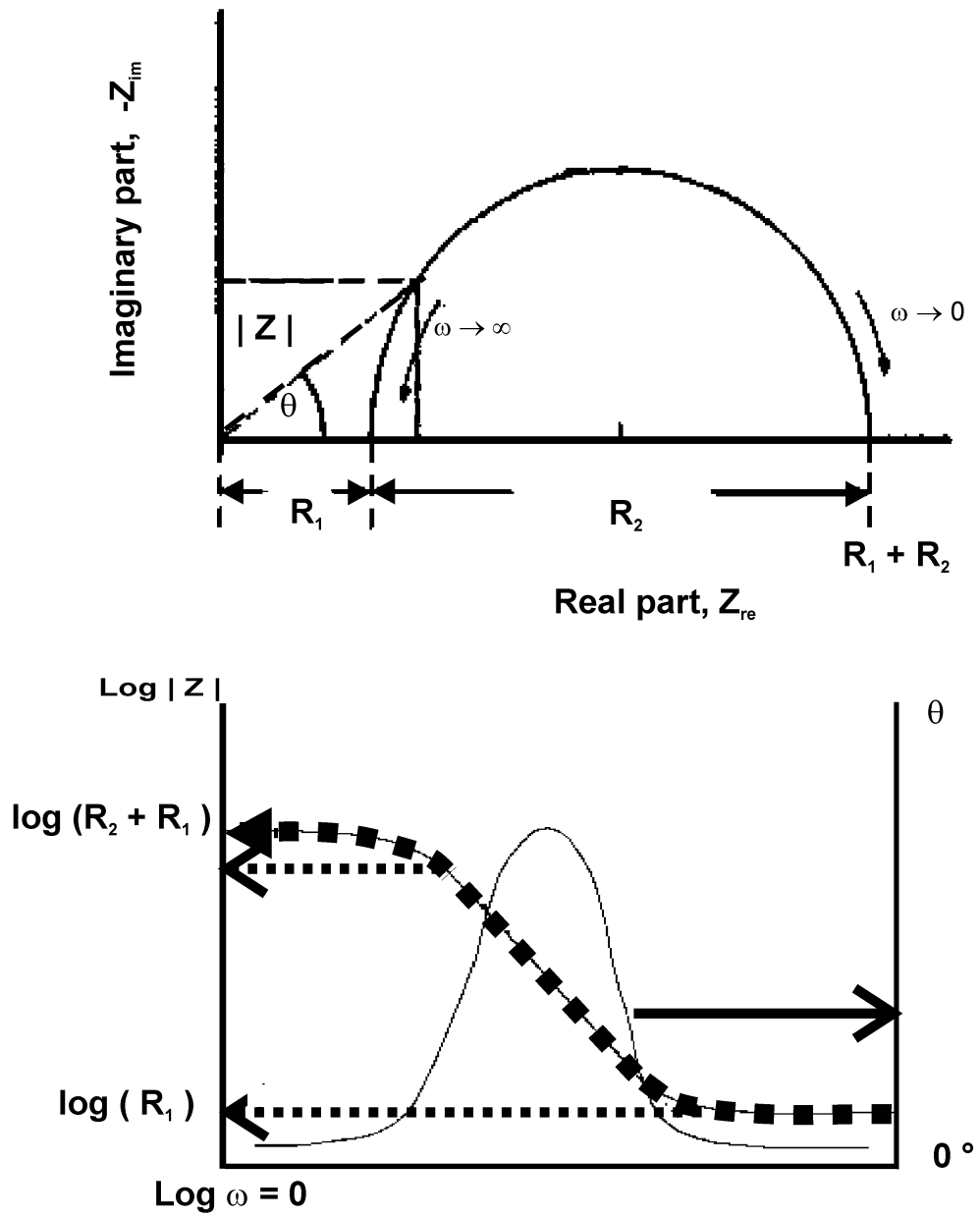
Figure 5:   Graphical representation of an impedance spectrum as Nyquist plot (top) and Bode plot (bottom).

Constant Phase Element, CPE

When modelling an electrochemical phenomenon, an ideal capacitor assumes that the surface under investigation is homogeneous. Irregular electrode surface, which is usually due to surface roughness or non-uniformly distributed properties, leads to a dispersion of the parameters [40]. The depression of the semicircles is always encountered in real systems, and thus the non-ideal behaviour is exhibited to some degree. Hence, commonly observed non-ideal capacitance can be simulated mathematically very well by introducing so-called the constant phase element, CPE [41, 42]. Thus, by replacing the capacitor in the RC element with CPE, one can deal with the frequently observed depressed semicircles. The circuits containing CPE are widely used to explain the behaviour of solid ionic conductors, solid-solid interfaces and rough solid-liquid interfaces. The impedance of a CPE element is expressed with:

$$Z_{CPE} \ = \ \frac{1}{Q.(i\omega)^n}$$

where, Q is the ideal capacitance and n is an empirical constant having values between 0 and 1. A CPE acts as an ideal capacitor when n is equal to 1, and an ideal resistance when n is equal to 0 [43]. In this manner, the parameter n is a measure for the degree of depression of such an arc. It is a perfect semicircle for n = 1 and a depressed semicircle for n < 1.

The Warburg Element

The Warburg element is introduced to describe impedances associated with mass transfer by diffusion. Warburg-impedance makes it possible to clarify the situations like a diffusion layer created near the electrode in ion conducting materials. It is expressed by means of the equation below, where W is a proportionality coefficient called Warburg coefficient.

$$Z \ = \ \frac{W}{\sqrt{i\omega}}$$

The impedance depends on the frequency of the potential perturbation. Thus, at low frequencies the reactants diffuse farther, leading to the Warburg impedance. This expression makes it possible to associate certain processes with predicted features in the impedance spectra.

On a Nyquist plot, the Warburg impedance appears as a diagonal line, which is called a spike, with a slope of 45°. On a Bode plot, the Warburg impedance exhibits a phase shift of 45°.

Parallel connection

Parallel connection of R and C, for a circuit shown in Figure 6, brings about a semicircle in Nyquist plot. The semicircle has an intercept on the Z' axis at zero and the maximum frequency at $\omega RC = 1$. A straightforward impedance expression can be derived by applying the Ohm's law to two components connected in parallel of an RC circuit, since resistances in parallel add as $1/R$ and capacitances in parallel add as $i\omega C$ [44]:

$$\frac{1}{Z} \;=\; \frac{1}{R} \;+\; i\omega C$$

The impedance can be evaluated as:

$$Z \;=\; \frac{R - i\omega R^2 C}{1 + \omega^2 R^2 C^2}$$

$$=\; \frac{R}{1 + (\omega RC)^2} \;-\; R\frac{i\omega RC}{1 + (\omega RC)^2}$$

Therefore,

$$Z'_{re} \;=\; \frac{R}{1 + (\omega RC)^2} \qquad \text{and} \qquad -Z''_{im} \;=\; R\frac{\omega RC}{1 + (\omega RC)^2}$$

Here, it is remarkable that impedance can easily be separated into real and imaginary parts. The above equation for the parallel connection of an RC (resistance and capacitance) circuit gives rise to a semicircle of radius $R/2$ and maximum value of $|Z''|$ defined by $\omega RC = 1$. The frequency where the imaginary part of the impedance reaches its maximum is the relaxation frequency, ω_R, of the RC element. It is given by $\omega_R = 1 / RC$.

Table 2: The characteristics of basic impedance elements and the representations in Nyquist and Bode plots.
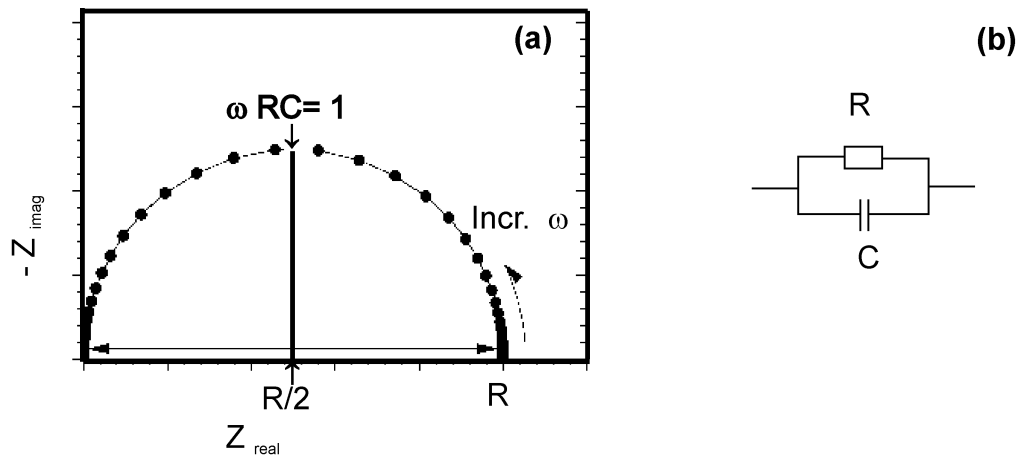
Figure 6:   (a) Impedance spectrum with one semicircle, and (b) equivalent circuit constructed from parallel combination of resistance and capacitance.
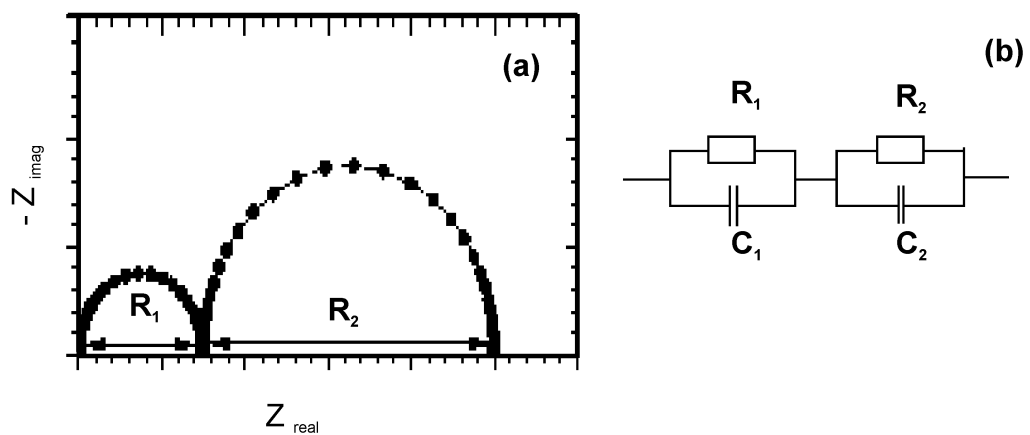
Figure 7: (a) Impedance spectrum with two semicircles, and (b) equivalent circuit for two serial connected RC elements.

Each parallel RC element gives rise to a semicircle in the complex impedance plane. Two well separated semicircles in the complex impedance plane are represented by constructing two serial RC elements as exemplified in Figure 7. For example, two semicircles can be observed due to bulk (i.e. R_1C_1 element for bulk) and grain boundary (i.e. R_2C_2 element for grain boundary) phenomena. This situation could be encountered when there is a difference in magnitude for the capacitances of the observed processes.

Therefore, the capacitance can be calculated for each process and its magnitude gives strong information on the physical origin of the semicircles [45]. Typical orders of magnitude for some common capacitances are tabulated in Table 3.

Table 3: Typical orders of magnitude of some common capacitances.

Capacitance [F]	Responsible Phenomenon
10^{-12}	Bulk
10^{-11}	Minor, second phase
$10^{-11} - 10^{-8}$	Grain boundary
$10^{-7} - 10^{-5}$	Sample $-$ electrode interface
10^{-4}	Electrochemical reaction

2.7.3   Impedance Spectroscopy Measurements

The schematic set up of the impedance spectroscopy measurement used in the present study is given in Figure 8. It was designated to collect response of a sample to an applied alternating wave signal between 25 °C and 700 °C.

Impedance spectroscopy measurements were performed with an impedance analyzer (Alpha-A 4.2 Analyzer, Novo Control, Hundsangen, Germany) which was combined with the ZG 4 impedance interface in a two-wire arrangement. Measurements and data recording were performed with the WinDeta program [46] by the central computer assisted controlling of all components. The equipment was designed to measure very high impedance values over a wide range of frequencies varying from 20 MHz down to 0.01 Hz.

The set up for impedance spectroscopy cell is schematically shown in Figure 9. Samples were pressed in the form of pellets by applying 350 MPa pressure. The diameters of the pellets were 6 mm and the thicknesses were in the range of 0.5 mm to 1 mm. Gold, platinum or silver electrodes were applied to measure ionic conductivities of compact samples. The sample squeezed between electrodes was mounted in between

two outer platinum electrodes, which established the connection to the impedance analyzer through platinum wires. The electrodes were made tight enough with the help of a steel spring load in order to keep the sample in contact with the electrodes. The cell was then covered with a quartz glass in order to allow the measurements to be performed under inert conditions [47]. Air sensitive samples were prepared in an argon filled glove box and transferred in argon filled quartz glass cell. After connecting the cell to the Schlenk line, the connection between the cell and the Schlenk line was evacuated three times by using a rotary vane pump (pKD 4, Saskia, Saugleistung $3.7\,\mathrm{m^3/h}$) and refilled with argon (purity 5.0). Then the joint between the cell and the Schlenk line was opened and the measurements were performed under argon atmosphere.

The cell was placed in a horizontal tube furnace, and the temperature was controlled by a thermocouple in close vicinity to the sample as shown in the Figure 8. The temperatures of the oven and inside the cell were measured by nickel/chromium/nickel thermocouples and controlled by using a temperature controller (Eurotherm 26/2704, Eurotherm, Germany). The measurements were performed with heating and cooling cycles having rates of $1\,°\mathrm{C\ min^{-1}}$.

The data generated by the impedance spectroscopy measurements were analyzed by using the WinFit program [48] and the bulk conductivities were determined by non linear mean square deviation curve fitting of the impedance spectra.

Each semicircle in the Nyquist plot is responsible for a phenomenon in the impedance data. Therefore, the possible interpretations were performed by extracting the capacitance, C, values for the parallel RQ element in the equivalent circuit.

After obtaining resistances of the ion conducting samples by fitting the impedance data, the ionic conductivities, σ, were calculated from the sample dimensions by applying:

$$\sigma \;=\; \frac{1}{R} \cdot \frac{d}{A}$$

where d is thickness in cm and A is cross sectional area in $\mathrm{cm^2}$.
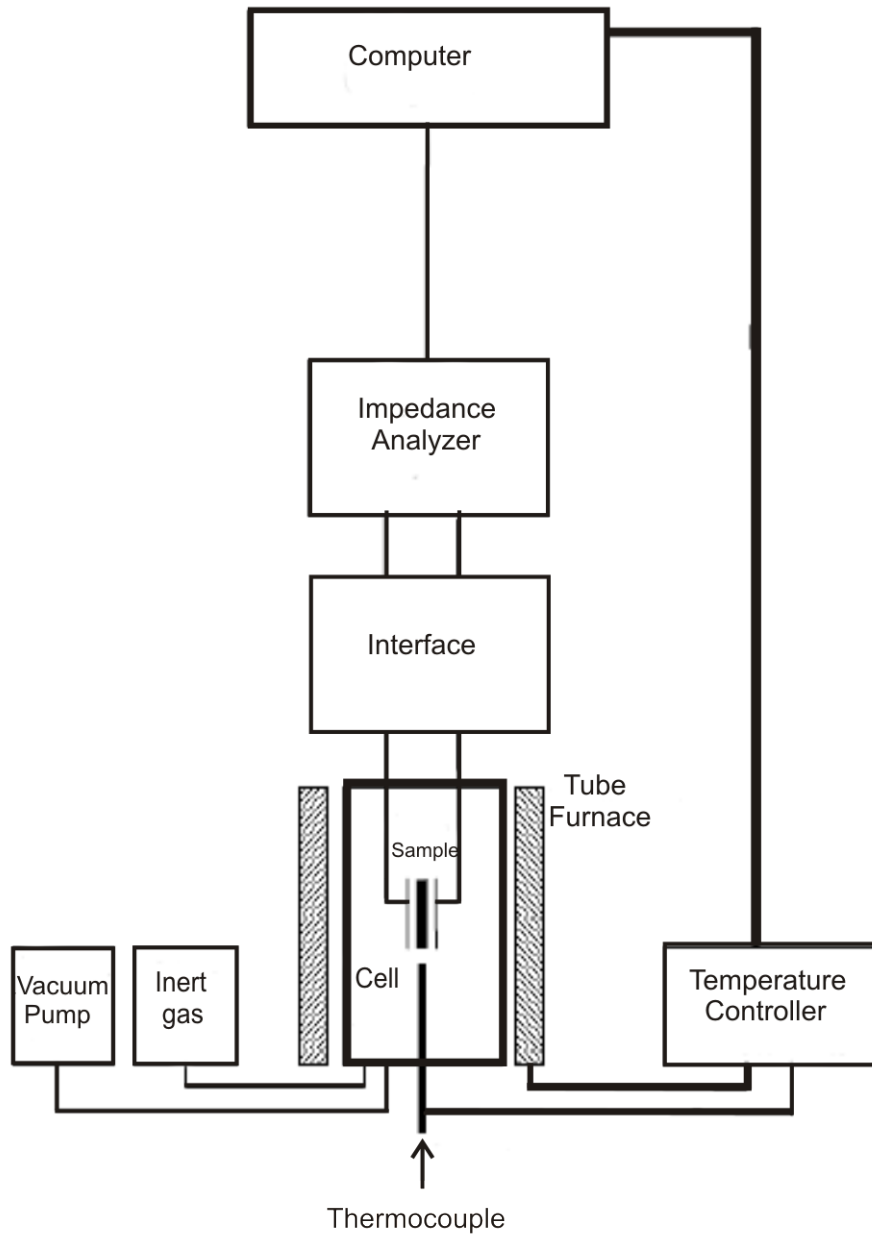
Figure 8: Schematic representation of the set up for impedance spectroscopy measurements.
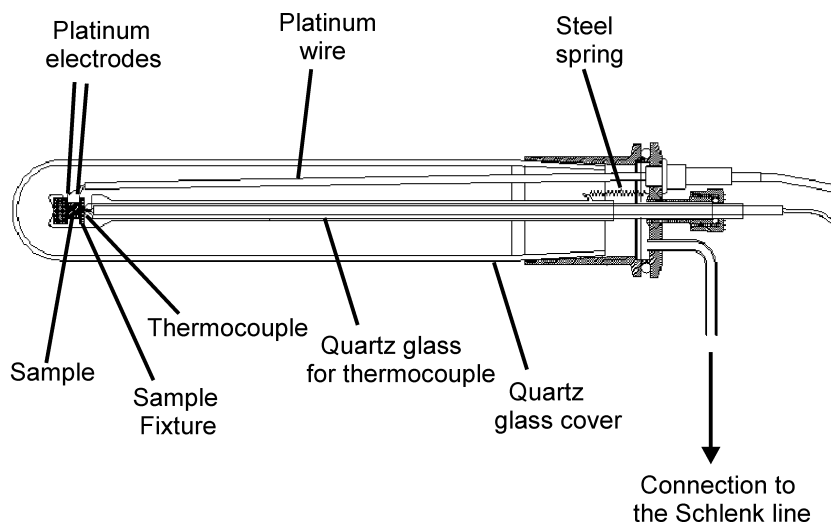
Figure 9: Schematic drawing of the impedance spectroscopy cell.

The temperature dependence of ionic conductivity obeys often the Arrhenius relation. Hence, the activation energy, E_a, can be obtained by using the ionic conductivity values at different temperatures by using Arrhenius relation:

$$\sigma = \frac{A}{T} \, e^{-\frac{E_a}{kT}}$$

In this manner, the activation energy is derived from the slope of the linear part of $\log(\sigma T)$ versus $1/T$ graph.

2.8 Direct Current (dc) Measurements

Anionic and cationic transference numbers were measured at different temperatures with a computer supported multipotentiostat (Model VMP, BioLogic, Claix, France), possessing eight individual channels and four supplementary channels. The current was measured at constant voltage with the supported software [49]. The dc current was monitored with time after a stepwise change of the cell voltage from $0\,$mV to $50\,$mV.

The aforementioned impedance cells in which samples were squeezed between blocking (gold, platinum or silver) or non-blocking (lithium or sodium) electrodes were used for the measurements.

2.9   Software Programs

In addition to the special programs, which were already mentioned above to record and analyze the measured data for the analytical mesurements, the programs utilized in the present work are listed as:

Lxy 1.6: Document processor for writing the thesis.

Microsoft Office 2003: Performing casual applications like writing texts.

Corel Draw: Redacting the post script data.

MDL ISIS/Draw: Producing the chemical formula.

Diamond 3.0b: Generating the structure graphics [50].

Origin 8G: Processing the graphics like impedance and FT-IR spectra.

3 Solid Ion Conductors

Electrical conduction is caused by the long range migration of electrons or ions. Even though most of the conductive materials possess only one type of charge carrier, ionic conduction can be accompanied by electronic conduction in mixed conductor materials. Conductive materials can generally be classified according to their charge carrier types and conductivity values, σ (Ω^{-1} cm^{-1} or S cm^{-1}). Figure 10 shows the typical conductivities for a range of materials. Conductivities are usually temperature dependent. The conductivity increases with increasing temperature in all materials, except metals. Metals have higher conductivities at lower temperatures [44].

Solid materials exhibiting high ionic conductivities and negligible electronic conductivities are named as solid ion conductors. Ionic conductivities of solid electrolytes vary between 10^{-10} and 10^{-5} S cm^{-1}. "Superionic solids" or "fast ion conductors" are solid electrolytes exhibiting exceptionally high ionic conduction at room temperature close to that of liquid electrolytes [51]. The conductivites span from 10^{-5} to 10^{0} S cm^{-1} for fast ionic conductors [52]. Some of the most important requirements of a solid electrolyte are a high ionic conductivity, a transference number of close to unity for the conducting ion and ease of fabrication. There are several important advantages of solid electrolytes compared to their liquid counterparts. These include the problems associated with the leakage of liquids, the likelihood of minituarized structures via simple fabrication techniques or longer shelf-lives along with wide operating temperature ranges [53].

The pioneering work of Tubandt and Lorenz in 1914 demonstrated that AgI exhibits an unusual electrical behaviour with ionic conductivities comparable to those in liquid electrolytes in the temperature range of 150 °C and 550 °C. They showed that the ionic conductivity of high temperature α phase of AgI was even higher than of the molten material and presented evidence for the first time that ions can carry electrical current in solids [54]. The discovery of RbAg$_4$I$_5$ and Na-β-alumina solid electrolytes in 1967 exhibiting exceptionally high Ag$^+$ and Na$^+$ ion conduction, respectively, at room/moderate high temperature attracted tremendous worldwide attentions on the solid state ionic materials [12, 55]. In the following decades, a large number of materials having a variety of ions as mobile species have been reported.

Ion Conductors	log σ	Electron Conductors
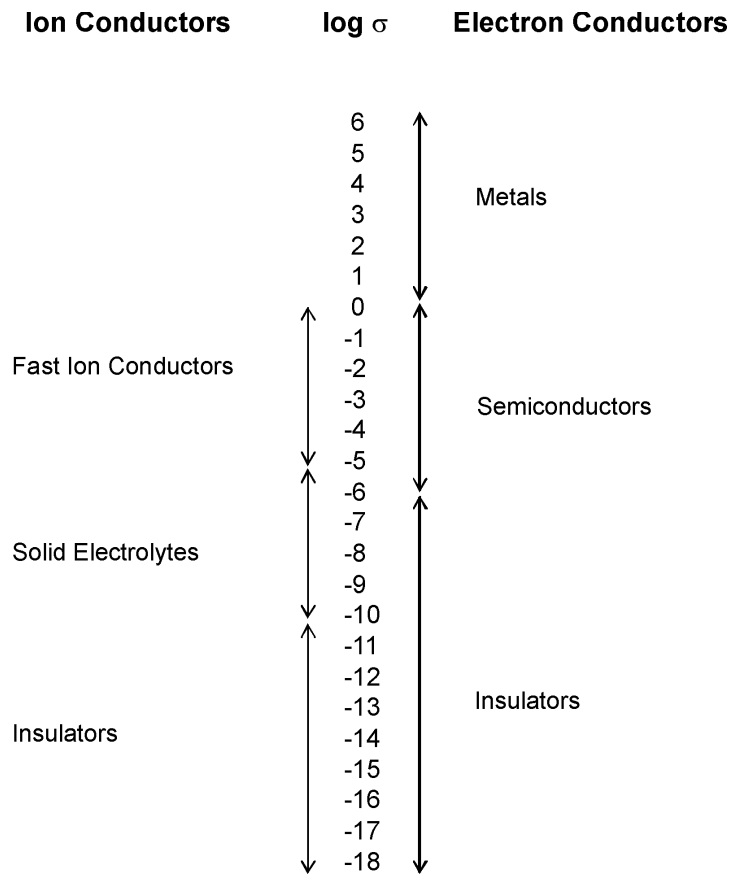
Figure 10: Classification of electrical conductivities of solids by magnitude.

Research in the field of fast ion transport in solids continues to receive attention owing to the many potential applications of these materials including batteries and fuel cells [53]. Solid electrolytes usually fall into three categories: crystalline compounds, polymers and glasses [56].

3.1   Polymer Electrolytes

The area of polymeric electrolyte materials have been developed remarkably after the discovery of the first ion conducting polymer in 1973, which was poly(ethylene oxide) (PEO) complexed with an alkali metal salt by Wright et al. [57]. Following that, Armand and coworkers examined the ionic conductivity of poly(ethylene oxide) (PEO) and poly(propylene oxide) (PPO) salt complexes and proposed their application as solid

polymer electrolytes in high-energy-density batteries [58]. The important requirements
of a polymer electrolyte to be used in applications are: high ionic conductivity (σ
$\geqslant 10^{-5}$ S cm^{-1}) at room temperature, a value approaching to 1 for the transference
number of the mobile ion ($t_{ion} \sim 1$), high mechanical strength, high chemical, thermal
and electrochemical stabilities [59, 60].

Using polymeric structures has attracted major attention owing to their noteworthy
advantages that stem from; i) having solid character, that eliminates the technological
problems relating to the confinement of liquids, ii) having low densities that would lead
to considerable weight savings, iii) having processability into all shapes and sizes, iv)
having good mechanical properties like being flexible and strong, v) ease of fabrication,
and vi) relatively low cost [61, 62, 63, 64].

3.1.1   Types of Polymer Electrolytes

The area of polymer electrolytes has passed through various stages in development
[65, 66]. The main classification of these promising materials can be performed in
three categories, which covers solid polymer electrolytes (SPE), polymer gel electrolytes
and polyelectrolytes. Solid polymer electrolytes are polymer salt complexes which
are obtained by dissolving a salt in the polymer matrix. Polymer-gel electrolytes are
prepared by incorporation of liquid electrolytes into a polymer matrix. Polyelectrolytes
are polymers which contain ionic centers as part of their constitutional repeating units
[8, 67].

The ionic conduction in polymer electrolytes is based on the mobility of inorganic
salts which are dissolved in a polymer matrix. Polymers with a low glass transition
temperature are needed because the mobility and ionic conduction are determined by
the flexibility of the polymer matrix. However, relatively few polymers have low glass
transition temperature with sufficient solvation properties for salts, at the same time.

The most widely investigated polymers are based on polyethylene oxide (PEO;
[—CH$_2$CH$_2$O—]$_n$), where ether oxygen atoms are coordinated to the cations of the
salts, and thus effect the solvation [1]. However, PEO - lithium salt systems are
highly crystalline at room temperature and their conductivity values are in the range
of 10^{-7}–10^{-8} S cm^{-1}. On the other hand, the minimum conductivity needed for
an electrolyte in battery applications is 10^{-5} S cm^{-1} [68]. Conductivity of PEO-
based electrolytes increases sharply at ~ 65 °C, which is related with the melting
of the crystalline PEO phase, and above this temperature PEO exists predominantly
in amorphous phase. However, the dimensional stability of these electrolytes is poor
at temperatures above 65 °C [69, 70]. Intensive efforts have been conducted in order to

obtain a higher degree of amorphous phase of polymer matrix at room temperature and decrease the glass transition temperature in order to enhance the ionic conductivity at ambient temperature. Some of the strategies include the addition of plasticizers or fillers, and modifying the polymer chain such as side chains [71, 72, 73, 74].

The dependence of ionic conductivity values on the salt concentration was also investigated. It was found that initially conductivity increased as a result of addition of the charge carriers; however, as the salt concentration increased further, the conductivity reached a maximum and then dropped [75, 76, 77]. This behavior was explained by the ion pair formation at higher salt concentrations, along with inhibited ion transport due to the hindered motion of the polymer chains [78]. Therefore, ionic conductivity values in these systems can not be enhanced simply by increasing the concentration of the salt because of the formation of ion pairing, which reduces the number of carriers.

Solid polymer electrolytes are bi-ionic conductors having relatively high values of t_- and the corresponding low values for t_+. The transference number for cations in SPE usually ranges from 0.06−0.3, showing that lithium ions are the minority charge carriers [79]. This major obstacle in the development of a successful solid polymer electrolyte lithium cell is ascribed to the localization of counteranions near the anode and, as a result suppressing of the alkali metal cation supply from the anode. Hence, the cell electrolytes will be polarized [7]. The conclusion drawn from the previous investigations is that the salt in polymer electrolytes is not strongly dissociated and present in the form of ion pairs or ion agglomerates [80, 81]. The conductivity appears to depend on the dissociation of ion agglomerates in order to produce mobile cations [76]. The strong interactions between cation and solvating chain are one of the most important effects lowering the mobility and cationic transport numbers [81]. The conductivity is dominated by anionic motion as a consequence of strong chelation of the lithium ions by ether oxygens in the chains [6]. Angell et al developed 'polymer-in-salt' materials in order to increase the number of carrier ions, which were formed by mixing lithium salts with small quantities of the polymers (i.e. PEO, PPO) [82]. Minority component of these systems was the polymer, which imparted the mechanical integrity, and the ionic conductivity was not associated with the local polymer segmental motion [79].

Polymer-gel electrolytes have usually higher ionic conductivities at room temperatures when compared with SPE [83]. They are polymer networks swollen in a solvent which are formed by incorporation of a large amount of liquid to a polymer matrix [59, 84, 85]. The trapped liquid solutions are lithium salt solutions in organic solvent mixtures and common polymer matrices are poly(acrylonitrile) (PAN), poly(methyl methacrylate) (PMMA), poly(vinylidene fluoride) (PVdF) [86, 87]. To exemplify, $LiPF_6$−EC−DMC−PAN is a gel electrolyte formed by immobilizing an ethy-

lene carbonate (EC)—dimethyl carbonate (DMC) lithium hexafluorophosphate solution in poly(acrylonitrile) [88]. The high ionic conductivity takes place through the material in a gel like environment. However, gel electrolytes have generally poor mechanical strengths and are also encountered with a number of drawbacks commonly faced in liquid/aqueous electrolytes [79, 88].

On the other hand, polyelectrolytes having the opposite charges fixed on the polymer backbone provide single ion conductive matrices [89, 90]. In such a system, either cationic or anionic groups are chemically bonded to polymer chains, and the counterions migrate [67]. Owing to their single ionic conductor behavior, they have high transference numbers for mobile ions. For applications, like dry batteries, a single ion conductive matrix is needed. While polyelectrolytes are "single-ion conductors" both cations and anions contribute to conductivity in solid polymer electrolytes [68]. Additionally, polyelectrolytes do not have leakage problems in contrast to polymer gel electrolyte. Thus, polyelectrolytes are promising systems to cover requirements of a battery electrolyte.

In order to prevent counterion conductivity in SPE, the anions are fixed to a macromolecule and these macromolecular salts are alloyed with PEO. In this manner, some polymeric Li salts reported are sulfonate, carboxylate and phenoxide salts, which are covalently bonded to silicone, phosphazene, styrene or acrylic polymer backbones [91, 92, 93, 94, 95, 96]. Relating to the conductivity values at room temperature, for these single ion conductors having fixed anions in the polymer, Kobayashi et al. reported $1 \times 10^{-7} \, \mathrm{S \, cm^{-1}}$ with a carboxylate system [91] and Benrabah et al. proved $6 \times 10^{-7} \, \mathrm{S \, cm^{-1}}$ with a sulfonate system [97]. Moreover, Fujinami et al. developed siloxy aluminate polymers having ethylene oxide side chains with bulky groups in the vicinity of anion to protect ion pairing and obtained $2 \times 10^{-5} \, \mathrm{S \, cm^{-1}}$ at RT; however, the transport number of this system was below 1 ($t_+ = 0.71$) [98].

3.1.2 Ion Conduction in Polymer Electrolytes

Ion conduction in polymer electrolytes is a complex process, which is governed preponderantly by local motion of polymer segments, long range ion motions and intra-interchain transport of ions among the coordinating sites [99].

The transport of ions takes place mainly in the amorphous phase in polymer electrolytes [100]. The lithium salt is electrolytically dissociated in the polymer matrix, as it would dissolved in a polar liquid, and Li^+ ions are coordinated to the polymer through oxygen atoms in the ether chain (Figure 11) [68]. Cations are transported via association and dissociation steps of Li—O along with the local thermal motion of the

polymer chains. As a result of local relaxation and segmental motion of the polymer chains, ions are transported in the polymer electrolytes, which is more favorable if the host polymer is highly amorphous [101, 102].
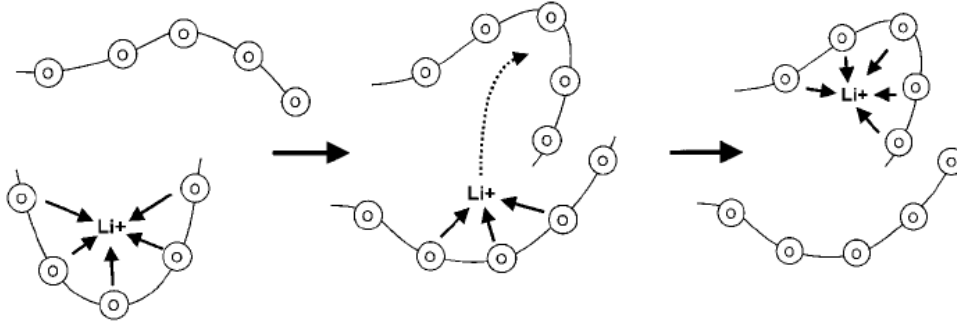
Figure 11: Schematic representation of Li diffusion assisted by the segmental motion of the PEO matrix. Ether oxygen atoms of PEO are represented with the circles.

It was previously preconceived that the amorphous phase in the polymeric host was predominantly responsible for the fast ion transport in SPEs. In accordance to that, the ionic conduction of polymeric electrolytes was believed to be higher when the amorphousity of the polymer matrix was increased [100]. The main investigations, in turn, were carried out to develop polymeric hosts having large amorphous phases and low glass transition temperatures with the purpose to obtain faster ion transport, supported by the good flexibility of the polymer chains. The disordered environment, created by the polymer chain motion at temperatures higher than glass transition temperature, was thought critical in ion transport. However, Bruce et al. have recently presented that crystalline polymer hosts in SPEs could also sustain high ionic conduction [103, 104].

Two dominant conduction mechanisms have been observed for the ion transport phenomenon in polymer electrolyte materials on the basis of the temperature dependent conductivity studies. Thus, these materials can further be separated into two groups depending on their conductivity variations with temperature [74].

The first group of polymer electrolytes obeys the Vogel-Tamman-Fulcher (VTF) equation:

$$\sigma \;=\; \frac{A}{\sqrt{T}} \, exp[-\frac{E_a}{k(T - T_o)}], \tag{1}$$

A = pre-exponential factor,

E_a = pseudoactivation energy,

T_o = equilibrium glass transition temperature, which T_o

is close to glass transition temperature of the polymer electrolyte.

The plot of VTF conductivity against reciprocal of temperature exhibits a typical nonlinear behavior [58]. This indicates that the ionic hopping motion of the conductivity mechanism couples with the segmental and/or relaxation, breathing motion of the polymeric chains [105].

On the other hand, the second group obeys the Arrhenius type equation:

$$\sigma = \sigma_o\, e^{-\dfrac{E_a}{kT}}.$$

The linear Arrhenius behavior indicates that the ion transport of the material is mediated by a simple hopping mechanism which is decoupled from the breathing of polymer chain.

3.2   Crystalline Electrolytes

3.2.1   Ion Conduction in Crystalline Electrolytes

Ionic conduction in crystalline electrolytes takes place with the hopping of ions from site to site in a crystal structure under the influence of an electric field. The mobile ions can be cations or anions such as H^+, Li^+, Na^+, Cu^+, Ag^+, O^{2-} and F^- [10, 106]. Vacancy and interstitial migrations are recognized as two general classes of mechanisms for ionic conduction for isolated hopping of ions [107]. As a result of formation of a thermally generated Schottky effect (a vacancy pair of a cation and anion) or existence of charged impurities, creation of some empty sites, which should be occupied in the ideal structure, led to the vacancy migration. In vacancy migration process, an ion can leave its site empty by hopping into an adjacent vacancy (Figure 12-a).

In order to form a Frenkel defect, the ions are moved from their lattice sites into an interstitial site, which are empty in an ideal structure. Following this, the ions located in interstitial sites can hope into the neighbouring interstitial sites (Figure 12-b) [108].

Apart from these two mechanisms, cooperative movement of two or more ions are also observed in solid electrolytes, which is named as interstitialcy mechanism. In order

to operate this mechanism, one or more neighbouring ions are to be pushed elsewhere in order for an ion to jump to a neighbouring or interstitial site (Figure 12-c) [109].

The immobile sublattice structure in crystalline electrolytes defines the sites of the mobile ions. The conduction pathways for the mobile ions can be a one, two or three dimensional immobile ion sublattice in crystalline electrolytes. The mobile ion sites in crystalline electrolytes are distinctly determined by the structure of the immobile sublattice. Therefore, a series of definite hops between adjacent sites in the conduction pathways will lead
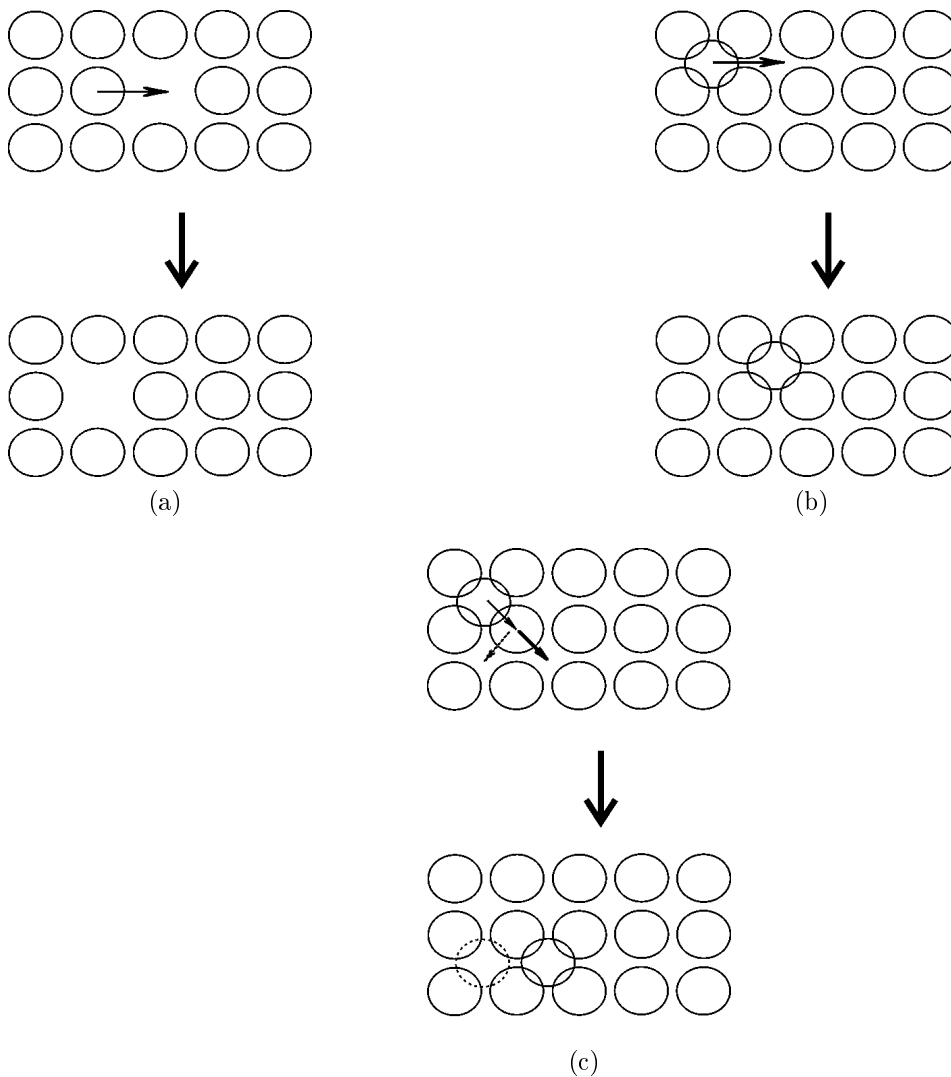
Figure 12: Transport of ions by (a) vacancy mechanism, (b) interstitial mechanism and (c) interstitialcy mechanism showing two possible locations of ions after movement.

to the ionic conduction. This random notion of ion hops represents the basis of random walk theory.

The ionic conductivity of a material is dependent on the concentration of the mobile species, n, their charge, q and mobility, μ, which can be expressed by the equation:

$$\sigma \;=\; n\; q\; \mu.$$

In order to increase the n value, aliovalent or heterovalent doping is an important way, which includes the partial replacement of one ion type with another ion having a different formal charge. Conductivity can increase sharply, if simultaneously generated interstitial ions or vacancies, that are formed to keep the charge balance, can migrate.

Richard et al. proposed a mechanistic classification and they suggest four types of mechanisms for ion migration, which are [110]:

1. Conventional transport of defects by uncorrelated jump processes. The transport is by means of conventional hopping process, and the only difference is the high concentration of defects.

2. Highly correlated mechanism, in which fast ion transport is effected by collective movement of several ions. Li_3N is an example of this type.

3. Liquid like diffusion mechanisms, which is observed if the mobile sublattice is highly disordered that cations can move in a more fluent manner with flat potential surface.

3.2.2   Random Walk Model

Ionic transport is a thermally activated diffusion process and the free energy required for an ion to jump to an energetically equivalent neighbour lattice site is represented by ΔG_m. To describe ion conduction, the generally used model is random walk of the mobile species. In this model, the mobile ions move independently of one another and diffusion is caused by the isolated jumps [10, 111, 112].

The ionic conductivity is expressed by the equation:

$$\sigma \;=\; n\; q\; \mu, \tag{2}$$

$\sigma =$ ionic conductivity,

n = charge carrier concentration,

q = charge of mobile ions,

μ = mobility of the charge carriers.

The concentration of charge carriers is defined with,

$$n \;\; = \;\; N \;\; c,$$

N = number of structural sites for the mobile ions,

c = degree of occupation of the N positions.

According to the Nernst-Einstein expression, the ionic conductivity is related to the diffusion coefficient of ions. Hence, this expression suggests the ionic conductivity as:

$$\sigma \;\; = \;\; \frac{nq^2}{kT} \;\; D \tag{3}$$

n = number of ions per unit volume

D = diffusion coefficient

k = Boltzmann constant

T = Absolute temperature

The mobility can be derived from the equations 2 and 3 as in the form of following expression:

$$\mu \;\; = \;\; \frac{q}{kT} \;\; D \tag{4}$$

where diffusion coefficient is defined by:

$$D \;\; = \;\; \frac{1}{2d} \; z \; (1-c) \; l^2 \; v_o \; e^{-\frac{\triangle G_m}{kT}}$$

d = dimensionality of the conduction for the mobile ion,

z = number of nearest neighbour sites,

$(1-c)$ = the availability of vacant sites,

l = jump distance between two energetically equivalent sites,

v_o = attempt frequency,

$$\triangle G_m = \text{motional free energy,}$$

with replacement of,

$$e^{-\frac{\Delta G_m}{kT}} = e^{-\frac{\Delta H_m}{kT}} \cdot e^{\frac{S_m}{k}}$$

and the geometry factor, γ, as,

$$\gamma = \frac{1}{2d} \, z \, e^{\frac{\Delta S_m}{k}}$$

the diffusion coefficient can be found as,

$$D = \gamma \, (1-c) \, l^2 \, v_o \, e^{-\frac{\Delta H_m}{kT}} \, .$$

Substitution of diffusion coefficient into equation 3 gives,

$$\mu = \frac{q}{kT} \, \gamma \, (1-c) \, l^2 \, v_o \, e^{-\frac{\Delta H_m}{kT}} \, ,$$

and substitution into equation 1 gives the relation for conductivity:

$$\sigma = \gamma \, N \, \frac{q^2}{kT} \, c \, (1-c) \, l^2 \, v_o \, e^{-\frac{\Delta H_m}{kT}} \, . \tag{5}$$

With the substitution of preexponential factor $A = N \, c \, \frac{q^2}{k} \, \gamma \, (1-c) \, l^2 \, v_o$ and $\triangle H_m$ = E_a in equation 5, the Arrhenius relationship is obtained:

$$\sigma = \frac{A}{T} \, e^{-\frac{E_a}{kT}} \, . \tag{6}$$

Arrhenius equation gives the temperature dependence of ionic conductivity. It is valid within the temperature regime where the material does not have any phase transformation.

The main requirements for the high diffusivity in solids are deduced as high density of mobile ions (c), the availability of vacant sites which can be accessed by the mobile ions $(1 - c)$ and good connectivity among the sites with conduction channels having low free energy barriers (E_a) between the sites. The ease of ion hopping is presented

by the activation energy, which is related to the openness of conduction pathways in the crystal structure [10, 113].

3.2.3   Crystalline Electrolytes

Solid electrolytes have rather special crystal structures, which can have open tunnels or layers and through which the mobile ion can move. Their structures are generally composed of 1-, 2- or 3- dimensional network of channels and these pathways for conduction are positioned throughout the materials immobile ion sublattice. The ions move along rapid diffusion pathways which are defined by the crystal structure [114].

Sodium $\beta-$aluminas and NASICON are well studied sodium ion conductors. Sodium $\beta-$aluminas are the archetypal 2-D conducting materials, which conduct well at room temperature (1×10^{-2} S cm^{-1}) [12, 115, 116]. The mobile Na$^+$ ions are situated between the densely packed spinel blocks of alumina that are bridged by oxygen in these non stoichiometric sodium aluminate compounds [117]. The crystal structure having open conduction pathways and a large number of partially occupied sites permit a 2 - dimensional diffusion of sodium ions and as a result a high Na$^+$ conductivity in beta aluminas [118].

$Na_3Zr_2PSi_2O_{12}$, which is generally referred to as NASICON (Na superionic conductor), is a ceramic material similar to $\beta-$aluminas; however, possessing a higher Na$^+$ conductivity at 300 °C [119]. The crystal structure allows a relatively open 3 - dimensional network of sites and pathways for the mobile sodium ions, and the ions can move through channels [120]. LISICON, which is an analogous compound to NASICON, was synthesized short after [13].

Another well known example of the layer structure is lithium nitride, Li$_3$N, which is a two dimensional conductor having sheets of Li$_2$N separated by Li$^+$ ions. It has the highest lithium ion conductivity of all crystalline materials (1×10^{-3} S cm^{-1} in plane; 1×10^{-5} S cm^{-1} perpendicular to the layers) [121, 122, 123].

AgI is one of the first materials, which shows high ionic conductivities. The concepts of average occupational of lattice sites and the "liquid sublattice" were introduced by Strock [124]. The discovery of high conductive RbAg$_4$I$_5$ was stimulated during the exploration of silver containing ternary systems [55].

The structural features required for a good ion conductor can be summarized as follow [10, 44]:

a) The number of mobile ions and available empty sites for the mobile ions to jump should be large.

b) The potential energies of the empty and occupied sites should be similar with a low activation barrier for jumping between neighbouring sites.

c) The structure should have a framework, preferably three dimensional, which has open channels allowing the migration of ions.

d) The immobile framework should be highly polarizable.

Part III

SPECIAL PART

4   Polyelectrolytes

4.1   State of the Arts and Concepts

The area of ion conductive solvent free polymer electrolytes has gained considerable attention due to their conduction of electricity by the migration of ions, which have potential applications in batteries [125]. There has been severable efforts to develop polymer-salt complexes which do not have leakage problems. Solid polymer electrolytes (SPEs), in contrast, are bi-ionic electrolytes and the bulk conductivity is primarily due to anion mobility [99, 126]. The transference number of lithium is far less than that of the anion; therefore, migrations of both, anions and cations, result in a local concentration of anions and significant decrease in ionic conductivity [7, 81, 90, 93, 127, 128, 129, 130]. As a result of strong coordination of lithium ions with the oxygen atoms of ether groups [131, 132], the lithium transference number in these conventional matrices like poly(ethylene oxide) is around 0.2−0.3 [2, 3, 4, 5, 6]. Since low lithium transference number in these systems is a major problem, the essential requirement in providing superior solid polymeric electrolytes is to design systems that exhibit only cation migration. In solid polyelectrolytes, anions are incorporated as part of a polymer chain [67]. Therefore, by chemically binding the opposite charges on the polymer chain in these single ion conductive matrices, contrary to SPEs, high lithium ion transference numbers are achieved, which is essential for applications [129, 133].

Hitherto, a number of approaches for generating single ion conductive polyelectrolyte matrices have been proposed. In order to avoid anion conduction, Takeoka proposed to resort to single ion-conductive systems, which are accessible by blending, copolymerization and homopolymerization [127]. In this manner, the first proposed route was blending polyelectrolytes with soft segments; i.e. poly(oxyethylene) [95, 134, 135]. Blends of poly(ethylene oxide) and poly(2-(4-carboxyhexafluoro-butanoyl-oxy) ethyl methacrylate-Li-salt) (Figure 13-a) were investigated for single ion conduction by Bannister et al. [136]. Thereby, polyethers and polyanions were mixed to obtain

single ion conductors; however, the different polymers should be compatible in order to avoid the gradual phase seperation problems in blend systems, which would decrease the ionic conductivity. Therefore, a single-component system is preferable. The two methods in order to achieve a single component system are copolymers and homopolymers. Copolymers from soft segments and polyelectrolytes were further developed [91, 93, 137, 138, 139, 140]. Room temperature conductivities of oligo(oxyethylene) methacrylate and alkali metal methacrylate copolymers were reported in the order of 10^{-7} S cm^{-1} [91, 93] (Figure 13-b). Different matrices, like siloxane copolymers having oligo(ethylene oxide) side chains with immobilized pendant sulphonate moieties, were also investigated and the conductivities were reported as 10^{-7} S cm^{-1} at room temperature [137] (Figure 13-b). In order to obtain a single component cation conducting polyelectrolyte, a monomer having a carrier ion source was homopolymerized [141, 142], an example of which is presented in Figure 13-c.
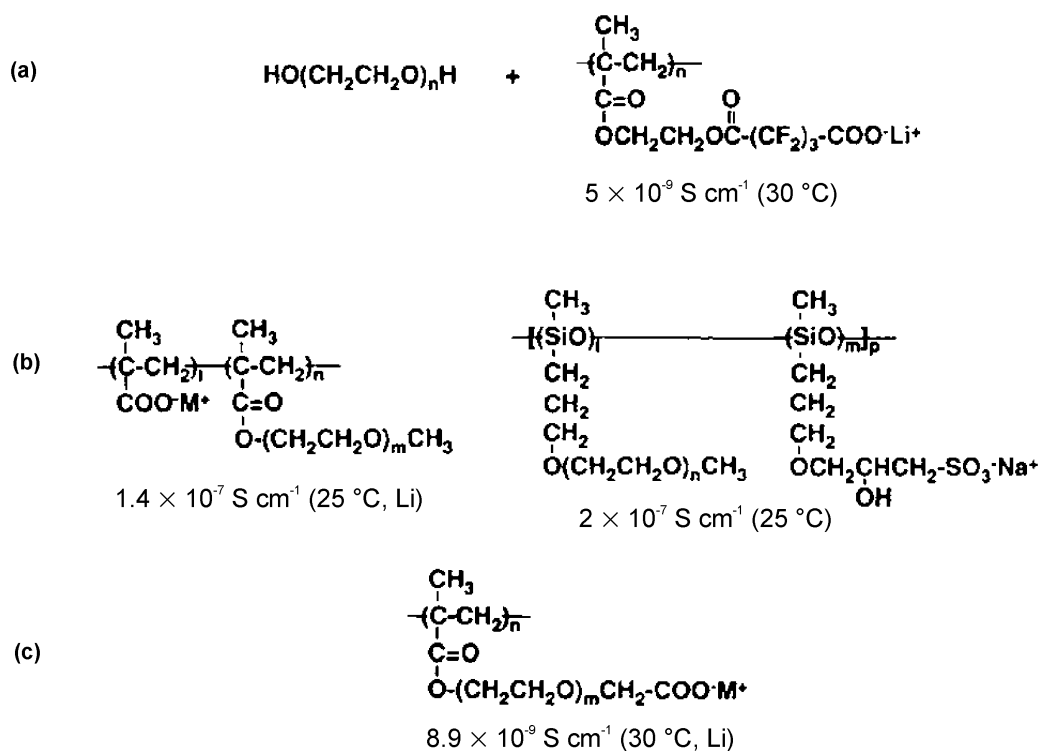
Figure 13: Examples of (a) blend, (b) copolymer and (c) homopolymer matrices for single ion conduction [127].

A number of strategies have been developed to obtain high conducting polyelectrolytes. However, tight ion pairing seems to occur which significantly reduces the

mobility of the charge carriers [143]. Ion pairing effect was reduced with bulky substituent groups which prevent close approach of the cations [126, 144, 145]. On the other hand, bulky substituents increase the rigidity and glass transition temperature which in turn lead to decrease the ion mobility [90]. Plasticizers, which are additives that enhance the plasticity or fluidity of the material, were added in order to enhance flexibility of these hard materials [90, 144, 146, 147, 148]. For example, poly(ethylene glycol) was added as a plasticizer to sodium poly(styrene sulfonate) [146]. Another approach was linking of short chain poly(ethylene oxide) groups covalently to the polyelectrolytes. Self-plasticization was provided with these short chains [90]. Comb like polyelectrolytes, bearing anionic groups and short chain polyether linkages in the backbone, were reported [9, 90, 149]. Therefore, incorporation of plasticizers enhance the ionic conductivity. On the other hand, they deteriorate the mechanical properties of the materials [147, 148].

In an alternative approach to decrease bi-ionic contribution, polymer matrices bearing anion trapping Lewis acidic units were developed [81]. For this purpose, Lewis acidic organoboron units were incorporated into the polymer chains of SPEs [150]. A number of groups carried out research concerning polymer electrolytes bearing borate functional groups. Kato et al. reported that increasing borate ester group concentration incorporated in polyethylene glycol polymer electrolytes increased the transference number of lithium of the dissolved salt (Figure 14-a) [151]. Materials having boroxine rings and pendant or network oligo(ethylene oxide) units were reported by Mehta and Fujinami et al. (Figure 14-b) [152, 153, 154]. The transference number of lithium in these polymer electrolytes was reported as 0.75 by using $LiBF_4$ salt [153, 154]. Although the transference number of lithium was higher than the convential SPEs obtained by dissolving salts in polymers, it was far below unity.

Matsumi et al. prepared polymer electrolytes from organoboron polymers. The authors reported that the transference number of lithium was increased over 0.5 in a poly(propylene oxide) polymer electrolyte having alkylborane end units [3]. They also investigated organoborate polymers bearing ethylene oxide units and generated polymer electrolytes from these polymers by addition of lithium salts, which is shown in Figure 14-c [155]. However, polymer electrolytes obtained from these polymers showed the transference number of lithium around 0.35 [155, 156]. Also, electrolytes were prepared by mixing comb like organoboron polymer bearing oligo(ethylene oxide) units with lithium salts [157]. These polymer electrolytes containing borate and oligo(ethylene oxide) units have low transference numbers for cation; i.e. $t_+ = 0.38$ at 30 °C [157]. An important approach to attain unity in lithium transference number is to immobilize the polymer network by covalently fixing opposite anions to the

macromolecular chain [158]. The mobility of anion is smaller than the cation as the anion sites are fixed on the chain. Solely cations will contribute to the conduction when the anions are chemically bound into the chain in these polyanionic species [129]. When anions are immobilized into the polymer matrix, the anions are not mobile and the number of charge carrier ions are decreased compared to the bi-ionic polymers; therefore, lower ionic conductivity values are obtained in single ion conductors. The design of the chains in immobilized anion bearing polymer matrices can be tailored in two different ways. The charged groups can be covalently bound either as a pendant group in the side chains or in the backbone of the polymer chain.
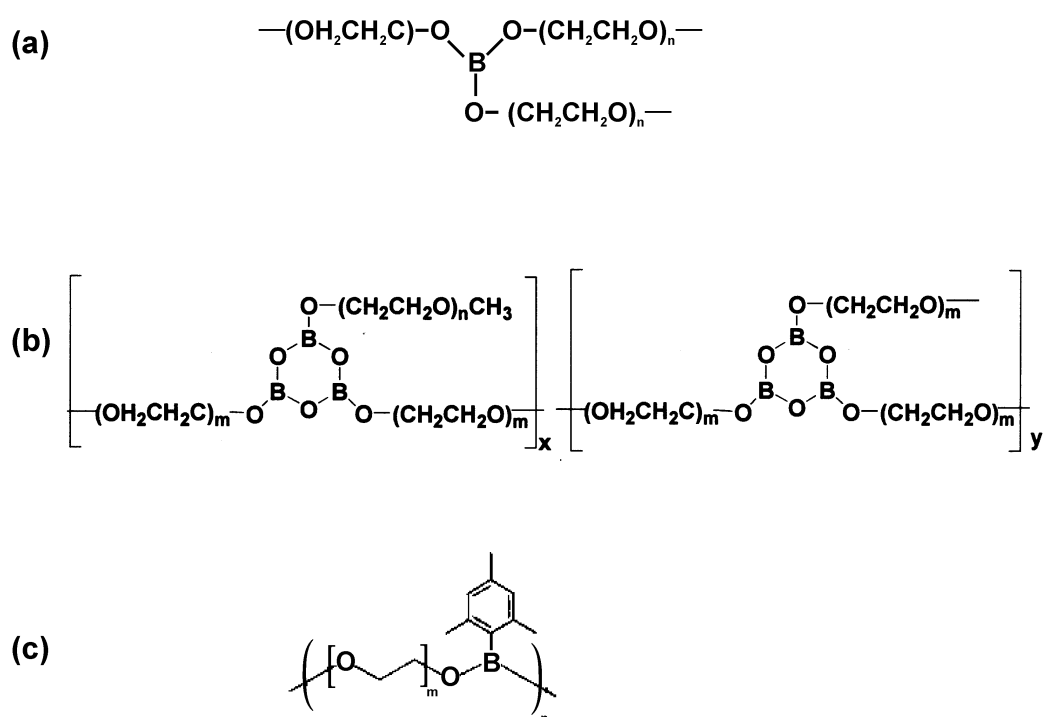
Figure 14: Examples of organoborate solid polymer electrolytes.

As a plausible model for the single ionic nature, several different side-chain anionic polymers with lithium ion counterparts were developed and some examples of charged groups investigated in these polyelectrolytes include :

- Carboxylate; —COO$^-$ [9, 91, 93, 136, 138, 140, 141, 142, 159, 160],
- Sulfonate; —SO$_2$O$^-$ [95, 136, 137, 139, 161, 162, 163, 164, 165, 166],
- Phenolate; —PhO$^-$ [145, 167].

For example, Florjanczyk et al. reported that the ionic conductivities for the lithium carboxylate polymers were in the range of 10^{-9}—10^{-7} S cm^{-1} at 30 °C [9]. Low conduc-

tivity values were obtained for the polyelectrolytes bearing the charged groups attached as a pendant group due to the tight ion pairing and ionic interactions.

In a further development, anions are covalently bounded in the main chain in order to decrease ion pairing. Some examples of the immobilized polyelectrolytes by anchoring the anionic groups in the main chain are:

— Tetraoxoborate; $(—O)_4B^-$ [4, 131, 135, 168, 169, 170, 171, 172, 173],

— Diphenyldioxoorganoborate; $(—O)_2Ph_2B^-$ [5, 174],

— Tetraoxoaluminate; $(—O)_4Al^-$ [128, 168, 175, 172, 173, 176, 177],

— Thioaluminate; $(—S)_4Al^-$ [178],

— Siloxyaluminate; $(—SiO)_4Al^-$ [98, 179, 129].

Chetri et al. prepared lithium, sodium and potassium derivatives of poly(vinyl borate) gel polyelectrolytes, which had the transport number of 0.83 for lithium [169]. These materials showed poor conductivity values (i.e. 7.3×10^{-9} S cm^{-1} at 25 °C for potassium derivative) and poor mechanical properties because of the jelly nature [170, 171] (Figure 15-a). Matsumi et al. immobilized the borate anion in the polymer chain containing oligo(ethylene oxide), which showed ionic conductivity of 9.45×10^{-7} S cm^{-1} at 50 °C with a lithium ion transference number of 0.82 [155, 156] (Figure 15-b). In another work, the same authors modified the chains of these oligo(ethylene oxide) containing poly(lithium organoborates), which is shown in Figure 15-c, but the transference number of these polyelectrolytes were not reported [180].

Doan et al. reported the main chain anionic polyelectrolytes containing a network of tetraalkoxyaluminates linked by polyethers and the ionic conductivity was about 10^{-7}–10^{-8} S cm^{-1} at 50 °C due to the strong ion pairing (Figure 15-d) [175]. Polyelectrolytes from lithium siloxy aluminate polymers with oligo ethylene oxide side chains were reported by Fujinami et al. (Figure 15-e) [98]. Although a high conductivity in the order of 10^{-5} S cm^{-1} was reported, the transference number of lithium was found as 0.71 [98]. Aoki et al. prepared polyelectrolytes with oligo(ethylene oxide) side chains bonded to the aluminate or borate backbones, which is shown in Figure 15-f. The authors showed that partial negative charge was dispersed on oxygen atoms around the boron or aluminum atoms, and ion pairing occured between lithium and these oxygen atoms. Furthermore, the same authors reported that borate polymers exhibited higher conductivities than aluminate polymers as a result of the increased mobility of lithium ion in borate polymers, because of the weaker interaction between lithium ion and oxygen atoms around the boron atom [173].

Single ionic conductors have one to two orders of magnitude lower ionic conductivities compared to bi-ionic conductors under the same conditions. This difference is originating from the fact that in polymer-salt complexes, the anion is usually the

predominant charge carrier with a transport number typically greater than the one of the cation, because cation motions are inhibited by solvation from the macromolecular chain. Thus, fixing and immobilizing the anion would result in lower conductivities because of having fewer ion carriers [167]. Ion pairing can also occur in polyelectrolytes between lithium cations and counter ions fixed to the polymer chains, which will reduce the number of available conduction ions and conductivity [98, 150]. Sterically hindered anionic centers can be employed to reduce the ion pairing [167]. However, simulations showed that the performance in battery applications was improved even by using polyelectrolytes with one order of lower conductivity in comparison to solid polymer electrolytes [7].
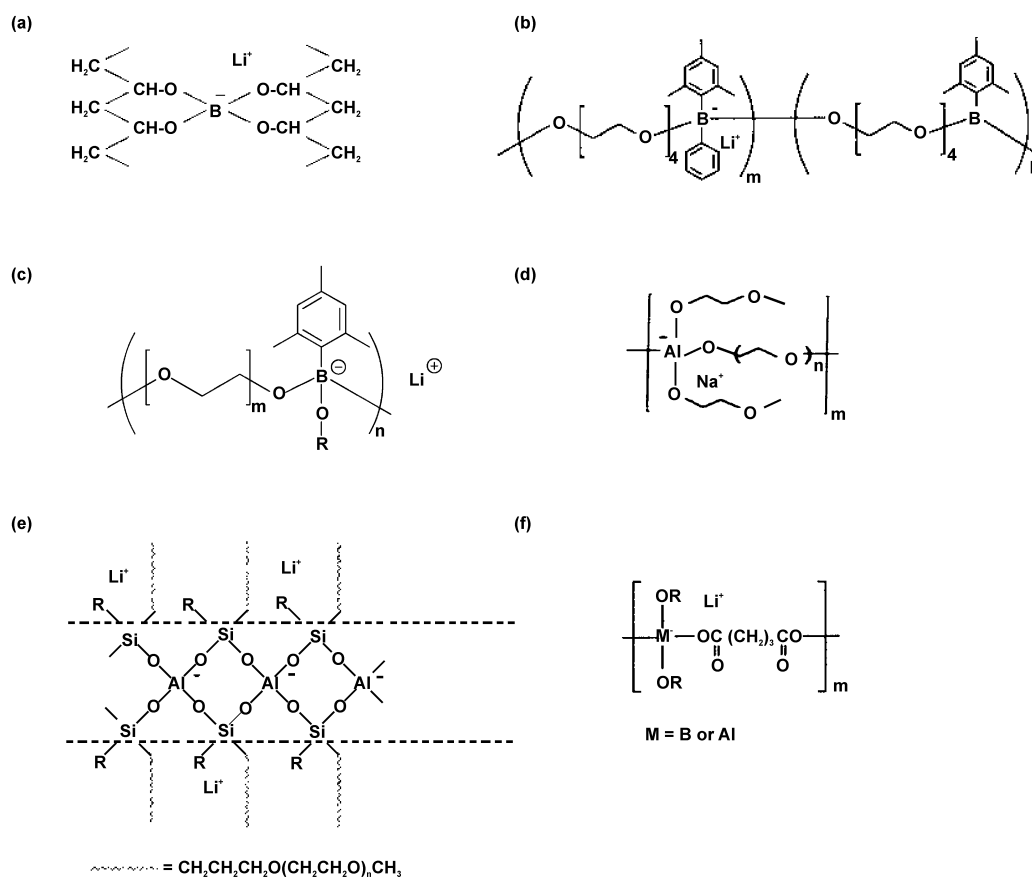
Figure 15: Examples of polyelectrolytes

Hence, a polyelectrolyte appears to be the best system to cover the requirements for a battery electrolyte. The research on polymer backbones has mostly been based on oxygen-containing monomers, such as ethers in poly(ethylene oxide) and poly(propylene oxide) and polysiloxanes [90]. Despite the fact that oxygen atoms strongly coordinate

towards lithium ion precluding the transport of cation, oxygen atom is characteristicly present and oligo(oxyethyleneoxide) is representatively employed in the ion conductive polymer matrices [4, 5, 131, 132]. Coulomb trapping of the cation can easily occur, and oxygen can coordinate to the mobile cation which creates locally fixed polymer framework [181, 182]. These effects lead to reduce the conductivity [81, 95]. Moreover, binding of lithium cations by ether oxygen atoms prevents the transport of the cation [6, 173, 132, 183] and; therefore, the transport number of cation becomes very low (around 0.2–0.3) in these polyether electrolytes [2, 5, 4, 3, 6]. To the best of our knowledge, all of the polyelectrolytes that were previously investigated have oxygen atoms or Lewis base groups either in the main backbone or on the side chains.

The goal in the present work is to obtain a polyelectrolyte with a high transference number, a high charge carrier concentration and no strong ion pairing. Our motivation was to develop solid polyelectrolytes bearing alkylborate units, in which the anionic groups were immobilized in the chain. Previously, a borate containing polyelectrolyte was also synthesized in our group; however, the material could not fully characterized [184]. Moreover, lithium conducting polyelectrolytes based on organoaminoalanates were developed by Jansen et al. and a high lithium conductivity ($\sigma = 0.01$ S cm^{-1} at 297 °C) was achieved for phenyl substituted polymer [185]. Bulky alkyl groups were incorporated around the anion in order to inhibit close approach of the lithium cations and reduce ion pairing. Ion pairing is a significantly important factor that decreases the conductivity by reducing the cation mobility in polyelectrolytes. The other important aspect in the design is that the polymer backbones do not bear oxygen groups, on contrary to the traditional oxygen atom bearing polyelectrolytes, which are known to inhibit the mobility of lithium ions by trapping them; therefore, reducing the conductivity. Lithium was inserted into the polymer by addition of alkyl lithium reagents or by the educt lithium tetravinylborate. The effect of different alkyl groups on conductivity was investigated. For this purpose, a series of lithium conducting solid anionic polyelectrolytes with the repeating units of tetrakis(alkylboryl)borate groups were prepared. The ionic conductivities and structures have been analyzed along with the effect of annealing. In order to develop these novel polyelectrolytes, hydroboration reactions were applied. In a further attempt, modifications in the main chain were proceded by incorporation of silicon atoms in the main alkyl borate chain of the lithium polyelectrolytes.

4.2   Poly[lithium tetrakis(ethyleneboryl)borate] (PLEB)

4.2.1   Synthesis and Characterization of Reactants

All reactions were carried out in a purified argon atmosphere using standard Schlenck techniques in rigorously dried reaction apparatus and solvents. Diethyl ether (Merck), n-hexane and boron trifluoride etherate (Merck) were distilled before usage. Commercially available tetravinyltin (Aldrich), n-butyl lithium (1.6 M in hexane, Acros) and monoborane-THF (1 M, Aldrich) complex were used without further purification.

The liquid NMR samples were prepared by using standard Schlenk techniques in a purified argon atmosphere. The samples were prepared in the NMR tubes at low temperatures by using 0.5 ml deuterated THF (C_4D_8O, Sigma Aldrich) and the measurements were carried out at -10 °C. $Si(CH_3)_4$ was used as an external standard for ^1H and ^{13}C NMR measurements. BF_3. $O(CH_2CH_3)_2$ and the solution of 9.7 m LiCl in D_2O was applied as an external standard for ^{11}B NMR and ^7Li NMR measurements, respectively.

4.2.1.1   Vinyllithium (1)

Vinyllithium was synthesized according to the procedure by Seyferth et al. [186] with the reaction:

$$Sn(CH{=}CH_2)_4 + x \text{ n-BuLi} \rightarrow \text{n-Bu}_x Sn(CH{=}CH_2)_{4-x} + x \text{ LiCH}{=}CH_2$$
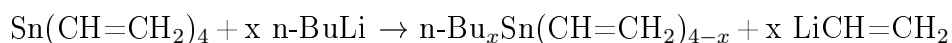
Transmetalation reaction of tetravinyltin and n-butyllithium in n-hexane was applied to synthesize vinyllithium, where x = 2.33 and n-Bu = $CH_2CH_2CH_2CH_3$. Vinyllithium is a highly pyrophoric material when exposed to the air. The product was kept below 0 °C and used directly after production.

Preparation of vinyllithium

The apparatus consisted of a 250 ml three-necked flask which was equipped with a filter (P3 pore size) from one neck. A 100 ml two-necked flask was placed on the other side of the filter. 2.7 ml (0.015 mol) tetravinyltin was added into the three-necked flask in the argon flow. Afterwards, 70 ml distilled n-hexane and subsequently 22 ml (0.035 mol) n-butyllithium solution (1.6 M, solvent n-hexane) were added under continuous stirring. White vinyllithium precipitates were observed in the solution after a short while. The reaction solution was concentrated with a rapid argon flow until approximately 30 ml of solution was left in the flask. Approximately 1.2 g (0.035 mol) precipitated vinyllithium was filtered and washed three times with 10 ml distilled hexane. It was further dissolved in 80 ml diethyl ether.

Characterization of vinyllithium

The identification of vinyllithium, which was dissolved in diethyl ether, was achieved with liquid NMR by measuring the signals of ^{13}C, ^{1}H and ^{7}Li.

The ^{13}C NMR of vinyllithium, which is given in Figure 16, showed the signals at 133.0 ppm assigned to the $=\underline{C}H_2$ and at 183.7 ppm assigned to $=\underline{C}HLi$. ^{1}H NMR spectrum indicated three sets of doublet of doublet chemical shifts which were positioned at 7.21 ppm, 6.60 ppm and 5.85 ppm for the $LiC\underline{H}^{gem}CH_2$, $LiCHCH\underline{H}^{trans}$ and $LiCHCH\underline{H}^{cis}$, respectively (Figure 17). The coupling constants for geminal H were found as 19.05 Hz for J (H^{gem},H^{trans}) and 23.88 Hz for J (H^{gem}, H^{cis}). For the trans H, the coupling constants had the values of 7.56 Hz for J (H^{trans}, H^{cis}) and 19.05 Hz for J (H^{trans}, H^{gem}). Finally, the observed coupling constants for cis H were 7.56 Hz for J (H^{cis}, H^{trans}) and 23.88 Hz for J (H^{cis}, H^{gem}). The ^{7}Li NMR spectrum of vinyllithium was also measured and the signal was found to be centered at -0.9 ppm as can be seen in Figure 18. Liquid NMR of vinyllithium in tetrahydrofuran solution was investigated by Bauer et al. The chemical shifts and the coupling constants in this study were found to be quite consistent with the results published by Bauer et al. [187].
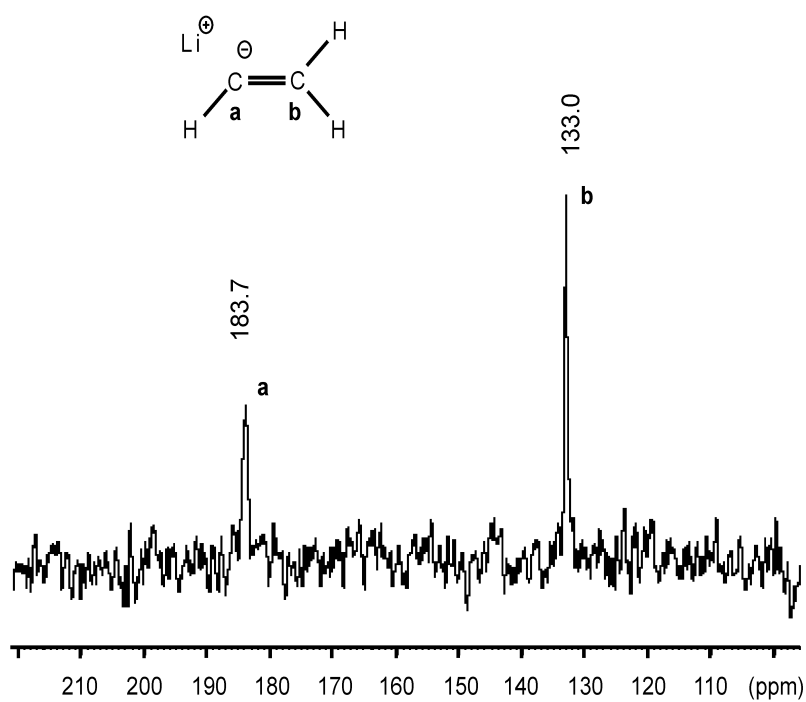
Figure 16: ^{13}C-NMR spectrum of vinyllithium solution in diethyl ether.
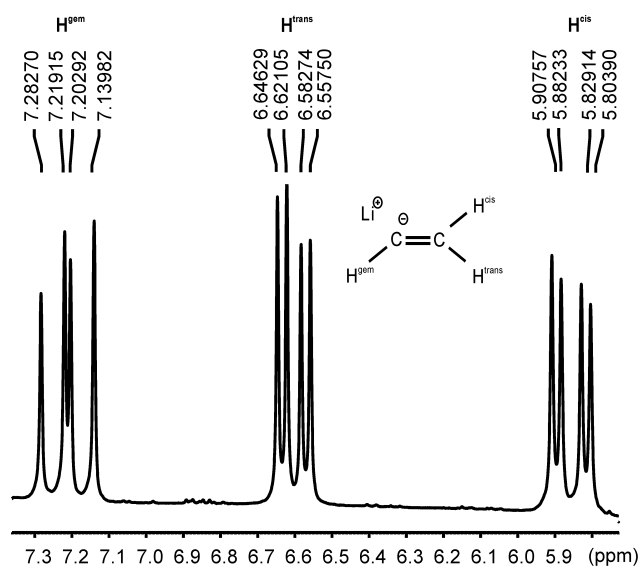
Figure 17: ^{1}H-NMR spectrum of vinyllithium solution in diethyl ether.
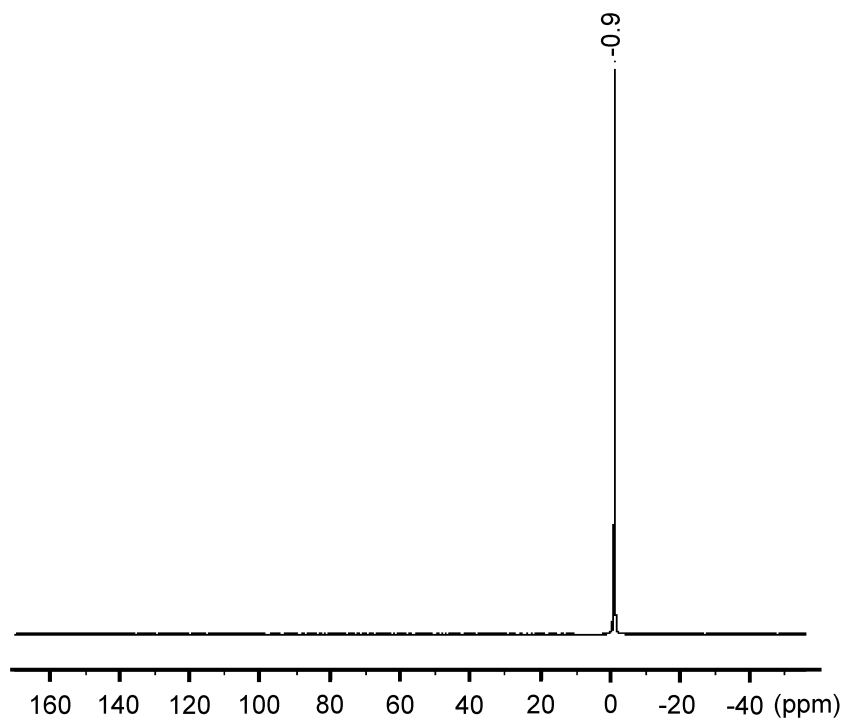
Figure 18: ^{7}Li-NMR spectrum of vinyllithium solution in diethyl ether.

4.2.1.2   Boron Trifluoride Etherate, $BF_3 \cdot O(CH_2CH_3)_2$

Boron trifluoride etherate (Merck) (bpt.: 126 °C) was distilled under argon, and the purified product was kept below 0 °C. In the synthesis, freshly distilled $BF_3 \cdot O(CH_2CH_3)_2$ was used.

$BF_3 \cdot O(CH_2CH_3)_2$ serves as a calibration standard for the NMR spectrometers, and the ^{11}B NMR of boron trifluoride etherate is given in the Figure 19 which shows the typical signal at 0 ppm.

4.2.1.3   Lithium Tetravinylborate, $Li[B(CH{=}CH_2)_4]$ (2)

Lithium tetravinylborate was synthesized by applying the route as developed by Seyferth et al. [186], according to the following equation:
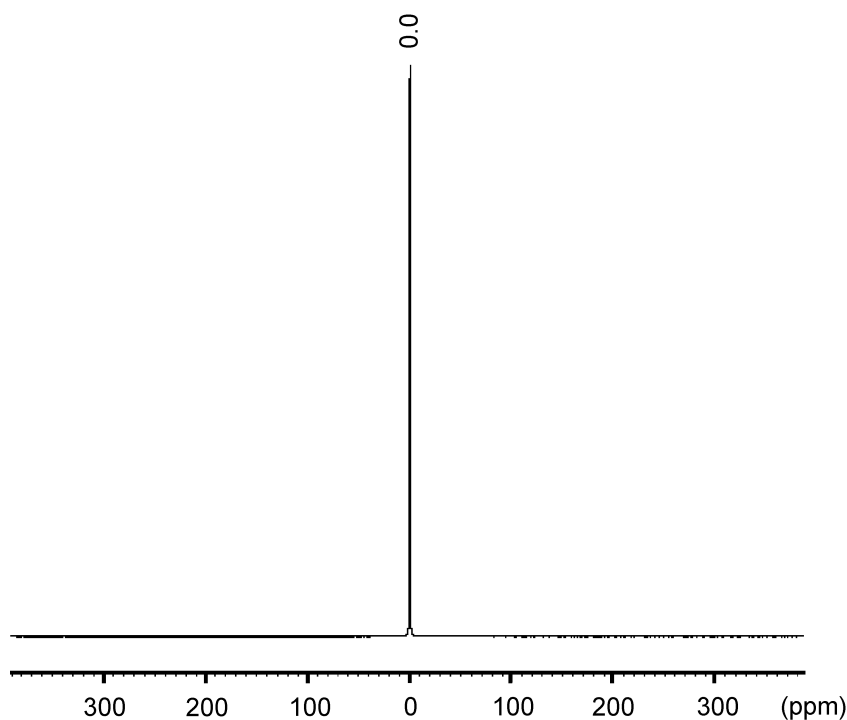
Figure 19: ^{11}B-NMR spectrum of boron trifluoride etherate.

$$4\,\mathrm{LiCH{=}CH_2} + \mathrm{BF_3{\cdot}O(CH_2CH_3)_2} \quad \rightarrow \mathrm{Li[B(CH{=}CH_2)_4]} + 3\,\mathrm{LiF} + \mathrm{O(CH_2CH_3)_2}$$

The reaction of vinyllithium in diethyl ether with the boron trifluoride etherate was produced the air sensitive lithium tetravinylborate in diethyl ether solution.

Preparation of lithium tetravinylborate

The apparatus consisted of a 250 ml three-necked flask which was equipped with a reflux column on one neck. Approximately 1.2 g (0.035 mol) vinyllithium, dissolved in 80 ml ether, was placed into the three-necked flask under the argon flow. Afterwards, 0.6 ml (0.005 mol) freshly distilled boron trifluoride etherate was added dropwise into the three-necked flask with vigorous stirring. The mixture was refluxed for 12 hours and subsequently filtered by using a filter with P3 pore size and 100 ml volume. The obtained lithium tetravinylborate/diethyl ether solution was stored below 0 °C.

Characterization of lithium tetravinylborate

An ether solution of lithium tetravinylborate was characterized by employing ^{13}C, ^{1}H, ^{11}B and ^{7}Li liquid NMR measurements. The ^{13}C NMR signals of lithium tetravinylborate were found at 113.1 ppm and 165.3 ppm that is given in Figure 20. The signal at 113.1 ppm was assigned to LiB $(CH=\underline{C}H_2)_4$ and the one at 165.3 ppm to LiB$(\underline{C}H=CH_2)_4$. The ^{1}H NMR spectra and the chemical shift values were given in Figure 21. The hydrogen chemical shifts were observed as doublet of doublet of quartets (ddq) for both cis (LiB$(CH=CH\underline{H}^{cis})_4$) and trans (LiB$(CH=CH\underline{H}^{trans})_4$) hydrogen atoms. The chemical shifts for cis and trans hydrogen atoms were centered at 4.77 ppm and 4.96 ppm, respectively. The geminal hydrogen atoms, LiB$(C\underline{H}^{gem}=CH_2)_4$, demonstrated a doublet of doublet which was positioned at a chemical shift of 6.30 ppm. The coupling constants of cis hydrogen atoms were found as 6.21 Hz for J (H^{cis}, H^{trans})
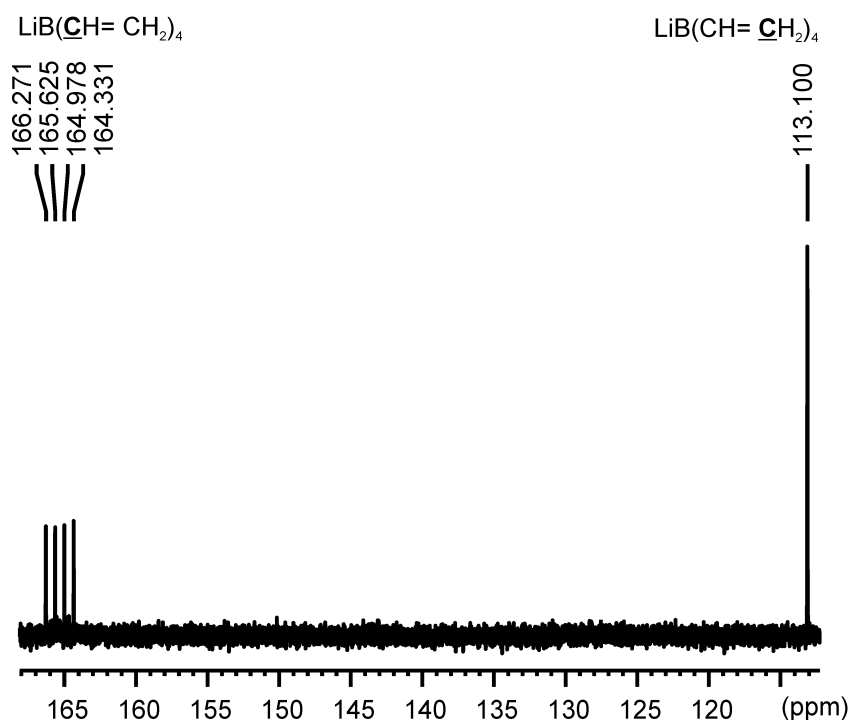
Figure 20: ^{13}C-NMR spectrum of lithium tetravinylborate, solution in diethyl ether.
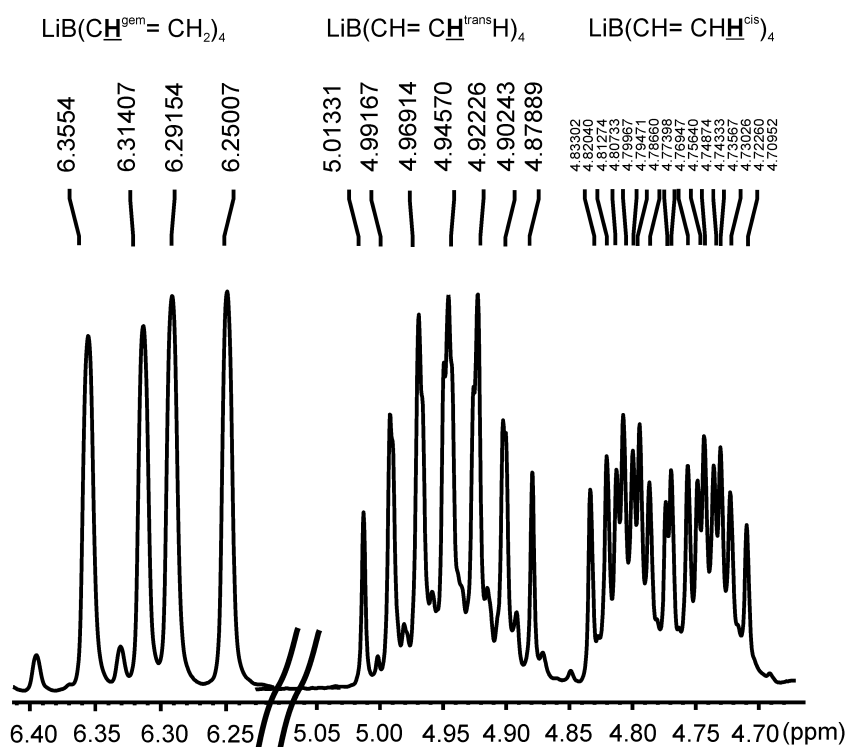
Figure 21: ^{1}H-NMR spectrum of lithium tetravinylborate, solution in diethyl ether.

and 19.20 Hz for J (H^{cis}, H^{gem}). Considering the trans hydrogen atoms, the coupling constant values were 12.71 Hz for J (H^{trans}, H^{gem}) and 6.21 Hz for J (H^{trans}, H^{cis}). The coupling constants of geminal hydrogen atoms were deduced as 12.71 Hz for J (H^{gem}, H^{trans}) and 19.20 Hz for J (H^{gem}, H^{cis}). The boron chemical shift of LiB(CH=CH$_2$)$_4$ was observed at −16.1 ppm with a sharp resonance as demonstrated in the Figure 22. The obtained ^{11}B signal is consisted with the one published by Thompson et al. [188]. The lithium chemical shift was measured at −2.6 ppm, which can be seen in Figure 23.
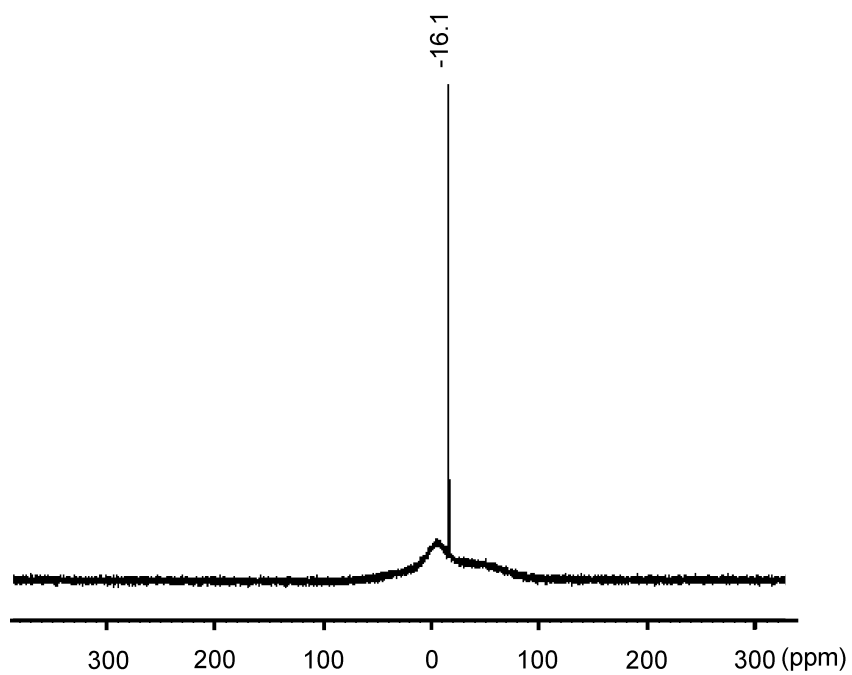
Figure 22: ^{11}B-NMR spectrum of lithium tetravinylborate, solution in diethyl ether.
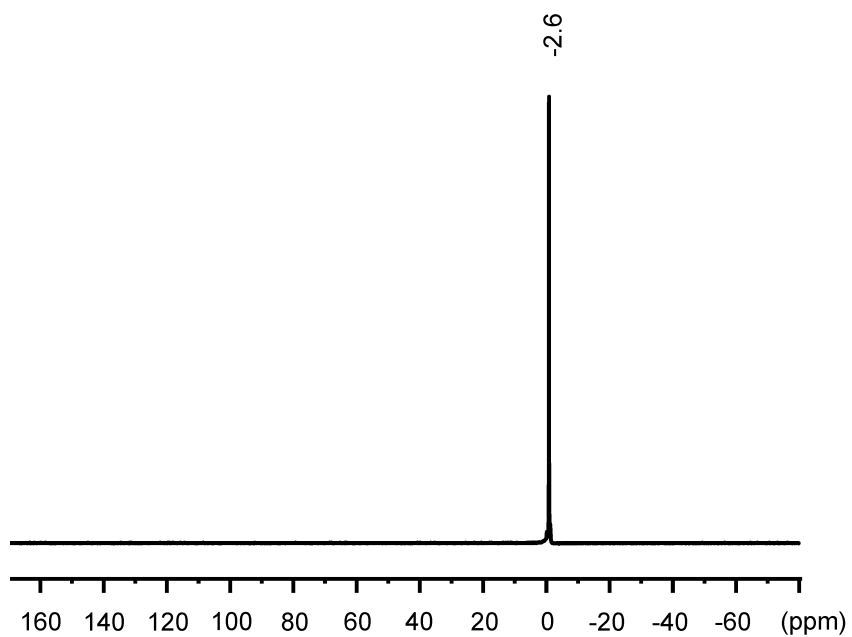
Figure 23: ^{7}Li-NMR spectrum of lithium tetravinylborate, solution in diethyl ether.

4.2.2   Synthesis of PLEB (3)

Hydroboration polymerization of lithium tetravinylborate in diethyl ether was performed by dropwise addition of $BH_3 \cdot THF$ at 0 °C to obtain PLEB according to the following equation:

$$3n \; Li[B(CH{=}CH_2)_4] + 4n \; BH_3 \cdot THF \rightarrow Polymer + 4n \; THF$$

where THF is tetrahydrofuran. The synthesis route showing all the steps to obtain as-synthesized poly[lithium tetrakis(ethyleneboryl)borate] (PLEB) is shown in Figure 24.

Preparation of PLEB

0.0067 mol (1 M solution in tetrahydrofuran) borane-tetrahydrofuran complex was dropwise added at 0 °C into a 0.63 g (0.005 mol) lithium tetravinylborate, which was dissolved in 80 ml diethyl ether, under vigorous stirring. The polymerization was carried out for 24 hours at 0 °C and allowed to proceed a further 24 hours at 25 °C. Further crosslinking was achieved by subsequently refluxing at 70 °C for 12 hours. Then, the reaction flask was connected to a cooling trap, where the solvent was collected. The obtained polymer was dried 24 hours at 70 °C under vacuum to obtain as-synthesized polymer.

$$Sn(CH{=}CH_2)_4 + x \; n\text{-}BuLi \xrightarrow{\;\; n\text{-hexane} \;\;} n\text{-}Bu_x Sn(CH{=}CH_2)_{4\text{-}x} + x \; LiCH{=}CH_2$$
$$\textbf{1}$$

$$4 \; LiCH{=}CH_2 + BF_3 \cdot O(CH_2CH_3)_2 \longrightarrow Li[B(CH{=}CH_2)_4] + 3 \; LiF + O(CH_2CH_3)_2$$
$$\textbf{2}$$

$$3n \; Li[B(CH{=}CH_2)_4] + 4n \; BH_3 \cdot THF \xrightarrow{\;\; 0 \; °C, \; diethylether \;\;} 4n \; THF + Polymer$$
$$\textbf{3}$$
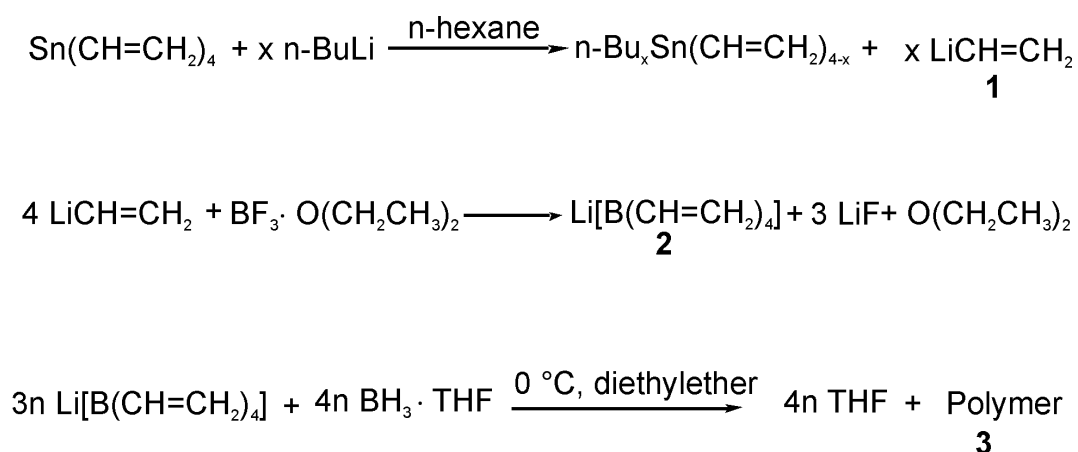
Figure 24: Synthesis route for PLEB polymer.

The as-synthesized PLEB polymer was annealed at 275 °C around 1 day under argon atmosphere to obtain the annealed PLEB polymer. Both the as-synthesized and the annealed PLEB polymers were extensively investigated in the present work.

4.2.3   As-synthesized PLEB

4.2.3.1   X-ray Powder Diffraction

The amorphous character of the as-synthesized PLEB polymer was confirmed by X-ray powder diffraction, the diffractogram is given in Figure 25.
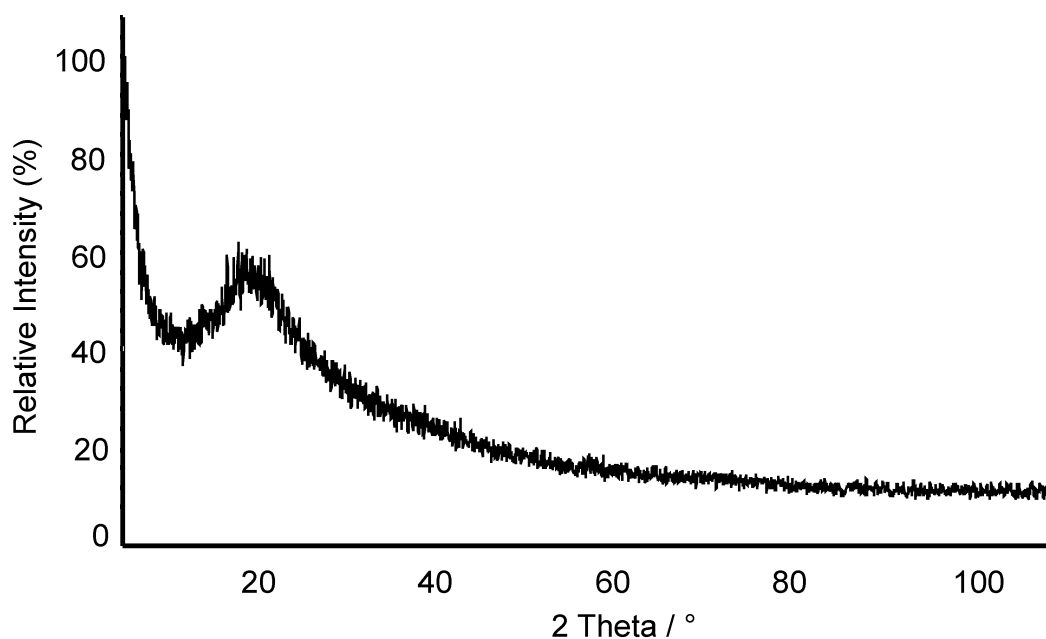
Figure 25: XRD pattern of as-synthesized PLEB polymer.

4.2.3.2   Elemental Analysis

The elemental analysis (except hydrogen) of the PLEB polymer resulted in the empirical formula $B_2C_{10}Li_1$, which matches the expected composition of the polymer. The chemical composition of the as-synthesized PLEB polymer (Table 4) gave the B:Li ratio as 2:1, which is in agreement with neutral boron and negatively charged borate to exist in the network in equal proportions, with lithium compensating the charge on the borate. Protons and minor amounts of remaining THF were accounted for the rest of the mass.

Table 4: Chemical composition of the as-synthesized PLEB polymer.

Element	Mass (%)	Empirical Formulae
B	10.27	$B_{1.8}C_{9.8}Li_1$
C	61.11	$(\approx B_2C_{10}Li_1)$
Li	3.61	

4.2.3.3 FT-IR Spectroscopy

The FT-IR spectrum of the as-synthesized PLEB polymer is displayed in Figure 26. The bands between 2925 cm^{-1} and 2853 cm^{-1} represent the aliphatic C—H stretching vibrations. The presence of a weak free B—H stretching band at 2292 cm^{-1} implies the formation of tetrahydroborate ions by ligand exchange reactions during the polymerization process. The band at 1632 cm^{-1} is assigned to the symmetric stretching vibrations of a B—H—B bridge structure. B—C asymmetric stretching bands are noticeable between 1040 cm^{-1} and 1124 cm^{-1} [189] and the CH$_2$ deformation vibrations are observed in the range of 1378–1465 cm^{-1}. The bands at 1262 cm^{-1}, 823 cm^{-1} and 754 cm^{-1} represent CH$_2$ wagging, CH$_2$ rocking and B—C stretching vibrations, respectively. No alkenyl C—H (3010–3095 cm^{-1}) bands could be detected in the FT-IR spectrum, which indicates that no residual vinyl groups are present. This also proves that the hydroboration reaction was completed. The band positions with intensities and interpretations are collected in Table 5.

4.2.3.4 Raman Spectroscopy

The Raman spectrum recorded for the as-synthesized PLEB polymer is given in Figure 27. The spectrum is indicating the main building blocks of the polymer (Table 6). Hence, the results are in clear agreement with the FT-IR spectrum. Asymmetric and symmetric vibrations of CH$_2$ bands are detected at 2968 cm^{-1} and 2911 cm^{-1}, respectively. The band at 2303 cm^{-1} implies the existence of the free B—H stretching vibrations of tetrahydroborate ions. CH$_2$ deformation, CH$_2$ wagging and C—C skeletal

Table 5: FT-IR band positions and assignments of as-synthesized PLEB polymer.

Wavenumber /cm^{-1}	Intensity	Assignment
2925	s	ν (C—H)
2853	s	ν (C—H)
2292	m	ν (B—H)
1632	w	ν (B—H—B)
1465	s	δ (C—H)
1378	s	δ (C—H)
1262	m	γ (C—H)
1124—1040	s	ν (B—C)
823	m	ρ (C—H)
754	w	ν (B—C)
530—427	w	ρ (C—H)

Figure 26: FT-IR spectrum of the as-synthesized PLEB polymer.
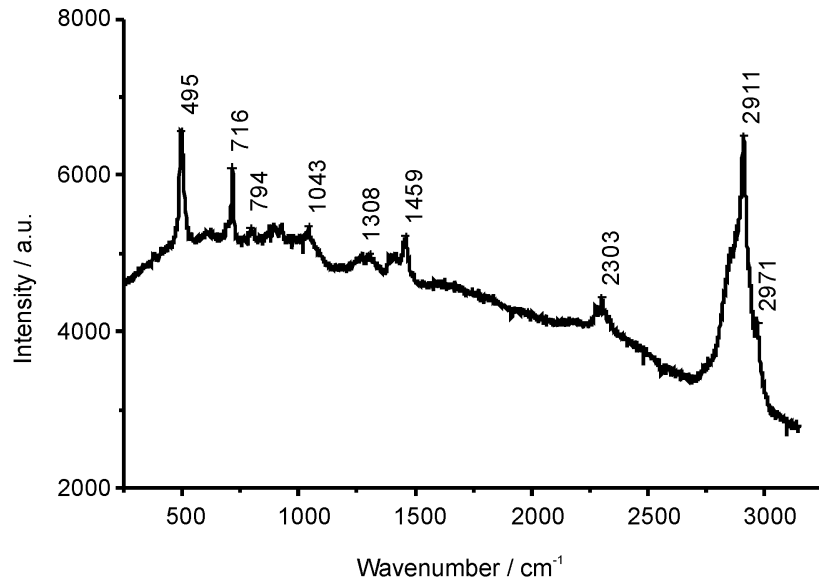
Figure 27: Raman spectrum of as-synthesized PLEB polymer.

Table 6:   Raman band positions and assignments for as-synthesized PLEB polymer.

Wavenumber /cm^{-1}	Intensity	Assignment
2971	m	ν (C—H)
2911	s	ν (C—H)
2303	w	ν (B—H)
1459	m	δ (C—H)
1308	w	γ (C—H)
1043	w	ν(C—C)
794	w	ρ (C—H)
716	s	ρ (C—H)
495	s	ν (C—H)

stretching vibrations appear at 1459 cm^{-1}, 1308 cm^{-1}, and 1043 cm^{-1}, respectively. The bands at 794 cm^{-1} and 716 cm^{-1} are assigned to CH$_2$ rocking, and at 495 cm^{-1} for CH$_2$ skeletal vibration bands.

4.2.3.5   Solid State NMR Measurements

Further characterization was performed by ^{13}C and ^{11}B solid-state NMR spectroscopies. The ^{13}C spectrum of the freshly prepared PLEB polymer (Figure 28) shows only one broad signal in the region of the spectrum that corresponds to aliphatic carbon atoms; this indicates that the hydroboration reaction was effective in transforming all vinyl groups, confirming the FT-IR results. Thus, this provides proof that the band at 1629 cm^{-1} in the IR spectrum is not caused by C=C stretching vibrations, but rather by those of B—H—B bridges in the structure. The single peak, centered around 27 ppm, is rather broad, but this is typical for amorphous samples. The chemical shift indicates that most of the carbon exists in CH$_2$ units and that therefore most of the addition reactions must have happened in an anti-Markovnikov fashion. The small peak at 70 ppm may be the result of some remaining THF coordinating to the trialkylborane units.
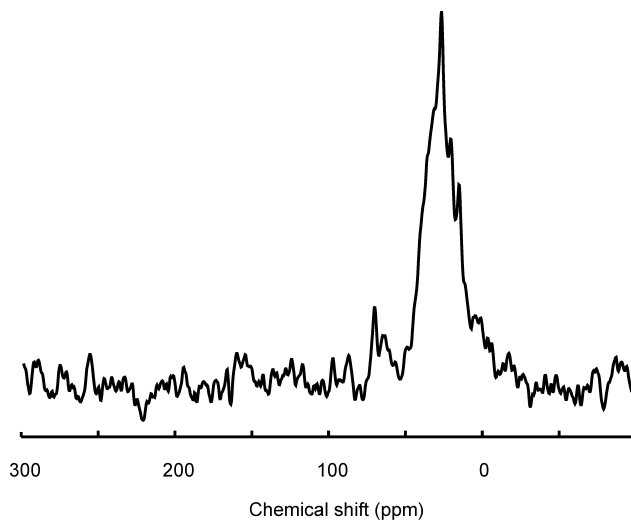
Figure 28: Solid state ^{13}C-NMR of as-synthesized PLEB polymer. $\omega_r(2\pi)^{-1} = 25\,\text{kHz}$.

^{11}B solid-state NMR spectra (Figure 29) were complicated by the presence of a strong ^{11}B background signal from the NMR probe. However, the MQMAS technique

suppresses this background and allows the separation of the various boron signals in the sample. After shearing transformation of the 2D MQMAS spectrum, one obtains an isotropic spectrum in the first dimension, while the width in the second dimension gives an impression of the amplitude of the quadrupolar coupling (CQCC). The axis labeling of the isotropic dimension follows a convention in which the position of a line becomes equal to the chemical shift in the case of vanishing quadrupolar coupling or infinite static field.
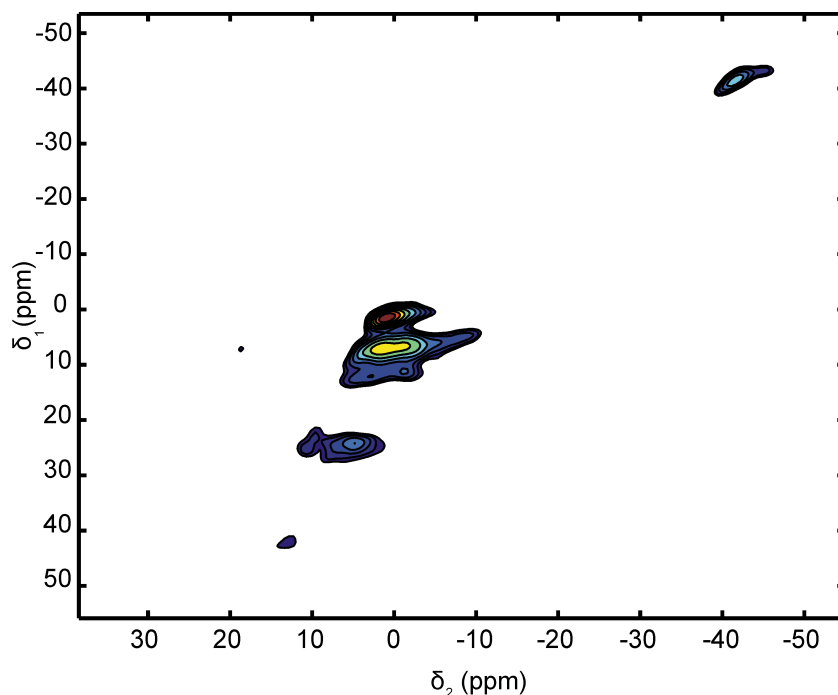
Figure 29: Solid state ^{11}B MQMAS spectrum recorded for as-synthesized PLEB polymer.

It is assumed that hydrogen-bridged boron has a larger quadrupolar coupling as compared to four-coordinated boron. In the PLEB polymer, two different boron species are expected: four-coordinated boron that originated from the tetravinylborate and hydrogen-bridged boron introduced with the borane. During the polymerization reaction, some ligand exchange takes place, leading to the formation of tetrahydroborate ions [190]. These ions have an almost vanishing quadrupolar coupling, leading to a narrow peak positioned at -42 ppm. The tetraalkylborate resonance also has a low quadrupolar coupling and forms narrow bands at 0 ppm and $+5$ ppm. The reduced local symmetry of the hydrogen-bridged alkylborane species leads to a larger

quadrupolar coupling, and as a consequence the peak is much broader (located at
+25 ppm and +40 ppm). Thus, three different boron species can be distinguished in
the as-synthesized PLEB polymer. Different types or different numbers of attached
alkyl groups are probably the reason behind the presence of multiple peaks for the
latter two species.

The deconvolution of the ^{1}H NMR spectrum of the as-synthesized PLEB polymer
into a collection of mixed Lorentzian/Gaussian peaks (Figure 30) revealed that at least
three different hydrogen species are present in the polymer structure with chemical
shifts of 0.6 ppm, 1.5 ppm and 5.4 ppm. The smallest and the sharpest peak, appearing
at 0.6 ppm, represent the tetrahydroborate species [191]. The largest proportion of the
hydrogen atoms in the structure are incorporated into alkane units and are responsible
for the spectral component at 1.5 ppm. The bridging hydrogen atoms possess the
highest chemical shift and are associated with the component at 5.4 ppm [192].
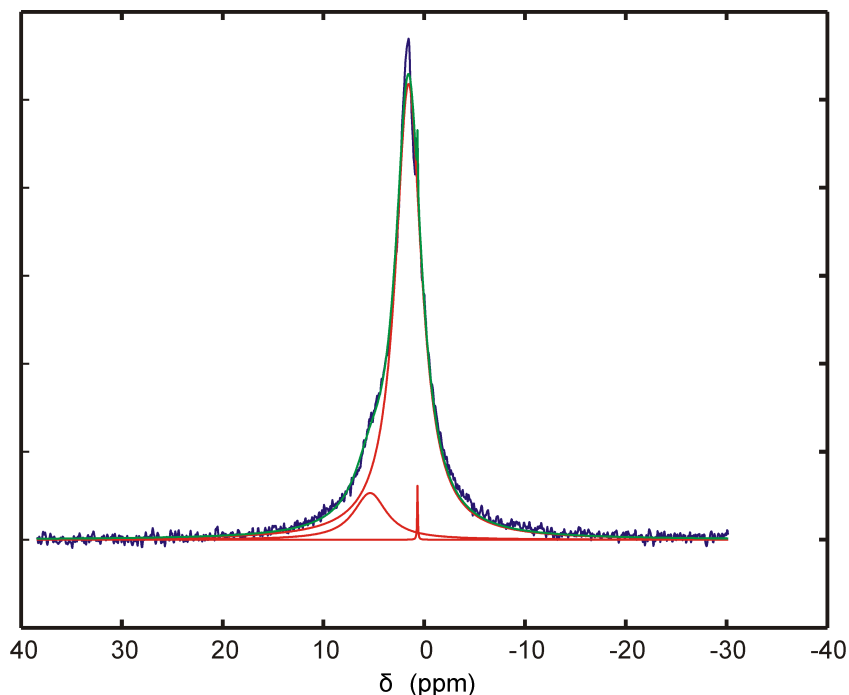
Figure 30: Solid state ^{1}H-NMR spectrum recorded for as-synthesized PLEB polymer
(red line: components of deconvolution, green line: sum of components, blue line:
experimental).

4.2.3.6   Thermal Analysis

Thermal stability of the as-synthesized PLEB polymer was monitored simultaneously by differential thermal analysis, thermogravimetric analysis and mass spectroscopy (DTA/TG/MS) under argon atmosphere. As shown in Figure 31, no mass loss was observed up to 150 °C. The volatile loss of the residual THF ($m/z = 42$) solvent entrapped in the sample started at 150 °C and continued up to 225 °C. It was followed by the loss of oligomers, which were not connected to the network or generated by cleavage and reorganization of endgroups [H_2 ($m/z = 2$), BC_2H_6 ($m/z = 41$), BCH_4 and C_2H_3 ($m/z = 27$), C_2H_4 ($m/z = 28$), BC_2H_4 ($m/z = 39$)] between 225 °C and 300 °C. The escape of H_2 in this temperature regime also indicates the dehydrogenation reactions. Hence, the loss of chain ends with temperature activation would lead to the rearrangement and recombination of chains giving a more crosslinked structure. The highest mass loss observed between 300 °C and 600 °C was due to the main degrada-
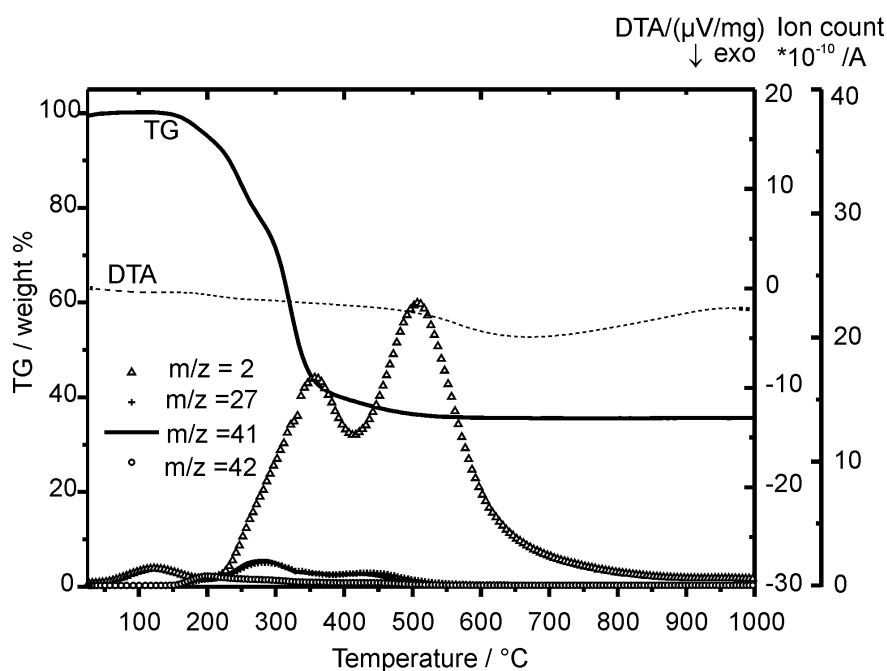
Figure 31: DTA/TG/MS curves for the as-synthesized PLEB polymer in argon flow at 10 °C min^{-1}.

tion of the network. The fragments of H_2 (m/z = 2), CH_3 (m/z = 15) and C_2H_4 (m/z = 28) were evolved between 440 and 575 °C due to the atomic rearrangement involved with the simultaneous ceramization and depolymerization processes. The ceramic yield was about 35 % after annealing to 1000 °C. Formation of thermally weak alkyl bridges by the hydroboration reaction might result in the formation of a high amount of volatile species during the pyrolysis [193].

4.2.3.7   Main Features of the Structure

The combination of the findings from the FT-IR, solid-state NMR and TG/MS analyses on the amorphous as-synthesized PLEB polymer are presented schematically in Figure 32. The drawing shows the building blocks that were identified. The main structural features of this highly crosslinked polymer include hydrogen-bridged borane units and tetraethylene borate units, with the negative charge on the borate units is compensated by lithium cations. Moreover, the borane and borate units are connected by ethylene linkages, formed by a hydroboration reaction that mainly followed the anti-Markovnikov rule.
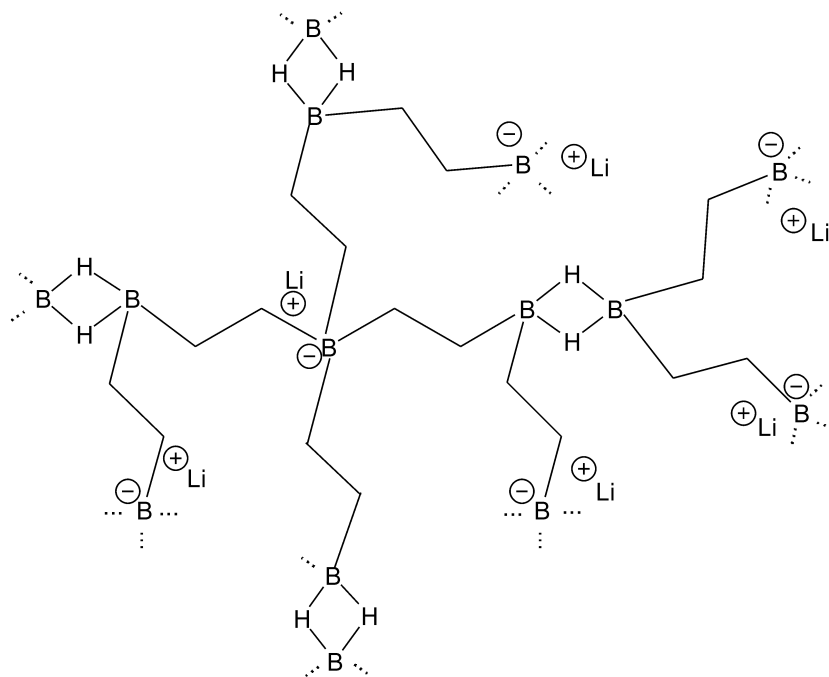
Figure 32: Schematic drawing of the structure of PLEB polymer showing the main building blocks.

4.2.4 Annealed PLEB

The detailed investigations for "as-synthesized" PLEB were presented in section section 4.1.2. In this section, the characterization of the poly[lithium tetrakis(ethyleneboryl)borate] (PLEB) after annealing for around 1 day at 275 °C will be discussed. The annealing was performed under argon atmosphere with 1 °C min^{-1} heating and cooling rates.

4.2.4.1 X-ray Powder Diffraction

The amorphous structure was preserved after annealing at 275 °C, as can be seen in the powder X-ray diffractogram in Figure 33.
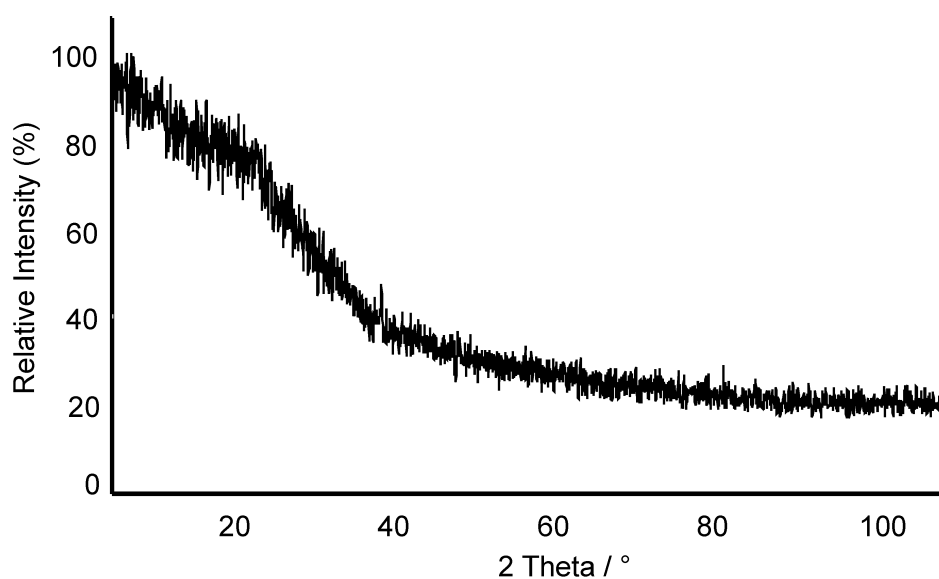
Figure 33: XRD pattern of annealed PLEB polymer at 275 °C.

4.2.4.2   Elemental Analysis

The annealing of the PLEB polymer resulted in a chemical composition of 1.5:4:1 for the ratio of B:C:Li (Table 7). Thus, carbon accounts for the main mass loss during the annealing process. This was also accompanied by a small loss of boron, which is consistent with the TG/MS results that the chain ends and oligomers were fragmenting during annealing to form a more crosslinked structure. Thus, the annealing process increases the concentration of charge carriers and shortens the distance between boron atoms which should enhance the ionic conductivity.

4.2.4.3   FT-IR Spectroscopy

Similar IR peaks have been observed for the annealed PLEB polymer like in as-synthesized PLEB polymer (Figure 34). The observed frequencies and assignments are tabulated in Table 8. However, there is a significant decrease in the intensity of the band corresponding to the non-bridging terminal B—H groups (2312 cm^{-1}). Furthermore, the dehydrogenation by temperature activation, which was detected by TG, has lead to a smaller amount of vinyl groups into the structure.
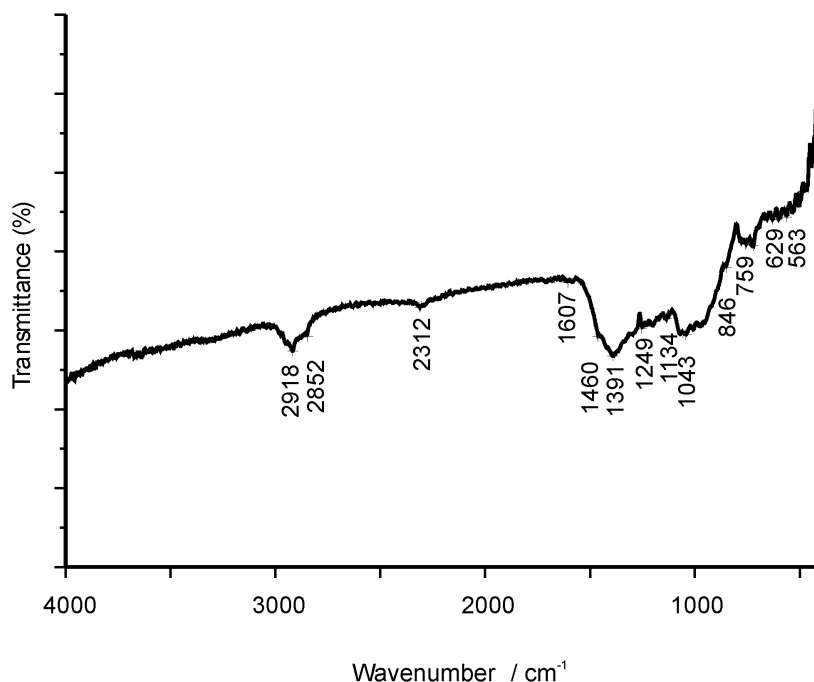
Figure 34: FT-IR spectrum of the annealed PLEB polymer.

Table 7: Chemical composition of the annealed PLEB polymer.

Element	Mass (%)	Empirical Formulae
B	20.95	$B_{1.49}C_{3.7}Li_1$
C	56.77	$(\approx B_2C_5Li_{1.3})$
Li	9.02	

Table 8: FT-IR band positions and assignments of annealed PLEB polymer.

Wavenumber /cm^{-1}	Intensity	Assignment
2918	s	ν (C—H)
2852	s	ν (C—H)
2312	w	ν (B—H)
1607	w	ν (B—H—B)
1460	s	δ (C—H)
1391	s	δ (C—H)
1249	m	γ (C—H)
1134−1043	s	ν (B—C)
846	m	ρ (C—H)
759	w	ν (B—C)
629−563	w	ρ (C—H)

4.2.4.4   Solid State NMR Measurements

^{13}C and ^{11}B MQMAS NMR measurements were also performed for the PLEB polymer annealed at 275 °C under argon atmosphere. The ^{13}C-NMR spectrum is dominated by the signal of saturated carbon atoms at 26 ppm (Figure 35). The smaller peak at 138 ppm indicates that the annealing process results in the formation of some unsaturated carbon-carbon bonds in the chain. TG measurements had revealed that the hydrogen evolution starts below the annealing temperature. Therefore, the formation of unsaturated bonds is probably associated with this dehydrogenation process. The unsaturated carbon-carbon bonds could also be the consequence of a reverse hydroboration in which some boron units, most probably those located at the chain ends, were eliminated by the formation of a gaseous hydroborane species. This process would leave unsaturated carbon-carbon bonds behind. A part of these vinyl functions subsequently reacts with remaining hydroborane species, providing a more cross-linked network.
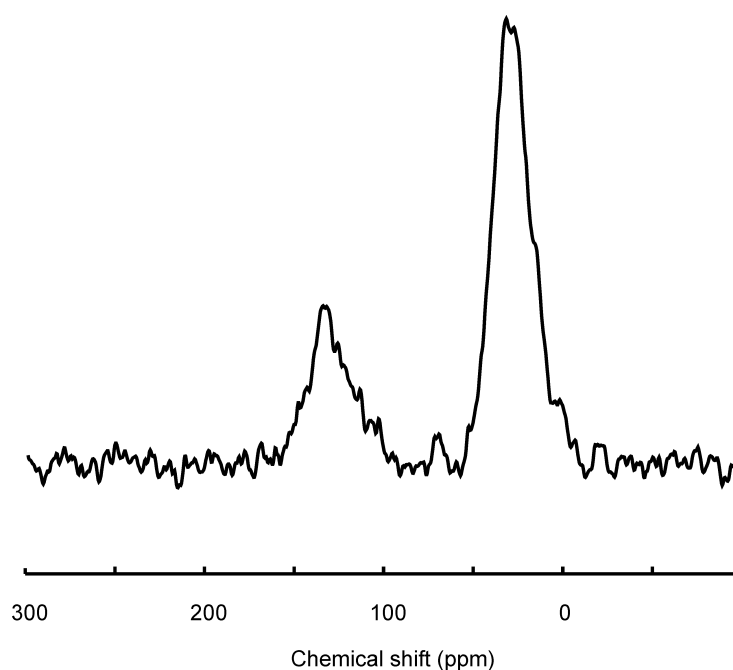
Figure 35: Solid state ^{13}C-NMR spectrum of annealed PLEB polymer. $\omega_r(2\pi)^{-1} = 25\,\mathrm{kHz}$.

The ^{11}B MQMAS spectrum of annealed PLEB polymer (Figure 36) also exhibits differences in comparison to the spectrum of as-synthesized polymer. The main components, which were presented in the spectra of the as-synthesized PLEB polymer, are still there. However, the peaks of the hydrogen-bridged boron atoms (positioned at $+25$ ppm and $+40$ ppm) which had small intensity in the as-synthesized PLEB polymer become more pronounced. It is thought that as a result of the reverse hydroboration, three-coordinated boron species that were previously invisible as a consequence of the large quadrupolar coupling become visible because these are now able to form hydrogen bridges. The peak representing tetrahydroborate species (at a chemical shift of -41 ppm) is lower in intensity with respect to the spectrum of the as-synthesized PLEB polymer, which is in agreement with the FT-IR results.
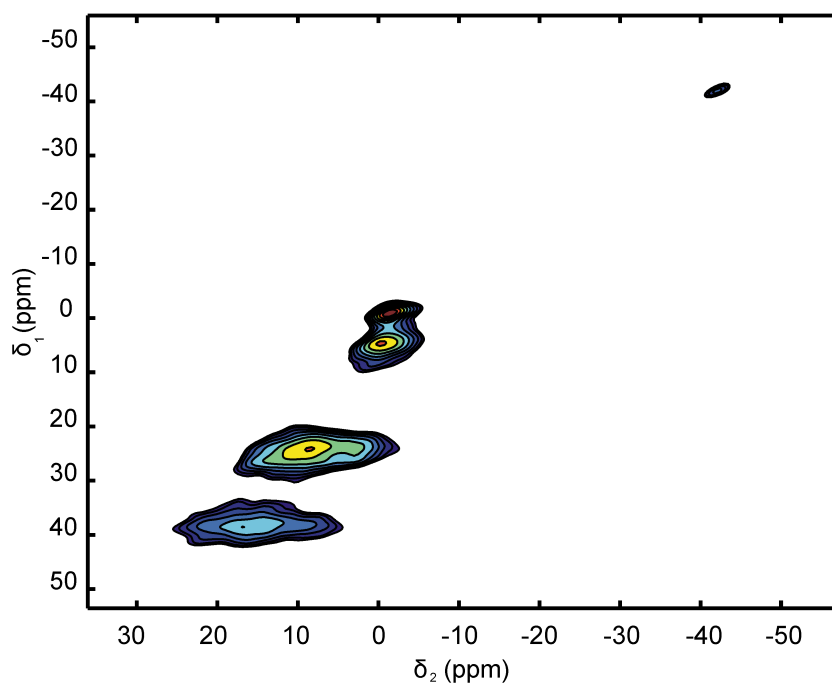
Figure 36: Solid state ^{11}B MQMAS spectrum recorded for annealed PLEB polymer.

The ¹H NMR spectrum of the annealed PLEB polymer was deconvoluted into three peaks like in the as-synthesized form. The three components have appeared at chemical shifts of 0.2 ppm, 1.5 ppm and 6.9 ppm (Figure 37). The smallest peak at 0.2 ppm indicates the presence of tetrahydroborate species. The intensity of this component is decreased with respect to the as-synthesized form by the annealing process, which is in agreement with the ¹¹B MQMAS results. The main peak at 1.5 ppm still shows that the hydrogen atoms in the material are in the form of CH_2 groups. The main difference with the as-synthesized form is the shift of the component at low field from 5.4 ppm to 6.9 ppm. However, this shift is quite reasonable as the annealed PLEB polymer structure contains additional unsaturated carbons that were identified with ¹³C NMR. Hence, the NMR signals of hydrogen atoms connected to the unsaturated carbon atoms and those of bridging hydrogen atoms overlap and form the peak at 6.9 ppm. It is also in agreement with the ¹¹B NMR results that annealing increases the concentration of bridging hydrogen atoms in the structure.
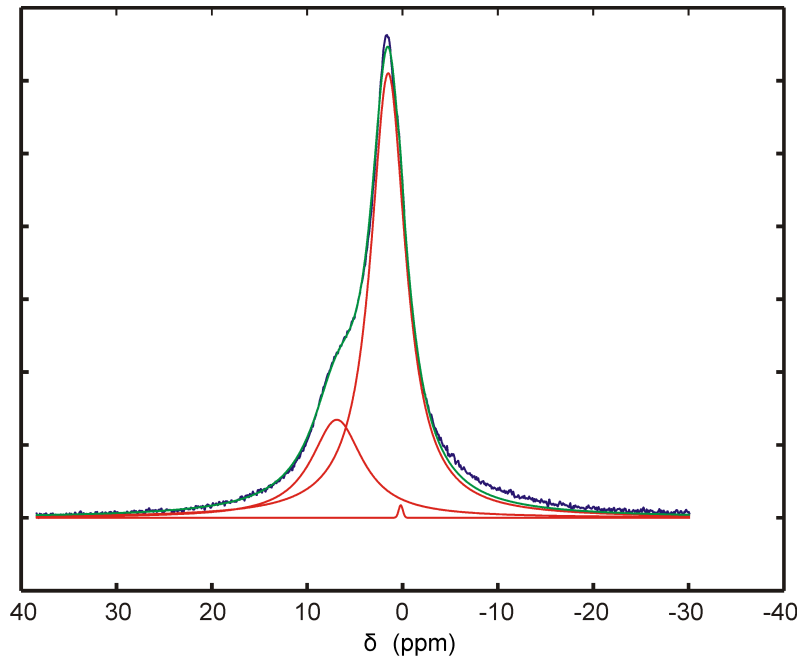
Figure 37: Solid state ¹H-NMR spectrum recorded for annealed PLEB polymer (red line: components of deconvolution, green line: sum of components, blue line: experimental).

4.2.4.5 Thermal Analysis

DTA/TG/MS data indicates that the annealed PLEB polymer has a lower mass loss as compared to the as-synthesized PLEB polymer, and 88 % ceramic yield has been obtained at 1000 °C (Figure 38). The main mass loss processes have been observed to occur by evolution of H_2 (m/z = 2), BC_2H_6 (m/z = 41), BCH_4 and C_2H_3 (m/z = 27), C_2H_4 (m/z = 28), BC_2H_4 (m/z = 39) and CH_3 (m/z = 15).
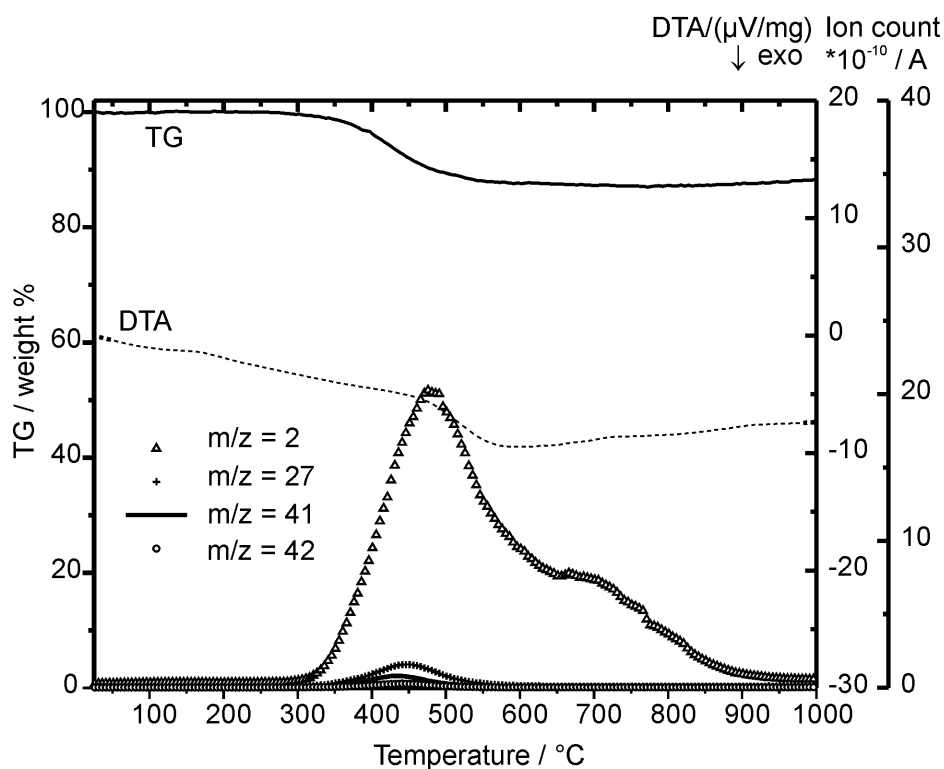
Figure 38: DTA/TG/MS curves for the annealed PLEB polymer in argon flow at $10\,°C\,min^{-1}$.

4.2.4.6 Main Features of the Structure

The results of the analyses indicate that the main features of the structure for the polymer remained the same after annealing. It still has the same building blocks (hydrogen bridged boranes and four coordinated borates), and, connectivities as the as-synthesized PLEB polymer, that are schematically depicted in Figure 32. The main differences in the annealed PLEB polymer are the formation of minor amounts of vinyl

groups as a result of reverse hydroboration and an increase in the concentration of the hydrogen bridged boron species.

4.2.5   Analysis of the Ionic Conduction

The bulk conductivity of PLEB was determined by non linear mean square deviation curve fitting of the impedance spectrum. Anionic and cationic transference numbers were measured at different temperatures with a multipotentiostat using cells in which polyelectrolytes were sandwiched with non-blocking (lithium) or blocking (gold) electrodes. The direct current (dc) was monitored with time after a stepwise change of the cell voltage from 0 mV to 50 mV. The motion of the cations were investigated by ^{7}Li-NMR at different temperatures.

4.2.5.1   Impedance Spectroscopy

Ionic conductivity measurements were conducted for the as-synthesized PLEB polymer until 110 °C and for the annealed PLEB polymer until 275 °C under argon atmosphere. The heating and cooling rates were 1 °C min^{-1}. The temperature dependent bulk ionic conductivities were plotted in Arrhenius type diagrams for both polymers (Figure 39). The activation energies of the polymers were derived from the slope of the conductivity curves, which were equal to 145 kJ mol^{-1} for the as-synthesized PLEB polymer and 70 kJ mol^{-1} for the PLEB polymer annealed at 275 °C. The conductivity values at different temperatures and activation energies for both polymers are given in Table 9. Low frequency diffusion spikes were observed in the Nyquist plots (Figure 40), when blocking electrodes were used. This proves that the conduction is ionic in nature.

The impedance data presented in the complex plane format exhibits only one semicircle until 100 °C, which can be interpreted as a parallel RQ element (Q:constant phase element) in the equivalent circuit. An additional low-frequency spike appears, representing the barrier to charge transfer between the sample and the ion-blocking gold electrodes at higher temperatures (Figure 40). Hence, Q_{el}, an additional constant phase element, was included for the equivalent circuit in series with the RQ element. The capacitance, C, can be determined according to $C = Q^{1/n} \times R^{(1/n)-1}$. The calculated values for the semicircles at different temperatures ($C \approx 4 \times 10^{-12}$ F) are typical for the bulk capacitance of a sample [45]. Therefore, the semicircle can be associated with the lithium ion conductivity in the bulk.
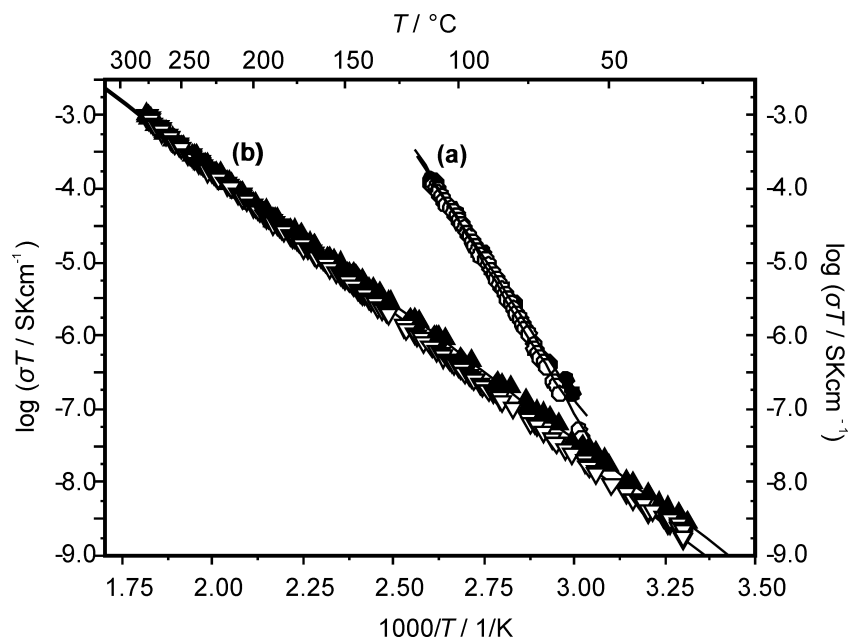
Figure 39: Temperature dependence of the ionic conductivities of the (a) as-synthesized and (b) annealed PLEB polymers at 275 °C. Heating and cooling are represented by filled and open symbols, respectively.

Table 9: Activation energies and ionic conductivities (at 80 °C, 110 °C and 275 °C) for PLEB.

	E_a / kJ mol^{-1}	σ /S cm^{-1}		
		80 °C	110 °C	275 °C
As-synthesized PLEB polymer	145	6.5×10^{-9}	3.0×10^{-7}	—
Annealed PLEB polymer at 275 °C	70	3.0×10^{-10}	2.5×10^{-9}	1.6×10^{-6}
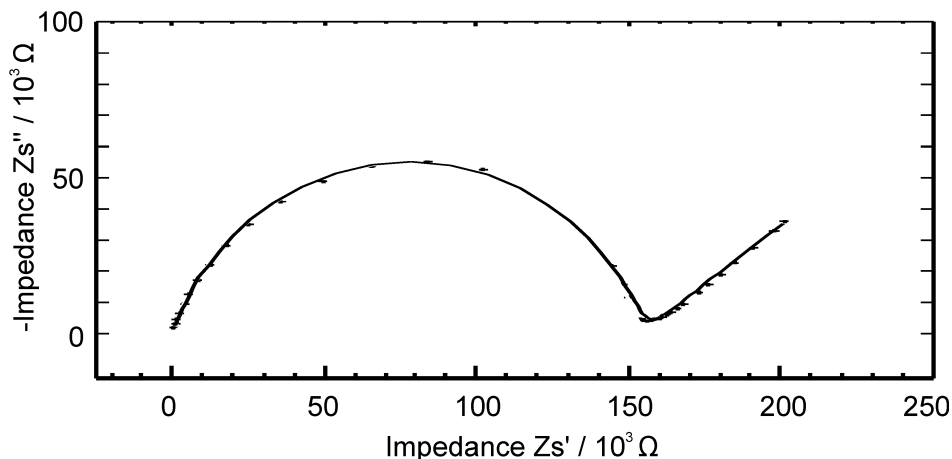
Figure 40: Nyquist plot of the PLEB polymer with blocking gold electrodes at 276 °C. The experimental and the simulated impedance spectrum are represented with dots and the solid line, respectively.

4.2.5.2   Direct Current Measurements

Transference numbers for cations were estimated by means of the potentiostatic polarization measurements on the polyelectrolyte sandwiched between two lithium electrodes. Dc measurements were performed by monitoring the electrical current response after a voltage step (Figure 41a). The effective lithium transference number (t_{Li^+}) was calculated from the ratio of the steady state current ($3.80(9) \times 10^{-7}$ mA) to the initial current ($3.5(8) \times 10^{-7}$ mA) as in the following equation (eqn (7));

$$t_{Li^+} = \frac{I_{(t \to \infty)}}{I_{(t \to 0)}} = \frac{\sigma_{Li^+}}{\sigma_{total}} \tag{7}$$

by using a cell with non-blocking lithium electrodes (Li/polymer/Li) [194]. The cationic transference number (t_+) was determined as 1.0(2) at 137 °C. The value of t_+, which approaches unity, indicates that the polymer is a virtually pure Li^+ conductor.

Dc potentials were also applied to a cell with ion blocking Au electrodes to test the contribution of the electronic component to the conductivity (Au/polymer/Au).
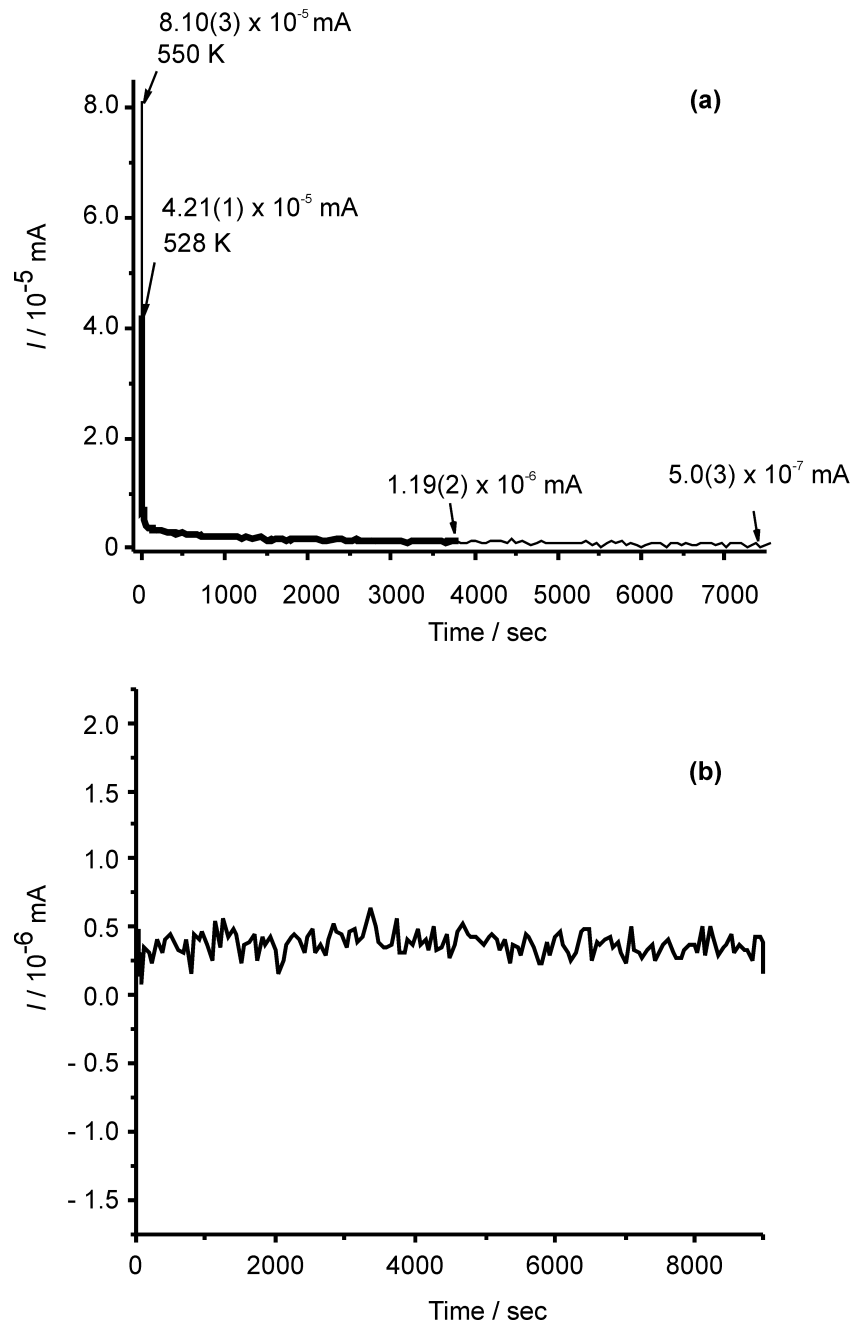
Figure 41: Electrical currents versus time for the cells (a) Au/polymer/Au (at 255°C and 277 °C) and, (b) Li/polymer/Li (at 137 °C) after switching on dc voltage at time zero.

As can be seen from the Figure 41b, smooth and gradual decays were observed. The initial current with blocking electrodes can be used to check whether the dc data is consistent with the ac data. At 277 °C, the initial resistance in the dc measurement is 6.2×10^5 Ω. The ac measurement at 276 °C gave a lower resistance value (1.6×10^5 Ω), but this is expected because the dc measurement has a steep negative slope at the start of the measurement. The dc steady state conductivity was determined as 1.2×10^{-9} S cm^{-1} at 277 °C, which was on the order of $1/1000$ that of the ionic conductivity determined by ac impedance (1.6×10^{-6} S cm^{-1} at 276 °C). The effective electronic transference numbers (t_{el}) were calculated as $t_{el} = 0.028(3)$ at 255 °C and $0.006(3)$ at 277 °C. The electronic transference numbers were almost close to 0, that there was negligible electronic contribution to the conductivity.

4.2.5.3   Static ^{7}Li-NMR Measurements

^{7}Li-NMR analyses were performed to track the motion of the cations. ^{7}Li, being a quadrupolar nucleus, has interaction both with the electric field gradient in the sample as well as with the magnetic dipole moments of other nuclei. The central transition is not broadened by the first-order quadrupolar interaction, but purely by dipolar interactions. Proton decoupling does not influence the linewidth, therefore the main line broadening mechanism must be the homonuclear dipolar interaction. When taking the full width at half height of the entire resonance line, the actual linewidth that one measures is that of the central transition, since the satellite transitions are more strongly broadened and will only influence the shape of the foot of the line.

Static ^{7}Li NMR was measured at different temperatures for the as-synthesized PLEB polymer (Figure 42). The static ^{7}Li linewidth undergoes motional narrowing as the temperature increases. Since the polymer is heavily crosslinked, the motion of the polymer backbone is restricted. Most of the motional narrowing will be caused by the lithium ions moving through the polymer. The linewidth as a function of temperature is given in Figure 42a.

At low temperatures, the resonance line has a full width at half maximum (FWHM) of 11 kHz. This value remains constant until -25 °C, indicating that the lithium ions are slow with respect to the NMR timescale. 11 kHz therefore represents the rigid lattice linewidth of the material. Above -25 °C, the NMR linewidth decreases due to the averaging of interactions between nuclear spins with other nuclear spins and between the spins with the environment, which is a consequence of the mobility of the
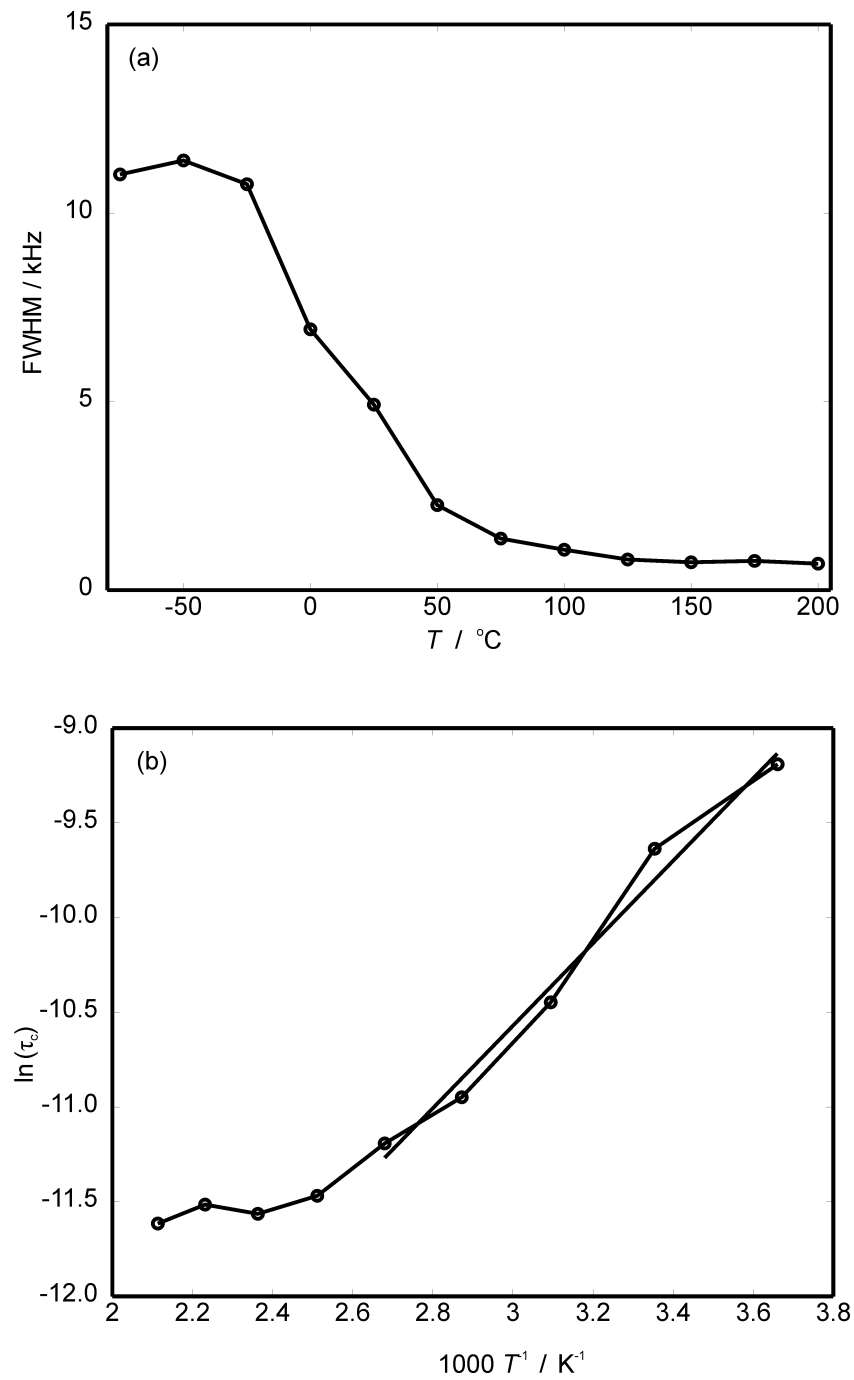
Figure 42: Temperature dependence of ^{7}Li-static NMR (a) line widths and (b) correlation time of the as-synthesized PLEB polymer.

cation entering the NMR timescale. Abragam gives a relation between the motional correlation time and the dipolar line narrowing as (eqn(8));

$$\tau_C = \frac{\alpha}{\Delta_{HT}} \tan\left[\frac{\pi}{2}\left(\frac{\Delta_{HT}}{\Delta_{RL}}\right)^2\right] \tag{8}$$

in which, τ_C is the correlation time, α is a constant of the order of unity, Δ_{HT} and Δ_{RL} are the FWHHs at a given temperature and in the rigid lattice [195].

The correlation time is related by an Arrhenius rule to the activation energy of the motional process as (eqn(9));

$$\tau_C = \tau_0 exp(E_a/kT) \tag{9}$$

The activation energy can be calculated from [7]Li line width measurements by fitting the equations 4.2 and 4.3. Only the linear part of the Arrhenius plot (Figure 4.27b) was taken into account. At temperatures above 100 ℃, the plot is no longer linear because the T_2 relaxation and other interactions start to dominate the linewidth. The slope of the linear part yields $E_a = 18.10\,\mathrm{kJ\,mol^{-1}}$. This activation energy is significantly lower than the activation energy obtained from conductivity measurements. Large differences in NMR and conductivity activation energies were also observed by other researchers; i.e., lithiumborate glasses [196] and poly(vinyl alcohol) based polymer electrolytes [197]. The most likely reason for this is that the motion causing the NMR line narrowing includes the local motions. The energy barriers encountered by the ions for long range motions are much higher than for local motions, leading to higher activation energy for the conductivity.

4.3   Poly[lithium tetrakis(triethylenephenylboryl)borate] (PLEPB)

4.3.1   Synthesis of PLEPB

Poly[lithium tetrakis(ethyleneboryl)borate] (PLEB) was synthesized as described in Section 4.2.2 [198]. 0.0049 mol (2.55 ml) phenyl lithium (1.9 M solution in dibutylether, Fluka) was added dropwise into a freshly synthesized 0.84 g (0.0077 mol tri-coordinated borane unit) PLEB in 70 ml distilled ether under continuous stirring at 25 °C. The reaction was carried out for 24 hours at 25 °C. Then, the polymer was dried for 24 hours at 70 °C under vacuum to obtain the "as-synthesized PLEPB polymer".

The "annealed PLEPB polymer" was obtained by tempering the as-synthesized PLEPB polymer at 275 °C for 24 h under argon atmosphere. In this work, the detailed investigations were carried out for both as-synthesized and annealed PLEPB polymers.

4.3.2   Characterization of as-synthesized PLEPB

4.3.2.1   X-ray Powder Diffraction

The X-ray powder diffraction pattern of the as-synthesized PLEPB polymer is given in Figure 43, indicating the amorphous character of the polymer.

4.3.2.2   Elemental Analysis

The elemental analysis of the PLEPB polymer was performed (except for hydrogen), the results of which are given in Table 10, and the empirical formula was found as $B_{1.1}C_{8.6}Li_1$. The PLEPB polymer contains boron and lithium in the ratio of B:Li as 2:1.8, which demonstrates that the number of lithium atoms per boron was increased in the PLEPB polymer by reacting as-synthesized PLEB, having the ratio of B:Li as 2:1, with phenyl lithium. Moreover, when the ratio of B:C is compared in both as-synthesized polymers before and after reacting with phenyl lithium, the respective results are 2:10 and 2:16. Thus, incorporation of phenyl lithium in the PLEB polymer increased both the carbon and lithium ratio with respect to boron in the as-synthesized
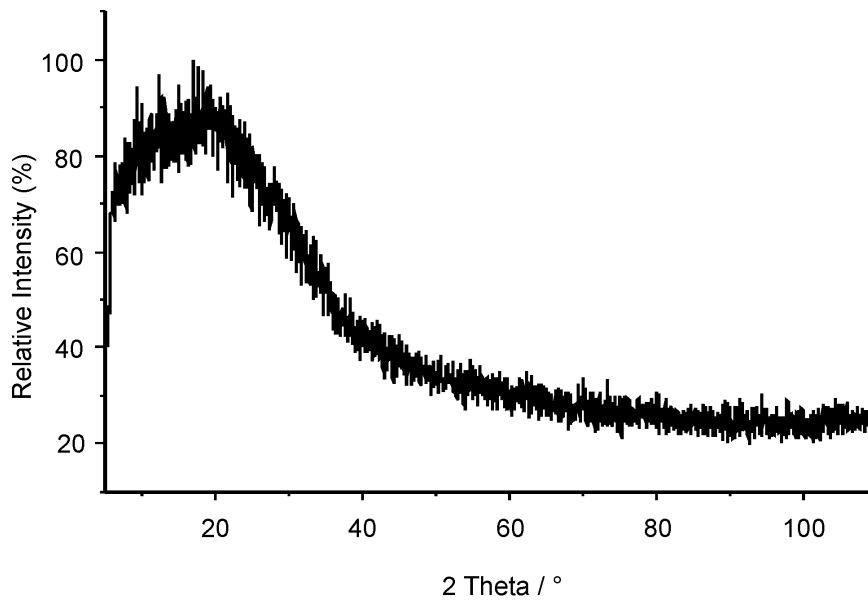
Figure 43: XRD pattern of as-synthesized PLEPB polymer.

Table 10: Chemical composition of the as-synthesized PLEPB polymer.

Element	Mass (%)	Empirical Formulae
B	7.70	$B_{1.1}C_{8.6}Li_1$
C	67.03	$(\approx B_2C_{16}Li_{1.8})$
Li	4.50	

polymers. The charge carrier concentration was thus increased in PLEPB, which should increase the ionic conductivity, along with the enhancement in the concentration of carbon atoms between boron atoms.

4.3.2.3 FT-IR Spectroscopy

In the FT-IR spectrum of the PLEPB polymer, which is presented in Figure 44, the C—H aromatic stretching of the phenyl group is noticeable at 3055 cm^{-1}, and the bands appear at 775 cm^{-1}, 704 cm^{-1} and 645 cm^{-1} stand for the monosubstituted aromatic C—H out of plane deformations [199]. The characteristic bands of the phenyl ring between 1593 cm^{-1} and 1380 cm^{-1} represent the aromatic C=C stretching vibrations. In the same region, where aromatic stretching vibrations occur, B—H—B symmetric
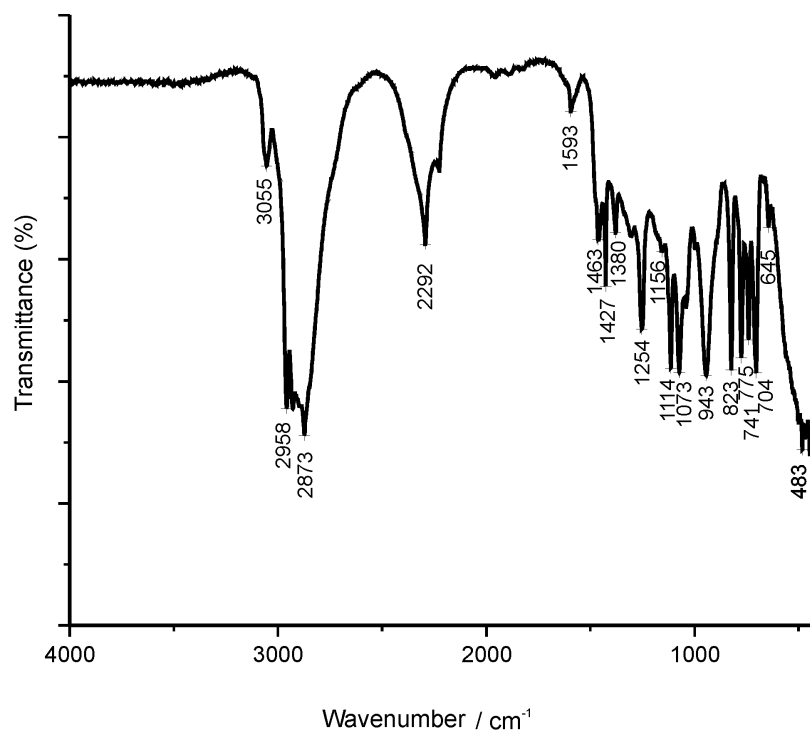
Figure 44: FT-IR spectrum of the as-synthesized PLEPB polymer.

Table 11: FT-IR band positions and assignments for PLPEB polymer.

Wavenumbers $/cm^{-1}$	Intensity	Assignment
3055	m	ν (C—H) aromatic
2958	s	ν (C—H)
2873	s	ν (C—H)
2292	m	ν (B—H)
1593	w	ν (C=C) aromatic and ν (B—H—B)
1463	m	ν (C=C) aromatic and δ (C—H)
1427	m	ν (C=C) aromatic
1380	m	ν (C=C) aromatic and δ (C—H)
1254	s	γ (C—H)
1156	w	δ (C—H) aromatic
1114−1073	s	ν (B—C)
943	s	δ (ring)
823	s	ρ (C—H)
775	s	δ (C—H) aromatic
741	s	ν (B—C)
704	s	δ (C—H) aromatic
645	w	δ (C—H) aromatic
483	m−s	ρ (C—H) and δ (ring)

stretching of the hydrogen bridged boranes at 1593 cm^{-1}, along with CH$_2$ deformation vibrations at 1463 cm^{-1} and 1380 cm^{-1} overlap. The B—H stretching band at 2292 cm^{-1} is assigned to the tetrahydroborate species, similar to the PLEB polymer. Further interpretations of assignments of wavenumbers together with intensities are compiled in Table 11. The IR spectrum of PLPEB polymer thus clearly indicates the incorporation of the phenyl groups in polymer, which can be figured out from the vibrations belonging to the phenyl group.

4.3.2.4   Raman Spectroscopy

The presence of the phenyl groups in the PLPEB polymer is identified with the characteristic aromatic C—H deformation vibrations at 1001 cm^{-1} and aromatic C=C stretching vibrations at 1594 cm^{-1} in the Raman spectrum of PLEPB, which can be seen in Figure 45 [200]. Other characteristic bands that represent phenyl groups are
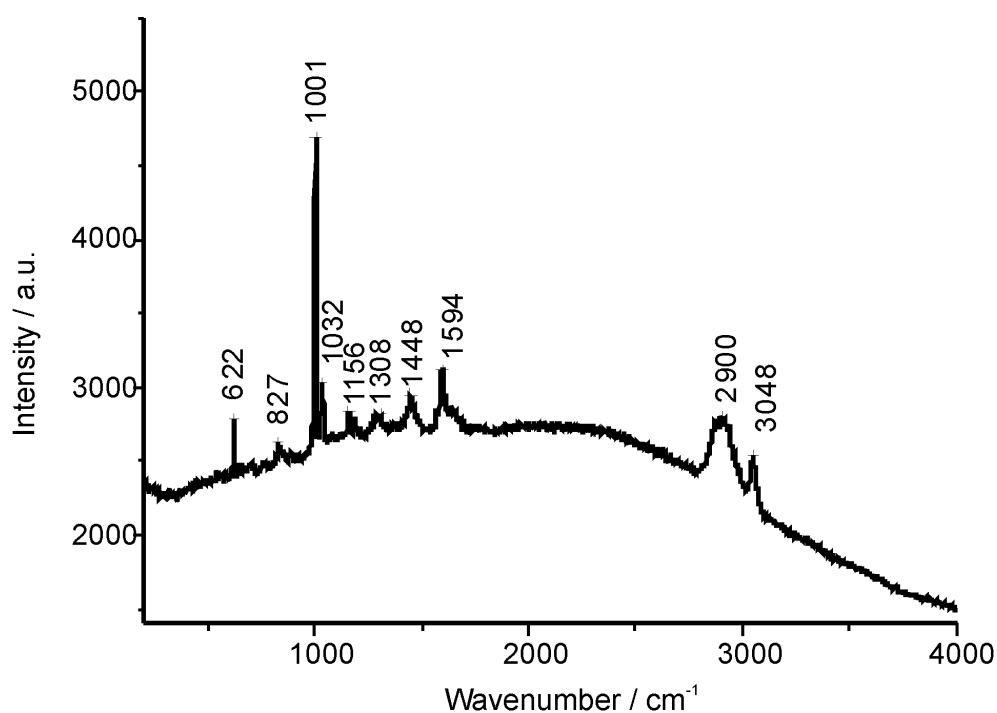
Figure 45: Raman spectrum of as-synthesized PLEPB polymer.

aromatic C—H stretching vibrations at 3048 cm^{-1}, C—H deformation vibrations at 1032 cm^{-1} and ring vibrations at 622 cm^{-1}. Existence of very strong band at 1001 cm^{-1} along with vibrations at 622 cm^{-1} and 1032 cm^{-1} are thus interpreted for mono substituted phenyl groups [200]. Moreover, the band at 1156 cm^{-1} is assigned to asymmetric stretching of phenyl attached to boron [201]. An overview of the further interpretations on the Raman bands and their assignments are summarized in Table 12.

Table 12: Raman band positions and corresponding assignments for PLEPB polymer.

Wavenumber /cm^{-1}	Intensity	Assignment
3048	m	ν (C—H) aromatic
2900	s	ν (C—H)
1594	m	ν (C=C) aromatic
1448	m	δ (C—H)
1308	w	γ (C—H)
1156	w	ν (B—phenyl)
1032	m	δ (C—H) aromatic and ν (C—C)
1001	vs	δ (C—H) aromatic
827	w	ρ (C—H)
622	m	δ (ring)

4.3.2.5   Solid State NMR Measurements

The as-synthesized PLEPB polymer was further characterized by ^{1}H, ^{11}B and ^{13}C solid-state NMR spectroscopy techniques. The ^{1}H NMR spectrum of the as-synthesized PLEPB revealed that at least two different hydrogen species exist in the structure of polymer with chemical shifts around 1.4 ppm and 7 ppm. Similar to PLEB, the largest proportion of the hydrogen atoms in the structure are responsible for the spectral component at 1.4 ppm, and they represent the hydrogen atoms incorporated into alkane units. The aromatic hydrogen atoms possess the highest chemical shift which are associated with the component exhibiting a shoulder at 7 ppm. This represents the incorporation of phenyl groups into the PLEB structure. Since the solid state ^{1}H NMR spectrum was highly unresolved, definite assignments of the peaks for hydrogen atoms

in the spectrum can not be stated here. Therefore, hydroborate and bridging hydrogen components of the polymer can not be separated from the broad peak.
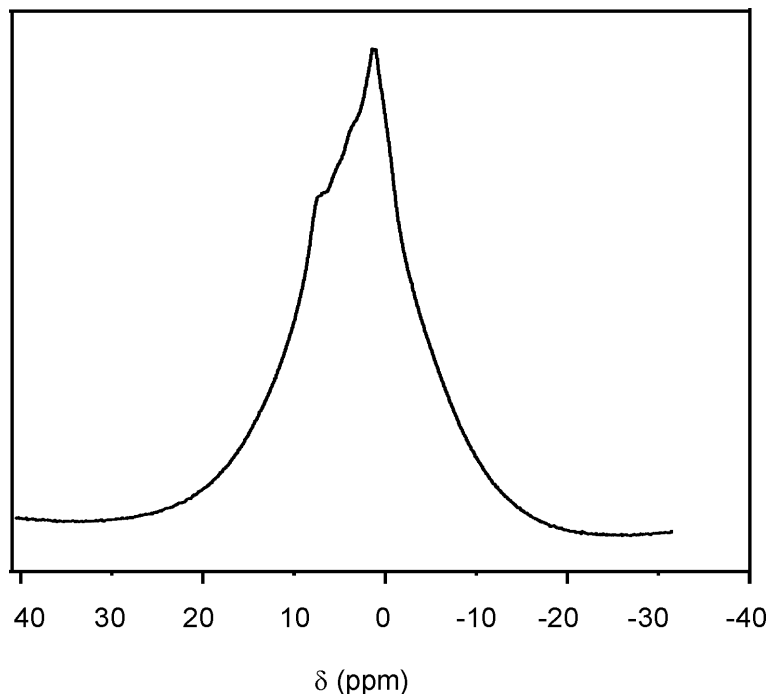
Figure 46:   Solid state ^{1}H-NMR spectrum recorded for the as-synthesized PLEPB polymer.

^{11}B solid state NMR spectrum of the as-synthesized PLPEB polymer, which is shown in Figure 47, was measured at room temperature by using the standard nutation pulse sequence. The lengths of nutation pulse sequence lengths were 5 μs for the π-pulse combined with a τ_r of 1/25000 s. The signal from the background is broadened and appeared between -60 ppm and $+40$ ppm in the bottom of the spectrum, which could be separated from the polymer's signal by using nutation spectra. In the spectrum, the chemical shifts for three different four-coordinated boron species were identified with the chemical shifts located at -15 ppm, -42 ppm and between 0 ppm and $+5$ ppm. Similar to the case for PLEB polymer, tetraalkylborate species form narrow bands between 0 ppm and $+5$ ppm with a resonance of low quadrupolar coupling. Tetrahydroborate ions, which form by some ligand exchange reactions during the polymerization reactions, exhibit a narrow peak at -42 ppm with a nearly vanishing quadrupolar constant. However, the majority of the four coordinated boron species form a narrow peak at -15 ppm. Hansen et al. reported the ^{11}B chemical shift for sodium tetraphenylborate as -9.2 ppm [202], and Thompson et al. determined the ^{11}B

chemical shift of lithium tetraethylborate as −17.5 ppm [188]. In accordance to the available chemical shift values in literature, the chemical shift at −15 ppm is assigned to the four-coordinated boron species substituted by three ethyl and one phenyl groups. Hence, ^{11}B NMR clearly depicts that phenyl lithium reacted with PLEB polymer, and phenyl groups were substituted into this four-coordinated boron species together with three ethyl groups forming the triethylenephenylborate groups in the structure of the PLEPB polymer. Apart from the four-coordinated boron species, hydrogen-bridged boron species, which were introduced via the borane species, are also expected to be present in the PLPEB polymer structure. It is assumed that as a result of the reduced local symmetry, hydrogen-bridged alkylborane species possess a larger quadrupolar coupling in comparison with the four-coordinated boron species. Hence, the broad peak located between +5 ppm and +50 ppm was assigned to the hydrogen-bridged alkylborane species. Therefore, four different boron species can be distinguished in the as-synthesized PLEPB polymer. A different aspect of this polymer is the formation of highly intense peak at −15 ppm, which stands for a phenyl and three ethyl substituted four-coordinated boron species.
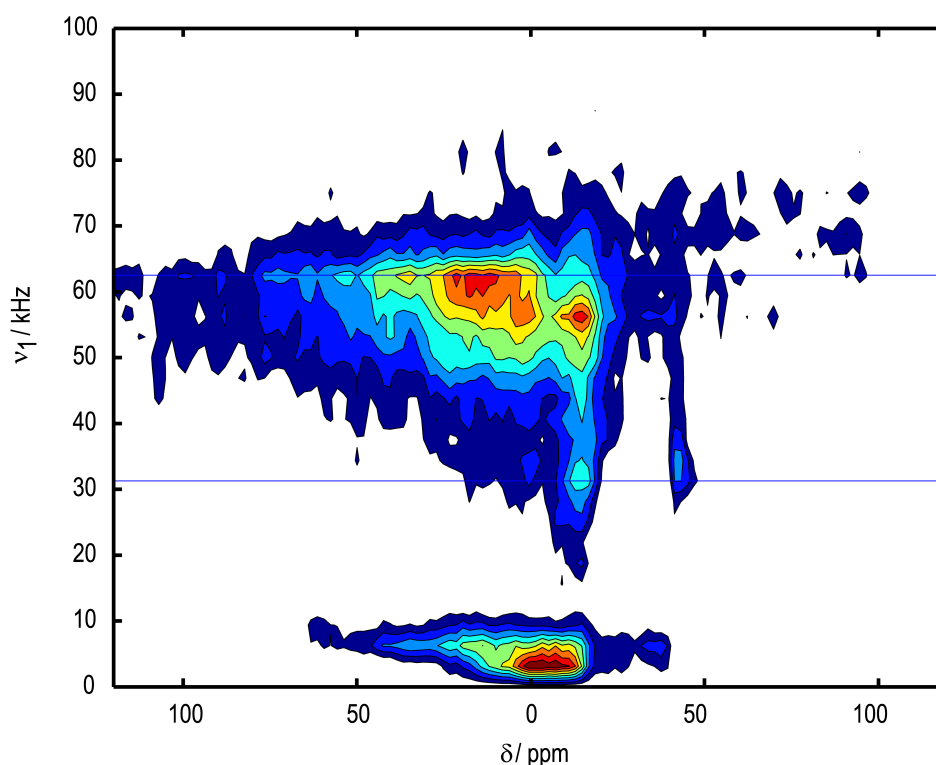
Figure 47:   Solid state ^{11}B nutation NMR spectrum recorded for the as-synthesized PLEPB polymer.

The solid state ^{13}C NMR spectrum of the PLPEB polymer, which is depicted in Figure 48, exhibits three peaks. The broad signal centered around 26 ppm is the dominating signal in the solid state ^{13}C NMR spectrum. This is attributed to the saturated carbon atoms and the chemical shift value points out that most of the carbon atoms exist in CH$_2$ units, similar to the PLEB polymer (without incorporation of phenyl lithium). The peak at 70 ppm most probably occurs as a result of the coordination of the some remaining THF to the trialkylborane units. The signal at 130 ppm, which was not observed in PLEB polymer, is assigned to the carbon atoms in the phenyl group, which clearly proves the incorporation of the phenyl groups into the PLPEB polymer.
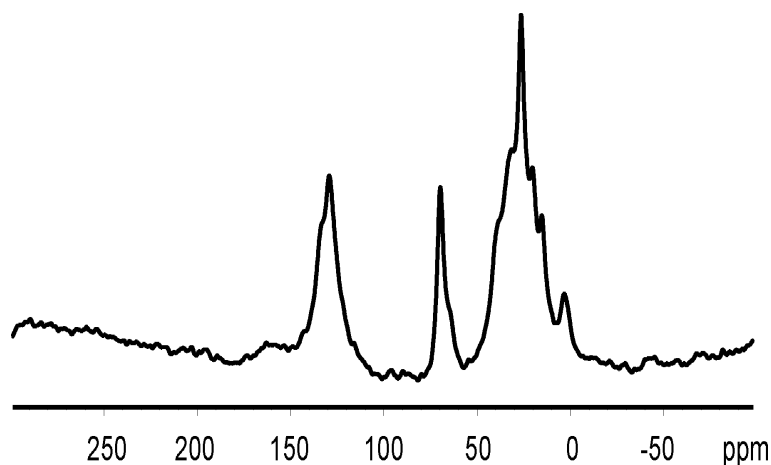
Figure 48: Solid state ^{13}C-NMR spectrum of the as-synthesized PLEPB polymer. $\omega_r \, (2\pi)^{-1} = 25$ kHz.

4.3.2.6 Thermal Analysis

In order to investigate the thermal stability and the decomposition behaviour of the PLEPB polymer, DTA/TG/MS analyses were performed under argon flow by heating rate of 10 °C min^{-1} between room temperature and 1000 °C. The measurements, see Figure 49, show that the PLEPB polymer is thermally stable up to 150 °C. The decomposition proceeded up to 500 °C and the ceramic yield at 1000 °C was found as 45 %. This shows that, phenyl substitution increased the ceramic yield at 1000 °C in comparison to the as-synthesized PLEB polymer. Most of the residual THF solvent entrapped in the PLEPB polymer was evolved until 210 °C (m/z = 42). The oligomeric groups and chain ends cleaved and reorganized at temperatures higher than

210 °C. The polymer network degraded mainly between 300 °C and 470 °C with the fragments of H_2 (m/z = 2), BC_2H_6 (m/z = 41), BCH_4 and C_2H_3 (m/z = 27), C_2H_4 (m/z = 28), BC_2H_4 (m/z = 39) and CH_3 (m/z = 15). The atomic rearrangement and depolymerization of the network proceeded beyond this latter temperature range with the evolution of C_2H_4 (m/z = 28) and CH_3 (m/z = 15) until 750 °C, and H_2 (m/z = 2) until 900 °C.
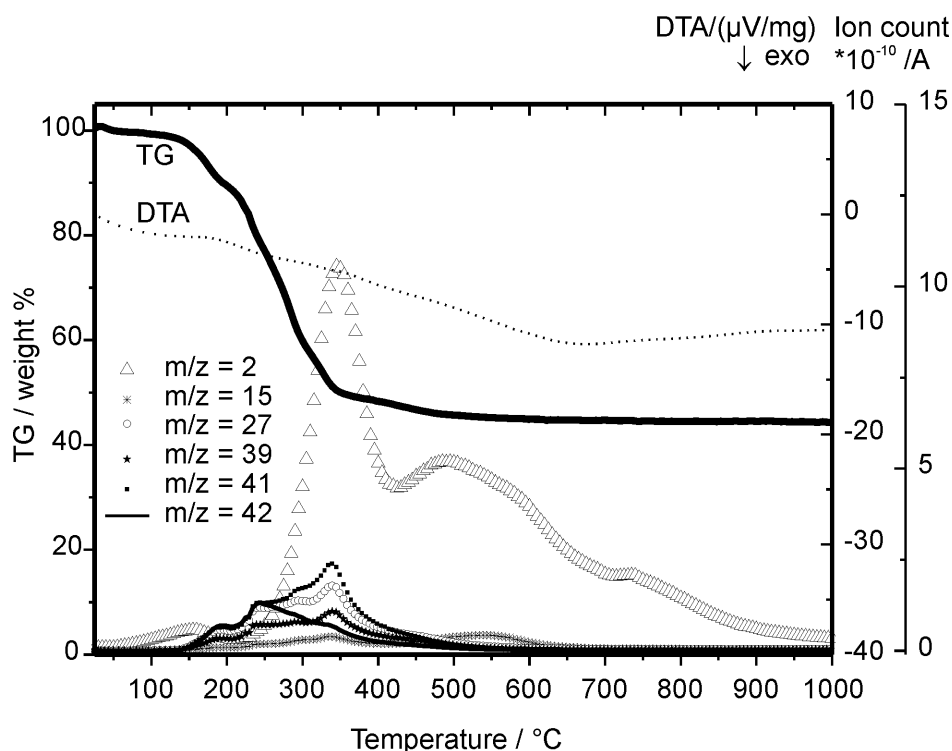
Figure 49: DTA/TG/MS thermograms for the as-synthesized PLEPB polymer in argon flow at 10 °C min^{-1} heating rate.

4.3.2.7   Main Features of the PLEPB Structure

The schematic drawing in Figure 50 shows the building blocks that we have identified via the combination of findings from the analyses conducted on the amorphous as-synthesized PLEPB polymer. The main features of the PLEB polymer remained almost the same after the reaction with phenyl lithium. The same building blocks

of hydrogen bridged boranes and four-coordinated borates as well as the connectivities were identified. However, the main differences between these two polymers are the incorporation of phenyl groups in the main polymer backbone of PLEB polymer, and a new building block was identified with three ethylene and a phenyl substituents forming a four-coordinated borate unit.
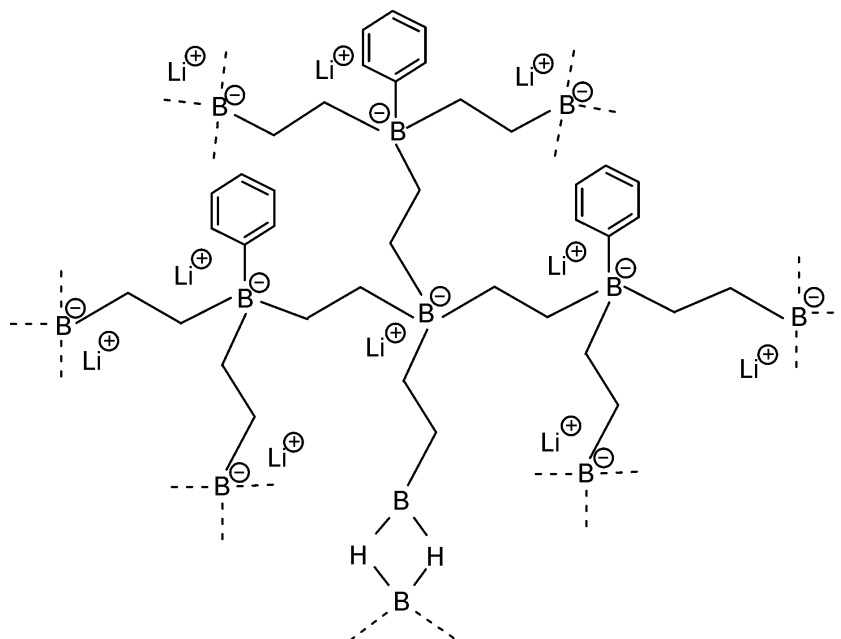
Figure 50: Schematic drawing of the structure of PLEPB polymer showing the main building blocks.

4.3.3   Characterization of annealed PLEPB

The characterization of the poly[lithium tetrakis(triethylenephenylboryl)bo- rate] after annealing will be discussed in this section. The annealing was performed for around one day at 275 °C under argon atmosphere with $1\,°C\,min^{-1}$ heating and cooling rates.

4.3.3.1   X-ray Powder Diffraction Analysis

The amorphous character of the PLEPB polymer was preserved after annealing and Figure 51 shows the X-ray powder diffraction pattern of the annealed PLPEB polymer.
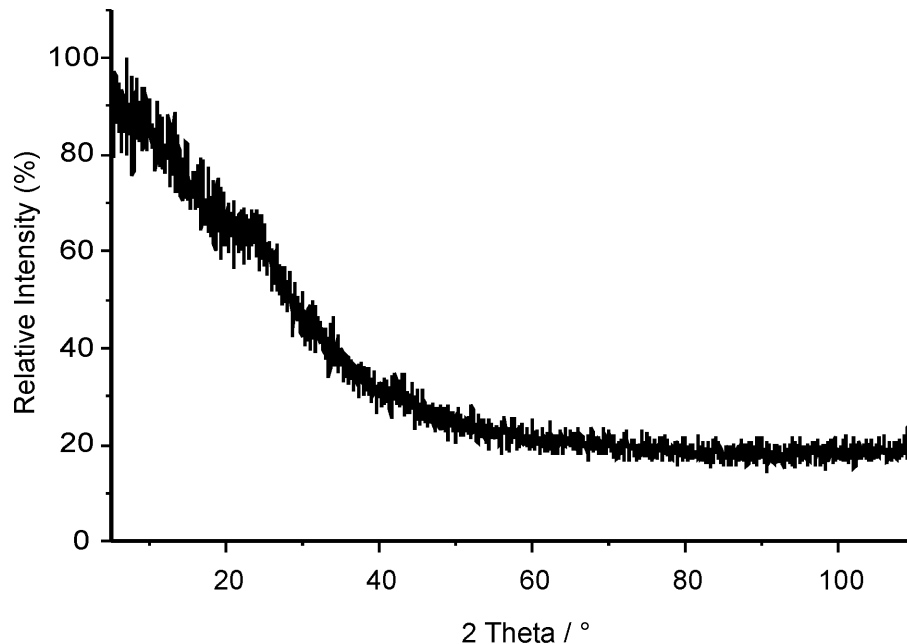
Figure 51: Powder XRD pattern of the annealed PLEPB polymer.

4.3.3.2   Elemental Analysis

The results of the elemental analysis for the annealed PLEPB polymer are presented in Table 13. According to the elemental analysis results, the ratio of B:C:Li is determined as 0.8:4.7:1. This shows that during annealing process, the major weight loss was due to the carbon atoms accompanied by the minor weight loss of boron atoms, in a similar manner as PLEB does. The ratio of carbon and boron atoms decreased and a high charge carrier concentration was obtained via annealing, which results a B:Li ratio as 2:2.4.

Table 13: Chemical composition of the annealed PLEPB.

Element	Mass (%)	Empirical Formulae
B	10.70	$B_{0.8}C_{4.7}Li_1$
C	66.25	$(\approx B_2C_{11}Li_{2.4})$
Li	8.16	

4.3.3.3   FT-IR Spectroscopy

In order to understand the effect of annealing on the PLEPB polymer, IR measurement was performed, and the assignment of the bands together with the intensities are given in Table 14. The similar peaks like in as-synthesized PLEPB polymer were detected as can be seen in Figure 52. However, the main difference is the clearly observable loss of the band representing non-bridging terminal B—H groups at 2292 cm^{-1} by annealing. The same effect was also observed in the PLEB polymer. As mentioned in Section 4.2.4.3, introduction of some vinylic groups into the structure via annealing were detected from the IR spectrum in PLEB polymer. However, these groups could not be distinguished for PLEPB polymer from the IR spectrum, since vinylic vibrations appear in the same range of the spectrum as phenylic vibrations do.

Table 14: FT-IR band positions and assignments of the annealed PLEPB polymer.

Wavenumbers $/\text{cm}^{-1}$	Intensity	Assignment
3047	m	ν (C—H) aromatic
2925	s	ν (C—H)
2855	s	ν (C—H)
1597	m	ν (C=C) aromatic and ν (B—H—B)
1439	s	ν (C=C) aromatic and δ (C—H)
1408	s	ν (C=C) aromatic
1298	s	ν (C=C) aromatic and δ (C—H)
1263	s	γ (C—H)
1071−1025	m−s	ν (B—C)
964	s	δ (ring)
881	s	ρ (C—H)
748	m	ν (B—C)
702	s	δ (C—H) aromatic
504−436	m−s	ρ (C—H) and δ (ring)

Figure 52: FT-IR spectrum of the annealed PLEPB polymer.

4.3.3.4   Thermal Analysis

DTA/TG/MS analysis of the annealed PLEPB polymer was performed between room temperature and 1000 °C under argon flow with a heating rate of 10 °C min^{-1}. The obtained ceramic yield was 73 % at 1000 °C, which is higher than for the as-synthesized PLEPB polymer, as expected. The main decomposition of the network was observed between 300 °C and 550 °C with the evolution of H_2 (m/z = 2), BC_2H_6 (m/z = 41), BCH_4 and C_2H_3 (m/z = 27), C_2H_4 (m/z = 28), BC_2H_4 (m/z = 39) and CH_3 (m/z = 15). The evolution of CH_3 (m/z = 15) until 700 °C, and H_2 (m/z = 2) until 900 °C were additionally observed, which indicates the atomic rearrangement and depolymerization processes.
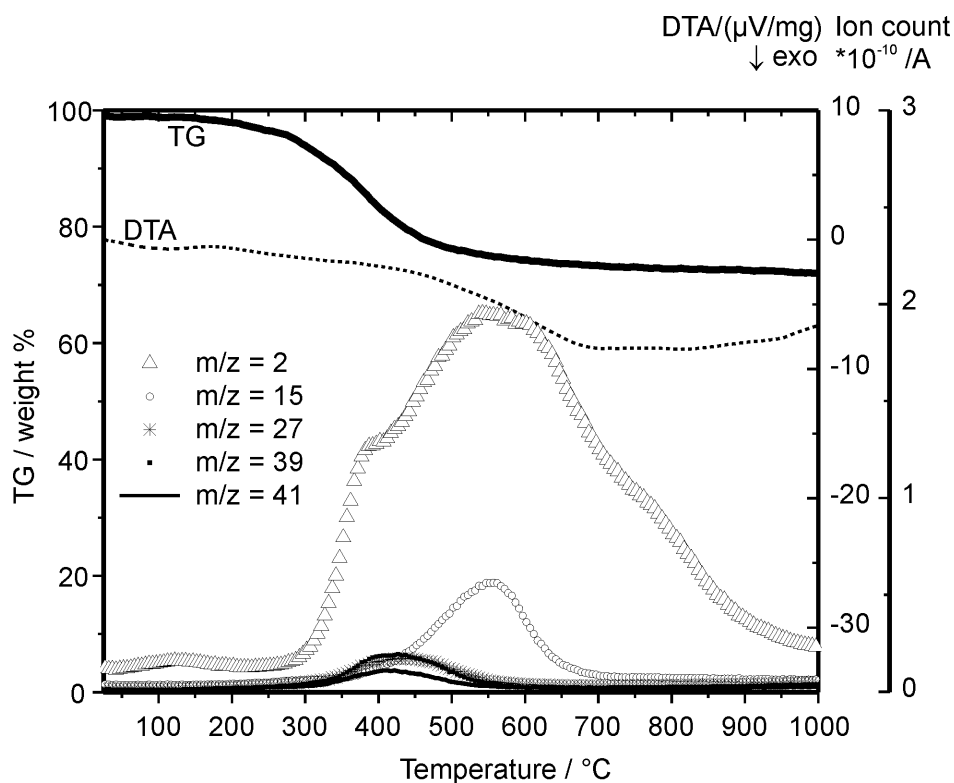
Figure 53: DTA/TG/MS thermograms for the annealed PLEPB polymer in argon flow with a 10 °C min^{-1} heating rate.

4.3.4   Impedance Spectroscopy

Ionic conductivity measurements were carried out via impedance spectroscopy by applying heating and cooling rates of 1 °C min^{-1}. The measurements were conducted from RT to 110 °C for the as-synthesized PLEPB polymer and up to 275 °C for the annealed PLEPB polymer, under argon atmosphere. Figure 54 shows the temperature dependent bulk ionic conductivities for both polymers, which were plotted in Arrhenius type diagrams. From the slope of the conductivity curves, activation energies were evaluated, with the values of 146 kJ mol^{-1} for the as-synthesized PLEPB polymer and 78 kJ mol^{-1} for the annealed PLEPB polymer at 275 °C. Resulting activation energies for both polymers are slightly higher in comparison to the PLEB polymer counterparts before incorporation of the phenyl lithium (see Table 9). This is probably due to the

enhancement in bulkiness of the PLEB polymer via incorporation of the phenyl groups. Moreover, incorporation of phenyl lithium increases the charge carrier concentration and thus enhances the ionic conductivity values for both as-synthesized and annealed PLEPB polymers.
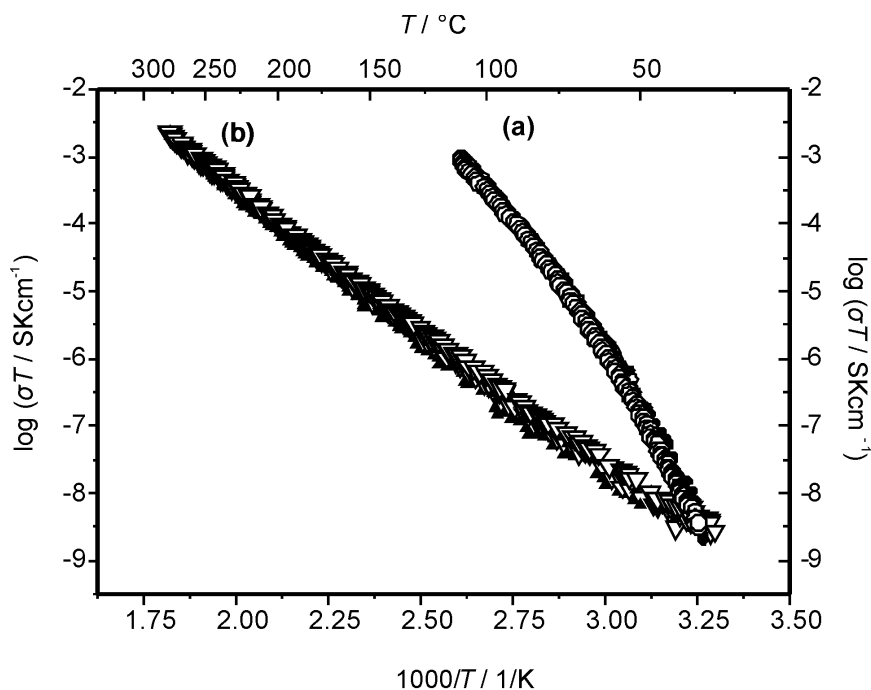
Figure 54: Temperature dependence of the ionic conductivities of the (a) as-synthesized and (b) annealed PLEPB polymers at 275 °C. Heating and cooling are represented by filled and open symbols, respectively.

Furthermore, bulky phenyl groups in PLEPB polymer attached to borate units are expected to prevent close approach of the lithium cations and reduce the possible ion pairing, which should enhance the ionic conductivity for the as-synthesized PLEB polymer. Compared to PLEB, one order of magnitude increase in the ionic conductivity values has been observed for as-synthesized PLEPB polymer at 110 °C. The ionic conductivities at different temperatures and corresponding activation energies, for both as-synthesized and annealed PLEPB polymers, were tabulated in Table 15. When the measurements were performed by ion blocking gold electrodes, low frequency diffusion spikes were observed in the Nyquist plots. Measurements were also recorded by using ion non-bocking lithium electrodes and no low frequency spike could be observed.

According to the these results, the nature of the conduction in PLEPB polymer is ionic.
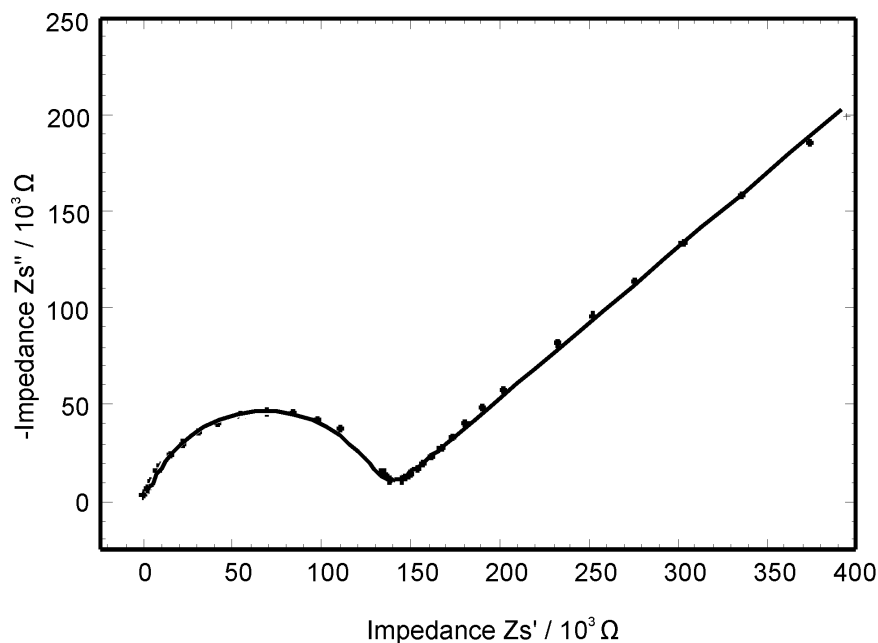
Figure 55: Nyquist plot of the PLEPB polymer with blocking gold electrodes at 276 °C. The experimental and the simulated impedance spectrum are represented with dots and the solid line, respectively.

The interpretation of the impedance data was performed by a parallel RQ element in the equivalent circuit up to 90 °C, which possesses one semicircle in the complex plane format, in this temperature regime. When the measurements were performed at higher temperatures, a low frequency spike was observed in addition to the semicircle in Nyquist plots (Figure 55), indicating the presence of a charge transfer barrier between the sample and ion-blocking gold electrodes. Therefore, an additional constant phase element Q_{el} was used in series with the RQ element in the equivalent circuit. The capacitance values for the semicircles at different temperatures were determined and the corresponding values were in the range of 10^{-12} F. This order of magnitude is typically associated with the bulk capacitance of a sample, which proves that the lithium ion conductivity in the bulk can be expressed with the semicircle [45].

Table 15:   Activation energies and ionic conductivities (at 80 °C, 110 °C and 275 °C) for PLEPB polymers.

	E_a / kJ mol^{-1}	σ /S cm^{-1}		
		80 °C	110 °C	275 °C
As-synthesized PLEPB polymer	146	8.0 x 10^{-8}	2.2 x 10^{-6}	—
Annealed PLEPB polymer at 275 °C	78	3.4 x 10^{-10}	2.9 x 10^{-9}	3.9 x 10^{-6}

4.4   Poly[lithium tetrakis(triethylenemethylboryl)borate] (PLEMB)

4.4.1   Synthesis of PLEMB

Poly[lithium tetrakis(triethylenemethylboryl)borate] (PLEMB) was synthesized by using standard Schlenk techniques. The reaction was performed by dropwise addition of 0.0064 mol (4 ml) methyl lithium (1.6 M solution in diethylether, Sigma Aldrich) into a freshly synthesized 0.6884 g PLEB polymer (0.0064 mol tri-coordinated borane unit) in 80 ml distilled ether under continuous mixing at 25 °C. The reaction was carried out for 72 hours at 25 °C and the product further dried for 64 hours at 70 °C.

4.4.2   X-ray Powder Diffraction

Figure 56 shows the X-ray powder diffraction pattern of the PLEMB polymer, which indicates that incorporation of methyl lithium into the polymer did not change the amorphous character of the PLEB polymer.

4.4.3   Elemental Analysis

According to the elemental analysis results, the empirical formulae of B:C:Li in PLEMB polymer was determined as 2:11:2.2. The lithium ratio per boron atom, which is 1.1 Li for each boron atom, is higher than the as-synthesized PLEB and PLEPB polymers. The ratio of carbon per boron atom is around 5.5, which is more than the PLEB polymer. Therefore, elemental analysis results show the expected increase in lithium and carbon concentrations in the PLEMB polymer via incorporating methyl lithium into the PLEB polymer.
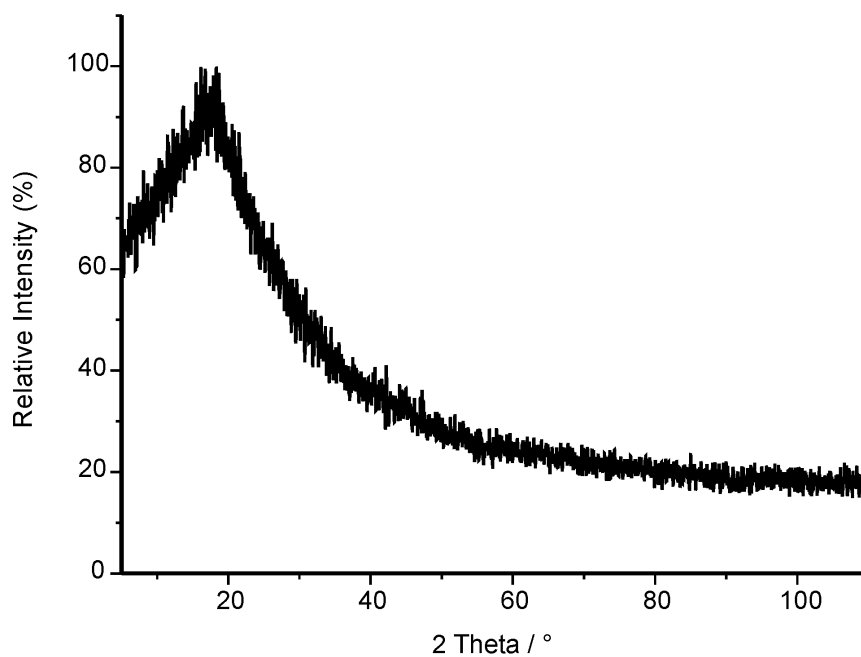
Figure 56: XRD pattern of PLEMB polymer.

Table 16: Chemical composition of the PLEMB polymer.

Element	Mass (%)	Empirical Formulae
B	10.51	$B_{0.9}C_5Li_1$
C	62.63	$(\approx B_2C_{11}Li_{2.2})$
Li	7.60	

4.4.4 FT-IR Analysis

Figure 57 displays the FT-IR spectrum of PLEMB polymer. The incorporation of methyl groups into the PLEMB polymer is characterized with the bands at 1392 cm^{-1} and 1294 cm^{-1} representing asymmetric and symmetric CH$_3$ deformation vibrations, respectively. CH$_3$ rocking and B—C asymmetric stretching vibrations appear at 934 cm^{-1} and in the range of 1039−1119 cm^{-1}, respectively. Similar to PLEB polymer, a free B—H stretching band is observed at 2292 cm^{-1}, which belongs to non-bridging B—H species. Furthermore, the band at 1578 cm^{-1} is attributed to the symmetric stretching vibration of a B—H—B bridge structure. An overview of the peak assignments along with intensities for IR bands are tabulated in Table 17.
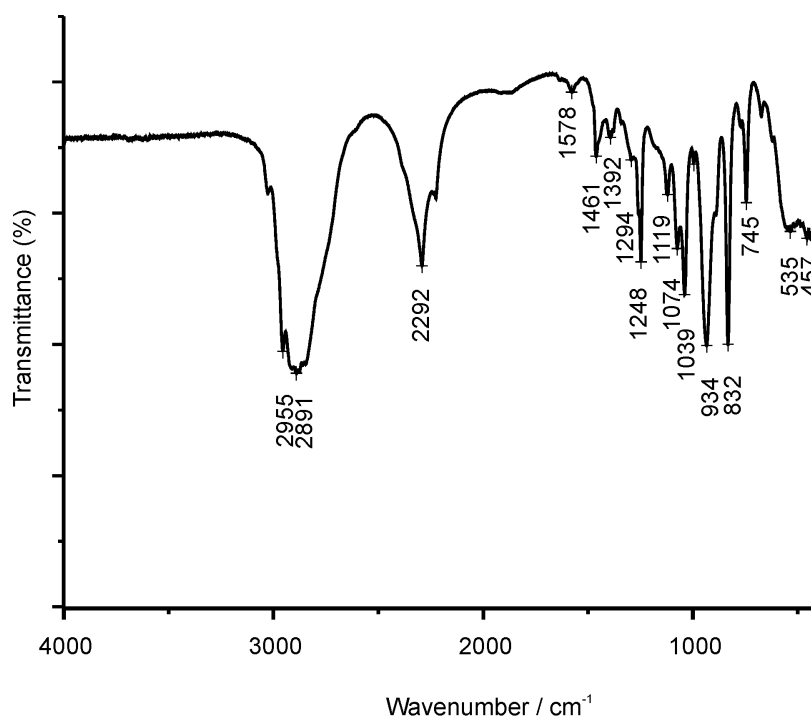
Figure 57: FT-IR spectrum of the PLEMB polymer.

Table 17: FT-IR band positions and assignments of PLEMB polymer.

Wavenumber /cm^{-1}	Intensity	Assignment
2955	s	ν (C—H)
2891	s	ν (C—H)
2292	m	ν (B—H)
1578	w	ν (B—H—B)
1461	m	δ (C—H)
1392	w	δ (C—H)
1294	m	δ (C—H)
1248	s	γ (C—H)
1119−1039	w−s	ν (B—C)
934	s	ρ (C—H)
832	s	ρ (C—H)
745	m	ν (B—C)
535−437	m	ρ (C—H)

4.4.5   Thermal Analysis

The thermal stability of the PLEMB polymer was analysed simultaneously by differential thermal analysis, thermogravimetric analysis and mass spectroscopy (DTA/TG/MS) technique from room temperature to 1000 °C under argon flow with a 10 °C min^{-1} heating rate. The mass loss for the PLEMB polymer starts at higher temperatures compared to phenyl lithium incorporated polymer (PLEPB). No mass loss for the PLEMB polymer was observed up to 175 °C, which can be seen in Figure 58. The major loss of volatile residual THF (m/z = 42), that were entrapped in the sample, was observed in the temperature range from 175 °C to 250 °C. The mass loss observed above 250 °C was assigned to the loss of oligomers that are not connected to the main network and the reorganization of the PLEMB network. The main decomposition of the network was proceeded approximately between 300 °C and 500 °C, and monitored with the evolution of the fragments such as H_2 (m/z = 2), BC_2H_6 (m/z = 41), BCH_4

and C_2H_3 (m/z = 27), C_2H_4 (m/z = 28), BC_2H_4 (m/z = 39), and CH_3 (m/z = 15). In addition, the fragments of CH_3 (m/z = 15) and C_2H_4 (m/z = 28) between 500 °C and 700 °C, and H_2 (m/z = 2) between 500 °C and 900 °C were evolved due to the atomic rearrangement involved with the simultaneous depolymerization and ceramization processes. The ceramic yield of the PLEMB polymer is determined as 50 % after heating up to 1000 °C. Methyl substitution thus increased the ceramic yield at 1000 °C compared to the both as-synthesized PLEB and PLEPB polymers.
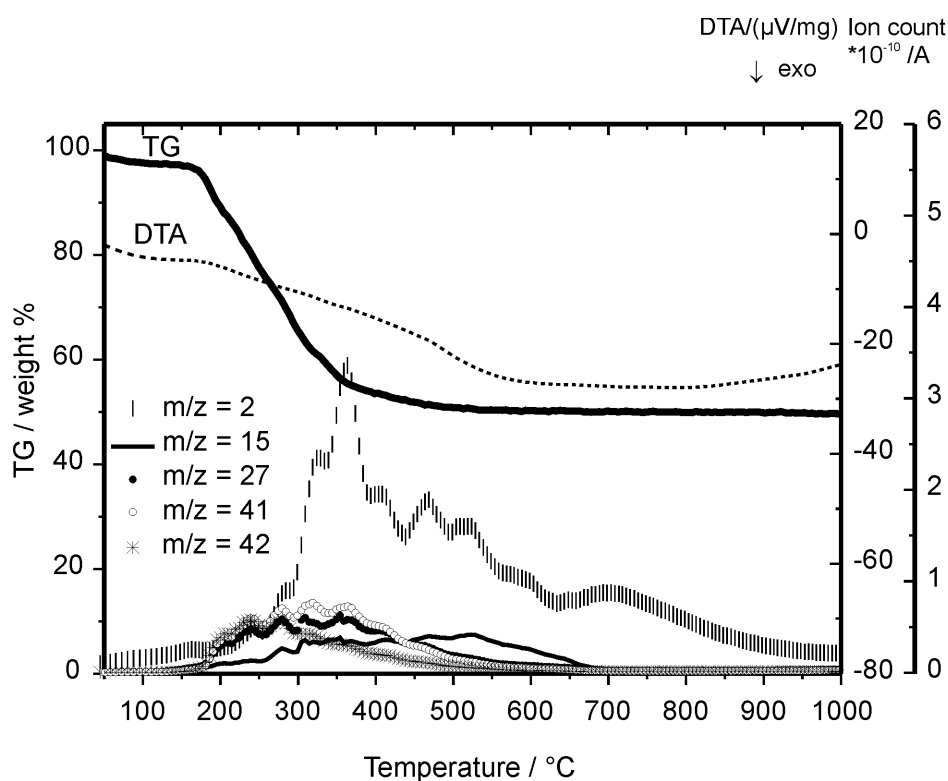
Figure 58: DTA/TG/MS thermograms for the PLEMB polymer in argon flow at $10 \, °C \, min^{-1}$.

4.4.6   Impedance Spectroscopy

Ionic conductivity measurements of the PLEMB polymer were performed up to 150 °C and 350 °C under argon flow with heating and cooling rates of $1 \, °C \, min^{-1}$. The PLEMB polymer was annealed under argon atmosphere up to the 350 °C and the annealed PLEMB polymer were used for ionic conductivity measurements. Figure 59 shows the

Arrhenius plots of the temperature dependent ionic conductivities for PLEMB poly-mers. The activation energies of PLEMB polymers were deduced from the slopes of the Arrhenius plots, which were found as 134 kJ mol^{-1} and 66 kJ mol^{-1} for the measure-ments performed up to 150 °C and 350 °C, respectively. The activation energies and the ionic conductivities at different temperatures for both measurements are tabulated in Table 18.
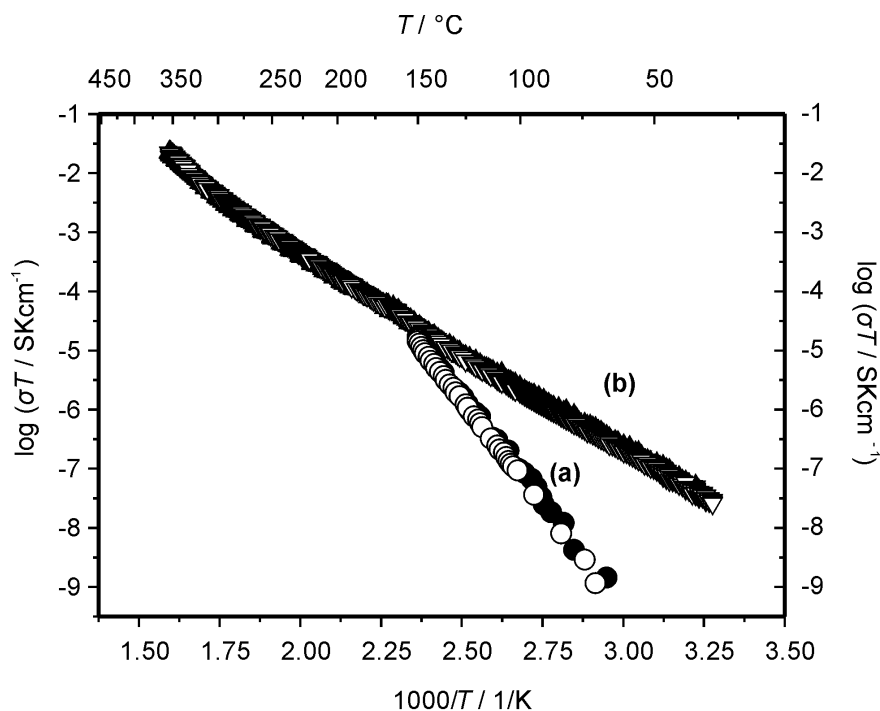
Figure 59: Temperature dependence of the ionic conductivities of the (a) as-synthesized and (b) annealed PLEMB polymers at 350 °C. Heating and cooling are represented by filled and open symbols, respectively.

Methyl lithium incorporation decreased the activation energy values of the PLEB polymers. In addition, lower ionic conductivity values are obtained for the PLEMB polymer measured up to 150 °C (see Figure 61); on the other hand, the ionic conduc-tivity is enhanced in the as-synthesized PLEB polymer with incorporated bulky phenyl groups. Ion pair formation of lithium cations with the immobilized negative charge on the chain is more probable in methyl incorporated polymer than in phenyl counter-part. It is also noteworthy to remember that PLEMB polymer possesses the highest lithium ratio per boron atom in these as-synthesized polymer series (ratio of boron to lithium is 1:1.1). Related to this, it is also plausible that a slight excess of lithium atoms per boron atom will increase the possibility of trapping of the lithium atoms by the small amount of THF solvent present in the polymer matrix. Obviously, 150 °C

is not a sufficiently high temperature to remove the THF entrapped in the polymer, which can also be seen in DTA/TG/MS thermograms. On the other hand, when the PLEMB polymer was annealed at 350 °C, removal of THF in polymer releases lithium atoms free from THF traps such that ionic conductivity of PLEMB polymer increases in this stage significantly, surpassing the conductivities of PLEB and PLEPB polymers. This is consistent with the higher lithium concentration in PLEMB polymer than its counterparts.

In the Nyquist plots, the one recorded at 350 °C is present in Figure 60, low frequency diffusion spikes were observed when ion blocking gold electrodes were used. Thus, it shows that the nature of the conduction is ionic. The impedance data presented in the complex plane format exhibit in all temperatures a semicircle and an additional low frequency spike, which corresponds to the charge transfer barrier between ion blocking gold electrodes and the sample. In the equivalent circuit, the semicircle was interpreted as a parallel RQ element, and an additional constant phase element was included in series with the RQ element to interpret the low frequency spike. The capacitance values for the semicircles were determined at different temperatures ($C \approx 7 \times 10^{-12}\,F$), which corresponds to the typical values for the bulk capacitance of the samples [45]. Therefore, the lithium ion conductivity of PLEMB in the bulk can be associated with the semicircle.
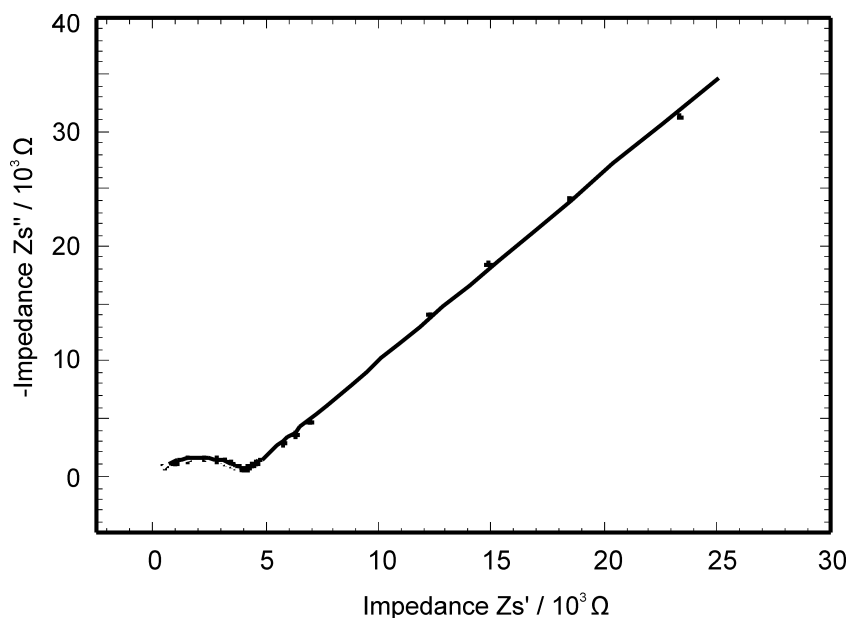
Figure 60: Nyquist plot of the PLEMB polymer with blocking gold electrodes at 350 °C. The experimental and the simulated impedance spectrum are represented with dots and the solid line, respectively.

Table 18:   Activation energies and ionic conductivities (at 80 °C, 150 °C and 350 °C) for PLEMB polymers.

	E_a / kJ mol^{-1}	σ /S cm^{-1}		
		80 °C	150 °C	350 °C
As-synthesized PLEMB polymer	134	3.4×10^{-11}	4.1×10^{-8}	—
Annealed PLEMB polymer at 350 °C	66	1.9×10^{-9}	1.9×10^{-7}	3.2×10^{-5}

4.5   Conclusions

A series of novel alkylborane type solid polyelectrolytes has been investigated. PLEB polymer was prepared by the hydroboration reaction of lithiumtetravinylborate and borane in tetrahydrofuran. In order to reveal the effect of annealing, ionic conductivities and structures were analyzed for both the as-synthesized and the annealed PLEB polymers. In order to enhance the ionic conductivity values, firstly, phenyl lithium was incorporated into PLEB polymer, which was investigated in detail for both as-synthesized and annealed forms. In another experiment, methyl lithium was incorporated into the PLEB polymer structure. The as-synthesized PLEMB polymer possesses the highest lithium to boron ratio compared to as-synthesized PLEB and PLEPB polymers.

The building blocks for the amorphous as-synthesized PLEB polymer, that we have identified by combination of findings from FT-IR, solid-state NMR and TG/MS analyses, are schematically presented in Figure 32. The polymer is composed of hydrogen-bridged borane and tetraethylene borate units as the main structural features, and lithium atoms compensate the negative charge on the borate units. The borane and borate units are connected by ethylene linkages. In as-synthesized polymers, which were dried at 70 °C after synthesis, the minor amount of THF remained in the polymer matrix. However, annealing leaves the polymer free from this residual THF according to thermal investigations and NMR results. When PLEB polymer was annealed at 275 °C, the main building blocks (hydrogen bridged boranes and four coordinated borates) composing the main features of the structure along with connectivities remain same. Additionally, minor amounts of vinyl groups have been detected in the annealed PLEB polymer as a structural feature. Incorporation of methyl groups into the PLEB polymer is assigned from the IR spectrum. Apart from the main structural units (hydrogen-bridged boranes and tetraethylene borate units), a new building block is identified from the combination of findings and solid-state NMR results performed on the as-synthesized PLEPB polymer. Appearance of this three ethylene and one phenyl substituted four coordinated borate unit, thus, shows the incorporation of phenyl groups into the polymer network (see Figure 50).

The comparison of temperature dependent ionic conductivities for these amorphous PLEB, PLEPB and PLEMB polymers is presented in Figure 61. The annealed PLEB polymer exhibits a lower activation energy for ionic conduction when compared with the as-synthesized PLEB polymer. In this pure lithium conductive polymer, t_+ value

was determined as 1.0 (2) at 137 ℃. The temperature induced crosslinking by an-
nealing modifies and densifies the structure along with increasing the charge carrier
concentration. Incorporation of phenyl lithium increases the ionic conductivity values
of both as-synthesized and annealed PLEB polymers, which is in accordance with the
presence of a higher charge carrier concentration in PLEPB polymer. Moreover, bulky
phenyl groups in PLEPB polymer should reduce the possible ion pairing by prevent-
ing close approach of the lithium cations and borate units immobilized on the chain.
On the other hand, incorporation of the methyl groups results in a lower conductivity
for the as-synthesized PLEMB polymer (see in Figure 61). However, when PLEMB
polymer was annealed up to 350 ℃, ionic conductivities exceed those of the PLEB and
PLEPB polymers in the temperature regime between ambient temperature and 250 ℃.
In addition, the lowest activation energy for ionic conduction in these polymer series
is obtained for the annealed PLEMB polymer up to 350 ℃. Since PLEMB polymer
possesses the highest lithium ratio per boron atom (that is 1.1) in these as-synthesized
polymer series, it is probable that the slightly excess lithium cations will increase the
possible trapping of lithium atoms by the small amount of THF solvent that has re-
mained in the polymer matrix. DTA/TG/MS thermograms indicates that 150 ℃ is
not adequate temperature to remove the THF entrapped in the polymer. On the other
hand, when the PLEMB polymer is annealed at 350 ℃, lithium atoms become free
from THF traps. Consequently, ionic conductivity of PLEMB polymer considerably
enhanced and exceeded the conductivities of PLEB and PLEPB polymers, consistent
with the higher lithium concentration of PLEMB polymer.
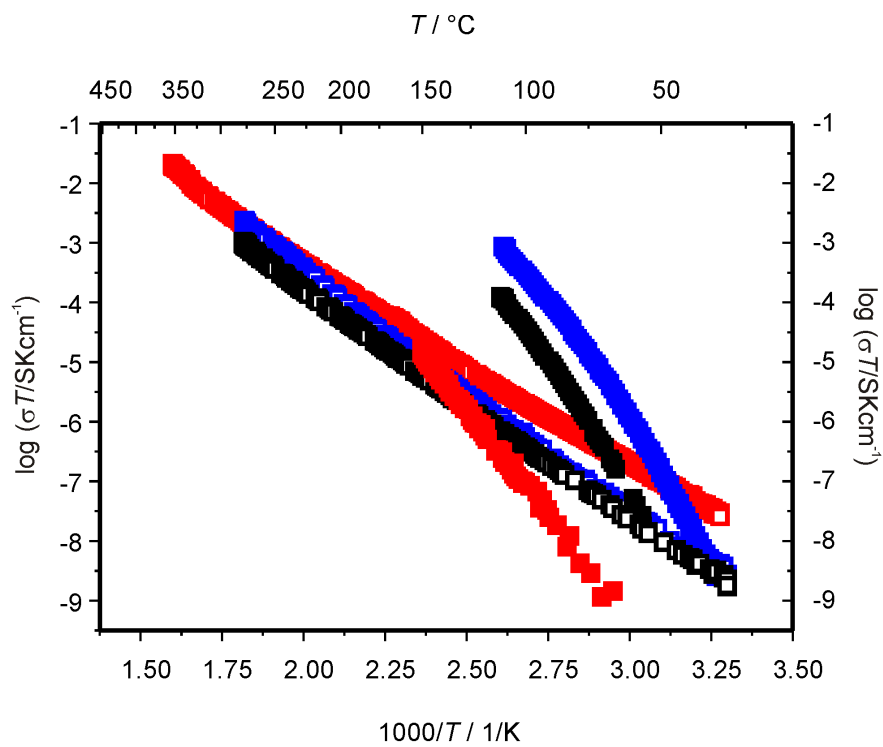
Figure 61:   A comparison of the temperature dependent ionic conductivities for the PLEB (plotted with black symbols), PLEPB (plotted with blue symbols) and PLEMB (plotted with red symbols) polymers. As-synthesized and annealed polymers are represented by respective closed and open symbols.

4.6   Poly[tris(tetraethylenesilyl)borane] (PESB)

4.6.1   Reactants

The reactions were performed by utilizing standard Schlenk techniques in a purified argon atmosphere via employing rigorously dried solvents and reaction apparatus. The solvent, diethyl ether (Merck), was distilled prior to the use. Commercially available tetravinylsilane (97 %, Sigma Aldrich), monoborane-dimethylsulfide (2 M solution in toluene, Sigma Aldrich), mono borane-THF (1 M, Aldrich), phenyllithium (1.9 M solution in dibutylether, Fluka), n-butyllithium (1.6 M solution in hexane, Alfa Aesar), t-butyllithium (1.7 M solution in pentane, Sigma Aldrich) were used without purification.

4.6.2   Synthesis of PESB

The PESB polymer was synthesized by hydroboration polymerization at $25\,°C$, which was conducted by dropwise addition of $BH_3 \cdot S(CH_3)_2$ into tetravinylsilane in diethyl ether. The PESB polymer was obtained according to the following reaction:

$$3n\ Si(CH{=}CH_2)_4 + 4n\ BH_3 \cdot S(CH_3)_2 \longrightarrow PESB + 4n\ S(CH_3)_2$$
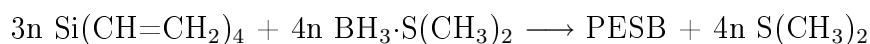
In further reactions, the PESB polymer was allowed to add phenyl lithium, n-butyl lithium or t-butyl lithium, respectively, in order to obtain the PLESPB, PLESnBB or PLEStBB polymers, which will be discussed in the following chapters. Figure 62 depicts the schematical representation of the main building blocks of the idealized structure of the PESB polymer, and its further reaction with organyl lithium compounds. Remarkably, in the Figure 62, alpha addition of borane to the vinylic units during the formation of the PESB polymer is not included, but this possibility should be noted as stated in the literature [203].

Preparation of PESB

0.02 mol $BH_3 \cdot S(CH_3)_2$ was added dropwise into a solution of 0.015 mol tetravinylsilane in 100 ml diethyl ether at room temperature under vigorous stirring. The polymerization reaction was allowed to proceed at this temperature for 23 hours. Then,

the temperature was increased slowly until 110 °C. Afterwards, the reaction flask was connected to a cooling trap in order to strip the solvent off. After the solvent was removed, the PESB polymer was dried for 23 hours at 110 °C under vacuum.
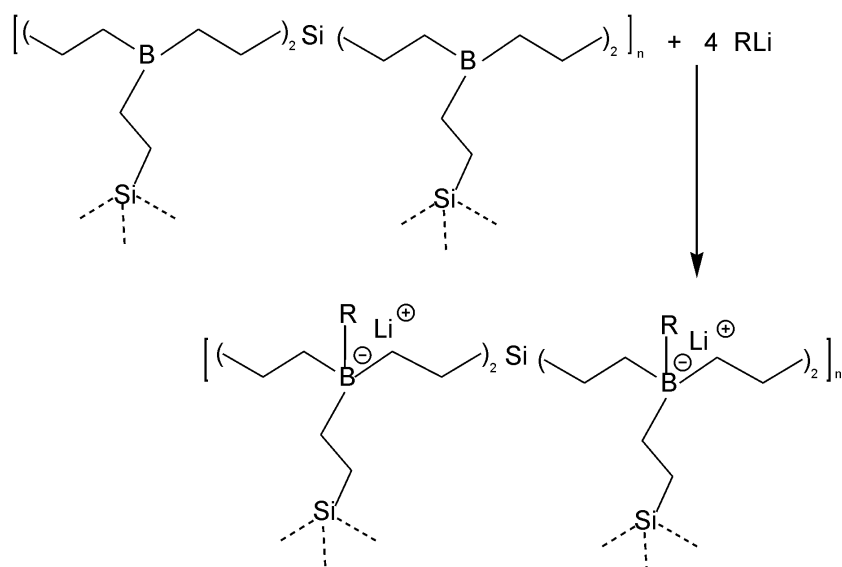
Figure 62:   Schematic drawing of the idealized reaction of the PESB polymer with RLi; where R is equal to phenyl, n-butyl or t-butyl groups.

4.6.3   X-ray Powder Diffraction

The X-ray powder diffraction pattern of the PESB polymer, which is given in the Figure 63, indicates the amorphous character of the polymer.

4.6.4   Elemental Analysis

According to the elemental analysis of the PESB samples as obtained, the approximate empirical formula of the PESB polymer was determined as $Si_1B_{1.8}C_8$ (without hydrogen). The chemical composition is given in the Table 19 and protons account for the rest of the mass. The calculated formula in accordance with the reactants for the PESB polymer is $Si_1B_{1.33}C_8$, which is in good agreement with the experimental formula acquired as $Si_1B_{1.8}C_8$.
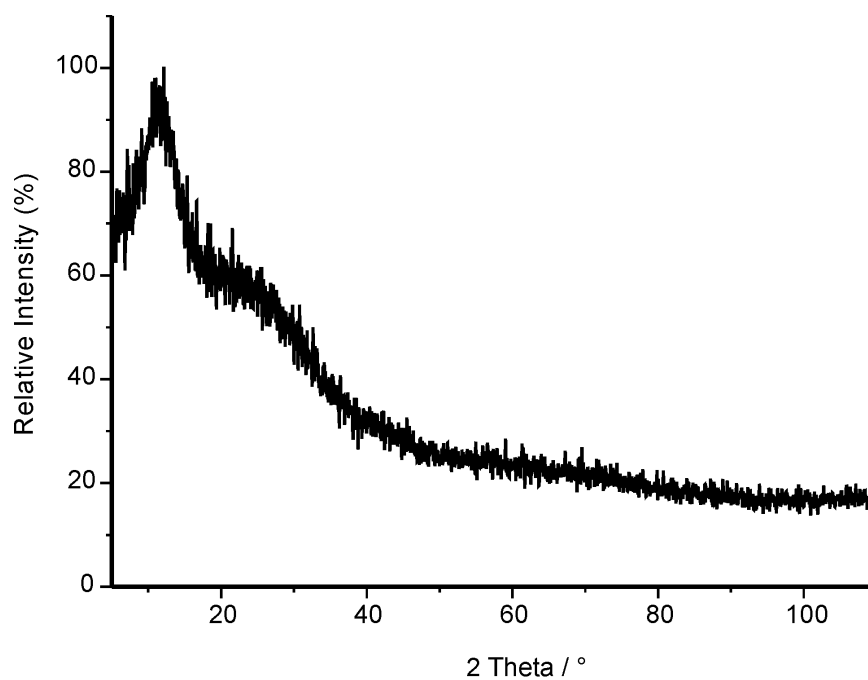
Figure 63: XRD pattern of the PESB polymer.

Table 19: Chemical composition of the PESB polymer.

Element	Mass (%)	Empirical Formulae
Si	18.25	$Si_1B_{1.82}C_{7.64}$
B	12.76	$(\approx Si_1B_{1.8}C_8)$
C	59.58	

4.6.5   FT-IR Spectroscopy

In the FT-IR spectrum of the PESB polymer, which is presented in the Figure 64, B—C asymmetric stretching vibrations are observed between $1155\,\mathrm{cm^{-1}}$ and $1013\,\mathrm{cm^{-1}}$. The band at $1262\,\mathrm{cm^{-1}}$ represents Si—C symmetric bending vibrations. Si—C rocking and B—C stretching vibrations appear at $799\,\mathrm{cm^{-1}}$ and $726\,\mathrm{cm^{-1}}$, respectively. The bands at $1720\,\mathrm{cm^{-1}}$ and $1631\,\mathrm{cm^{-1}}$ are attributed to the vinylic terminal groups connected to the polymer chain. This is supported by the chemical shifts acquired between $125\,\mathrm{ppm}$ and $138\,\mathrm{ppm}$ in the ^{13}C NMR liquid NMR spectrum of the PESB polymer. (As a footnote, the chemical shifts of vinylic carbon atoms connected to silicon atom are in accordance with the available literature data; i.e., Delmulle et al. reported the assignments for $(CH_3)_3$—Si—$(C^aH=C^bH_2)$ as C^a at $138.7\,\mathrm{ppm}$ and C^b at $129.6\,\mathrm{ppm}$ [204].) The possible presence of hydrogen bridged boron species is not clearly distinguishable from the FT-IR spectrum, since they appear in the same range as vinylic groups. However, in contrast to the PLEB polymer, no terminal B—H bonds, which exhibit the stretching vibrations around $2300\,\mathrm{cm^{-1}}$, seem to be present in the PESB polymer. The assignments together with intensities of the IR bands are given in the Table 20.

4.6.6   Thermal Analysis

The pyrolytic conversion of the PESB polymer to the ceramic was monitored by simultaneous thermal gravimetric analysis, differential thermal analysis and mass spectrometry (DTA/TG/MS) upon heating up to 1000 °C under argon atmosphere via a heating rate of 10 °C min^{-1}. The PESB polymer exhibits almost no weight loss up to 300 °C, and it loses % 39 of its initial mass up to 1000 °C as presented in the Figure 65. H_2 (m/z = 2) and CH_3 (m/z = 15) species were mainly detected during the decompositon, evolving between 300 °C and 710 °C. The observed mass change between 300 °C and 640 °C is attributed to the main thermal degradation of the PESB polymer. In this temperature range, the main volatile thermolysis products detected by mass-spectrometric investigations include H_2 (m/z = 2), CH_3 (m/z = 15), C_2H_3 and BCH_4 (m/z = 27), C_2H_5 (m/z = 29) and BCH_3 (m/z = 26) species.
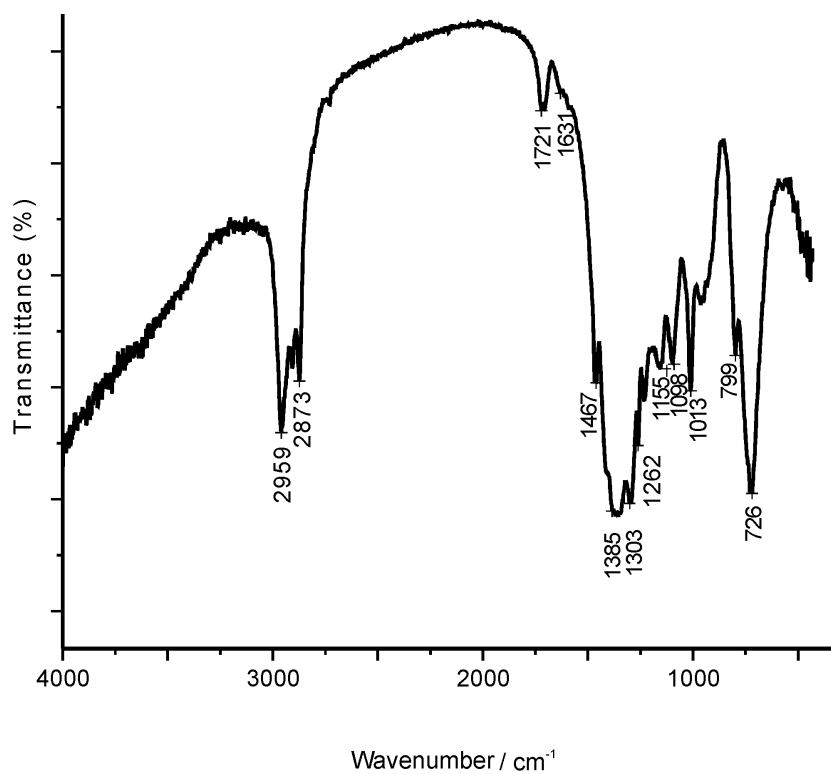
Figure 64: FT-IR spectrum of the PESB polymer.

Table 20: FT-IR band positions and assignments for the PESB polymer.

Wavenumber /cm^{-1}	Intensity	Assignment
2959	s	ν (C—H)
2873	s	ν (C—H)
1721−1631	w	ν (C=C)
1467	m	δ (C—H)
1385	s	δ (C—H)
1303	s	γ (C—H)
1262	m	δ (Si—C)
1155−1013	m	ν (B—C)
799	m	ρ (Si—C) and ρ (C—H)
726	m	ν (B—C)

Figure 65: DTA/TG/MS thermograms for the PESB polymer in argon flow with a $10\,°C\,min^{-1}$ heating rate.

4.7   Poly[lithium tris(tetraethylenesilyl)phenylborate] (PLESPB)

4.7.1   Synthesis

The synthesis of the PLESPB polymer was carried out by dropwise addition of 0.02 mol phenyl lithium into a solution of PESB polymer (0.02 mol borane unit) in 100 ml diethyl ether under vigorous mixing at room temperature. The polymerization reaction was allowed to proceed 24 hours at room temperature. Afterwards, the PLESPB polymer was dried for 24 hours at 110 °C under vacuum.

4.7.2   X-ray Powder Diffraction

The amorphous character of the PESB polymer was preserved after the incorporation of phenyl lithium, that can be seen in the powder X-ray diffractogram of the PLESPB polymer in the Figure 66.

4.7.3   Elemental Analysis

The results of the elemental analysis for the PLESPB polymer pointed out an approximate ratio for Si:B:C:Li as 1:1.8:12:1, which is tabulated in the Table 21. The chemical composition of the PLESPB polymer represents a uniform Si:B ratio likewise the PESB polymer possesses. Furthermore, incorporation of the phenyl lithium into the PESB polymer increased the carbon ratio in the resulting polymer, as expected.

Figure 66: XRD pattern of the PLESPB polymer.

Table 21: Chemical composition of the PLESPB polymer.

Element	Mass (%)	Empirical Formulae
Si	13.17	$Si_1B_{1.84}C_{12.06}Li_{1.03}$
B	9.37	$(\approx Si_1B_{1.8}C_{12}Li_1)$
C	68.04	
Li	3.40	

4.7.4   FT-IR Spectroscopy

In the Figure 67, FT-IR spectrum of the PLESPB polymer is shown. The specterum presents the C—H aromatic stretching vibrations of the phenyl groups at 3054 cm^{-1} along with the aromatic C=C stretching vibrations of phenyl ring between 1594 cm^{-1} and 1379 cm^{-1}. The other observable characteristic aromatic vibrations include the ring deformation at 950 cm^{-1}, and the aromatic C—H out of plane deformations at 703 cm^{-1} and 626 cm^{-1}. The vibrations at 1687 cm^{-1} and 1594 cm^{-1} are attributed to the C=C stretching vibrations of terminal vinyl groups in the PLESPB polymer, which are overlapped with the aromatic C=C stretching vibrations. The observed vibrations of the PLESPB polymer and assignments, together with intensities are given in the Table 20.
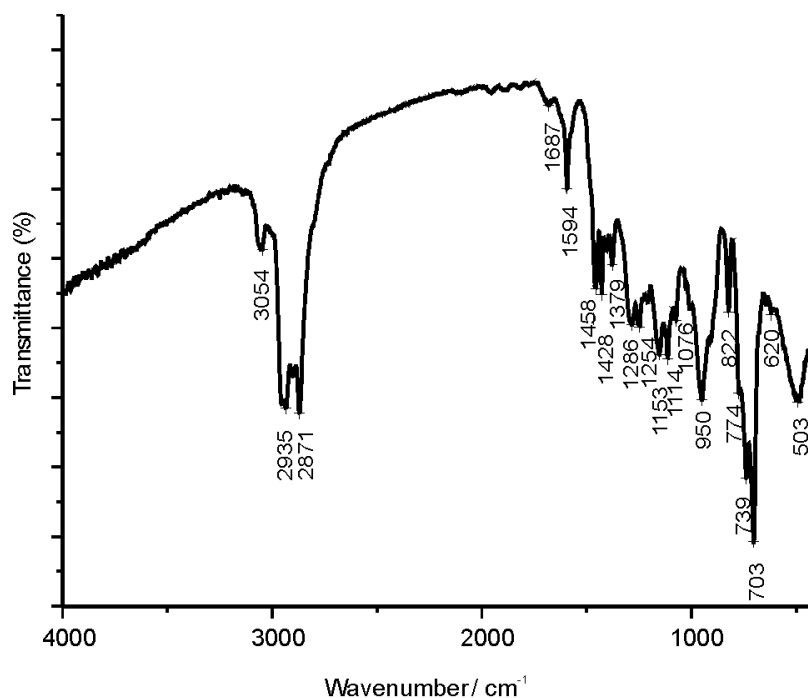
Figure 67:   FT-IR spectrum of the PLESPB polymer.

Table 22: FT-IR band positions and assignments for the PLESPB polymer.

Wavenumber $/\text{cm}^{-1}$	Intensity	Assignment
3054	m	ν (C—H) aromatic
2935	s	ν (C—H)
2871	s	ν (C—H)
1687	w	ν (C=C)
1594	m	ν (C=C) aromatic
1458	s	ν (C=C) aromatic and δ (C—H)
1428	s	ν (C=C) aromatic
1379	m	ν (C=C) aromatic and δ (C—H)
1286	s	γ (C—H)
1254	s	δ (Si—C)
1153−1076	s	ν (B—C)
950	s	δ (ring)
822	m	ρ (C—H)
774	s	ρ (Si—C) and δ (C—H) aromatic
739	s	ν (B—C)
703	s	δ (C—H) aromatic
620	w	δ (C—H) aromatic
503	w	ρ (C—H) and δ (ring)

4.7.5   Thermal Analysis

In order to monitor the thermal stability of the PLESPB polymer, simultaneous DTA /TG/MS analysis was carried out. During the measurement, the sample was heated with a rate of 10 °C min^{-1} in the range between room temperature and 1000 °C under argon flow. Incorporation of the phenyl lithium into the PESB polymer has reduced the onset temperature of the mass loss from 300 °C to 150 °C, as seen in the Figure 68. In parallel, the ceramic yield of PESB polymer at 1000 °C (which was equal to 60 %) is decreased due to incorporating the phenyl groups, and consequently a ceramic yield of only 44 % at 1000 °C is attained for the PLESPB polymer. A two step pyrolytic conversion is observed in the PLESPB polymer. The observed mass change in the first step up to 260 °C is 13 % and is attributed to the evaporation of unconnected oligomers or the reorganization of end groups. The significant mass loss of the polymeric product is observed between 260 °C and 550 °C suggesting the decomposition of the polymer network. In this temperature range, % 43 of the initial mass is evolved and the main volatile thermolysis products detected by mass-spectrometric investigations include
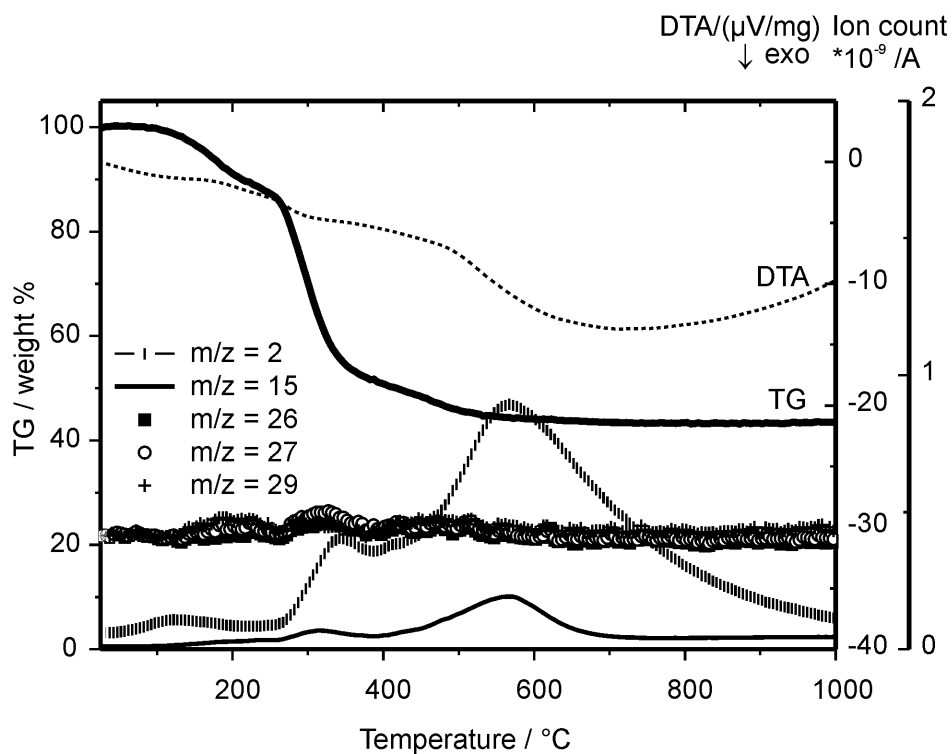
Figure 68: DTA/TG/MS thermograms for the PLESPB polymer in argon flow with a 10 °C min^{-1} heating rate.

H_2 (m/z = 2), CH_3 (m/z = 15), C_2H_3 or BCH_4 (m/z = 27), BCH_3 (m/z = 26) and C_2H_5 (m/z = 29) species. Then, simultaneous ceramization and depolymerization processes are continued by the evolution of fragments of CH_3 (m/z = 15) up to 700 °C and H_2 (m/z = 2) up to 1000 °C.

4.7.6   Impedance Spectroscopy

The ionic conductivity measurements for PLESPB polymer were carried out via impedance spectroscopy by using gold electrodes. The measurements were performed up to 115 °C by applying heating and cooling rates as $1\,°C\,min^{-1}$ under argon flow. The temperature dependence of bulk ionic conductivities are figured out in Arrhenius type diagrams, which is shown in the Figure 69. The PLESPB polymer exhibits an activation energy of 69 $kJ\,mol^{-1}$, determined from the slope of the conductivity curve, and a bulk ionic conductivity of 2.8×10^{-11} S cm^{-1} at 140 °C. The activation energy and ionic conductivities of the PLESPB polymer at different temperatures are represented in the Table 27.

Figure 69: Temperature dependence of the ionic conductivities of the PLESPB polymer. Heating and cooling cycles are represented by filled and open symbols, respectively.

The interpretation of the impedance data was performed by a parallel RQ element in the equivalent circuit, since the impedance data presented in the complex plane format exhibits one semicircle. The capacitance values of the semicircles are calculated at different temperatures, and which possess values of approximately 5×10^{-12} F . These values correspond to the typical bulk capacitance values of a sample, thus representing that lithium ion conductivity in the bulk is associated with the semicircle.

4.8   Poly[lithium tris(tetraethylenesilyl)t-butylborate] (PLEStBB)

4.8.1   Synthesis

The PLEStBB polymer was synthesized by dropwise addition of 0.02 mol t-butyl lithium into the solution of PESB polymer (0.02 mol borane unit) in 100 ml diethyl ether at room temperature under continuous mixing. The reaction was allowed to proceed for 25 hours at room temperature. After removal of the solvent, the PLEStBB polymer was allowed to dry for 25 hours at 110 °C under vacuum. In order to comprehend the coordination of the boron as a consequence of the alkyl lithium addition to the PESB polymer, an ether solution of the PLEStBB polymer in $CDCl_3$ was analyzed as an example within the series by employing ^{11}B NMR analysis at room temperature. In the light of this preliminary acquisition, two chemical shifts are discerned at 82.3 ppm and −19.6 ppm. The chemical shift at 82.3 ppm is interpreted as the tri-coordinated boron species and the chemical shift at −19.6 ppm is assigned to the four-coordinated boron species [205, 206]. Accordingly the latter chemical shift implies that t-butyl groups are incorporated into the polymer, leading to the formation of four-coordinated boron species.

4.8.2   X-ray Powder Diffraction

Powder X-ray diffractogram of the PLEStBB polymer, which is given in the Figure 70, indicates the amorphous structure similar to the PESB and PLESPB polymers.

4.8.3   Elemental Analysis

An ratio of 1:1.8:11.4:0.9 was attained for the PLEStBB polymer, accounting for the corresponding ratio of Si:B:C:Li, as provided by the elemental analysis measurements. It is depicted in the Table 23 that the Si:B ratio matches well with that of the PESB

polymer. Additionally, an increase in the carbon ratio of the polymer has also been verified via incorporation of the t-butyl groups.
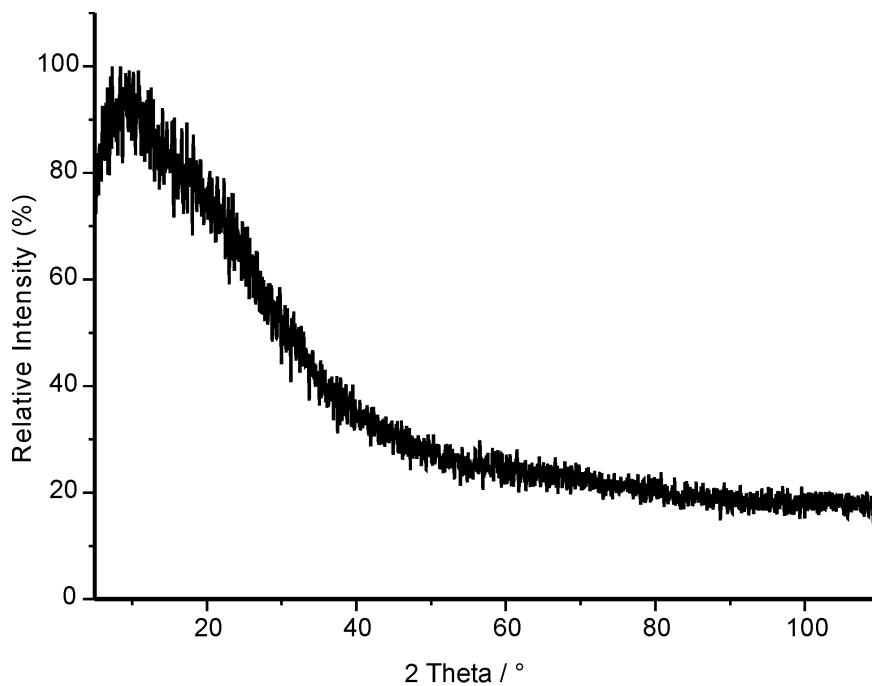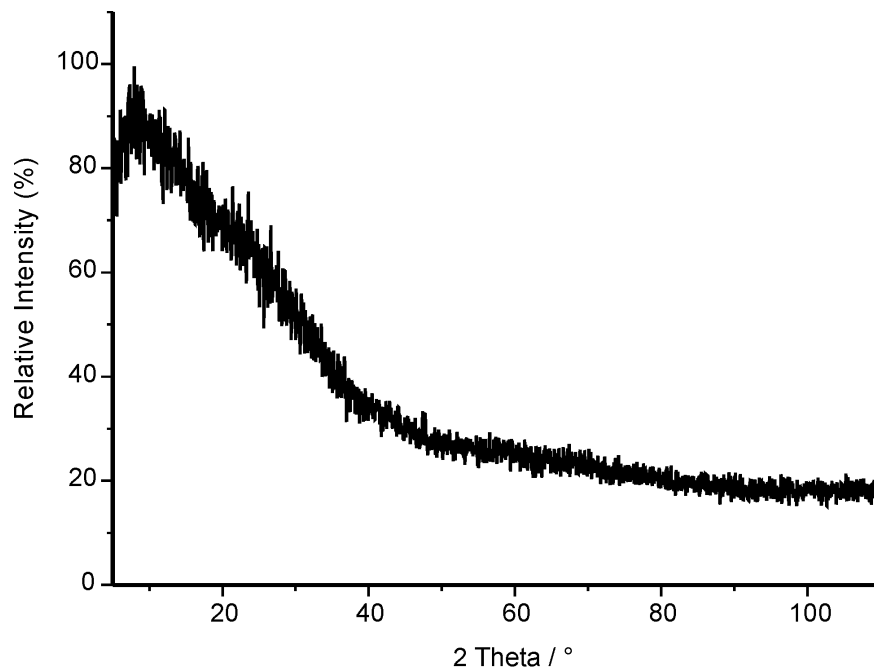

Figure 70: XRD pattern of the PLEStBB polymer.

Table 23: Chemical composition of the PLEStBB polymer.

Element	Mass (%)	Empirical Formulae
Si	12.22	$Si_1B_{1.81}C_{11.36}Li_{0.89}$
B	8.52	$(\approx Si_1B_{1.8}C_{11.4}Li_{0.9})$
C	59.38	
Li	2.74	

4.8.4 FT-IR Spectroscopy

The FT-IR spectrum of the PLEStBB polymer is presented in the Figure 71. The similar peaks as for the aforementioned PESB polymer are discerned in the PLEStBB polymer including Si—C and B—C vibrations of the main polymer backbone. The bands appeared at 1409 cm^{-1} and 971 cm^{-1} are assigned for the respective CH$_3$ deformation and CH$_3$ rocking vibrations along with the CH$_3$ deformation vibration at 1377 cm^{-1}, wherefore pointing out the presence of the t-butyl groups in the polymer. The bands at 1693 cm^{-1} and 1597 cm^{-1} are assigned for C=C terminal groups. Table 24 illustrates the assignments and intensities of all the corresponding vibrations observed in the PLEStBB polymer.
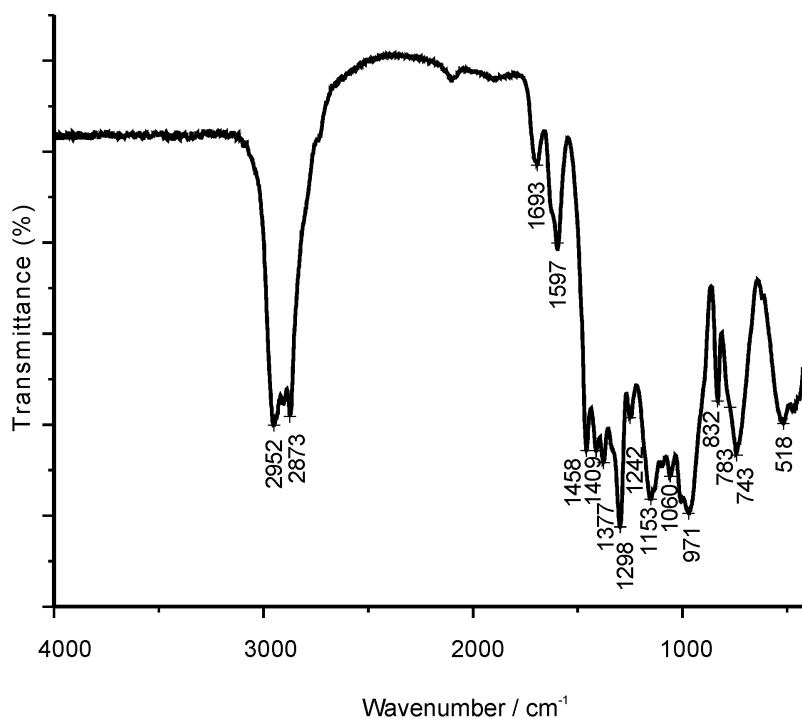
Figure 71: FT-IR spectrum of the PLEStBB polymer.

4.8.5 Thermal Analysis

As plotted in the Figure 72, thermal stability of the PLEStBB polymer was investigated by simultaneous DTA/TG/MS analysis. Therefore, a 10 °C min^{-1} heating rate was utilized up to 1000 °C under argon flow. The PLEStBB polymer is thermally stable

up to 210 °C and 51 % ceramic yield is acquired at 1000 °C. Insertion of the t-butyl lithium into the PESB polymer lowered the onset temperature for the mass loss from 300 °C to 210 °C, as well as decreased the ceramic yield at 1000 °C by 10 %. On the other hand, within the series of alkyl lithium incorporated PESB polymers, the PLEStBB polymer has the highest thermal stability and the ceramic yield at 1000 °C. The species detected by MS during decomposition of the network up to 540 °C are H_2 (m/z = 2), CH_3 (m/z = 15), C_2H_3 or BCH_4 (m/z = 27), BCH_3 (m/z = 26) and C_2H_5 (m/z = 29). Depolymerization and simultaneous ceramization processes are attributed to be proceeded by the evolution of H_2 (m/z = 2) and CH_3 (m/z = 15) fragments up to 780 °C as designated via the mass spectroscopy.

Table 24: FT-IR band positions and assignments for the PLEStBB polymer.

Wavenumber /cm^{-1}	Intensity	Assignment
2952	s	ν (C—H)
2873	s	ν (C—H)
1693—1597	w	ν (C=C)
1409	s	δ (C—H)
1458	s	δ (C—H)
1377	s	δ (C—H)
1298	s	γ (C—H)
1242	m	δ (Si—C)
1153—1060	s	ν (B—C)
971	s	ρ (C—H)
832	m	ρ (C—H)
783	m	ρ (Si—C)
743	s	ν (B—C)
518	m	ρ (C—H)

Figure 72: DTA/TG/MS thermograms for the PLEStBB polymer in argon flow with a 10 °C min^{-1} heating rate.

4.8.6 Impedance Spectroscopy

Ionic conductivity measurements for the PLEStBB polymer were conducted via impedance spectroscopy up to 200 °C by using 1 °C min^{-1} heating and cooling rates under argon flow for the samples squeezed between gold electrodes. Figure 73 represents the temperature dependent bulk ionic conductivities of the PLEStBB polymer, that is plotted as an Arrhenius type diagram. The activation energy of the PLEStBB polymer was evaluated from the slope of Arrhenius plot, which is appraised to a value of $81\,\mathrm{kJ\,mol^{-1}}$. The bulk ionic conductivity of this polymer is assessed as $1.1 \times 10^{-9}\,\mathrm{S\,cm^{-1}}$ at 200 °C. The activation energy and conductivity values at different temperatures are charted in the Table 27.

The interpretation of the impedance data was performed by a parallel RQ element in the equivalent circuit, since a semicircle was discerned in the complex plane format. The capacitance values for the semicircles are calculated at different temperatures,

yielding an approximate value of $\approx 1.6 \times 10^{-12}$ F and, accordingly, typical for the bulk capacitance of a sample, prevailing upon that the semicircle ergo represents the lithium ion conductivity in the bulk.
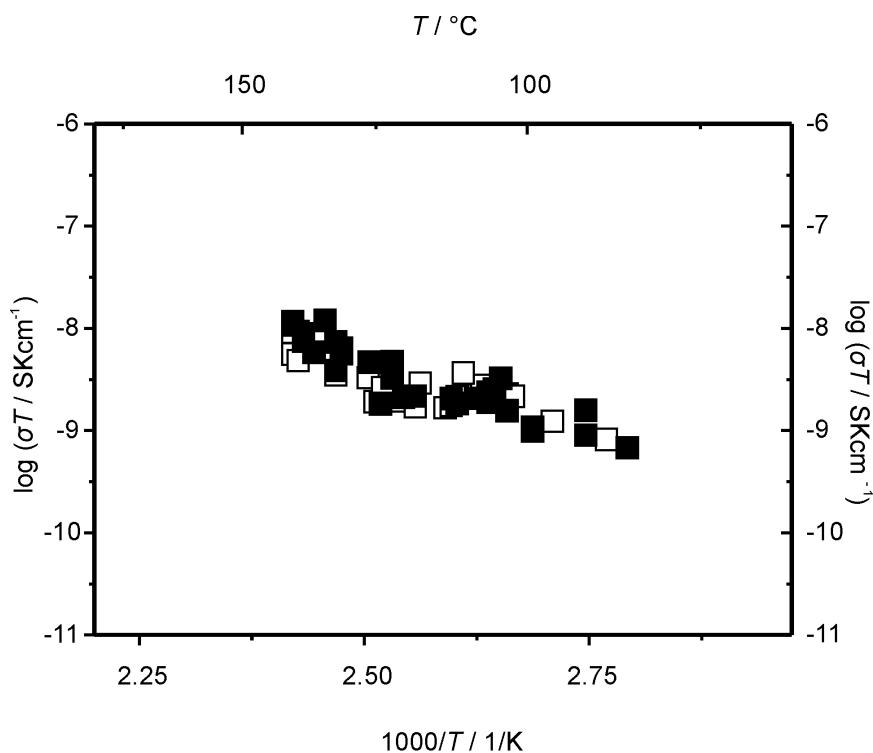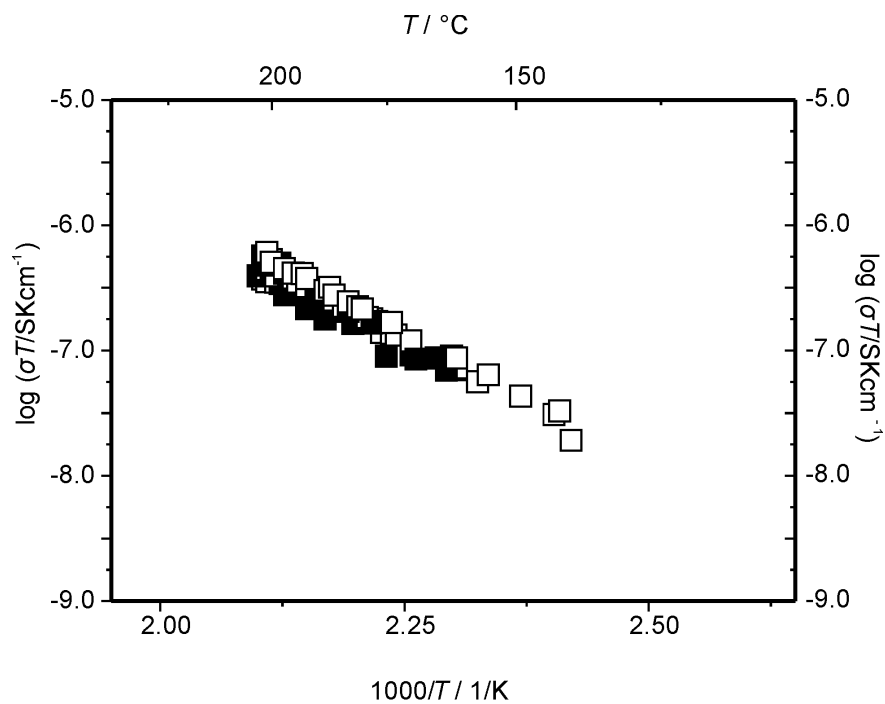

Figure 73: Temperature dependence of the ionic conductivities of the PLEStBB polymer. Heating and cooling cycles are represented by filled and open symbols, respectively.

4.9   Poly[lithium tris(tetraethylenesilyl)n-butylborate] (PLESnBB)

4.9.1   Synthesis

The synthesis of the PLESnBB polymer was accomplished by dropwise addition of 0.02 mol n-butyl lithium into a solution of PESB polymer (0.02 mol borane unit) in 100 ml diethyl ether at room temperature under continuous mixing. Then, the reaction was carried out for 20 hours at room temperature. In order to obtain the PLESnBB polymer, following on the solvents were stripped off from the polymer under vacuum for 24 hours at 110 °C.

4.9.2   X-ray Powder Diffraction

The powder X-ray diffractogram of the PLESnBB polymer is given in the Figure 74, which manifests the amorphous structure of the PLESnBB polymer similar to the PESB, PLEStBB and PLESPB polymers.
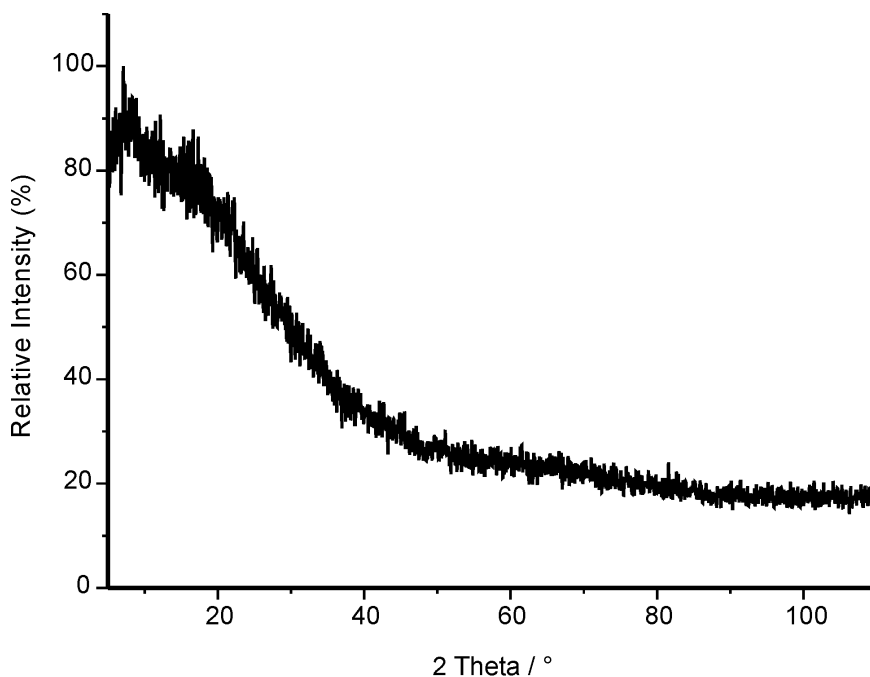
Figure 74: XRD pattern of the PLESnBB polymer.

4.9.3   Elemental Analysis

Incorporation of the n-butyl lithium groups into the PESB polymer demonstrates an increase in the carbon ratio, while at the same time providing no change in the Si:B ratio, as consequently figured out from the investigations on elemental analysis. The results reveal a composition for the ratio of 1:1.8:12.7:1.1 that accounts for the depicted sequence of the Si:B:C:Li as presented in Table 25.

Table 25: Chemical composition of the PLESnBB polymer.

Element	Mass (%)	Empirical Formulae
Si	11.59	$Si_1B_{1.80}C_{12.68}Li_{1.07}$
B	8.04	$(\approx Si_1B_{1.8}C_{12.7}Li_{1.1})$
C	63.00	
Li	3.11	

4.9.4   FT-IR Spectroscopy

In the FT-IR spectrum of the PLESnBB polymer, which is graphed in the Figure 75, similar characteristic vibrations of the PESB polymer are observed. Moreover, the PLESnBB polymer exhibits deformation vibrations of CH_3 at 1405 cm^{-1} and 1377 cm^{-1}. Also, the band at 966 cm^{-1} represents the rocking vibration of CH_3 groups. The detailed information about the vibrations and their corresponding assignments for the PLESnBB polymer are tabulated in Table 26.
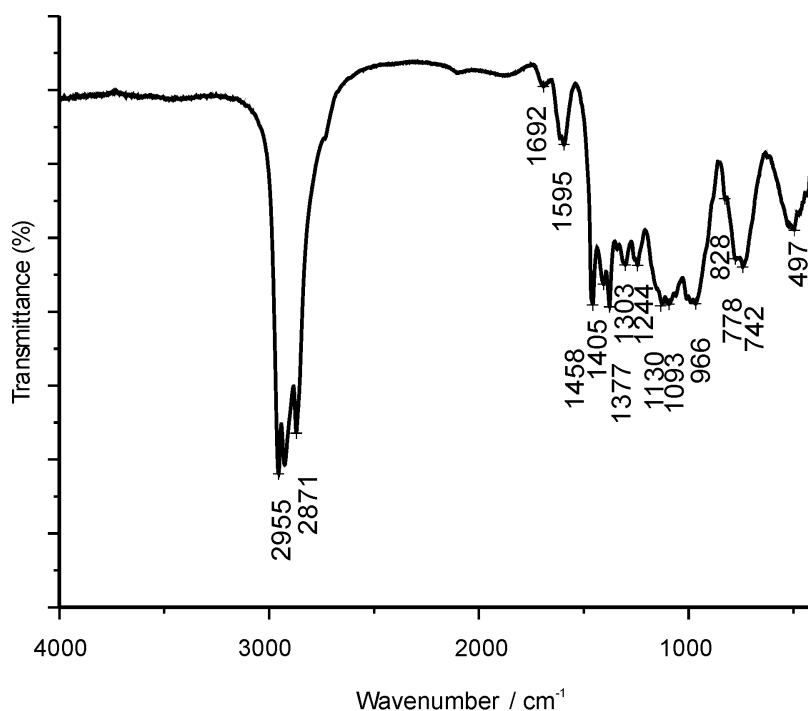
Figure 75: FT-IR spectrum of the PLESnBB polymer.

4.9.5   Thermal Analysis

The pyrolysis of the PLESnBB polymer was monitored by simultaneous DTA/TG/MS analysis. The measurement was proceeded with a 10 °C min^{-1} heating rate from room temperature up to 1000 °C under argon flow. As can be revealed from the Figure 76, the thermolytic behaviour of the n-butyl substituted polymer upon pyrolsis is in good agreement with the t-butyl substituted PESB polymer. In a similar manner to the other alkyl lithium incorporated PESB polymers, incorporation of n-butyl lithium decreased the decomposition temperature of the PESB polymer. However, onset temperature for the mass loss in the PLESnBB polymer is detected at a higher temperature than in the PLESPB polymer. The PLESnBB polymer has a ceramic yield of 50 % at 1000 °C, which is as similar to that monitored as for the PLEStBB polymer, and also is only 10 % less than the PESB polymer. The PLESnBB polymer demonstrates almost no weight loss upon 190 °C.

Following that in the subsequent temperatures, the decompositon of the PLESnBB polymer is realized and then proceeds up to 540 °C by volatilization of H_2 (m/z = 2), CH_3 (m/z = 15), C_2H_3 or BCH_4 (m/z = 27), BCH_3 (m/z = 26) and C_2H_5 (m/z = 29) species. This process is thereafter followed by the evolution of H_2 (m/z = 2) and CH_3 (m/z = 15) species up to 1000 °C and 840 °C, respectively, in a parallel manner to its other polymer counterparts.

Table 26: FT-IR band positions and assignments for the PLESnBB polymer.

Wavenumber $/cm^{-1}$	Intensity	Assignment
2955	s	ν (C—H)
2871	s	ν (C—H)
1692−1595	w	ν (C=C)
1458	s	δ (C—H)
1405	s	δ (C—H)
1377	s	δ (C—H)
1303	s	γ (C—H)
1244	m	δ (Si—C)
1130−1093	s	ν (B—C)
966	s	ρ (C—H)
828	m	ρ (C—H)
778	s	ρ (Si—C)
742	s	ν (B—C)
497	m	ρ (C—H)

DTA/(uV/mg)   Ion count
      ↓ exo   *10⁻⁹ /A

Figure 76: DTA/TG/MS thermograms for the PLESnBB polymer in argon flow with a 10 °C min⁻¹ heating rate.

4.9.6   Impedance Spectroscopy

Ionic conductivity measurements were performed up to 180 °C under argon flow for the PLESnBB polymer. The heating and cooling rates were $1\,°\mathrm{C\,min^{-1}}$, and gold electrodes were used. Arrhenius type diagrams are plotted to figure out the temperature dependent bulk ionic conductivities, as illustrated in Figure 77. The activation energy was derived from the slope of the conductivity curve, which exhibits a value of $183\,\mathrm{kJ\,mol^{-1}}$. Table 27 depicts the activation energy and conductivity values at different temperatures.

A parallel RQ element was used in the equivalent circuit to interpret the semicircle thus expressing the impedance data in the complex plane. The capacitance values are determined for the semicircles at different temperatures, which indicate an approximate value of $\approx 3 \times 10^{-12}$ F. Therefore, the semicircle can be associated with the lithium ion conductivity in the bulk, since the attained values are typical for the bulk capacitance of the sample.
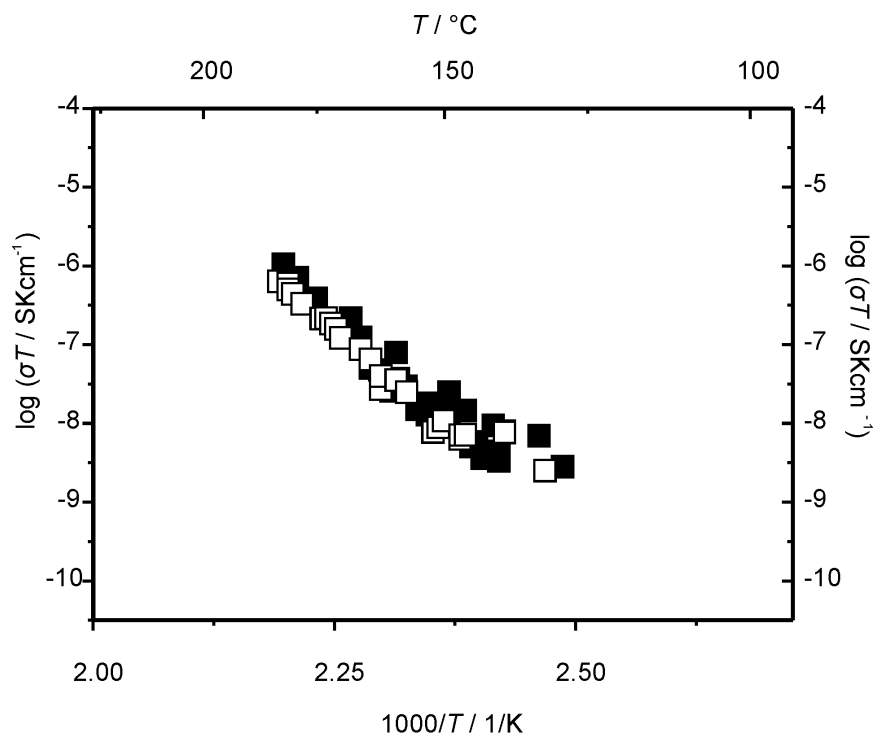
Figure 77: Temperature dependence of the ionic conductivities of the PLESnBB polymer. Heating and cooling cycles are represented by filled and open symbols, respectively.

4.10   Conclusions

In this chapter, a series of novel poly[lithium tris(tetraethylenesilyl)organylborate] polymers are presented. The synthesis of PESB polymer was accomplished by the initial hydroboration of tetravinylsilane by borane. The PESB polymer was modified in a second step by reacting it with a variety of organyl lithium compounds; i.e. RLi, where R denotes for phenyl, n-butyl or t-butyl. Investigations of the thermal stabilities of these polymers via DTA/TG/MS analysis have revealed that insertion of alkyl lithium groups decreases not only the decomposition temperature but also the ceramic yield of the original PESB polymer. Within the series, the thermal stability of the phenyl containing polymer is not as high as its counterpart polymers possessing t-butyl or n-butyl groups.

In addition, the ionic conductivities of the polymers obtained by incorporating various organyl substituent units into the PESB polymer have been analyzed. The tabulated data of activation energies and ionic conductivities at different temperatures for PESB polymers are compiled in the Table 27. Resultingly, the series of poly[lithium tris(tetraethylenesilyl)organylborate] polymers are recognized with their lower ionic conductivities as compared those values depicted within the poly[lithium tetrakis(triethylenealkylboryl)borate] polymer series (see Figure 61). Overall, to acco-

Table 27: Activation energies and ionic conductivities (at 140 °C, 180 °C and 200 °C) for the PLESPB, PLEStBB and PLESnBB polymers.

	E_a / kJ mol^{-1}	σ /S cm^{-1}		
		140 °C	180 °C	200 °C
PLESPB	69	2.8×10^{-11}	—	—
PLEStBB	81	4.6×10^{-11}	4.9×10^{-10}	1.1×10^{-9}
PLESnBB	183	1.9×10^{-11}	9.7×10^{-10}	—

unt for this difference, the most probable interpretation is that insertion of tetraalkylsilane groups between borate groups increases the hopping distance as well as decreases the charge carrier concentration of lithium ions; therefore, reduces the ionic conductivity in the resulting polymer.

5   Alkali fluorooxoborates

5.1   State of the Arts and Concepts

Solid alkali electrolytes, where only ionic species serve as an electric charge carrier in solids, are one of the key functional materials in solid state batteries. Therefore, particular attention has recently been given to discover new solid electrolytes possessing high ionic conductivity. One of the materials investigated in that respect is alkali borate systems. In the literature, alkali borate glasses have been reported to have certain ionic conductivity but those values appeared not to be sufficient to compete with the best ion conducting materials, i.e. Na-β-Alumina [12]. An alternative approach was considered to incorporate fluorine atoms into glass network in order to increase the ionic conductivity in alkaline borate glasses and a significant improvement in ionic conductivity was reported [207]. Although alkali borate materials have been extensively studied, there is very limited knowledge about fluorooxoborates. Moreover, no reports have become available before this work, concerning neither the ionic conductivity in crystalline alkali fluorooxoborates nor the crystal structures of these compounds. Potassium and sodium fluorooxoborates have been mentioned, however insufficiently studied and identified in the literature as far as our knowledge, while no identification of lithium fluorooxoborate has been traced.

The first alkali fluorooxoborate was reported on the example of the sodium compound by Ryss et al., which was obtained from aqueous solutions [208]. Maya et al. performed Raman spectroscopy analysis of this compound synthesized in aqueous solution and indicated the presence of boroxine ring by pointing out the similarities in frequencies of the Raman bands to those in metaboric acid [209]. Further, the same authors studied the phase diagram of the $NaF-NaBF_4-B_2O_3$ system and reported the formation of $Na_3B_3O_3F_6$, but accompanied with NaF and $NaBF_4$ by-products [210]. Solely an attempt to determine the lattice parameters of $Na_3B_3O_3F_6$ from the powder data was undertaken by Babich et al., and an orthorhombic unit cell with $a = 10.245\,\text{Å}$, $b = 14.462\,\text{Å}$, $c = 9.46\,\text{Å}$ and Z = 8 was contended, while no structure determination has been reported up to now [211].

On the other hand, Ryss et al. postulated potassium derivative of fluorooxoborate anion, and stated that it decomposed with water leading to replacement of some fluorines by hydroxyl groups [212]. Babich et al. reported the formation of potassium

fluorooxoborate in $K_2CO_3-KBF_4$ system [211]. Andriiko et al. communicated the formation of $K_3B_3O_3F_6$ from mixtures in $KF-KBF_4-B_2O_3$ system and further indexing of the powder X-ray diffraction data depicted an orthorhombic crystal system with the lattice parameters $a = 10.126(4)$ Å, $b = 14.88(2)$ Å and $c = 9.662(3)$ Å [213].

Overall, the given literature data on sodium and potassim fluorooxoborates show that a hexafluorotriborate ring was postulated only on the basis of IR [214] and Raman [209] spectra as a derivative of the boroxine ring, but no structural investigations of the $B_3O_3F_6{}^{3-}$ anion were reported before the present work. Concerning the lithium fluorooxoborates, no report was communicated.

Altogether, fluorooxoborate anions are unknown, or not conclusively confirmed, in inorganic solid state compounds. More common are fluoride oxoborates like jeremejevite ($Al_6[BO_3]_5F_3$) [215], to examplify. A feature that received attention is that isolated F^- anions are included in all those compounds, which interact with cations without forming any B—F bonds.

One of the basic requirements for high conductivity is high long range mobility of charge carriers. On the other hand, the mobile cations can be trapped easily if oxygen atom is in terminal positions (bearing a charge of -1) like in oxoanionic matrices. These traps for the mobile cations alleviate the mobility of the charge carriers, and thus the conductivity. Consequently, in order to improve conductivity of the cation, the aim is to avoid these terminal oxygen atoms, which are possible traps comprised of negative charges accumulated on the pathways of the mobile cations. A promising candidate to achieve this goal is thought to be alkali fluorooxoborates. In these compounds, the addition of fluorine atom to a boron atom coordinated with oxygen atoms reduces the effective negative charge of fluorine by adopting the respective adjacent four-coordinated boron atom with a formal charge of -1. Moreover, borate based anionic matrices are promising to achieve good weight capacities.

With these aims, the present thesis reports for the first structural characterization of alkali fluorooxoborates via the single crystal X-ray analysis, namely, lithium fluorooxoborate (LiB_6O_9F) and sodium fluorooxoborate ($Na_3B_3O_3F_6$). These two compounds have further been characterized by FT-IR, Raman, DTA/TG/MS, impedance spectroscopy and direct current measurement techniques. Furthermore, the structure of $K_3B_3O_3F_6$ has been manifested by comparing its vibrational spectrum with that of its sodium analogue. Finally, the ionic conductivities of crystalline alkali fluorooxoborate compounds as a foremost are evaluated and reported.

5.2   Lithium Fluorooxoborate, LiB_6O_9F

LiB_6O_9F was synthesized from LiF and B_2O_3 in all-solid state reaction. However, this synthetic approach implies a number of pitfalls: (1) the driving force for the reaction between LiF and B_2O_3 is rather low because lithium fluoride is a weak fluoride base only, (2) BF_3 may form and easily escape from the reaction mixture, (3) traces of water in the system might lead to hydrolysis, and evolution of HF, and (4) borate systems show a strong tendency to glass formation. In order to avoid such intricacies, or to at least minimize them, we have used thoroughly dried starting materials, have intensively milled the starting mixtures, annealed them repeatedly, and have chosen the reaction temperature as low as possible, but as high as necessary.

Finally, fully crystalline, single phase powders of the new fluorooxoborate LiB_6O_9F have been obtained that contained single crystals of a size sufficient for a single crystal X-ray structure determination. The colourless compound is sensitive to humid air, and decomposes slowly at room temperature into an amorphous solid residue.

5.2.1   Synthesis of LiB_6O_9F

All reactions were carried out in a purified argon atmosphere using standard Schlenk techniques and glove boxes (M.Braun GmbH, Garching, Germany), and rigorously dried reaction apparatus. Stoichiometric amounts of anhydrous B_2O_3 (Puratronic anhydrous glass disc, 99.9995 %, Alfa Aesar, Karlsruhe, Germany) and anhydrous LiF (ultra dry, 99.99%, Alfa Aesar, Karlsruhe, Germany) were used to prepare appropriate starting mixtures, these were wet ball milled with distilled hexane (5 ml) for 1 hour. The mixtures were dried inside Teflon crucibles in a Schlenk system at 150 °C to remove hexane. 6 mm pellets of reactants were placed inside gold crucibles, which were sealed under argon atmosphere in glass ampoules. The reactions were carried out at 400 °C following a specific temperature schedule: 2 hours heated until 400 °C, held 552 hours at 400 °C, cooled 99 hours to 200 °C, held 9 hours at 200 °C and cooled 99 hours to room temperature. The reacted samples were ground, wet ball milled and the same process (except by holding 297 hours at 400 °C) repeated once more time in order to increase the crystallinity of the products.

5.2.2   Single Crystal Structure Analysis

A colourless single crystal was chosen from the product, which was suitable for single crystal X-ray diffraction and has allowed to solve the crystal structure. The single crystal was placed on top of a glass capillary and sealed within another glass capillary, in a glove box.

The experimental intensity data of the single crystal were collected with a dual wavelength diffractometer system: Smart APEX II three circle single crystal diffractometer (Bruker AXS, Karlsruhe, Germany) equipped with a CCD-detector, a Siemens X-ray sealed tube (MoK$_\alpha$ radiation, $\lambda = 0.71073$ Å), an Incoatec (Geesthacht, Germany) microfocus X-ray source IμS (CuK$_\alpha$ radiation, $\lambda = 1.54178$ Å). Because of the light elements contained in the title compound and the small crystal size (Table 28) the copper source was used. The collection, done at 23 (2) °C, and reduction of data were carried out with the Bruker Suite software package [216]. Intensities were corrected for absorption effects applying a semi-empirical method [217].

The structure was solved by direct methods and refined by full-matrix least-squares fitting with the SHELXTL software package [218]. Experimental details on crystallographic data and data collection are given in the Table 28. Table 29 shows the atomic parameters and equivalent isotropic displacement parameters, and Table 30 tabulates the anisotropic displacement parameters from the single crystal data. Further details may be obtained from Fachinformationszentrum Karlsruhe, 76344 Eggenstein-Leopoldshafen, Germany (fax: (+49)-7247-808-666; e-mail: crysdata(at)fiz-karlsruhe.de, http:// www.fiz-karlsruhe.de/request for deposited data.html) on quoting the CSD number: 420286.

5.2.3   X-ray Powder Analysis

Powder X-ray diffraction patterns were recorded at room temperature using a high resolution laboratory X-ray powder diffractometer (D8 ADVANCE with CuK$_{\alpha 1}$, Bruker AXS, Karlsruhe, Germany), which was operating in Debye-Scherrer geometry. The samples were sealed inside the glass capillary (Ø = 0.3 mm) under argon atmosphere, and diffraction patterns were collected between 5 and 95° in 2θ during 18h. The refinement of lattice constants was performed by using the program TOPAS (AXS, Bruker, Karlsruhe) [219]. Le-Bail fit [220] yielded the precise values as $a = 7.6555(1)$ Å, $b = 8.5318(1)$ Å and $c = 10.7894(2)$ Å, based on 349 reflections. The X-ray powder diffractogram of the LiB$_6$O$_9$F and fitted profile are presented in Figure 78.

Table 28: Crystallographic data for LiB_6O_9F.

Chemical formula	LiB_6O_9F
Formula weight	234.80
Crystal system	orthorhombic
Space group (no.), Z	$Pna2_1$ (33), 4
Lattice constants /Å	$a = 7.6555(1)$
	$b = 8.5318(1)$
	$c = 10.7894(2)$
Volume /Å^3	$V = 704.70(2)$
Density (calculated) /g cm^{-3}	$\rho = 2.213$
Crystal size /mm^3	$0.12 \times 0.09 \times 0.06$
Diffractometer	Smart APEX II, Bruker AXS
X-ray source	IμS microfocus, Incoatec
X-ray radiation, λ /Å	CuKα, 1.54178
Monochromator	Montel optic, Incoatec
Absorption coefficient μ /mm^{-1}	1.981
θ range /°	6.61 to 55.03
Index range	$-8 \leq h \leq 8, -9 \leq k \leq 8, -11 \leq l \leq 11$
Absorption correction	multi-scan, SADABS [217]
Reflections collected	2656
Independent reflections, R_{int}	853, 0.023
Transmission t_{min}, t_{max}	0.7970, 0.8904
No. of parameters	154
$R_1[F^2 > 2\sigma(F^2)]$, $wR(F^2)$	0.0184, 0.0481
Absolute structure parameter	0.20(16)
$\triangle\rho_{max}$, $\triangle\rho_{min}$ /e Å^{-3}	0.122, -0.105

Table 29: Atomic coordinates and equivalent isotropic displacement parameters U_{eq} /Å^2 for LiB$_6$O$_9$F. Estimated standard deviations are given in parentheses.

Atom	*Wyckoff* position	x	y	z	U_{eq}
F(1)	$4a$	$-0.2658(1)$	$0.9326(1)$	$0.6947(1)$	$0.0316(6)$
O(1)	$4a$	$0.4320(2)$	$0.9582(2)$	$0.6639(1)$	$0.0253(4)$
O(2)	$4a$	$0.0640(2)$	$0.7060(2)$	$0.0650(1)$	$0.0281(4)$
O(3)	$4a$	$0.3640(2)$	$0.9896(2)$	$0.9966(2)$	$0.0260(4)$
O(4)	$4a$	$0.2485(2)$	$0.1697(1)$	$0.7303(2)$	$0.0288(4)$
O(5)	$4a$	$0.0837(1)$	$0.9547(1)$	$0.8105(1)$	$0.0240(4)$
O(6)	$4a$	$-0.0999(2)$	$0.7519(2)$	$0.8869(1)$	$0.0242(4)$
O(7)	$4a$	$0.0660(2)$	$0.2114(2)$	$0.8985(1)$	$0.0274(4)$
O(8)	$4a$	$-0.1091(2)$	$0.0051(2)$	$0.9788(1)$	$0.0270(4)$
O(9)	$4a$	$0.1053(2)$	$0.7528(2)$	$0.5801(2)$	$0.0250(4)$
B(1)	$4a$	$0.5986(3)$	$0.9144(3)$	$0.6046(2)$	$0.0224(6)$
B(2)	$4a$	$-0.0614(3)$	$0.6510(3)$	$0.9844(2)$	$0.0223(6)$
B(3)	$4a$	$0.3715(3)$	$0.1068(3)$	$0.6534(2)$	$0.0246(6)$
B(4)	$4a$	$0.1353(3)$	$0.1113(3)$	$0.8138(2)$	$0.0243(6)$
B(5)	$4a$	$-0.0423(3)$	$0.9049(2)$	$0.8928(2)$	$0.0223(5)$
B(6)	$4a$	$0.0499(3)$	$0.8421(2)$	$0.4859(2)$	$0.0236(4)$
Li(1)	$4a$	$0.2647(4)$	$0.8023(3)$	$0.7265(4)$	$0.0309(8)$

Table 30: Anisotropic displacement parameters U_{ij} /$\mathring{\mathrm{A}}^2$ for LiB_6O_9F. Estimated standard deviations are given in parentheses.

Atom	U_{11}	U_{22}	U_{33}	U_{12}	U_{13}	U_{23}
F(1)	0.0331(6)	0.0269(5)	0.0347(7)	−0.0010(4)	−0.0117(6)	−0.0020(5)
O(1)	0.0279(7)	0.0230(8)	0.0249(9)	0.0023(6)	0.0031(6)	0.0031(6)
O(2)	0.0339(8)	0.0204(8)	0.0300(8)	−0.0029(7)	−0.0090(8)	0.0036(9)
O(3)	0.0309(7)	0.0206(7)	0.0264(7)	0.0037(5)	−0.0059(8)	−0.0030(6)
O(4)	0.0328(7)	0.0235(6)	0.0302(8)	0.0004(7)	0.0097(6)	0.0024(7)
O(5)	0.0283(8)	0.0201(8)	0.0236(8)	0.0000(5)	0.0018(6)	−0.0016(7)
O(6)	0.0327(8)	0.0198(9)	0.020(1)	−0.0014(5)	−0.0035(8)	0.0009(7)
O(7)	0.0325(8)	0.0204(7)	0.0291(9)	−0.0019(6)	0.0094(8)	−0.0014(8)
O(8)	0.0338(7)	0.0217(8)	0.0254(9)	−0.0031(5)	0.0078(7)	−0.0017(6)
O(9)	0.0331(8)	0.020(1)	0.022(1)	−0.0012(6)	−0.0031(7)	−0.0004(6)
B(1)	0.026(1)	0.016(1)	0.025(1)	−0.000(1)	−0.001(1)	−0.000(1)
B(2)	0.026(1)	0.022(1)	0.019(1)	0.003(1)	0.000(1)	−0.004(1)
B(3)	0.026(1)	0.025(1)	0.023(1)	−0.001(1)	0.001(1)	−0.000(1)
B(4)	0.028(1)	0.021(1)	0.024(1)	0.002(1)	−0.002(1)	0.001(1)
B(5)	0.026(1)	0.021(1)	0.019(1)	0.0012(9)	−0.002(1)	0.000(1)
B(6)	0.026(1)	0.020(1)	0.021(1)	0.001(1)	0.003(1)	0.001(1)
Li(1)	0.033(1)	0.028(1)	0.031(1)	−0.002(1)	−0.002(1)	0.000(1)
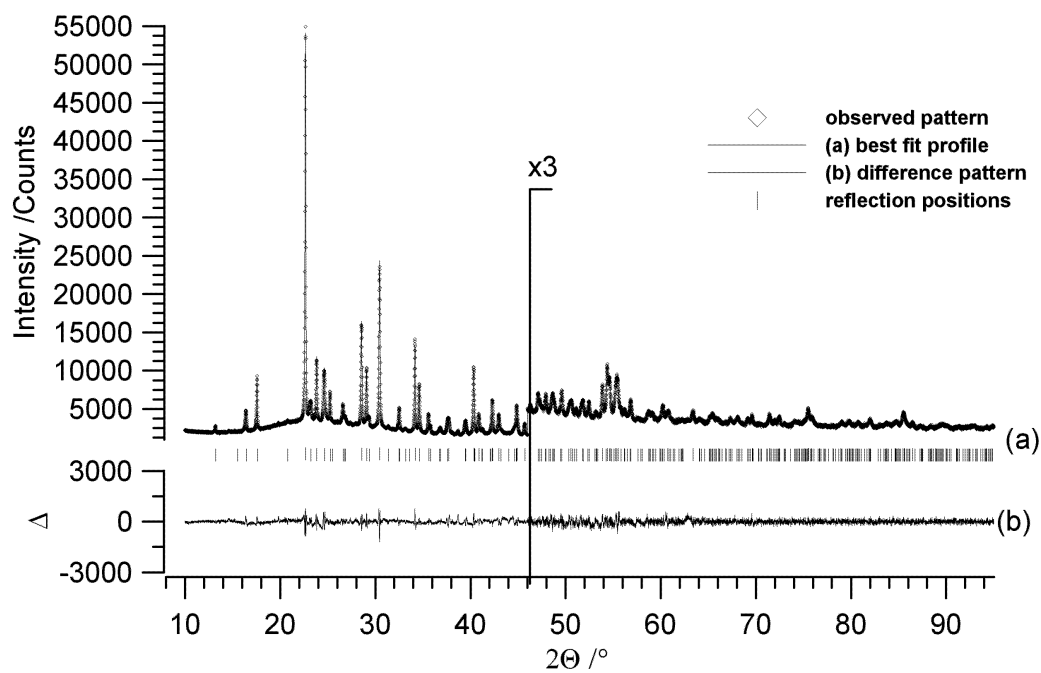
Figure 78: Plot for LeBail refinement of LiB_6O_9F at RT ($\lambda = 1.54015\text{Å}$). Observed pattern indicated by squares. (a) Best fit profile together with reflection positions is shown in upper part, and (b) difference curve between measured and calculated profiles is shown in lower part of the figure.

5.2.4   Structure Description

LiB_6O_9F crystallizes in a new type of structure with the orthorhombic space group $Pna2_1$ (no. 33, Pearson code $oP68$). The structure is composed of boroxine rings (B_3O_3) and fluorinated boroxine rings (B_3O_3F) in the ratio 1:1. A pair of boroxine rings, one of them bearing the fluoride ion, represents the repetition unit for the polymeric anion (Figure 79). These two rings are connected to each other, and to next neighbouring rings, by B—O—B linkages such that each boroxine ring connects to three others. Figure 80 displays a perspective view of the unit cell, emphasizing the principle of connectivity.
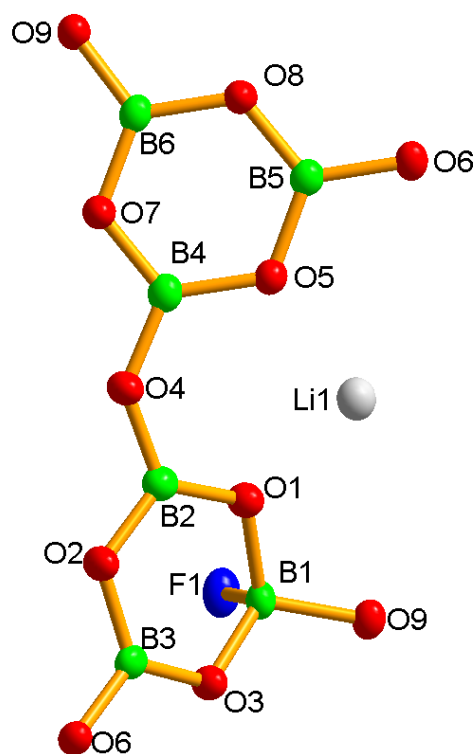
Figure 79: Repetition unit of the polymeric anion in LiB_6O_9F, showing the atom labelling scheme. Displacement ellipsoids are drawn at the 50% probability level.

The BO$_3$F geometry deserves particular attention. The boron atom B(1) is the only one in this structure, which is tetrahedrally coordinated by three oxygen and one fluorine atom. All other boron atoms B(2)−B(6) are trigonally surrounded by three O atoms (Table 31). The mean distances d(B—O) are 1.365 Å within the BO$_3$ units and 1.460 Å for the BO$_3$F unit, and are in good agreement with the respective sums of covalent radii (Table 31). They are also similar to the B—O distances in other borates [221]. The structure refinement, based on X-ray intensities, does not allow to discriminate between oxygen and fluorine. However, the F(1) atom is the only atom which is connected to one boron, exclusively. All other anions O(1)−O(9) are linking
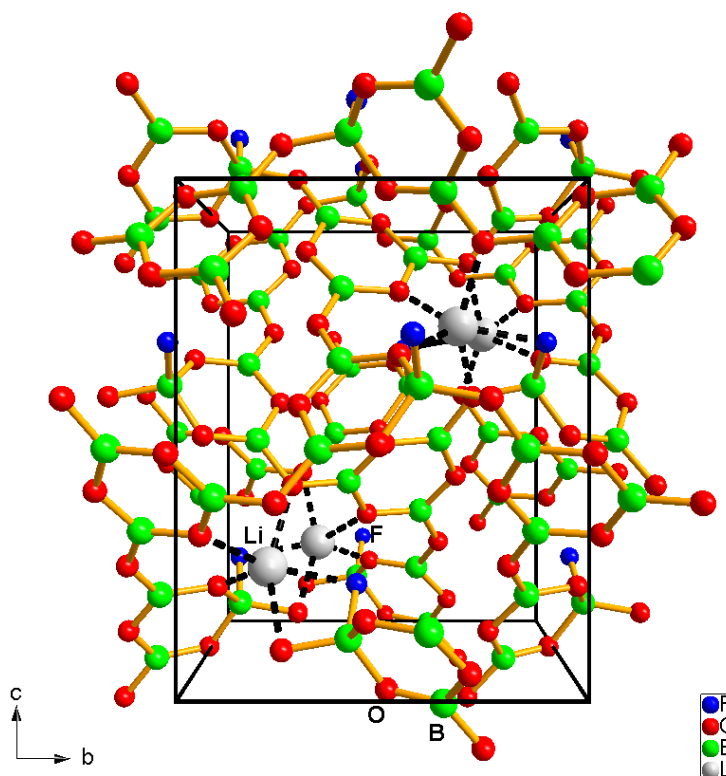
Figure 80: Perspective representation of the crystal structure of LiB$_6$O$_9$F, with the margins of the unit cell (black).

Table 31: Selected interatomic distances /Å and bond angles /° of the $B_6O_9F^-$ anion for LiB_6O_9F. Estimated standard deviations are given in parentheses.

Atom contact	Distance	Atom contact	Angle
BO_3F Tetrahedron			
$B(1)$—$F(1)^{vii}$	1.431(3)	$F(1)^{vii}$—$B(1)$—$O(1)$	107.8(2)
$B(1)$—$O(1)$	1.475(3)	$F(1)^{vii}$—$B(1)$—$O(3)^{viii}$	109.9(2)
$B(1)$—$O(3)^{viii}$	1.452(3)	$F(1)^{vii}$—$B(1)$—$O(9)^{iv}$	101.8(2)
$B(1)$—$O(9)^{iv}$	1.452(3)	$O(9)^{iv}$—$B(1)$—$O(3)^{viii}$	113.7(2)
mean	1.452(3)	$O(9)^{iv}$—$B(1)$—$O(1)$	111.0(2)
mean B—O	1.459(3)	$O(3)^{viii}$—$B(1)$—$O(1)$	112.1(2)
		mean	109.4(2)
BO_3 triangles			
$B(2)$—$O(2)$	1.377(3)	$O(3)^{ii}$—$B(2)$—$O(2)$	122.8(2)
$B(2)$—$O(3)^{ii}$	1.335(3)	$O(3)^{ii}$—$B(2)$—$O(6)$	122.7(2)
$B(2)$—$O(6)$	1.391(3)	$O(2)$—$B(2)$—$O(6)$	114.5(2)
mean	1.368(3)	mean	120.0(2)
$B(3)$—$O(1)$	1.355(3)	$O(1)$—$B(3)$—$O(4)$	123.6(2)
$B(3)$—$O(2)^{ix}$	1.367(3)	$O(1)$—$B(3)$—$O(2)^{ix}$	120.9(2)
$B(3)$—$O(4)$	1.365(3)	$O(4)$—$B(3)$—$O(2)^{ix}$	115.5(2)
mean	1.362(3)	mean	120.0(2)
$B(4)$—$O(4)$	1.346(3)	$O(4)$—$B(4)$—$O(5)$	121.4(2)
$B(4)$—$O(5)$	1.393(3)	$O(4)$—$B(4)$—$O(7)$	118.0(2)
$B(4)$—$O(7)$	1.359(3)	$O(7)$—$B(4)$—$O(5)$	120.6(2)
mean	1.366(3)	mean	120.0(2)
$B(5)$—$O(5)$	1.378(3)	$O(8)$—$B(5)$—$O(6)$	120.4(2)
$B(5)$—$O(6)$	1.379(3)	$O(8)$—$B(5)$—$O(5)$	120.5(2)
$B(5)$—$O(8)$	1.361(3)	$O(5)$—$B(5)$—$O(6)$	119.1(2)
mean	1.373(3)	mean	120.0(2)
$B(6)$—$O(7)^{x}$	1.372(3)	$O(9)$—$B(6)$—$O(7)^{x}$	122.45(2)

Table 31 continued

Atom contact	Angle	Atom contact	Angle
B(6)—O(8)^x	1.382(2)	O(9)—B(6)—O(8)^x	118.3(2)
B(6)—O(9)	1.340(3)	O(7)^x—B(6)—O(8)^x	119.2(2)
mean	1.365(3)	mean	120.0(2)

B—O—B angles			
Atom contact	Angle	Atom contact	Angle
B(1)^v—O(3)—B(2)^{iv}	120.1(2)	B(4)—O(4)—B(3)	134.85(1)
B(1)—O(1)—B(3)	119.8(2)	B(4)—O(5)—B(5)	118.5(2)
B(1)^{ii}—O(9)—B(6)	133.3(2)	B(4)—O(7)—B(6)^{vi}	120.3(2)
B(2)—O(2)—B(3)^{iii}	118.8(2)	B(5)—O(8)—B(6)^{vi}	120.5(2)
B(2)—O(6)—B(5)	118.9(2)		

Symmetry transformations used to generate equivalent atoms:
$^{[ii]}$ x−1/2, −y+3/2, z ; $^{[iii]}$ −x+1/2, y−1/2, z+1/2 ; $^{[iv]}$x+1/2, −y+3/2, z ;
$^{[v]}$ −x+1, −y+2, z+1/2 ; $^{[vi]}$ −x, −y+2, z+1/2 ; $^{[vii]}$ x+1, y, z ;
$^{[viii]}$ −x+1, −y+2, z−1/2 ; $^{[ix]}$ −x+1/2, y+1/2, z−1/2 ; $^{[x]}$ −x, −y+2, z−1/2

two boron atoms, forming the boroxine rings, and the bridges between them. This is suggesting that the F(1) position is the most likely position where the fluoride ions are placed. The distance d(B(1)—F) = 1.431 Å is slightly smaller than the remaining B(1)—O contacts. The BO$_3$F tetrahedra are oriented approximately along the c-direction, with a significant tilt of 47.07° (Figure 80). This results in a polar structure, in accordance with the acentric space group $Pna2_1$. The mean values of O—B—O angles for BO$_3$ triangles are in all cases 120°, within limits of the experimental errors. In the BO$_3$F tetrahedra, the mean O—B—O angle is 112.3° and the mean O—B—F angle is 106.5°. O—B—F angle is slightly decreased from the ideal tetrahedral angle in order to compensate the splitting of O—B—O angle due to the ring.

Interconnected boroxine rings were found previously in amorphous B$_2$O$_3$ [222] and in numerous oxoborates [223]. In the case discussed here, to one boron atom in every second ring a fluorine atom is added, thus generating the desired situation where (part of) the negative charge is shifted to the central boron atom, and thus will be experienced by lithium at a longer distance only.

The fluorooxoborate anion forms a two-dimensional infinite network represented as $^2_\infty$[B$_6$O$_9$F]$^-$. These strongly corrugated layers, oriented in the b-c-plane (Figure 81), reveal huge meshes ($\sim$7 Å) build from six boroxine rings. The meshes are filled by Li$^+$

ions on the one hand and closed by the bumps of neighbouring layers on the other hand. The layers are packed along the a-direction and interconnected by Li$^+$ ions (Figure 82). The distance between two sheets is given as $a/2 = 3.8277$ Å. The connectivity of the boroxine rings inside the layers, as well as the arrangement of the layers, is directly related to the structure of black phosphorous. This topological relationship is becoming obvious when comparing the barycenters of the boroxine rings in LiB$_6$O$_9$F and atom positions in black phosphorous (Figure 83).

The lithium atoms are located inside the cavities formed by the fluorooxoborate anion. The coordination sphere contains both fluorine and oxygen atoms. Lithium atom is coordinated by four oxygen atoms, mean d(Li—O) $= 2.046$ Å, and by one fluorine atom, d(Li—F) $= 2.047$ Å, forming a slightly distorted trigonal bipyramid, with F$^-$ located in the basal plane (Figure 84). Although five-fold coordination for lithium atom is not very common, it was suggested that the mean Li—O distances for five-coordinate lithium atom should be $2.10(6)$ Å [224], which is in fair agreement with the distances observed in LiB$_6$O$_9$F, as listed in Table 32.
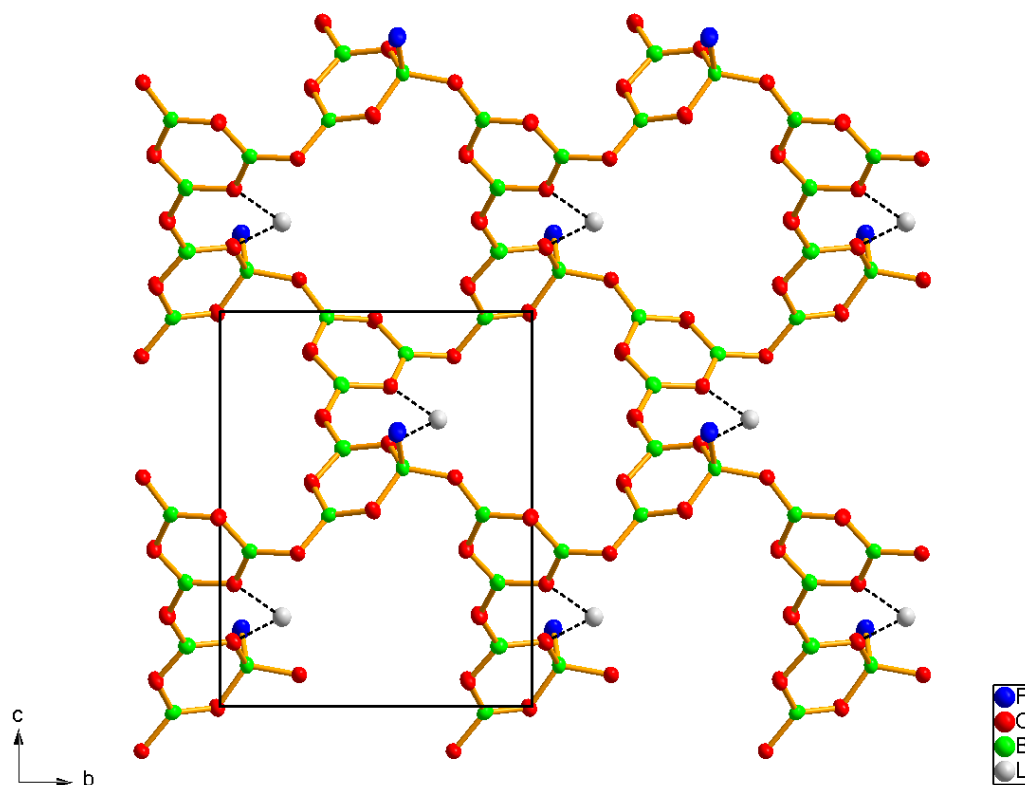
Figure 81: View of a corrugated mono layer along the [100] direction.
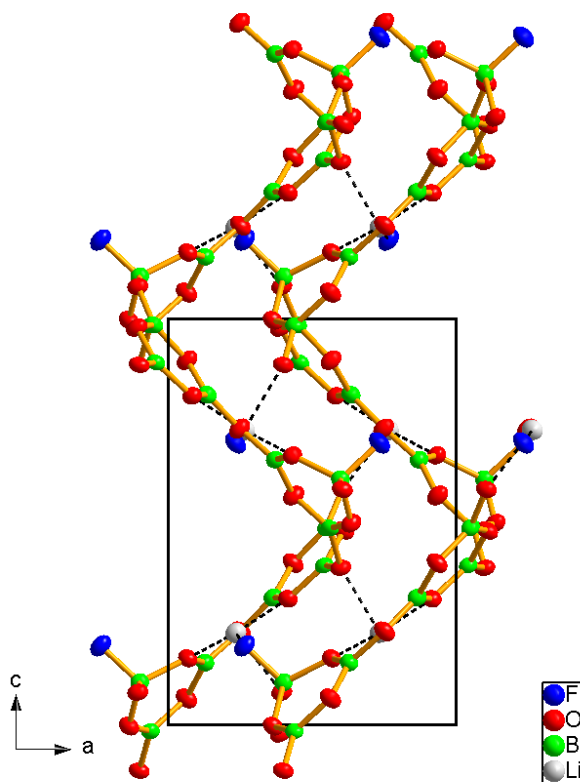
Figure 82: View along the [010] direction showing two layers interconnected by lithium atoms.
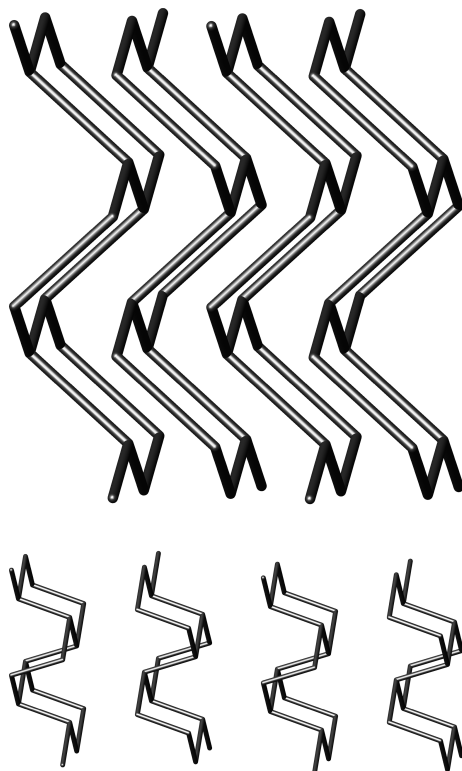
Figure 83: Topological relationship between LiB_6O_9F (top) and black phosphorous (bottom): Drawn are connection lines between the centres of the B_3O_3 boroxine rings, showing the analogy to the P—P bond in P_{black}.
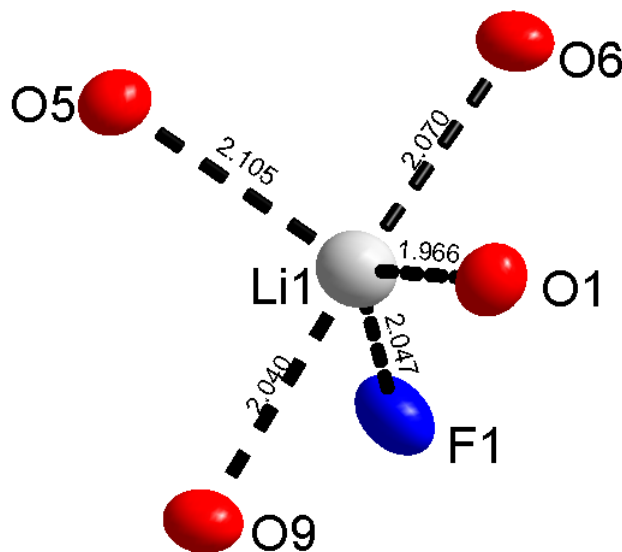
Figure 84: Representation of the lithium coordination in LiB$_6$O$_9$F.

Table 32: Selected bond lengths /Å and bond angles /° of lithium coordination for LiB$_6$O$_9$F. Estimated standard deviations are given in parentheses.

Atom contact	Distance	Atom contact	Angle
Li(1)—F(1)^{iv}	2.047(3)	O(1)—Li(1)—O(9)	105.3(2)
Li(1)—O(1)	1.966(3)	O(1)—Li(1)—F(1)^{iv}	132.8(2)
Li(1)—O(5)	2.106(4)	O(1)—Li(1)—O(6)^{iv}	96.46(15)
Li(1)—O(6)^{iv}	2.070(4)	O(1)—Li(1)—O(5)	99.1(1)
Li(1)—O(9)	2.040(4)	O(9)—Li(1)—F(1)^{iv}	66.4(1)
mean	2.046(4)	O(9)—Li(1)—O(6)^{iv}	154.2(2)
Li(1)—B(1)^{ii}	2.601(4)	O(9)—Li(1)—O(5)	93.85(15)
Li(1)—B(3)	2.835(4)	F(1)^{iv}—Li(1)—O(6)^{iv}	88.75(13)
		F(1)^{iv}—Li(1)—O(5)	127.0(2)
		O(5)—Li(1)—O(6)^{iv}	96.2(2)

5.2.5   Thermal Analysis

Differential thermal analysis, thermogravimetric analysis and mass spectroscopy (DTA /TG/MS) were applied simultaneously under argon atmosphere to investigate the thermal stability of lithium flurooxoborate (Figure 85). The compound represents almost no weight loss up to 470 °C, and then reveals a one-step weight loss up to 900 °C. The decomposition proceeds with thermal evolution of BF_3, which was detected as F (m/z = 19) and BF_2 ($^{10}BF_2$ m/z = 48, $^{11}BF_2$ m/z = 49) species with the mass-spectroscopy. 92 % of the initial mass is remained at 1000 °C.
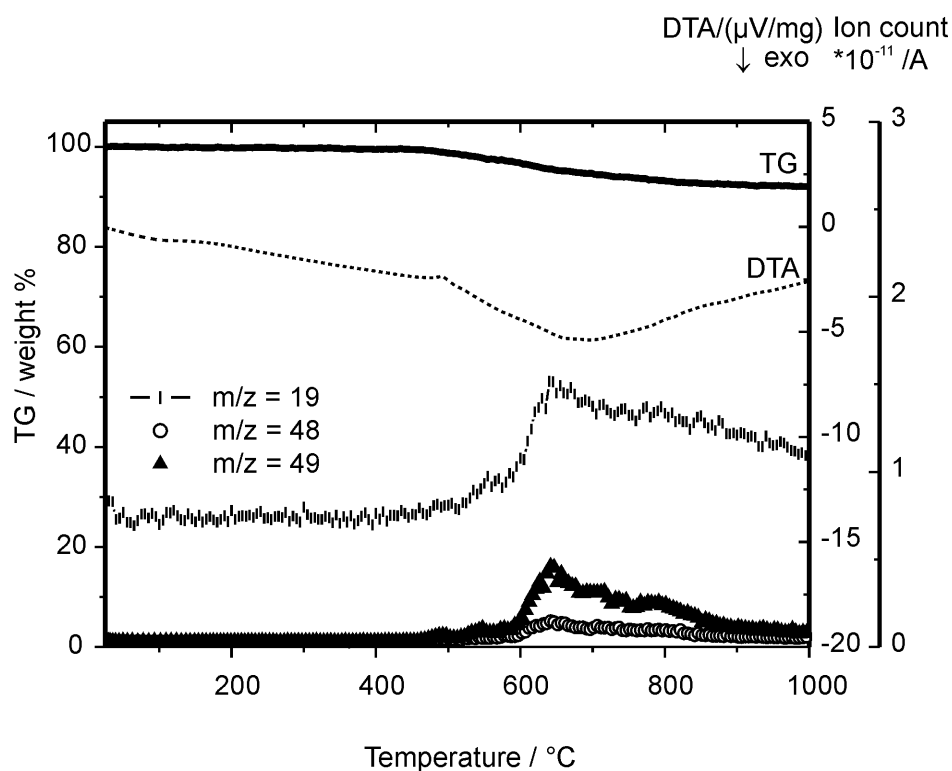
Figure 85: DTA/TG/MS thermograms of LiB_6O_9F in argon flow with a $10\,°C\,min^{-1}$ heating rate.

5.2.6   FT-IR Spectroscopy

The FT-IR spectrum of LiB_6O_6F is depicted in Figure 86. Single crystal analysis has revealed that LiB_6O_6F possesses a triborate unit (having a BO_3F tetrahedra) connected to a cyclic metaborate unit through a bridging oxygen. Even though the existence of BO_3F tetrahedra was claimed for BiB_2O_4F, no vibrational assignments for this unit were reported [225]. It appears that LiB_3O_5 has the closest structural silmilarities to LiB_6O_6F. Therefore, the assigments for IR absorptions of LiB_6O_6F are mainly performed according to the available data for lithium triborate, LiB_3O_5 [226].

Moreover, literature data available for alkali borates have additionally been considered for the interpretation of IR peaks. Relatedly, early investigations in IR spectra of various alkali borates assigned IR vibrational regions between $1450\,\mathrm{cm}^{-1}$ and $1250\,\mathrm{cm}^{-1}$ as B—O stretching vibrations of trigonal BO_3 groups [227]. Analogously, the vibrations at $1482\,\mathrm{cm}^{-1}$ and $1370\,\mathrm{cm}^{-1}$ are attributed to the asymmetric stretching vibrations of B—O bonds in BO_3 triangles. The band at $1223\,\mathrm{cm}^{-1}$ is assigned to the ring stretching vibrations [226]. The asymmetric stretching vibrations of BO_3F tetrahedra are represented with the bands at $1085\,\mathrm{cm}^{-1}$ and $1059\,\mathrm{cm}^{-1}$, while the symmetric stretching vibrations of the corresponding group appear at $871\,\mathrm{cm}^{-1}$ and $832\,\mathrm{cm}^{-1}$ in accordance with the typical vibrations of the BO_4 tetrahedra [228, 229]. The bands appear between $971\,\mathrm{cm}^{-1}$ and $921\,\mathrm{cm}^{-1}$ are assigned to BO_3 symmetric stretching vibrations. The deformation vibrations of BO_3F and BO_3 groups are responsible for the respective bands centering at $724\,\mathrm{cm}^{-1}$ and $706\,\mathrm{cm}^{-1}$. The other vibrations positioned between

Table 33:   FT-IR band positions and assignments for LiB_6O_9F.

Wavenumber /cm^{-1}	Intensity	Assignment
1482−1370	s—vs	$\nu_{asym}\ BO_3$
1223	vs	ν (ring)
1085−1059	s	$\nu_{asym}\ BO_3F$
971−921	s	$\nu_{sym}\ BO_3$
871−832	s	$\nu_{sym}\ BO_3F$
724	s	$\delta\ BO_3F$
706	m	$\delta\ BO_3$
600−400	w—m	γ (ring) and δ (ring)
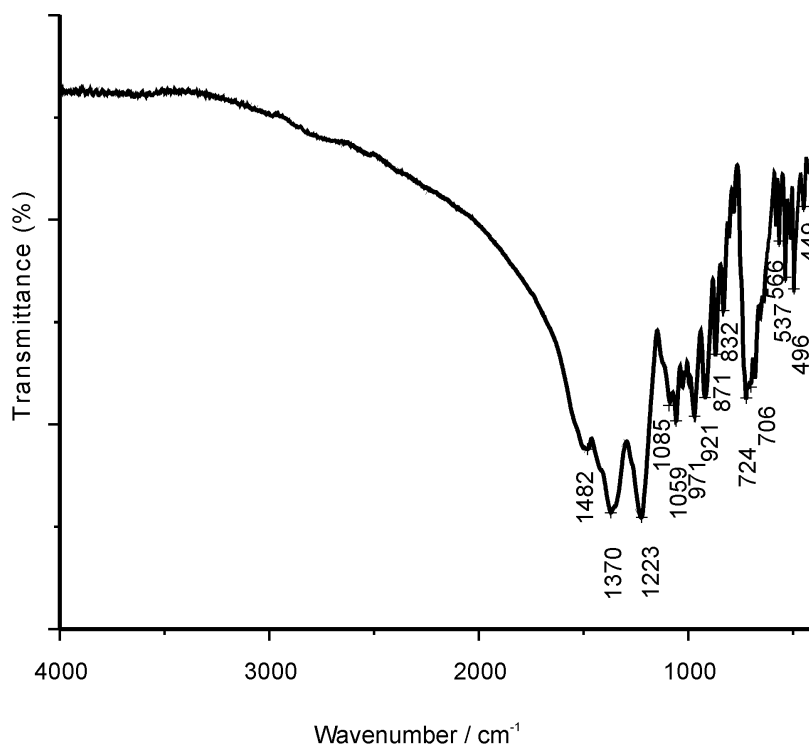
Figure 86: FT-IR spectrum of LiB_6O_9F.

$400\,cm^{-1}$ and $600\ cm^{-1}$ are associated with the bending and ring deformation vibrations. An overview of the most important IR absorptions of LiB_6O_6F together with the corresponding assignments are compiled in Table 33.

5.2.7   Impedance Spectroscopy

Ionic conductivity measurements were carried out for LiB_6O_9F from RT to 400 °C under argon atmosphere by means of impedance spectroscopy. The measurements were recorded at 1 °C min^{-1} heating and cooling rates. Arrhenius type diagrams were used to plot the temperature dependent bulk ionic conductivities (Figure 87). The activation energy for ionic conduction was deduced from the slope of the conductivity curves and amounts to $160\,kJ\,mol^{-1}$.

Lithium fluorooxoborate can be regarded as a solid electrolyte ($10^{-5}\,S\,cm^{-1} < \sigma < 10^{-10}$ S cm^{-1}) according to the classification suggested by Tuller and Moon [52]. The bulk ionic conductivity of LiB_6O_9F was determined as 6.6×10^{-9} S cm^{-1} at 400 °C.
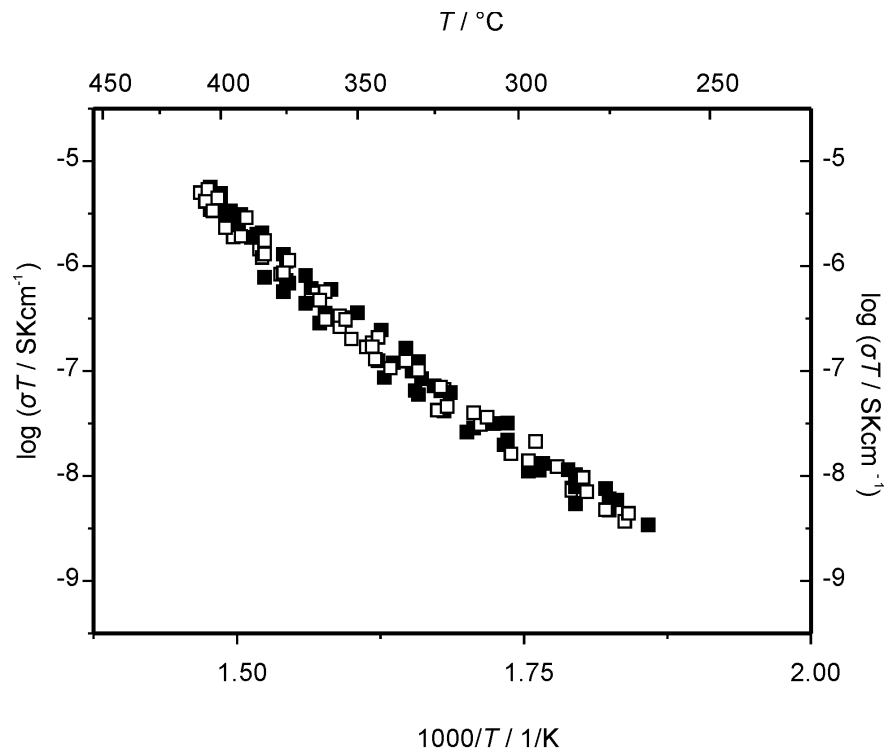
Figure 87: Temperature dependence of bulk ionic conductivities for lithium fluorooxob-orate. Heating and cooling are represented by filled and open symbols, respectively (two cycles are given).
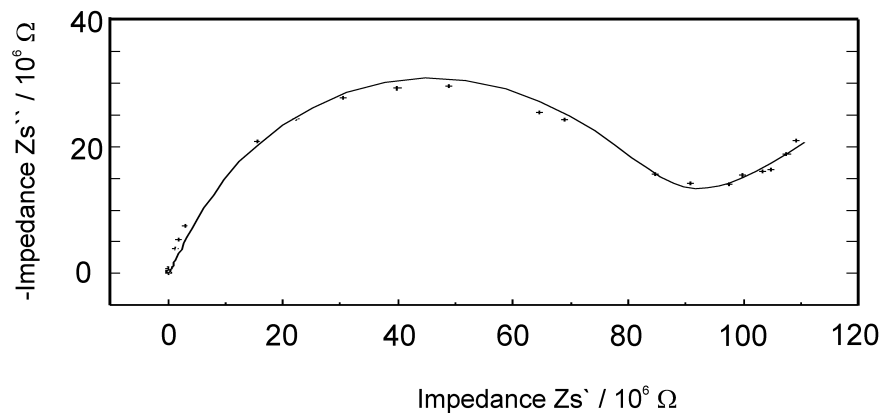
Figure 88: Nyquist plot of lithium fluorooxoborate at T = 400 °C with ion-blocking gold electrodes. The experimental and the simulated impedance spectrum are represented with dots and the solid line, respectively.

However, the ionic conductivity value may be further enhanced by aliovalent doping of the material. Low frequency diffusion spikes were observed in the Nyquist plots (Figure 88), when blocking electrodes were used, which proves that the conduction is ionic in nature.

Only one semicircle in the complex plane format of the impedance data occurred in the temperature range up to 350 °C. In the equivalent circuit, it can be interpreted as a parallel RQ element (Q:constant phase element). An additional low-frequency "spike" appeared at higher temperatures, which indicates the barrier to charge transfer between the sample and the ion-blocking gold electrodes (Figure 88). Thus, it can be expressed in the equivalent circuit with an additional constant phase element, Q_{el}, in series with the RQ element. The capacitance C, can be determined according to C = $Q^{1/n} \times R^{(1/n)-1}$. The capacitance values for the semicircles at different temperatures ($C \approx 6 \times 10^{-12}$ F) are corresponding to the typical values for the bulk capacitance of a sample [45]. Therefore, the lithium ion conductivity in the bulk can be associated with the semicircle.

5.2.8   Conclusions

Single phase, crystalline LiB_6O_9F has been synthesized from LiF and B_2O_3 by solid state reaction. At this example, we present the first crystal structure of an alkali fluorooxoborate. The principal building unit is a pair of boroxine rings, one bearing a fluoride ion. This unit is connected through bridging oxygen to two dimensionally corrugated sheets. Lithium cations are located in between the layers.

Fluorooxoborate anions are unknown, or not conclusively confirmed, in inorganic, solid state compounds. More common are fluoride oxoborates like jeremejevite ($Al_6[B\ O_3]_5F_3$) [215], $Ba_5[B_2O_5]_2F_2$ [230], or $Gd_3[BO_3]_2F_3$ [231], just naming a few examples. As a distinguished feature, all those compounds contain isolated F^- anions which are interacting with cations, exclusively, and no B—F bonding is observed.

B—F bonds were supposed to exist in $BaBOF_3$ [232], with isolated, tetrahedral $[BOF_3]^{2-}$ anions. But the results are highly questionable, this very compound has been assumed later to be the sulfate, in fact [233]. BiB_2O_4F, containing one dimensional infinite $\frac{1}{\infty}[B_2O_4F]^{3-}$ chains, might also be considered to be a fluorooxoborate [225]. $(C_2H_{10}N_2)[BPO_4F_2]$ has to be mentioned within this context [234]. It is not a real fluorooxoborate in the strict sense, but the first fluoroborophosphate, where BO_2F_2 and PO_4 tetrahedra share common corners, forming $\frac{1}{\infty}[BPO_4F_2]^{2-}$ chains, separated by the protonated organic templates. The observed bond distances, $d(B—O) = 1.463$ Å

and d(B—F) = 1.395 Å are in good agreement with the values specified for LiB$_6$O$_9$F (Table 31).

To our knowledge, LiB$_6$O$_9$F is the first lithium fluorooxoborate, unambiguously characterized.

5.3   Sodium Fluorooxoborate, $Na_3B_3O_3F_6$

5.3.1   Synthesis of $Na_3B_3O_3F_6$

$Na_3B_3O_3F_6$ was acquired by applying solid state syntheses with different reactants. The reaction mixtures of $NaF-B_2O_3-NaBF_4$, $NaF-H_3BO_3-NaBF_4$, $NaF-Na_2B_4O_7 \cdot 10\,H_2O-NaBF_4$, $H_3BO_3-NaBF_4$, $B_2O_3-NaBF_4$ and $NaBO_2-NaBF_4$ were utilized to attain $Na_3B_3O_3F_6$, employing appropriate amounts of the reactants. The purest phase and the highest crystalline $Na_3B_3O_3F_6$ was obtained by solid state reaction of a mixture formed from H_3BO_3 and $NaBF_4$ at a temperature of 350 °C according to the following reaction:

$$3\,NaBF_4 + 2\,H_3BO_3 \rightarrow Na_3B_3O_3F_6 + 2\,BF_3 \uparrow + 3\,H_2O\uparrow$$
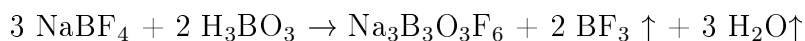
The white colored sodium fluorooxoborate is found to be highly soluble in water. On the contrary, it is insoluble in ethanol and methanol.

Preparation of $Na_3B_3O_3F_6$

Purity of the reactants was confirmed by X-ray powder diffraction and FT-IR prior to the reactions. In a typical reaction, 3 ml hexane (> 99 %, Merck) was added into a 2 g mixture prepared from appropriate amounts of $NaBF_4$ (> 98 %, Sigma Aldrich) and H_3BO_3 (99.99 %, Alfa Aeasar). Then, wet ball milling of the mixture with hexane was performed for 1 hour. Afterwards, the mixture was allowed to stay at 150 °C for overnight in a platinum crucible in order to strip the hexane off. The reaction was accomplished in air in a platinum crucible at 350 °C following a specific temperature schedule: 48 hours heated up to 350 °C, held 90 hours at 350 °C, cooled 24 hours to 325 °C, held 48 hours at 325 °C, cooled 24 hours to 300 °C, held 48 hours at 300 °C and cooled 48 hours down to the room temperature.

Preparation of Na$_3$B$_3$O$_3$F$_6$ single crystal

The single crystal of the title compound was obtained by further crystallization of one part of the obtained compound (0.001 mol) via solvothermal reactions applying ethanol (0.075 mol) and water (0.030 mol) as solvents. The reactions were carried out at 170 °C for more than one month by using 10 ml autoclaves. The products were filtered, washed with ethanol and then dried in air. A single crystal was chosen from the residue which was suitable for single crystal X-ray analysis, and placed on top of a glass capillary.

5.3.2   Single Crystal Structure Analysis of Na$_3$B$_3$O$_3$F$_6$

The experimental intensity data of the single crystal were collected with a Bruker AXS Smart APEX three circle single crystal diffractometer (MoK$_\alpha$ radiation, graphite monochromator) equipped with a CCD-detector at 23 °C. Intensities were corrected for absorption effects by applying a semi-empirical method using the SADABS program [217].

The crystal structure was solved by using the program package SHELXS-97 with direct methods [25]. The structure refinement was carried out by using full-matrix least-square techniques in SHELXL-97 [26], which is implemented in the WinGX Software [27].

Further experimental details on the crystallographic data and the data collection are listed in Table 34. The atomic parameters and the equivalent isotropic displacement parameters are compiled in Table 35. Moreover, Table 36 displays the values for the anisotropic displacement parameters from the single crystal data.

5.3.3   Structure Description

Na$_3$B$_3$O$_3$F$_6$ crystallizes in monoclinic space group $C2/c$, possessing four formula units in the unit cell. Therefore, as claimed by Babich et al, indexing of the powder data for Na$_3$B$_3$O$_3$F$_6$ based on a orthorhombic unit cell together with lattice parameters $a = 10.245$ Å, $b = 14.462$ Å, $c = 9.46$ Å appears inappropriate [211]. Three BO$_2$F$_2$ tetrahedra that are connected through sharing corners from O(1) or O(2) assemble together and compose the hexafluorotriborate rings. The main repetition unit of the structure is, thus consisting of a hexafluorotriborate ring, which is displayed in Figure 89. The ring contains a two fold axis passing from B(1) through O(2) with a C$_2$ symmetry. Based on the fact that B—F distances are not significantly differing with-

Table 34: Crystallographic data for $Na_3B_3O_3F_6$.

Chemical formula	$Na_3B_3O_3F_6$
Crystal system	monoclinic
Space group (no.), Z	$C2/c(15)$, 2
Lattice constants	$a = 11.866(7)$ Å
	$b = 6.901(4)$ Å
	$c = 9.367(6)$ Å
	$\beta = 113.724(9)°$
Volume /Å^3	702.32(28)
Density (calculated) /g cm^{-3}	2.491
Temperature /°C	23 (2)
Diffractometer	Bruker AXS, Smart APEX CCD
Monochromator	Graphite
Wavelength	MoK_α ($\lambda = 0.71073$ Å)
hkl - range	$-14{<}h{<}14$, $-8{<}k{<}8$, $-11{<}l{<}11$
Absorption correction	Program SADABS
F (000)	504.0
Theta range for data collection /°	$3.50 \leq \theta \leq 26.57$
Reflections collected	2719
Independent reflections	730 [$R_{int} = 0.0555$]
Completeness to theta = 26.57°	99.3 %
Absorption coefficient μ /mm^{-1}	0.44
Structure refinement	WinGX 1.64.05 /SHELXL 97
Refinement method	Full-matrix least-squares on F^2
Parameters refined	71
R_1 ($F_0 > 4\sigma$ F_0 /all)	0.074, 0.094
wR_2 ($F_0 > 4\sigma$ F_0 /all)	0.1798, 0.1957
Goodness of fit on F^2	1.207
$\Delta\rho$ min, $\Delta \rho$ max /e Å^{-3}	-0.43, 1.03

Table 35:   Atomic coordinates and equivalent isotropic displacement parameters, U_{eq} /Å² for $Na_3B_3O_3F_6$. Estimated standard deviations are given in parentheses.

Atom	*Wyckoff* position	x	y	z	U_{eq}
Na(1)	4d	3/4	1/4	0	0.0267(7)
Na(2)	8f	0.5933(1)	0.2247(2)	0.4982(1)	0.0259(6)
F(1)	8f	0.2876(2)	0.4135(3)	0.1192(2)	0.0276(7)
F(2)	8f	0.4541(2)	0.9181(3)	0.1163(2)	0.0272(7)
F(3)	8f	0.6256(2)	0.4088(3)	0.1135(3)	0.0314(8)
O(1)	8f	0.4004(2)	0.6807(4)	0.2555(3)	0.0241(8)
O(2)	4e	1/2	0.3782(5)	1/4	0.024(1)
B(1)	4e	1/2	0.789(1)	1/4	0.020(1)
B(2)	8f	0.3956(4)	0.4758(7)	0.2536(5)	0.022(1)

in the experimental errors (B(2)—F(1), B(2)—F(3) and B(1)—F(2) distances are 1.454(5) Å, 1.443(5) Å and 1.450(5) Å, respectively), thus these distances can be assumed to be equal. Hence, it is plausible that three boron atoms are located at the sites of C_{2v} symmetry, whereas hexafluorotriborate ring is of point group symmetry D_{3h}. The novel crystal structure is composed of layers formed by rings of hexafluorotriborate $(B_3O_3F_6{}^{3-})$ anions, and sodium cations are located in between these layers. The layer structure is illustrated in Figure 90 along the [100] direction and the distance between layers of planar hexafluorotriborate anions is evaluated as 4.421(3) Å.

Table 36:   Anisotropic thermal displacement parameters, U_{ij} /Å^2, for Na$_3$B$_3$O$_3$F$_6$. Estimated standard deviations are given in parentheses.

Atom	U_{11}	U_{22}	U_{33}	U_{12}	U_{13}	U_{23}
Na(1)	0.026(1)	0.028(1)	0.019(1)	0.003(1)	0.003(1)	0.0016(9)
Na(2)	0.032(1)	0.025(2)	0.018(1)	0.0022(7)	0.0081(8)	0.0014(6)
F(1)	0.027(1)	0.027(1)	0.022(1)	−0.005(1)	0.002(1)	−0.005(1)
F(2)	0.038(1)	0.021(1)	0.018(1)	0.003(1)	0.005(1)	0.0059(9)
F(3)	0.041(1)	0.033(1)	0.021(1)	0.006(1)	0.014(1)	−0.004(1)
O(1)	0.024(1)	0.020(1)	0.027(1)	0.00(1)	0.009(1)	−0.001(1)
O(2)	0.022(2)	0.016(2)	0.033(2)	0	0.008(1)	0
B(1)	0.024(3)	0.020(3)	0.013(3)	0	0.002(2)	0
B(2)	0.025(2)	0.023(2)	0.018(2)	−0.001(2)	0.005(1)	0.001(1)

Herein, the uniqueness of the structure should be itemized, since Na$_3$B$_3$O$_3$F$_6$ is the first compound that is originating solely from BO$_2$F$_2$ subunits. Figure 91 illustrates the crystal structure focusing on the polyhedral representation comprised of tetrahedral BO$_2$F$_2$ groups. The coordination environments of the boron atoms are slightly distorted tetrahedra. The BO$_2$F$_2$ tetrahedra feature a mean tetrahedral angle of 109.4(3)° and the mean value for O—B—F angles is assessed as 108.9(2)°. It is to be discerned that the F—B—F angle is slightly smaller than the ideal tetrahedral angle (104.6(4)°) in order to compensate for the widening of the O—B—O angle (116.14(45)°) due to the hexafluorotriborate ring. The selected bond lengths and angles for the B$_3$O$_3$F$_6^{3-}$ anion with their standard deviations are compiled in Table 37.
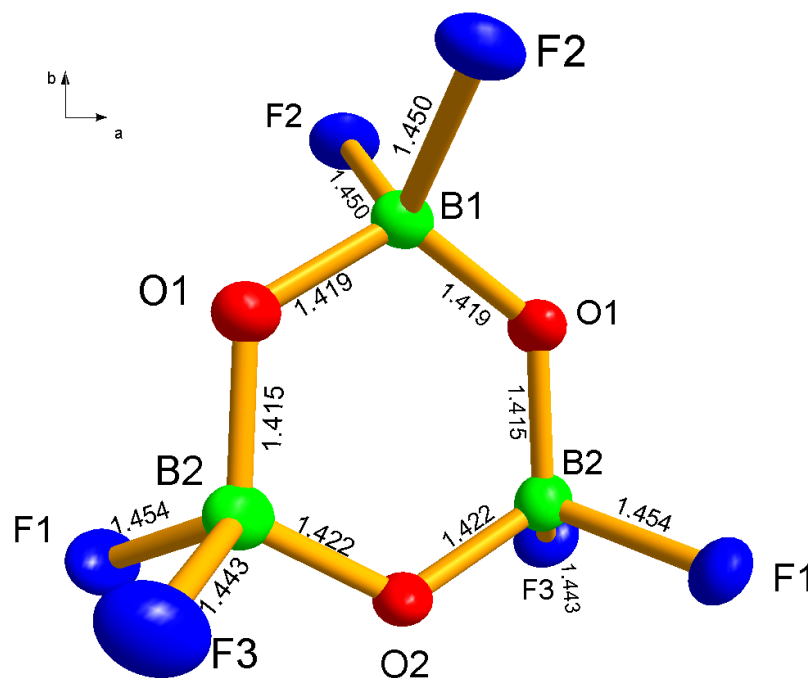
Figure 89: Representation of the hexafluorotriborate ring along the [001] direction in Na$_3$B$_3$O$_3$F$_6$, showing the atom labelling scheme. Displacement ellipsoids are drawn at the 50% probability level.

The hexafluorotriborate anion, represented in Figure 89, exhibits the planar configuration of a six membered ring. The average of O—B—O angles and B—O—B angles are recognized as 116.14(45)° and 123.8(4)°, respectively. Therefore, an overall sum of 720° is assembled, which supports the fact that the planarity of the ring is sustained. The overall sum of the torsion angles in the ring amounts to zero. The almost planar six membered hexafluoroborate ring sets only slight variations forth concerning the torsion angles, in a specifically elaborated manner recites the minimum as −1.7(5)° for the B(1)—O(1)—B(2)—O(2) and the maximum as 0.9(5)° for the B(2)—O(1)—B(1)—O(1). Thus, the previous consideration reporting the nonplanarity of the B$_3$O$_3$F$_6{}^{3-}$ ring originating from the spectroscopic data is herein proven to be improper [235]. Further information´s about the torsion angles of the B$_3$O$_3$F$_6{}^{3-}$ ring are compiled in Table 38.
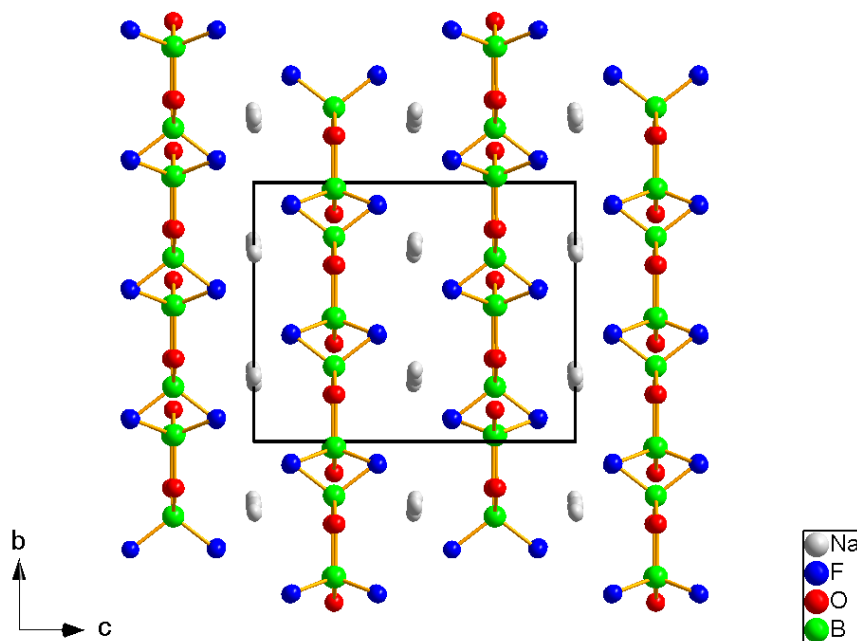
Figure 90: Representation of the crystal structure along the [100] direction of $Na_3B_3O_3F_6$ with the margins of the unit cell (black).

The mean B—F distance is found as 1.449(5) Å, and is thus slightly larger than the corresponding distance of the BO_3F tetrahedron in LiB_6O_9F (1.431 Å) [236]. Then, the mean distance between boron and oxygen in $Na_3B_3O_3F_6$ is attained as 1.418(5) Å. Similar distances in the corresponding bond have been frequently encountered [221, 236]. To exemplify, a similar value was reported for the corresponding average B—O distances in LiB_3O_5 (1.473 Å in BO_4) [237], which contains triborate rings, $[B_3O_5]^-$, consisting of two BO_3 units fused to a BO_4 unit. Hence, the replacement of two oxygen atoms in a BO_4 unit by two fluorine atoms in the title compound creates a slight decrease (0.05 Å) in the B—O distance. In turn, the B—O distances in the hexafluorotriborate ring are much larger than in the boroxine ring in sodium metaborate, $[NaBO_2]_3$, (1.38 Å) which is composed of three BO_3 groups [238], showing a clear difference to the tetrahedral arrangement of the BO_2F_2 groups in $Na_3B_3O_3F_6$.

Table 37: Selected interatomic distances /Å and bond angles /° of B$_3$O$_3$F$_6$$^{3-}$ anion for Na$_3$B$_3$O$_3$F$_6$. Estimated standard deviations are given in parentheses.

Atom contact	Distance	Atom contact	Angle
B(1)—O(1)	1.419(5)	F(2)^{vii}—B(1)—F(2)	104.6(4)
B(1)—O(1)^{vii}	1.419(5)	O(1)—B(1)—F(2)	109.1(2)
B(1)—F(2)	1.450(5)	O(1)—B(1)—F(2)^{vii}	108.7(2)
B(1)—F(2)^{vii}	1.450(5)	O(1)^{vii}—B(1)—F(2)	108.7(2)
mean	1.434(4)	O(1)^{vii}—B(1)—F(2)^{vii}	109.1(2)
		O(1)^{vii}—B(1)—O(1)	116.0(5)
		mean	109.4(3)
B(2)—O(1)	1.415(6) [2×]	F(1)B—(2)—F(3)^{vii}	104.6(3) [2×]
B(2)—O(2)	1.422(5) [2×]	O(2)—B(2)—F(3)^{vii}	109.0(3) [2×]
B(2)—F(3)^{vii}	1.443(5) [2×]	O(2)—B(2)—F(1)	108.3(3) [2×]
B(2)—F(1)	1.454(5) [2×]	O(1)—B(2)—F(1)	108.9(3) [2×]
mean	1.433(5)	O(1)—B(2)—F(3)^{vii}	109.2(3) [2×]
		O(1)—B(2)—O(2)	116.3(4) [2×]
		mean	109.4(3)
		B—O—B angles	
		B(2)—O(1)—B(1)	124.0(4) [2×]
		B(2)^{vii}—O(2)—B(2)	123.5(3)

Symmetry transformation used to generate equivalent atoms: $^{[vii]}$ −x−1, y, −z+1/2
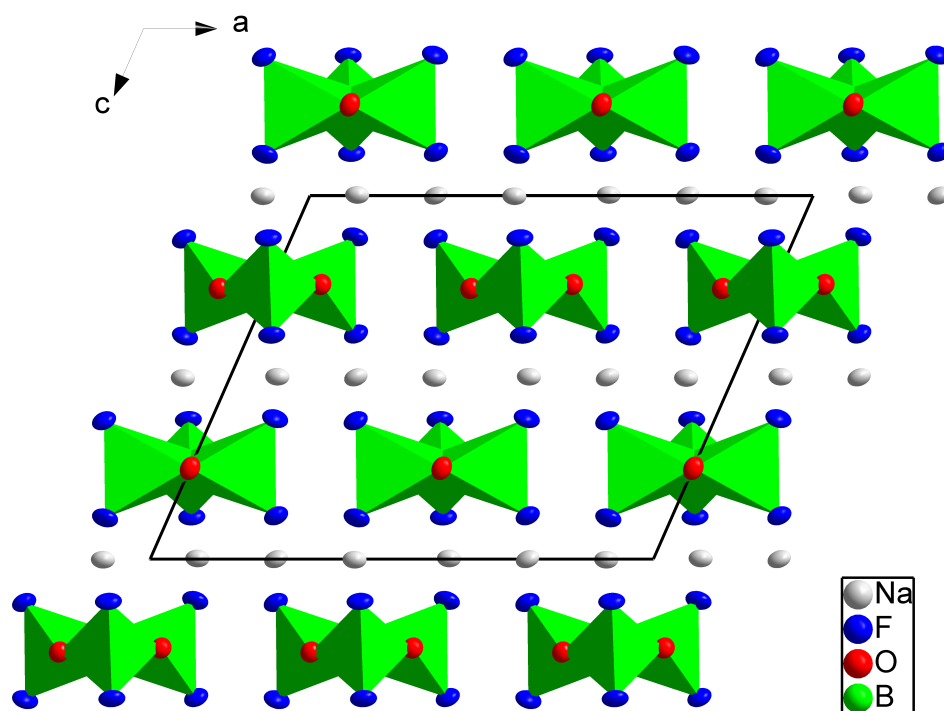
Figure 91: Representation of the crystal structure along the [010] direction of $Na_3B_3O_3F_6$ with the margins of the unit cell (black).

Table 38: Torsion angles /° of the $B_3O_3F_6{}^{3-}$ ring in $Na_3B_3O_3F_6$.

Atom contact	Angle
B(1)—O(1)—B(2)—O(2)	−1.7(5)
B(2)—O(2)—B(2)^{vii}—O(1)	0.8(5)
B(2)—O(1)—B(1)—O(1)^{vii}	0.9(5)

The crystal structure of Na$_3$B$_3$O$_3$F$_6$ is assembled from two kinds of sodium ions. Na(1) atom is eightfold coordinated by six fluorine and two oxygen atoms in the form of a distorted cubic polyhedra with an average distance of 2.458(3) Å composed of two equidistant atoms of O(1) with 2.389(3) Å, F(3) with 2.402(3) Å, F(2) with 2.505(3) Å and F(1) with 2.538(3) Å, as illustrated in Figure 92a. The bond angles for all pairs (namely, F(1)—Na(1)—F(1), F(2)—Na(1)—F(2), F(3)—Na(1)—F(3), O(1)—Na(1)—O(1)) are equal with each other and account to 180°. Two equidistant F(3) and O(1) compose a square planar with identical F(3)—Na(1)—O(1) angles of 90° within the distorted cubic polyhedra.

Similar to Na(1), Na(2) also presents an eightfold coordination implicated by O(1), O(2), F(1), F(2) and F(3). Thus, a mean distance of 2.480(3) Å is attested for this irregular polyhedra, which is figured out in Figure 92b. It was reported that sodium atoms in NaBF$_4$ also form eight coordinated irregular polyhedra, akin to the Na(2) in Na$_3$B$_3$O$_3$F$_6$. Moreover, the mean distances are evaluated as 2.376(3) Å for the Na(2)—O and 2.514(3) Å for the Na(2)—F, while the nearest boron atom is located at a distance of 2.972(5) Å.

The connection polyhedra of Na(1)O$_2$F$_6$ and Na(2)O$_2$F$_6$ have been denoted in Figure 93. Thus, Na(1) and Na(2) atoms are connected with the boron atom through sharing edges constituted of oxygen and fluorine atoms. Hence, Na(1) atom is connected with six Na(2) atoms through sharing edges comprised from the F(1)—F(2), F(2)—F(1), F(1)—F(3), F(3)—F(1), F(2)—F(3) and F(3)—F(2). Furthermore, Na(2) atoms are connected to both three of Na(2) atoms by sharing the edges composed of F(1)—F(1), F(2)—F(2), F(3)—F(3), and also three of Na(1) atoms by sharing the edges enclosed by F(1)—F(3), F(1)—F(2), F(2)—F(3).

Accordingly, the mean distances are evaluated as 2.39 Å for the Na(1)—O and 2.38 Å for the Na(2)—O, wherefore both Na(1) and Na(2) exhibits contacts shorter than the Na—O distances in NaBO$_2$, for which the shortest Na—O distance was reported as 2.46 Å [238]. The contacts of Na(1) and Na(2) with fluorine atoms are in well agreement with the corresponding distances in NaBF$_4$ (2.29—2.61 Å) [239]. Further details disclosing the Na—O and Na—F distances have been represented in Table 39, displaying the selected interatomic distances as well as the bond angles concerning the sodium coordination for Na$_3$B$_3$O$_3$F$_6$.

The structures of almost all of the fluorine containing oxoborates thus for represented in the literature manifests isolated fluorine anions which are located at the cation polyhedra, without formation of any B—F bonds. To illustrate, the reaction of 2Al$_2$O$_3$· B$_2$O$_3$· 5H$_2$O and B$_2$O$_3$ in the presence of a fluorine containing mineralizer
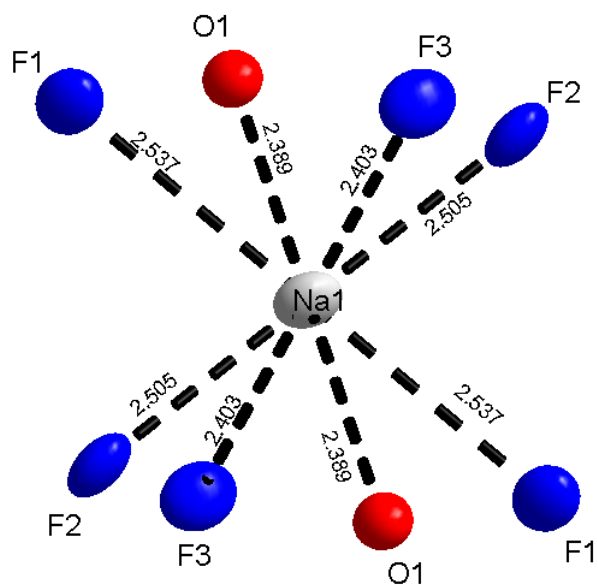
(a)
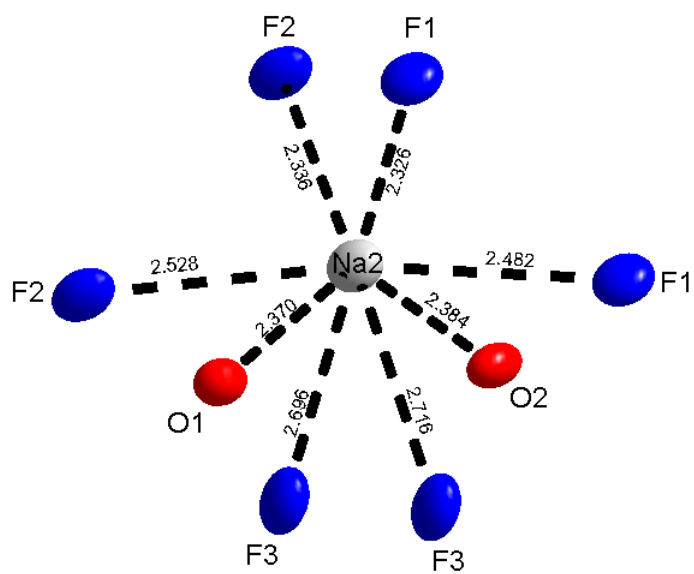
(b)

Figure 92: Representation of the (a) Na(1) and (b) Na(2) coordinations in $Na_3B_3O_3F_6$.

resulted the formation of $Al_6[BO_3]_5F_3$, the structure of which consists of fluorine atoms at the vertices of aluminum octahedra without forming the B—F bonds and boron atoms form $[BO_3]^{3-}$ triangles [240]. As explained in Section 5.2, the crystal structure of $Na_3B_3O_3F_6$ is the first example illustrating the BO_2F_2 tetrahedra. Indeed, following to the crystal structure of LiB_6O_9F (see Section 5.2), $Na_3B_3O_3F_6$ is the second "true" alkali fluorooxoborate known.
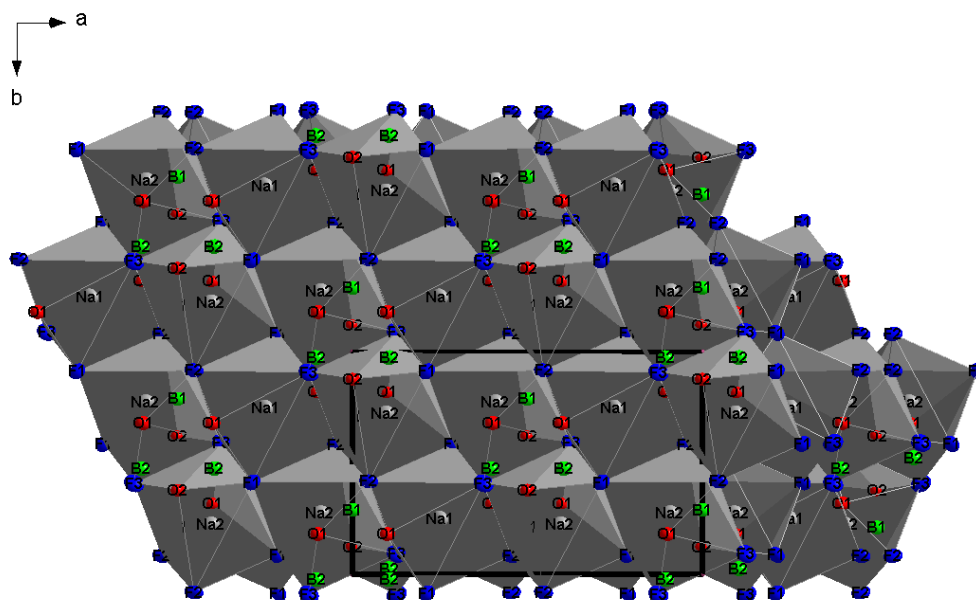
Figure 93: Representation of the connection of the sodium polyhedra along the [001] direction in the $Na_3B_3O_3F_6$, with the margins of the unit cell (black).

Table 39: Selected interatomic distances /Å and bond angles /° of the sodium coordination for $Na_3B_3O_3F_6$ from the single crystal data. Estimated standard deviations are given in parentheses.

Atom contact	Distance	Atom contact	Angle
Na(1)—O(1)^i	2.389(3)	O(1)^i—Na(1)—O(1)^{ii}	180.0(1)
Na(1)—O(1)^{ii}	2.389(3)	O(1)^i—Na(1)—F(3)^{iii}	90.4(1)
Na(1)—F(3)^{iii}	2.402(3)	O(1)^{ii}—Na(1)—F(3)^{iii}	89.6(1)
Na(1)—F(3)^{iv}	2.402(3)	O(1)^i—Na(1)—F(3)^{iv}	89.6(1)
Na(1)—F(2)^i	2.505(3)	O(1)^{ii}—Na(1)—F(3)^{iv}	90.4(1)
Na(1)—F(2)^{ii}	2.505(3)	F(3)^{iii}—Na(1)—F(3)^{iv}	180.0(0)
Na(1)—F(1)^i	2.538(3)	F(1)^{iii}—Na(1)—F(1)^{iv}	180.0(0)
Na(1)—F(1)^{ii}	2.538(3)	F(2)^{iii}—Na(1)—F(3)^{iv}	180.0(0)
mean	2.458(3)		
Na(1)—B(1)^i	2.961(1)		
Na(1)—B(1)^{ii}	2.961(1)		
Na(1)—B(2)^i	2.984(5)		
Na(1)—B(2)^{ii}	2.984(5)		
Na(2)—F(1)^v	2.326(3)	F(1)^v—Na(2)—F(2)^{vi}	82.0(1)
Na(2)—F(2)^{vi}	2.337(3)	F(1)^v—Na(2)—O(1)^{ii}	90.1(1)
Na(2)—O(1)^{ii}	2.369(3)	F(2)^{vi}—Na(2)—O(1)^{ii}	127.1(1)
Na(2)—O(2)	2.384(2)	F(1)^v—Na(2)—O(2)	129.6(9)
Na(2)—F(1)^{vii}	2.482(3)	F(2)^{vi}—Na(2)—O(2)	91.3(1)
Na(2)—F(2)^{viii}	2.528(3)	O(1)^{ii}—Na(2)—O(2)	130.4(1)
Na(2)—F(3)^{vii}	2.696(3)		
Na(2)—F(3)^{viii}	2.716(3)		
mean	2.480(3)		
Na(2)—B(2)^{vii}	2.972(5)		
Na(2)—B(1)^{ii}	2.983(2)		

Symmetry transformations used to generate equivalent atoms:
[i] x+1/2, y−1/2, z+1 ; [ii] −x−1, −y+1, −z+1 ; [iii] −x−1/2, −y+1/2, −z+1 ;
[iv] x, y, z+1 ; [v] x+1/2, −y+1/2, z+1/2 ; [vi] −x−1, y−1, −z+1/2 ;
[vii] −x−1, y, −z+1/2 ; [viii] x, −y+1, z+1/2

5.3.4   FT-IR Spectroscopy

Further characterization of the sodium fluorooxoborate was contrived by recording the FT-IR spectrum between 400 cm^{-1} and 4000 cm^{-1}, as demonstrated in Figure 94. The characteristic stretching vibrations manifesting the hexafluorotriborate ring are the very strong vibrations centering at 918 cm^{-1}, 1072 cm^{-1} and 1203 cm^{-1} [210]. The other characteristic strong band is observed at 797 cm^{-1}, which discloses the B—F stretching vibration of BO_2F_2 groups [235]. Furthermore, two small shoulders appear at 1447 cm^{-1} and 1374 cm^{-1}, which are also ascribed for the ring stretching vibrations [241]. The band at 580 cm^{-1} is interpreted for the ring deformation vibration. The assignments and the corresponding intensities are tabulated in Table 40.
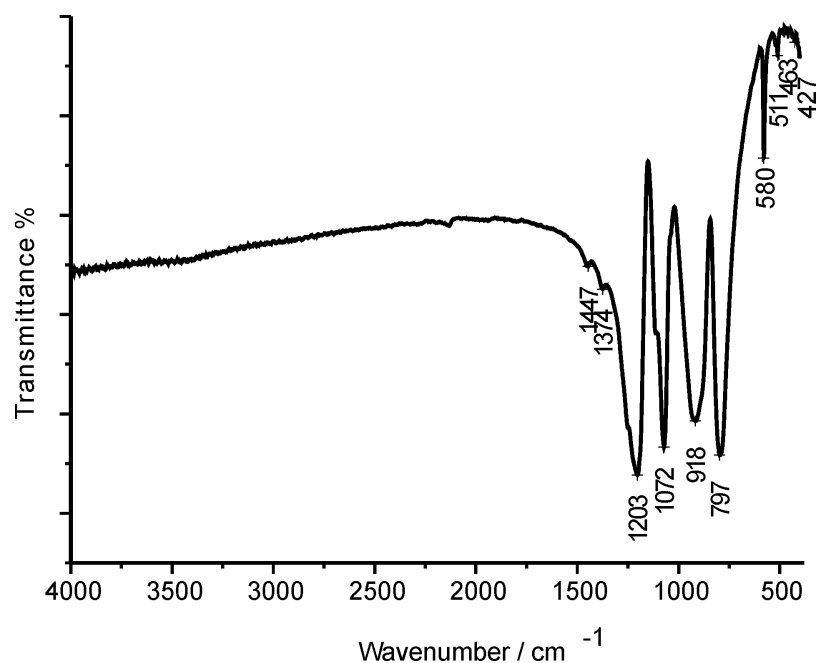
Figure 94:   FT-IR spectrum of $Na_3B_3O_3F_6$.

Table 40: FT-IR band positions and assignments of $Na_3B_3O_3F_6$.

Wavenumber /cm^{-1}	Intensity	Assignments
1447−1374	w	ν (ring)
1203	s	ν (ring)
1071	s	ν (ring)
918	s	ν (ring)
797	s	ν (B—F)
579	m	δ (ring)
511−427	w	δ (B—O)

5.3.5   Raman Spectroscopy

The strongest Raman band assessed at 600 cm^{-1} is construed to the breathing vibration of the $B_3O_3F_6{}^{3-}$ ring [235], as discerned in Figure 95. The other band belonging to the ring is the ring deformation band attained at 304 cm^{-1}. The band at 333 cm^{-1} is ascribed as the BF_2 rocking and the band at 735 cm^{-1} is attributed to the B—F symmetric stretching of BF_2 [235]. The bands centering at 374 cm^{-1}, 527 cm^{-1} and 513 cm^{-1} are assigned to bending modes of BO_2F_2 groups [235]. The circumstantial of the band interpretations together with the intensities are gathered in Table 41.

5.3.6   Thermal Analysis

Thermal behavior of the $Na_3B_3O_3F_6$ was investigated via DTA/TG/MS measurements up to 1000 °C (Figure 96). The endothermic peak observed at 400 °C in DTA is accounted for the decomposition of $Na_3B_3O_3F_6$ by yielding NaF and an amorphous
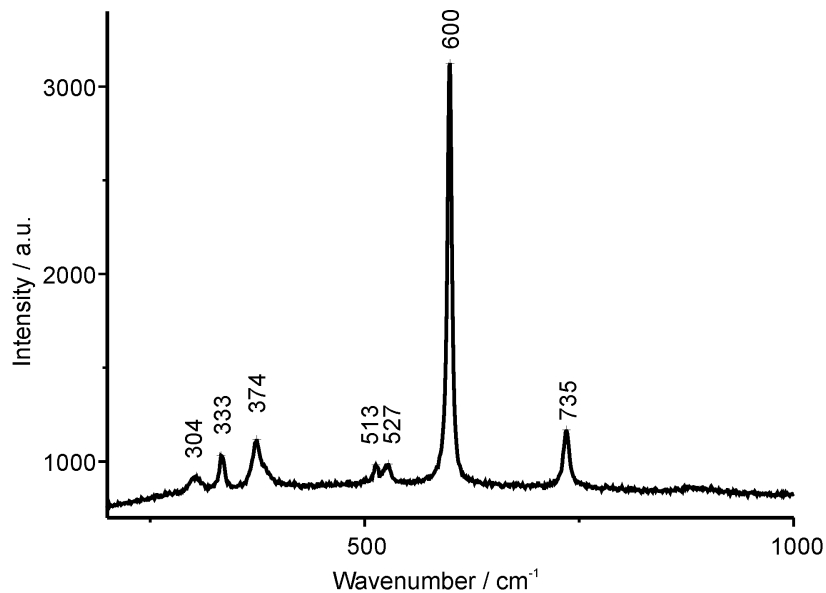
Figure 95:   Raman spectrum of the Na₃B₃O₃F₆.

Table 41: Raman band positions and assignments of Na₃B₃O₃F₆.

Wavenumber $/cm^{-1}$	Intensity	Assignments
735	m	ν (B—F)
600	vs	ν (ring)
527	w	δ (BO$_2$F$_2$)
513	w	δ (BO$_2$F$_2$)
374	m	δ (B—F)
333	w	ρ (B—F)
304	w	δ (ring)

Figure 96: DTA/TG/MS thermograms of $Na_3B_3O_3F_6$ in argon flow with a 10 °C min^{-1} heating rate.

phase. It is remarkable that no recognizable weight loss is attained accompanying the decomposition. Therefore, it is attributed that the decomposition should probably lead to an amorphous phase of $Na_2B_3O_3F_5$ in addition to NaF, confirming the results of Maya et al. [210].

The results reveal that no weight loss is espied up to 550 °C. Onwards to this temperature, an amorphous phase, originated from the decomposition of $Na_3B_3O_3F_6$, starts to decompose. The decomposition occurred between 550 °C and 850 °C, and in this temperature range the evolution of F (m/z = 19) and BF_2 ($^{10}BF_2$ m/z = 48, $^{11}BF_2$ m/z = 49) species are detected by mass spectroscopy. 91 % of the initial mass is attained at 1000 °C.

In order to grasp the thermal demeanor of the material, DSC measurements were also conducted up to 500 °C under argon flow, as plotted in Figure 97. Accordingly, the consequent thermogram reveals a well-matching result with the DTA. When the thermogram is analyzed in detail, the most prominent peak is noticed possessing the peak maximum at 409 °C. In addition to that, the substantial change of the slope in the

thermogram can be recognized at 215 °C. However, this effect can not be as a consequence of a phase transition since it is hardly discerned in the thermogram. Moreover, X-ray powder diffraction measurements performed at high temperatures, involving this temperature interval, have not distinguished a phase transition. The decomposition of the material is assessed at 409 °C. In order to identify the decomposition products, X-ray powder diffraction of the material was consummated following the DSC measurements. Thus, it is figured out the presence of NaF in the material as a single phase without any remaining traces of the $Na_3B_3O_3F_6$ reflections. Eventually, the material decomposes into NaF and an amorphous phase (which could be $Na_2B_3O_3F_5$).
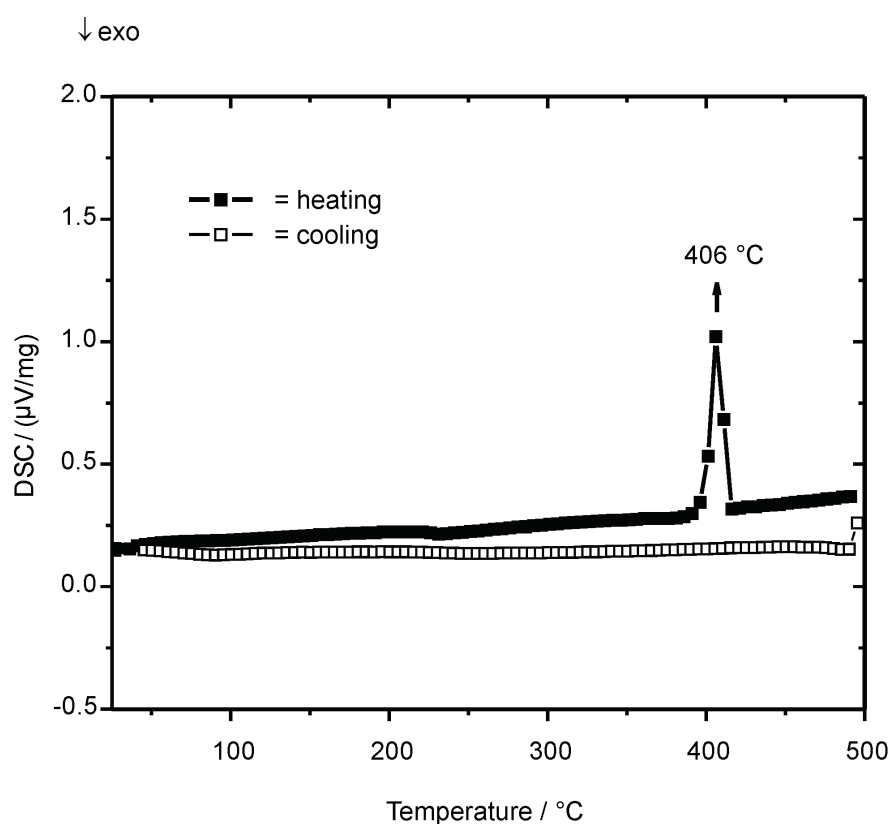
Figure 97: DSC thermograms of $Na_3B_3O_3F_6$ in argon flow with 5 °C min^{-1} heating and cooling rates up to 500 °C.

5.3.7 Impedance Spectroscopy

The ionic conductivity measurements were attained via the impedance spectroscopy under argon flow with 1 °C min^{-1} heating and cooling rates up to 350 °C. Prior to

the measurements, the samples were dried in vacuum at 150 °C in a Schlenck line to remove the effect of water. The Arrhenius type diagram representing the temperature dependent bulk ionic conductivities are graphed in Figure 98. The material demonstrates fully reversible ionic conductivity values upon heating and cooling cycles. The activation energies were derived from the slopes of the conductivity curves. The activation energy is found as 67 kJ mol^{-1} between the temperatures of 25 °C and 200 °C. The slope of the conductivity curve alters at 200 °C and the material represents an activation energy of 107 kJ mol^{-1} between 200 °C and 350 °C. According to the powder X-ray diffraction analysis conducted at higher temperatures, no change in the reflections of the material is distinguished in the specified temperature regime, explicitly onwards to 200 °C. Thus, the nebulous change in the slope is not attributed to a phase change in the material. On the other hand, this kind of alters in the Arrhenius plot for ionic conduction is typical for ionic conductors and is established for a crossover from the extrinsic to the intrinsic region. Accordingly, it is interpreted for $Na_3B_3O_3F_6$ that the regime below 200 °C corresponds to the extrinsic region of the material, in which defect motion accounts only for E_a. While, onwards to 200 °C is associated with the energies not only for defect motion but also for defect formation, thus both sums up for the resulting activation energy [242].

The activation energies and ionic conductivity values at different temperatures are summarized in Table 42. The ionic conductivity values of this material range from 1.1×10^{-3} S cm^{-1} at 310 °C to 3.6×10^{-3} S cm^{-1} at 350 °C. The high ionic conductivity values of $Na_3B_3O_3F_6$ points out that this material is a fast ion conductor, and indeed the ionic conductivity values are comparable with the well known ion conductors like Li-β-alumina. The latter material was reported to possess an ionic conductivity of 9.2×10^{-3} S cm^{-1} at 300 °C [243].

The impedance data represented in the complex plane exhibit only one semicircle until 67 °C, which is fitted by utilizing a R_1Q_1 element (Q:constant phase element) in the equivalent circuit. At higher temperatures, the low frequency spike is discerned which accounts for the barrier to charge transfer between the sample and the ion blocking gold electrodes. Thus, in the equivalent circuit a supplemental constant phase element (Q_{el}) was used in series with the R_1Q_1 element. The capacitance, C, can be determined according to the equation of $C = Q^{1/n} \times R^{(1/n)-1}$. The capacitance values of the semicircle at different temperatures are derived, and an approximate value of 3×10^{-12} F is evaluated, which is typical for the bulk capacitance of a sample. Hence, the semicircle is associated with the sodium conductivity in the bulk.
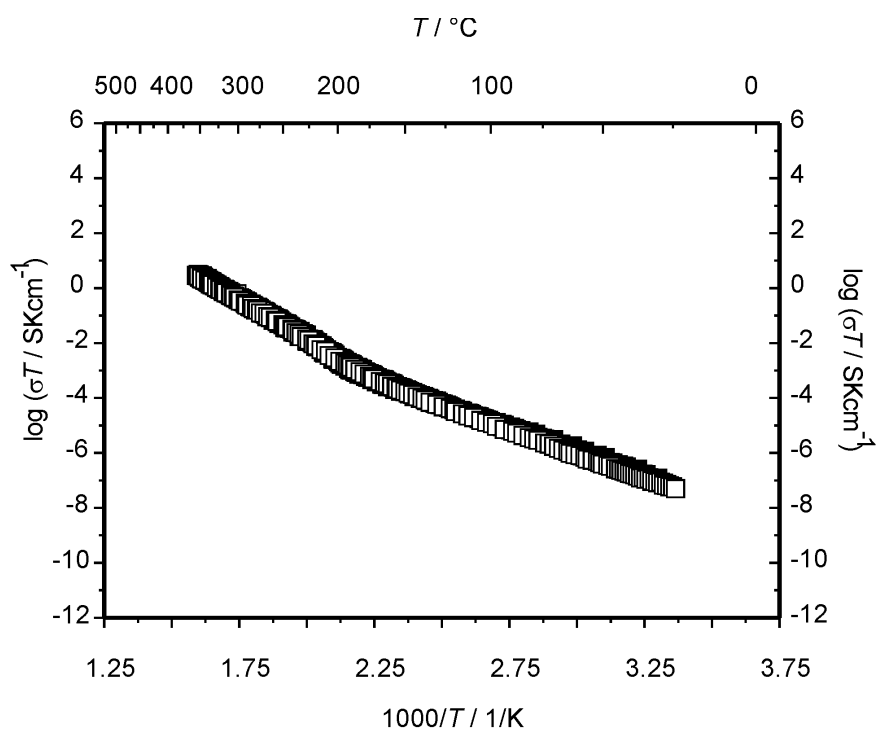
Figure 98:   Temperature dependence of the ionic conductivities of Na$_3$B$_3$O$_3$F$_6$ with gold electrodes. (Heating and cooling cycles are represented by filled and open symbols, respectively.)

Table 42:   Activation energies and ionic conductivity values at different temperatures for Na$_3$B$_3$O$_3$F$_6$.

σ /S cm^{-1}	E_a /kJ mol^{-1}
3.6×10^{-3} (350 °C)	107 (200 °C–350 °C)
8.7×10^{-5} (250 °C)	67 (25 °C–200 °C)
1.5×10^{-8} (85 °C)	
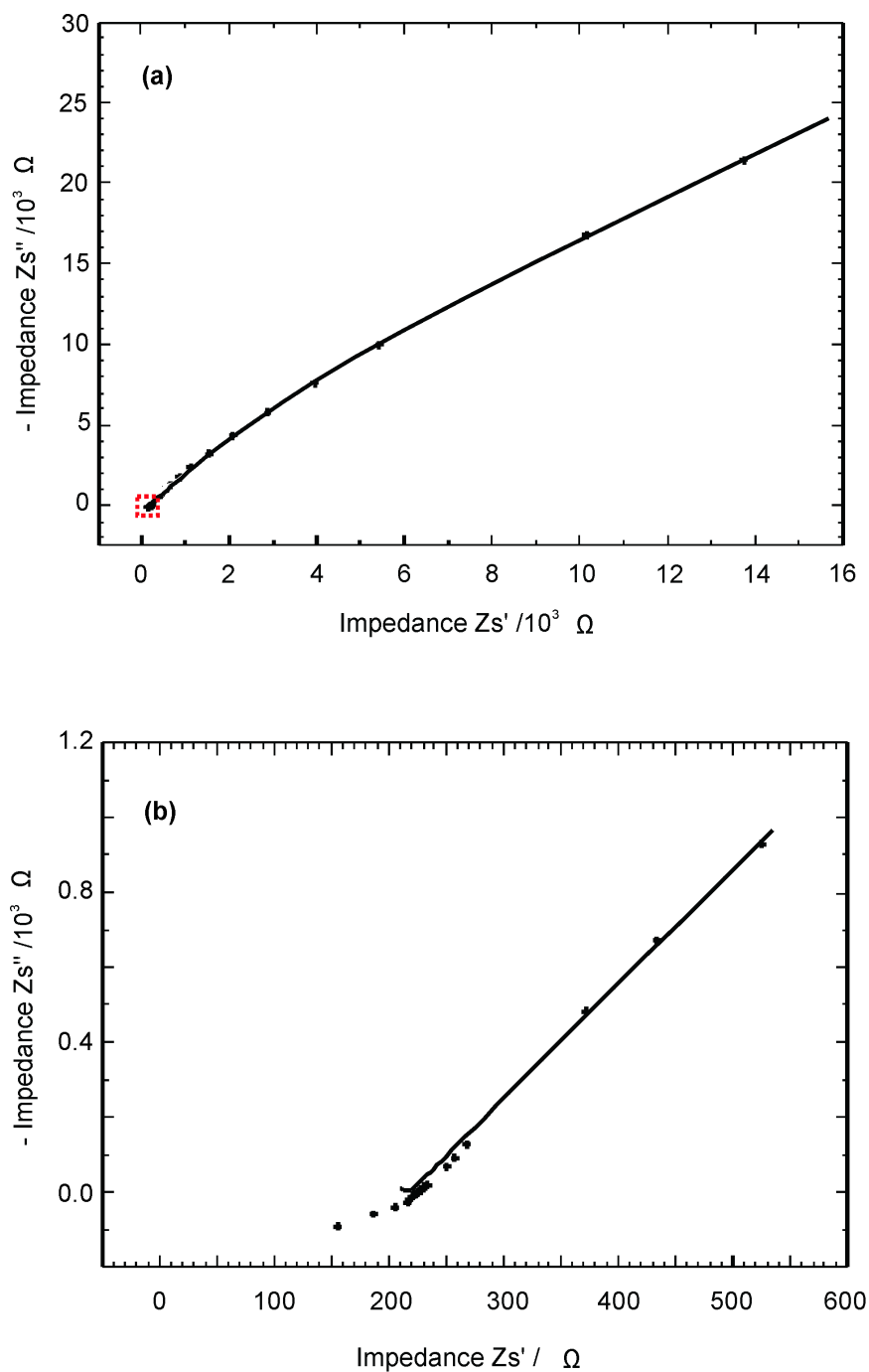
Figure 99: (a) Nyquist plot of $Na_3B_3O_3F_6$ with blocking gold electrodes at 350 °C, (b) enlarged view emphasizing the part framed by the red box in the Figure 99a. The experimental and the simulated impedance spectrum are represented with dots and the solid line, respectively.

At temperatures higher than 175 °C, the low frequency spike is replaced with a second semicircle. The Nyquist plot at 350 °C in Figure 99-a depicts the bulk conductivity along with the accompanied second semicircle. Figure 99-b also illustrates the Nyquist plot at 350 °C, however with an elaborate on the high frequency region consorted via the enlargement of the issued part. Hence, the interpretation is accomplished in the equivalent circuit via replacing the constant phase element with an additional R_2Q_2 element. Ergo, R_1Q_1 element is connected in series with the R_2Q_2 element in the equivalent circuit. The capacitance values of the second semicircle at different temperatures are $C \approx 3 \times 10^{-7}$ F, which then infers that the second semicircle could be as a result of a surface layer formed at higher temperatures or of the sample-electrode interface.
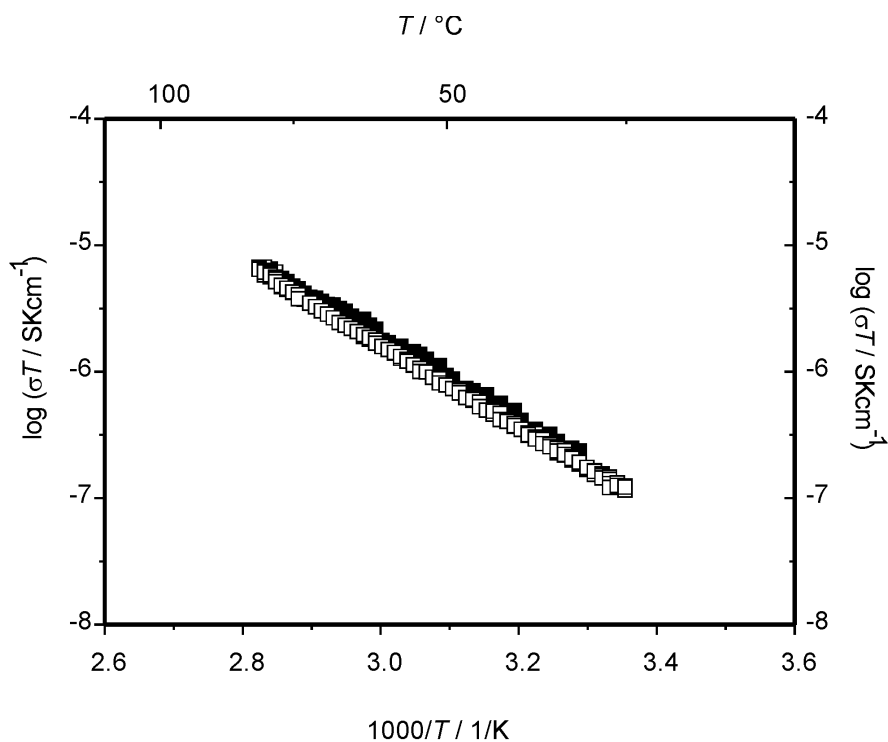
Figure 100: Temperature dependence of the ionic conductivities of $Na_3B_3O_3F_6$ with sodium electrodes. (Heating and cooling cycles are represented by filled and open symbols, respectively)

The ionic conductivities have also been analyzed by employing a cell composed of squeezing the sample between ion blocking sodium electrodes. The measurements have been conducted up to 80 °C. Temperature dependence of ionic conductivities are

sketched in an Arrhenius type of graph, which is displayed in Figure 100. The activation energies are derived from the slope of the conductivity curve by using the Arrhenius equation which appraises a value of 62 kJ mol^{-1} for both heating and cooling cycles. The evaluated ionic conductivity at 85 °C amounts to 2.2×10^{-8} S cm^{-1}.

The impedance data presented in the complex plane exhibits only one semicircle, as graphed in Figure 101, for all temperatures within the measurement is performed, and the fitting of data is performed by using a RQ element in the equivalent circuit. No low frequency spike is detected, which in turn proves that no barrier for the charge transfer has occured between the material and ion non-blocking sodium electrodes. The semicircle reveals an approximate capacitance value of 2.5×10^{-12} F, which is typical for the bulk capacitance. Hence, the semicircle is related with the sodium conductivity in the bulk.

5.3.8   Direct Current Measurements

The potentiostatic polarization measurements have been utilized in order to estimate the cationic and electronic transference numbers of the material. In dc measurements, the electrical current response has been monitored following a voltage step as can be discerned in Figure 102. The sodium transference numbers are evaluated by using a cell, in which the material has been squeezed between non-blocking sodium electrodes. Subsequently, the effective sodium transference numbers (t_{Na^+}) have been derived from the ratio of steady state current to the initial current. The cationic transference numbers are inferred as 1.0 at 55 °C and 0.91 at 77 °C. The values of t_{Na^+}, which approach to unity, manifest that the material is almost a pure sodium conductor.

In order to delineate the contribution of the electronic component to the conductivity, dc potentials have also been applied to the cell composed of squeezing the sample between ion blocking gold electrodes. Figure 103 depicts the results evaluated at 180 °C and 287 °C, which discloses smooth and gradual decays in the current. The effective electronic transference numbers (t_{el}) are calculated from the ratio of steady state current to the initial current. The t_{el} values are attained as 0.046 at 180 °C and 0.0016 at 287 °C. Hence, the electronic contribution to the conductivity is negligible as the electronic transference number values are very close to zero. The initial resistance in the dc measurement performed at 287 °C amounts to 3.9×10^4 Ω . While the ac measurements at the same temperature have been pointed out to a lower resistance value (1.1×10^3 Ω), which is in turn expected as a consequence of the associated steep negative slope at the onset of the dc measurement. The dc steady state conductivity

is also assessed in order to establish a comparison between ac and dc conductivities. The dc conductivity is deduced as 3.5×10^{-8} S cm^{-1} at 287 °C, which is rather on the order of 1/10000 that of the ionic conductivity evaluated from the ac impedance (4.2×10^{-4} S cm^{-1} at 287 °C).
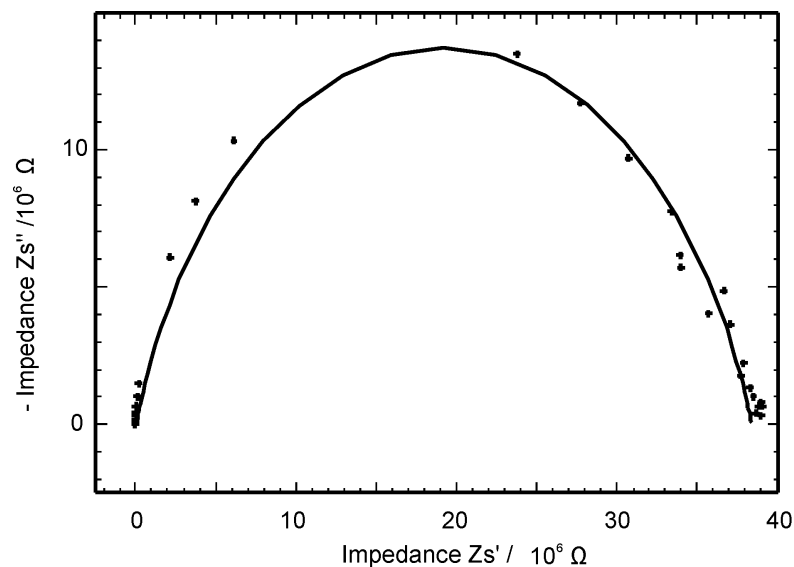
Figure 101: Nyquist plot of Na$_3$B$_3$O$_3$F$_6$ with sodium electrodes at 79 °C. The experimental and the simulated impedance spectrum are represented with dots and the solid line, respectively.

In consequence of direct current measurements performed via ion blocking gold as well as ion non-blocking sodium electrodes, it is attributed that Na$_3$B$_3$O$_3$F$_6$ is almost a pure sodium conductor.
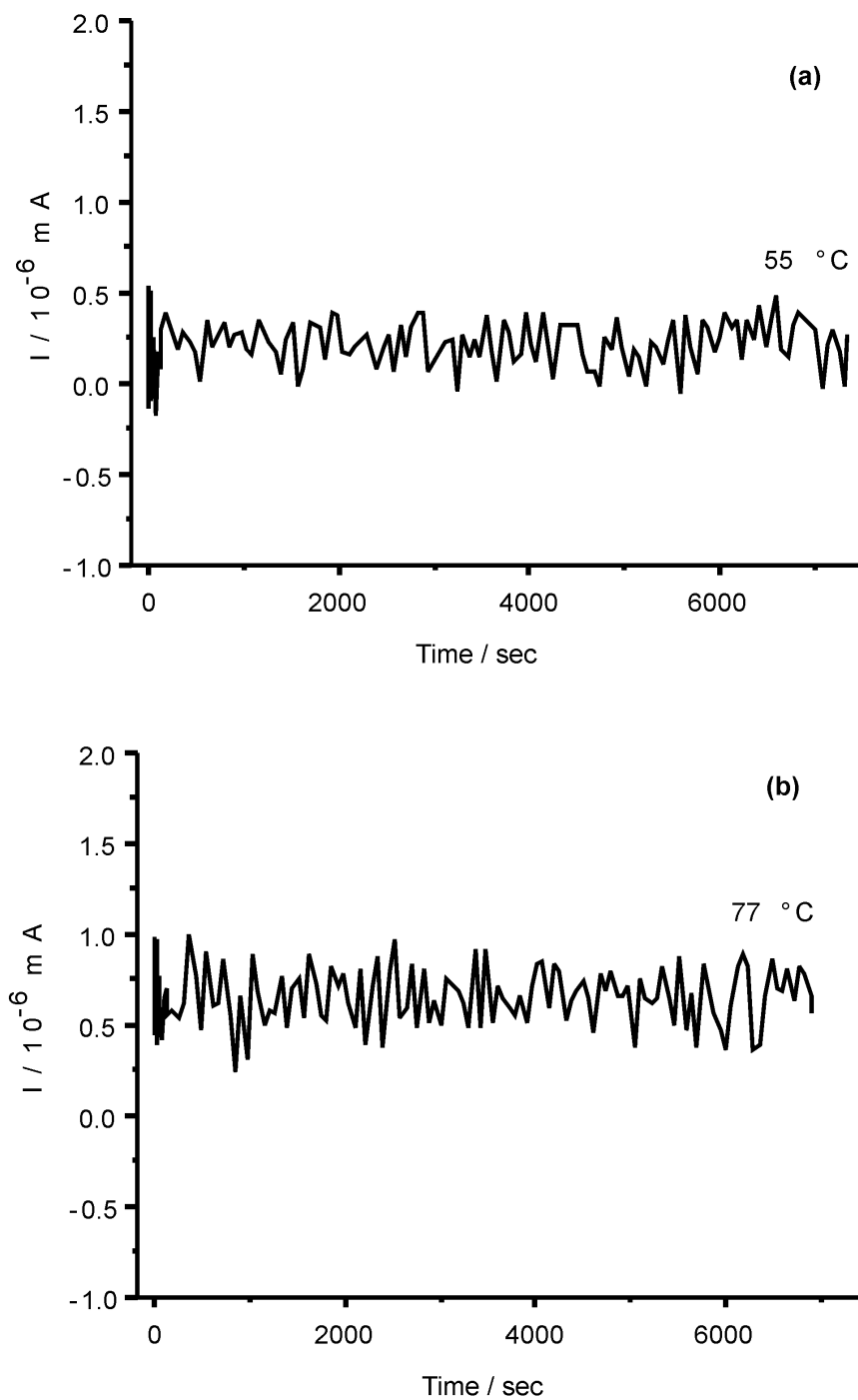
Figure 102: Electrical currents versus time for the cells composed of Na/ $Na_3B_3O_3F_6$/Na after switching on dc voltage at time zero at (a) 55 °C and (b) 77 °C.
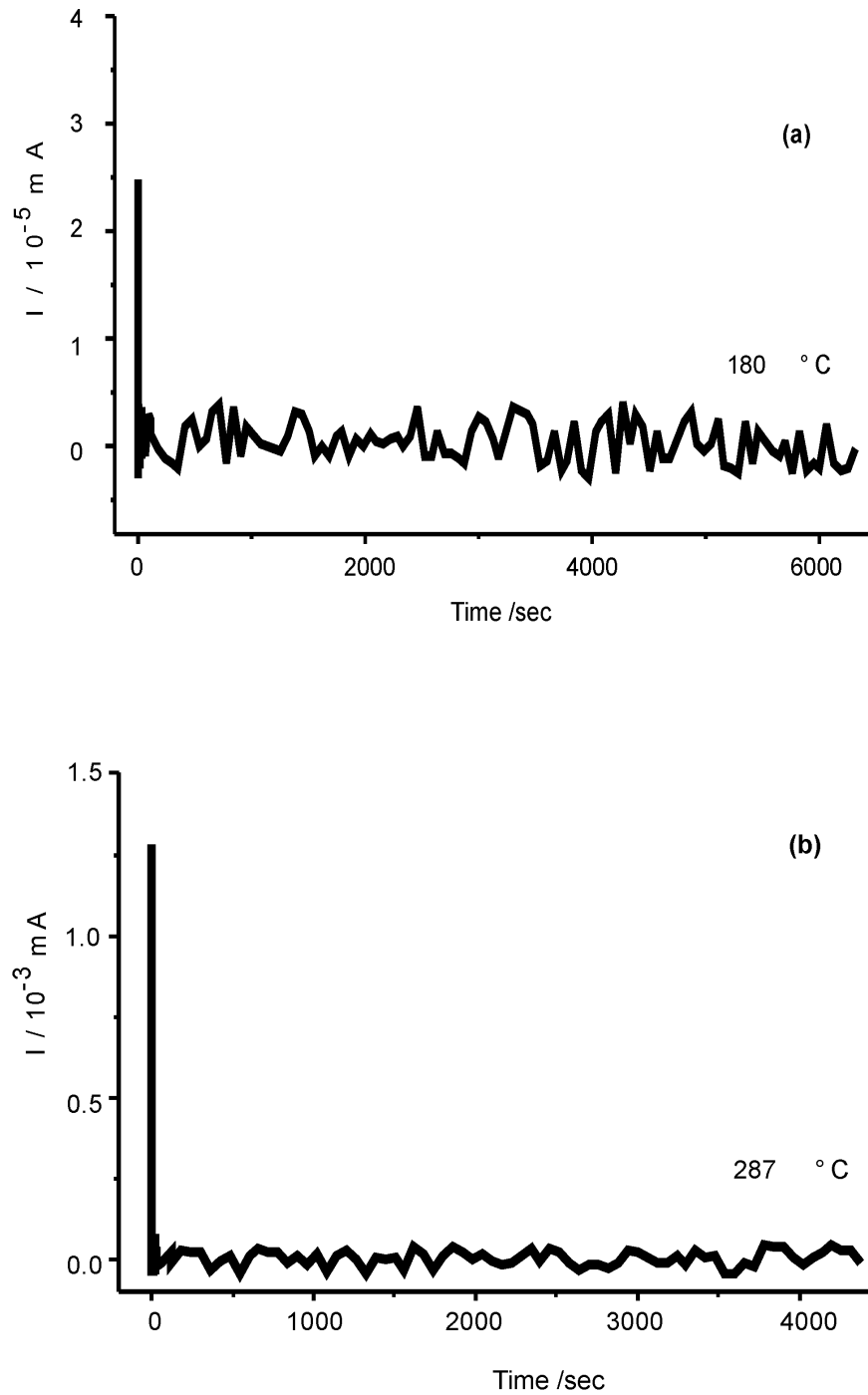
Figure 103:   Electrical currents versus time for the cells composed of Au/ $Na_3B_3O_3F_6$/Au after switching on dc voltage at time zero at (a) 180 °C and (b) 287 °C.

5.3.9   Conclusions

The $Na_3B_3O_3F_6$ has been synthesized and characterized successfully in both structural and electrochemical manners. Thus, it is represented here the crystal structure of the first sodium fluorooxoborate, namely the $Na_3B_3O_3F_6$. Besides, the structure is the unique example of an alkali fluorooxoborate within the exempt of LiB_6O_9F. The fundamental building unit of the $Na_3B_3O_3F_6$ comprises of unique corner sharing BO_2F_2 tetrahedra. Three of these tetrahedra solely then generate the hexafluorotriborate rings forming the repetition unit of the anion in the structure. The structure is composed of planar hexafluorotriborate rings forming the layers and sodium ions are located within these layers. This material can also be classified as a fast ion conductor, with an ionic conductivity of 3.6×10^{-3} S cm^{-1} at 350 ℃ and an activation energy for ionic conduction as 107 kJ mol^{-1} between 200 ℃ and 350 ℃. Furthermore, it is demonstrated via the direct current measurements that $Na_3B_3O_3F_6$ exhibits a pure sodium conductivity, with $t_+ = 1$ at 55 ℃ and $t_{el} = 0.0016$ at 287 ℃.

5.4 Potassium Fluorooxoborate, K$_3$B$_3$O$_3$F$_6$

5.4.1 Synthesis of K$_3$B$_3$O$_3$F$_6$

All reactions were carried out in a purified argon atmosphere using standard Schlenk techniques and glove boxes in rigorously dried reaction apparatus. The complete drying of the reactants were accomplished prior to the reactions. For this purpose, KBO$_2$ (purum, Fluka Analytical, UK) and KBF$_4$ (99.99%, Sigma-Aldrich, USA) were exposed upon vacuum for four days at 200 °C and 150 °C, respectively. Stoichiometric amounts of anhydrous KBO$_2$ and anhydrous KBF$_4$ were used in order to prepare the appropriate starting mixtures. The pellets, having 6 mm diamaters, were pressed from finely ground reactants, and then positioned inside gold crucibles, which in turn were sealed under argon atmosphere in glass ampoules. The reactions were carried out at 400 °C by following a specific temperature schedule composed of 48 hours heating from room temperature to 400 °C, 120 hours dwelling at 400 °C, and cooling down to the room temperature within 72 hours.

Resultingly, solving the structure of K$_3$B$_3$O$_3$F$_6$ from the powder data is inhibited since the powder pattern of this compound was highly overcrowded. Moreover, an appropriate crystal of K$_3$B$_3$O$_3$F$_6$ could not be picked up even though the product was further subjected for annealing to enhance the crystallinity. As a consequence possessing either bad quality or small size of crystals prevented to solve the structure from single crystal data. On the other hand, identification of the K$_3$B$_3$O$_3$F$_6$ has been performed from spectroscopy techniques by taking into account the similarities with the sodium analog (namely, Na$_3$B$_3$O$_3$F$_6$).

5.4.2 FT-IR Spectroscopy

FT-IR measurements were acquired in order to appoint the K$_3$B$_3$O$_3$F$_6$, as depicted in Figure 104. It is remarkable that the FT-IR spectrum of the K$_3$B$_3$O$_3$F$_6$ possesses the same vibrations assigned for the Na$_3$B$_3$O$_3$F$_6$ (see Figure 94), together with the accompanied matching in the corresponding intensities. Furthermore, the centers of all bands for K$_3$B$_3$O$_3$F$_6$ exhibit a shift to the lower wavenumbers in the spectrum if compared to the Na$_3$B$_3$O$_3$F$_6$.
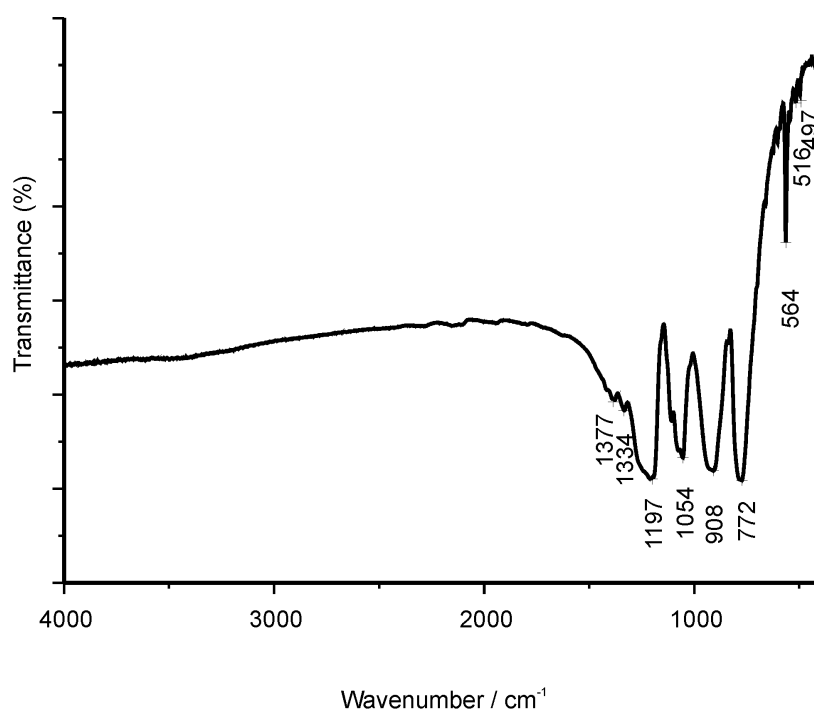
Figure 104: FT-IR spectrum of $K_3B_3O_3F_6$.

Table 43: FT-IR band positions and assignments of $K_3B_3O_3F_6$.

Wavenumber /cm^{-1}	Intensity	Assignments
1377−1334	w	ν (ring)
1210	s	ν (ring)
1054	s	ν (ring)
908	s	ν (ring)
772	s	ν (B—F)
564	m	δ (ring)
500−400	w	δ (B—O)

Resultingly, the band at 772 cm^{-1} is assigned for the B—F stretching vibrations. Moreover, the characteristic bands for the ring stretching vibrations of the fluorooxoborate ring appear at 908 cm^{-1}, 1054 cm^{-1} and 1197 cm^{-1}. Further assignments along with the intensities are given in Table 43.

Conclusively, the highly analogous behaviour among the IR bands in the new single phase potasium compound and $Na_3B_3O_3F_6$ is attributed that this compound is potassium analog of $Na_3B_3O_3F_6$, namely $K_3B_3O_3F_6$. This is in turn supported by the Raman measurements as will be reported in the next section.

5.4.3   Raman Spectroscopy

Raman spectrum of the $K_3B_3O_3F_6$ also reveals the congeneric vibrations like evaluated for the $Na_3B_3O_3F_6$ conforming the analogy in the corresponding IR spectra. The distinguishable sharp vibration appeared at 594 cm^{-1} manifests the presence of the fluorooxoborate ring also in the $K_3B_3O_3F_6$ compound connate to its sodium analog. The identified vibrations and assignments are given in Table 44. Consequently, the completely kindred peculiarities in IR and Raman spectra of the entitled compound to the $Na_3B_3O_3F_6$ attests that the attributed material is $K_3B_3O_3F_6$. Moreover, as a remark that Raman spectrum confirms the X-ray powder diffraction results hereof the sample is attained in a single phase via manifesting the consumption of all the reactants during the reaction, since neither KBF_4 (exhibiting a strong band at 775 cm^{-1} [235, 244]) nor KBO_2 (possessing the strongest vibration at 612 cm^{-1} [245]) is traced in the sample.

5.4.4   Thermal Analysis

Thermal stability of the $K_3B_3O_3F_6$ was assessed by using differential thermal analysis, thermal gravimetry and mass spectrum techniques simultaneously between ambient temperature and 1000 °C under argon flow and upon a 10 °C min^{-1} heating rate (Figure 106). The decomposition of the $K_3B_3O_3F_6$ is detected with an onset temperature at 421 °C and a peak maximum at 436 °C, as illustrated in the DTA thermogram. The decomposition proceeds without the detection of any volatile products abide by the unperceivable mass loss in the depicted TG thermogram.
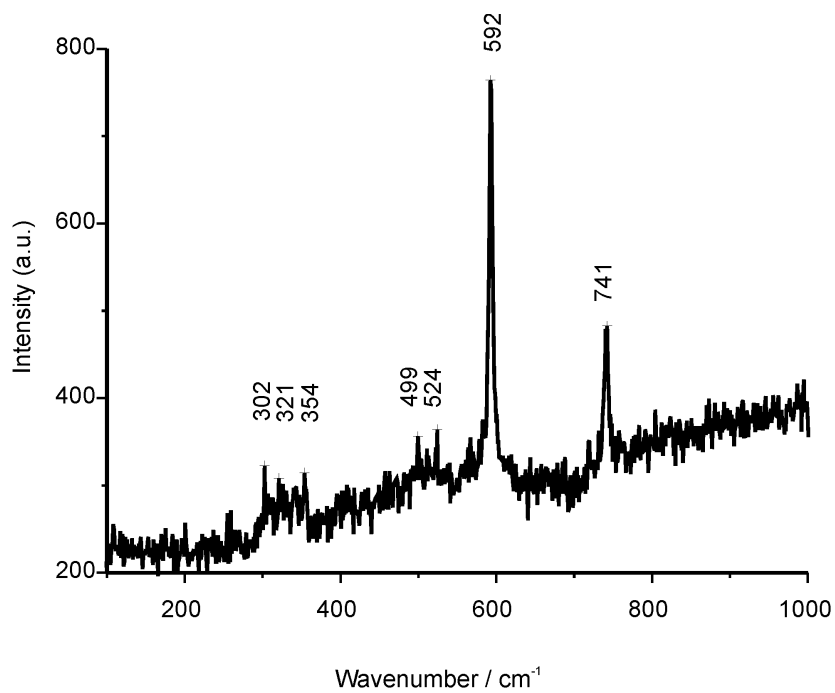
Figure 105: Raman spectrum of $K_3B_3O_3F_6$.

Table 44: Raman band positions and assignments of $K_3B_3O_3F_6$.

Wavenumber $/cm^{-1}$	Intensity	Assignments
741	s	ν (B—F)
592	vs	ν (ring)
524	w	δ (BO$_2$F$_2$)
499	w	δ (BO$_2$F$_2$)
354	w	δ (B—F)
321	w	ρ (B—F)
302	w	δ (ring)
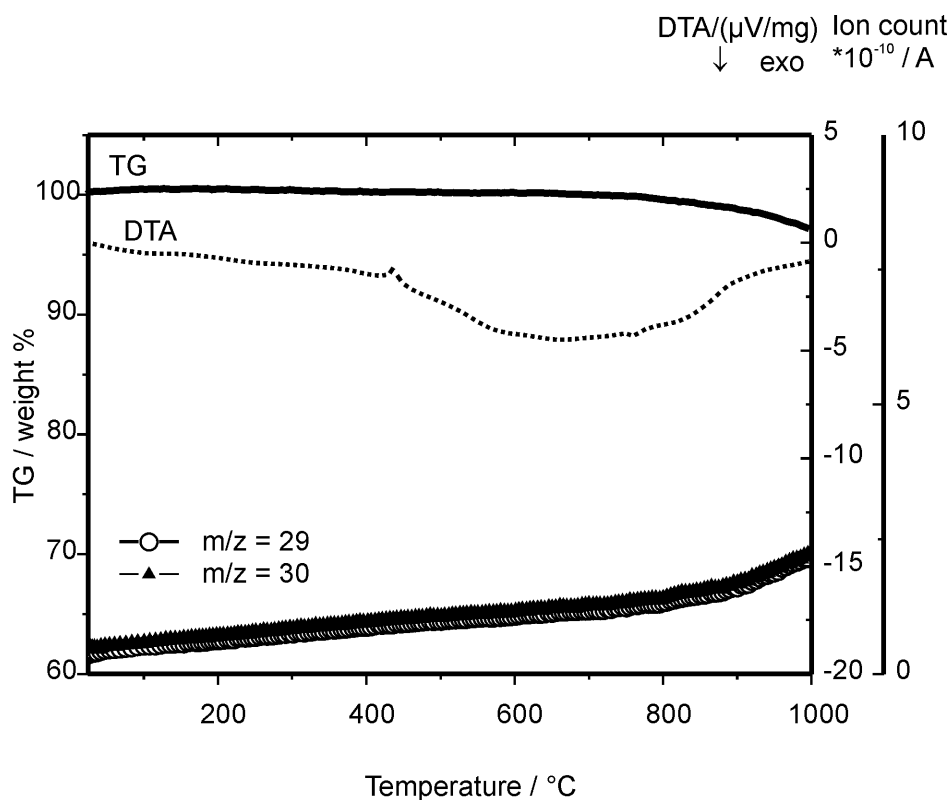
Figure 106: DTA/TG/MS thermograms of $K_3B_3O_3F_6$ in argon flow with a 10 °C min^{-1} heating rate.

The onset of the mass loss in the sample is discerned at 720 °C and only 3 % of the material is evolved onwards up to 1000 °C. The material possesses a ceramic yield of 97 % at 1000 °C, in turn, when compared to its sodium analog, $K_3B_3O_3F_6$ is distinguished with its higher ceramic yield. On the contrary to its sodium counterpart, neither BF_2 nor F species is evolved upon thermal treatment of the sample comprehended by the mass spectrum. Consequently, the distinction in the decomposition process is described for the $K_3B_3O_3F_6$ by contrast to its sodium analog. Rather, the decomposition of the $K_3B_3O_3F_6$ is espied by the evolution of the BF species, which is assessed by the mass spectroscopy with ^{10}BF (m/z = 29) and ^{11}BF (m/z = 30). Moreover, the decomposition of the potassium fluorooxoborate is originated at a higher temperature confronting with the sodium analog as well as the onset for the mass loss commences.

In order to investigate the thermal behaviour in detail, $K_3B_3O_3F_6$ was also subjected to DSC measurements up to 500 °C by 5 °C min^{-1} heating and cooling rates under

argon flow, as illustrated in Figure 107. A sharp endothermic peak is depicted with a peak maximum at 440 °C along with a shoulder possessing a peak maximum at 422 °C. The peak at 422 °C denotes the melting of the $K_3B_3O_3F_6$, and afterwards the decomposition is detected by conversion of the material into an amorphous phase at 440 °C. The last mentioned process is also observable by the formation of a new peak discerned at 125 °C in the cooling cycle. Thus, it represents a phase is formed upon heating up to 500 °C and manifests the decomposition of the $K_3B_3O_3F_6$, since this peak is not existed in the heating cycle (see Figure 107) as well as during the cycling of the $K_3B_3O_3F_6$ up to 350 °C (see Figure 108); the latter will be presented in Section 5.4.5. When a further cycle in DSC analysis has been performed after 500 °C, a new endothermic peak appears with an onset temperature of 201 °C possesing a peak maximum of 210 °C belonging to the decompositon product, which further affirms the decomposition of $K_3B_3O_3F_6$. The $K_3B_3O_3F_6$ sample has also been heat treated at 500 °C, and afterwards, analyzed via X-ray powder diffraction. KF reflections have been originated as a single phase, and no $K_3B_3O_3F_6$ reflections has been traced. Thus, according to these findings, the decomposition is proceeded by the formation of KF and companied with an amorphous phase. Andriiko et al. claimed that the melting point of the $K_3B_3O_3F_6$ is at 560 °C [213]. However, no peak could be observed at 560 °C from the DTA as well as from the DSC analyses that have been conducted both up to 1000 °C. Moreover, the obvious decomposition of the $K_3B_3O_3F_6$ is further proved from the described findings via the X-ray powder diffraction analysis.

5.4.5   Impedance Spectroscopy

Ionic conductivities of $K_3B_3O_3F_6$ were acquired by utilizing impedance spectroscopy measurements under argon flow within a range comprised of room temperature up to 360 °C. The heating and cooling rates were 1 °C min^{-1} and the sample in the form of a pellet was squeezed between gold electrodes for measurements. The temperature dependent bulk ionic conductivities are graphed in Arrhenius type diagrams as illustrated in Figure 109. The associated activation energies (E_a) are deduced from the slope of the conductivity curves by employing the Arrhenius equation. Both the activation energies and also the ionic conductivities at selected temperatures are assembled in Table 45.

A considerable increase in the ionic conductivity is recognized with the temperature, and the ionic conductivity curve is compiled of two different regimes which differentiates from each other with respect to their slopes. The conductivity at 150 °C is detected

as 4.5×10^{-10} S cm^{-1}. However, the steep slope positioning up to 275 °C accounts for a five-orders of magnitude increase in the conductivity and a value of 4.2×10^{-5} S cm^{-1} is retrieved at 275 °C. Then, a change in the slope of the Arrhenius plot is discerned at 275 °C. Eventually, onwards this temperature, the material exhibits a higher ionic conductivity and it reaches to 1.2×10^{-4} S cm^{-1} at 360 °C. When the comparison is performed between sodium and potassium fluorooxoborates, it is depicted that the potassium compound does not exhibit as high ionic conductivity as the sodium counterpart represents. On the other hand, $K_3B_3O_3F_6$ can also be classified as a fast-solid ion conductor at temperatures higher than 275 °C, and moreover, this high conductivity is accompanied with a flatten slope of 46 kJ mol^{-1}. In this temperature regime, a contribution of one order of magnitude increase in the conductivity is recognized. A highly reversible conductivity values are attained upon heating and cooling cycles. Furthermore, when the material is analyzed with the X-ray powder diffraction following the impedance measurements, completely same material is recovered. In order to
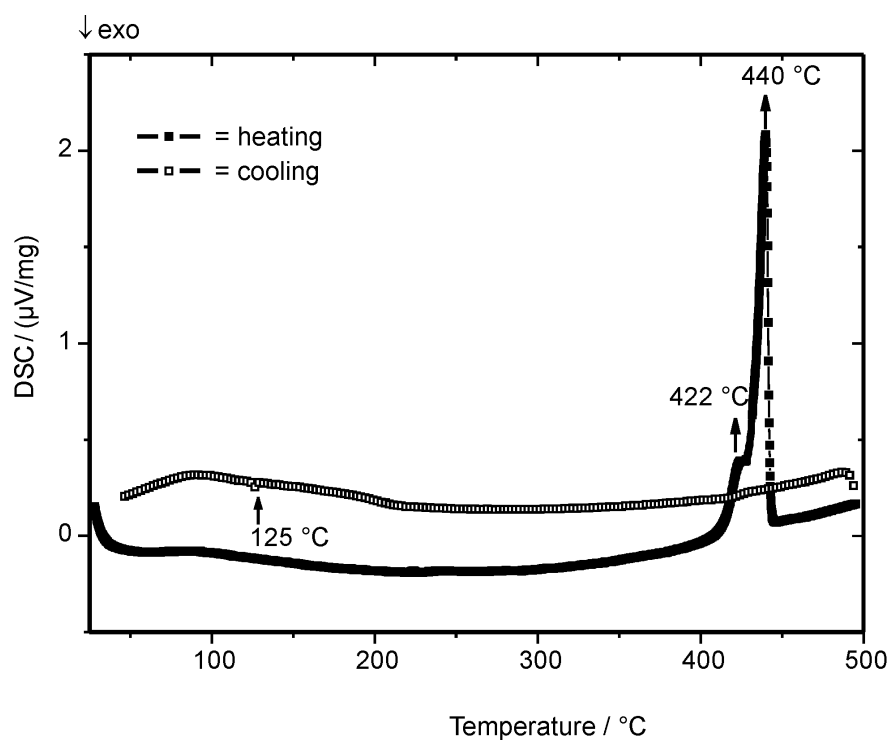
Figure 107:   DSC thermograms of $K_3B_3O_3F_6$ in argon flow with 5 °C min^{-1} heating and cooling rates up to 500 °C.

grasp whether the material reveals a phase transition during heating or not, the material is further analyzed by DSC measurements from room temperature up to 350 °C under argon flow, as depicted in Figure 108. Resultingly, as already discussed in Section 5.4.4, no noticable transition is distinguished within the temperature range that impedance measurements are performed and thus no conclusive evidence for a phase transition is appeared.
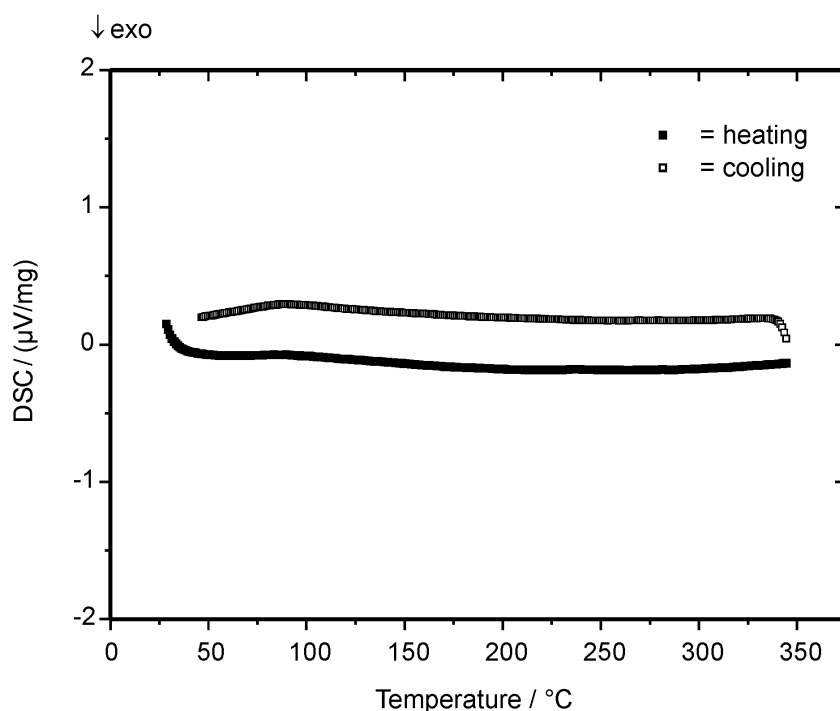
Figure 108: DSC thermogram of $K_3B_3O_3F_6$ with 5 °C min^{-1} heating and cooling rates up to 350 °C.

$K_3B_3O_3F_6$ reveals two semicircles in the complex plane format up to 165 °C. The interpretation of the impedance data was proceeded via utilizing a parallel R_1Q_1 element representing the first semicircle, and this element was further connected in series with another RQ element, namely R_2Q_2, to account the second semicircle in the equivalent circuit. A low frequency spike was discerned at higher temperatures displaying the barrier for the transfer of the charge between the sample and ion-blocking gold electrodes. In order to expound the spike, a supplemental constant phase element, Q_{el}, was inclosed in the equivalent circuit in series with the other RQ elements. In order to elucidate the response of the material, the capacitance values originating from both of
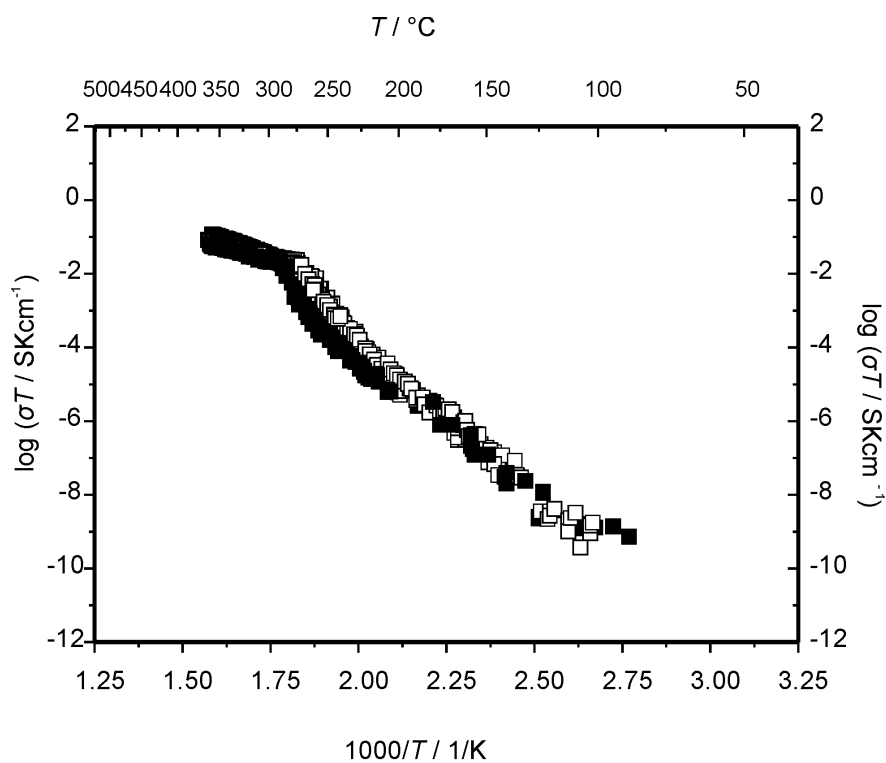
Figure 109:   Temperature dependence of the ionic conductivities of $K_3B_3O_3F_6$ with gold electrodes. (Heating and cooling cycles are represented by filled and open symbols, respectively.)

Table 45:   Activation energies and ionic conductivity values at different temperatures for $K_3B_3O_3F_6$.

σ /S cm^{-1}	E_a /kJ mol^{-1}
1.1×10^{-4} (350 °C)	46 (275 °C–360 °C)
4.0×10^{-6} (250 °C)	173 (25 °C–275 °C)
4.5×10^{-10} (150 °C)	

the semicircles were calculated using the relation of $C = Q^{1/n} \times R^{(1/n)-1}$. According to the ensued results of the capacitance values, the semicircle appearing at higher frequencies possesses an approximate value of 5×10^{-12} F. Therefore, the high frequency semicircle is attributed to the bulk resistance of the $K_3B_3O_3F_6$.
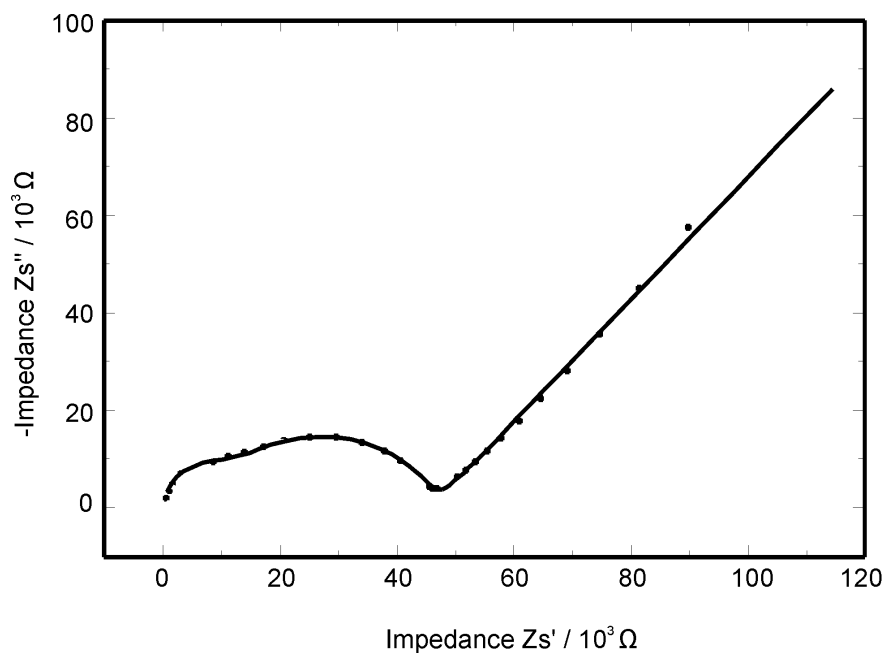
Figure 110: Nyquist plot of $K_3B_3O_3F_6$ with gold electrodes at 287 °C. The experimental and the simulated impedance spectrum are represented with dots and the solid line, respectively.

5.4.6   Direct Current Measurements

In order to estimate the contribution of the electronic component to the conductivity, $K_3B_3O_3F_6$ was analyzed via direct current measurements conducted by means of monitoring the electrical current response after a voltage step, as illustrated in Figure 111. The electronic contribution to the conductivity has been evaluated via using a cell which assembled from squeezing the sample between ion blocking gold electrodes. The ratio of steady state current to the initial current has been used to calculate the effective electronic transference number of the $K_3B_3O_3F_6$. Smooth and gradual decays are recognized as depicted in Figure 111. The effective electronic transference number (t_{el}) is calculated as 0.0025 at 185 °C. Therefore, it points out that the electronic con-

tribution to the conductivity is negligible as the electronic transference number reveals
a value that amounts almost close to zero.
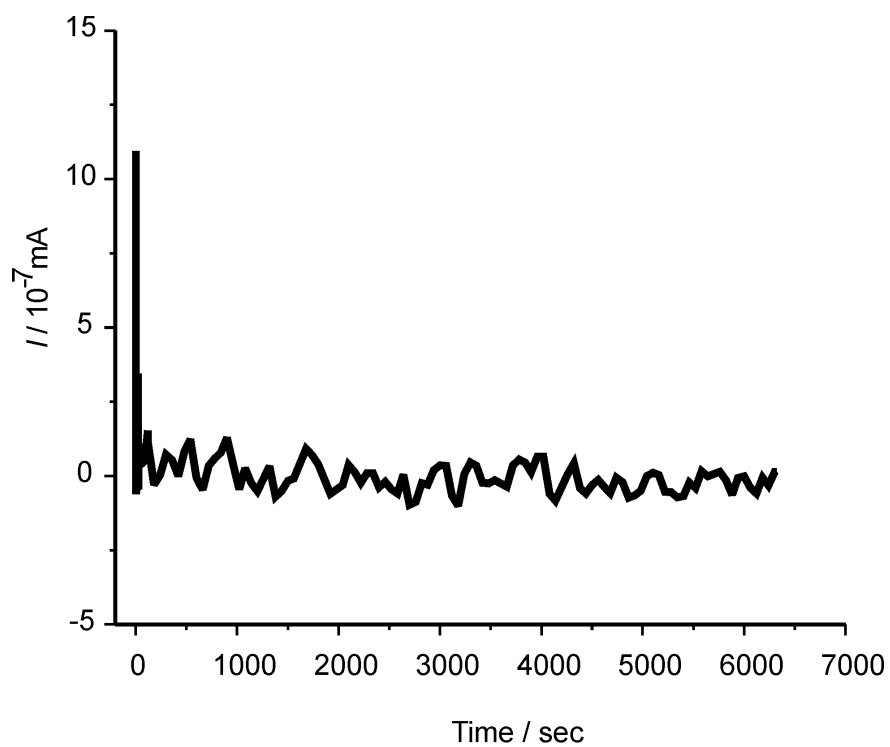
Figure 111: Electrical currents versus time for the cell $Au/K_3B_3O_3F_6/Au$ after switch-
ing on dc voltage at time zero at 185 °C.

5.4.7   Conclusions

$K_3B_3O_3F_6$ has been synthesizesd from anhydrous KBO_2 and KBF_4 at 400 °C by solid state reaction. The thermal investigations reveal that $K_3B_3O_3F_6$ decomposes at 440 °C into an amorphous phase and KF. The complete similarities of the titled compound with the $Na_3B_3O_3F_6$ have been deduced from the spectroscopical investigations, verifying that the structure of the $K_3B_3O_3F_6$ also consists of hexafluorotriborate rings connate to its sodium analog. The material exhibits an ionic conductivity of 1.2×10^{-4} S cm^{-1} at 360 °C and an accompanied activation energy between 275 °C and 350 °C as 46 kJ mol^{-1}. Moreover, negligible electronic contribution to the ionic conductivity is observed since t_{el} is found as 0.0025 at 185 °C. Thus, $K_3B_3O_3F_6$ can be classified as a fast-solid ion conductor, although the attained ionic conductivity does not reach to its sodium analog.

6 Summary

Polyelectrolytes

The polyelectrolytes studied in the present work are divided into two general groups, namely poly(lithium organylborylborates) and poly[lithium tris(tetraethylenesilyl)organylborates]. The representative polymers have been synthesized for each group, which have further been modified with incorporation of various organyl lithium compounds.

Such representative polymer for poly(lithium organylborylborates) is poly[lithium tetrakis(ethyleneboryl)borate], PLEB. This polymer has been reacted with RLi reagents, where R denotes for methyl or phenyl. All the polymers of poly(lithium organylborylborates) have been further annealed and the effect of annealing on the structure and the ionic conductivity have additionally been investigated. Analogously, the representative polymer for poly[lithium tris(tetraethylenesilyl)organylborates] is poly[tris(tetraethylenesilyl)borane], PESB, which has further been reacted with RLi reagents, where R is phenyl, n-butyl or t-butyl. The PLEB polymer has been synthesized through a hydroboration reaction between lithium tetravinylborate and $BH_3 \cdot$ THF, whereas the PESB polymer has been prepared through a hydroboration reaction of tetravinylsilane with $BH_3 \cdot S(CH_3)_2$.

Amorphous nature of all these polyelectrolytes has been deduced by powder X-ray analysis. Structural properties have been studied via FT-IR and solid-state NMR spectroscopy techniques. Elemental analyses have been performed to characterize the chemical compositions. Thermal properties have been investigated by DTA/TG/MS analysis. Ionic conductivities of these polyelectrolytes have been analysed by impedance spectroscopy.

Poly(lithium organylborylborates)

Novel alkylborane-type single ionic solid polyelectrolytes have been prepared with immobilized anions, reduced ion trapping and a lithium transference number close to one in this thesis. Even though poly[lithium tetrakis(ethyleneboryl)borate] (PLEB) is

a polyelectrolyte, it has additionally been served as a starting material for the other poly(lithium organylborylborates). According to results from FT-IR, solid-state NMR and DTA/TG/MS analyses, the main structural building blocks of the poly[lithium tetrakis(ethyleneboryl)borate] (PLEB) has been determined to contain mainly tetraethylene borate and hydrogen-bridged borane units, which are connected through ethylene linkages. In these three dimensional network, lithium atoms are compensated by the negative charge on the borate units. The ionic conductivities and structures have been analyzed along with the effect of annealing, which has been performed at 275 °C. Annealing of the PLEB polymer reveals that the main building blocks and connectivity of the structure for the polymer have been remained the same but minor amount of vinyl groups have additionally been observed. The activation energy of the ionic conduction was lower for the annealed PLEB polymer (70 kJ mol^{-1}) as compared to the as-synthesized PLEB polymer (145 kJ mol^{-1}). The temperature induced crosslinking by annealing modifies the structure along with increasing the charge carrier concentration. Most salts and linear or crosslinked networks which were investigated in the literature have the cationic transference number in the range of 0.3 to 0.5. In contrast, poly[lithium tetrakis(ethyleneboryl)borate] is a pure lithium conductor having t$_+$ value of 1.0(2) at 137 °C.

Incorporation of phenyllithium into PLEB polymer (which is poly[lithium tetrakis-(triethylenephenylboryl)borate], PLEPB) increases the ionic conductivity values (i.e. 3×10^{-7} S cm^{-1} for PLEB and 2.2×10^{-6} S cm^{-1} for PLEPB at 80 °C) both for the as-synthesized and annealed PLEB polymers, while no significant improvement in activation energies (145 kJ mol^{-1} for PLEB and 146 kJ mol^{-1} for PLEPB) is emerged. In addition to the main structural units of the PLEB polymer, a new building block has been identified from the combination of performed analyses, which is a four coordinated borate unit substituted by three ethylene and one phenyl in PLEPB polymer. Moreover, incorporation of methyllithium into PLEB polymer (which is poly[lithium tetrakis(triethylenemethylboryl)borate], PLEMB) has also been examined, and among these polyelectrolytes, the highest conductivity has been obtained for the annealed PLEMB as 3.2×10^{-5} S cm^{-1} at 350 °C. In all cases, annealing decreases the activation energies.

Poly[lithium tris(tetraethylenesilyl)organylborates]

Analogous to polyelectrolytes based on poly[lithium tetrakis(ethyleneboryl)borates], various lithium conducting polyelectrolytes have been synthesized by reacting poly[tris-(tetraethylenesilyl)borane] (PESB) polymer with phenyl- , n-butyl- and t-butyllithium,

which are poly[lithium tris(tetraethylenesilyl)phenylborate] (PLESPB), poly[lithium tris(tetraethylenesilyl)n-butylborate] (PLESnBB) and poly[lithium tris(tetraethylenesilyl)t-butylborate] (PLEStBB), respectively. Compared to the polyelectrolytes based on poly[lithium tetrakis(ethyleneboryl)borates], all of the polyelectrolytes based on poly[tris (tetraethylenesilyl)borane] have lower ionic conductivities, which is most probably resulted from increase in hopping distances and decrease in charge carrier concentration of lithium ions due to incorporation of tetraalkylsilane groups between borate groups in the polymer networks.

Alkali Fluorooxoborates

Lithium Fluorooxoborate, LiB_6O_9F

An all-solid state reaction between LiF and B_2O_3 at 400 °C has been applied for the synthesis of crystalline LiB_6O_6F. This work presents the first crystal structure analysis of an alkali fluorooxoborate. LiB_6O_6F crystallizes in the orthorhombic space group $Pna2_1$ with lattice parameters $a = 7.6555(1)$ Å, $b = 8.5318(1)$ Å and $c = 10.7894(2)$ Å. The structure of LiB_6O_6F contains a pair of boroxine rings, which are connected via a bridging oxygen atom constituting the basic building unit of the fluorooxoborate anion. Moreover, fluoride ion is bonded to one of the boroxine rings. The fluorooxoborate anions form two-dimensional corrugated sheets, whereas lithium cations are embedded between the layers.

DTA/TG/MS analysis has shown that LiB_6O_6F has almost no weight loss up to 470 °C and only 8 % of the initial mass is exhausted at 1000 °C under argon atmosphere. The activation energy for ionic conduction amounts to 160 kJ mol^{-1} and according to the ionic conductivity measurements deduced by impedance spectroscopy, this material can be classified as a solid electrolyte with a lithium ion conductivity of 6.6×10^{-9} S cm^{-1} at 400 °C.

Sodium Fluorooxoborate, $Na_3B_3O_3F_6$

Crystalline $Na_3B_3O_3F_6$ has been synthesized by reacting H_3BO_3 and $NaBF_4$ at 350 °C. The crystal structure of this compound is a unique example of a fluorooxoborate anion with alkali ions (besides LiB_6O_9F). As well, it is the first crystal structure known

which is composed solely from BO_2F_2 tetrahedra. Herein, the hexafluoro derivation of the boroxine ring, namely $B_3O_3F_6{}^{3-}$ anion, is also manifested. $Na_3B_3O_3F_6$ crystallizes in the monoclinic space group $C2/c$ with lattice parameters $a = 11.866(7)$ Å, $b = 6.901(4)$ Å, $c = 9.367(6)$ Å, $\beta = 113.724(9)°$. Two fluorine atoms are coordinated with each boron atom forming BO_2F_2 tetrahedral units. The basic building unit of the structure is a six-membered hexafluorotriborate ring with constitution of $B_3O_3F_6{}^{3-}$. The $B_3O_3F_6{}^{3-}$ anions form a layered structure and sodium cations are located in space between these layers.

$Na_3B_3O_3F_6$ has been characterized by single crystal X-ray analysis, FT-IR, Raman, DTA/TG/MS, DSC, direct current measurements and impedance spectroscopy techniques. Direct current measurements at 55 °C yield t_+ as 1, and at 287 °C reveal t_{el} as 0.0016; in turn confirming that $Na_3B_3O_3F_6$ is a pure sodium conductor. The compound has a sodium ion conductivity of 3.6×10^{-3} S cm^{-1} at 350 °C and an activation energy for ion conduction as 107 kJ mol^{-1} between 200 °C and 350 °C. Hence, $Na_3B_3O_3F_6$ can be classified as a fast ion conductor.

Potassium Fluorooxoborate, $K_3B_3O_3F_6$

Crystalline $K_3B_3O_3F_6$ has been synthesized by a solid-state reaction between anhydrous KBO_2 and KBF_4 at 400 °C. Based on the full characterization of $Na_3B_3O_3F_6$ (which is analogous to the titled compound) in this work by single crystal analysis and spectroscopic techniques, the complete similarity in the spectroscopic analyses between these two analogous compounds manifests the structure of $K_3B_3O_3F_6$. Conclusively, the structure of $K_3B_3O_3F_6$ is proven to compose of six-membered hexafluorotriborate rings of the $B_3O_3F_6{}^{3-}$ anions, in which two fluorine atoms are coordinated to each boron atom, forming BO_2F_2 tetrahedral units in a similar manner to the $Na_3B_3O_3F_6$ analog. $K_3B_3O_3F_6$ can also be classified as a fast ion conductor since it exhibits an ionic conductivity of 1.2×10^{-4} S cm^{-1} at 350 °C, and a negligible electronic contribution is observed.

7 Zusammenfassung

Polyelektrolyte

Die Polyelektrolyte, die im Rahmen dieser Arbeit untersucht wurden, lassen sich in zwei Gruppen einteilen, nämlich Poly-Lithium-organylborylborate und Poly-Lithium-tris(tetraethylensilyl)organylborate. Repräsentatives Polymer synthetisiert, welches durch den Einbau verschiedener Lithiumorganyle modifiziert wurde.

Ein repräsentatives Polymer für Poly-Lithium-organylborylborate ist beispielsweise Poly-Lithium-tetrakis(ethylenboryl)borat, PLEB. Dieses Polymer wurde mit Lithiumorganylen RLi, mit R = Methyl, Phenyl, umgesetzt. Alle Polymere auf Poly-Lithium-organylborylborate Basis wurden getempert und der Einfluß des Temperns auf die Struktur und Ionenleitfähigkeit wurde untersucht. Entsprechend wurde das für Poly-Lithium-tris(tetraethylensilyl)organylborate repräsentative Polymer Poly-tris(tetraethylensilyl)boran, PESB, mit Lithiumorganylen RLi (R = Phenyl, n-Butyl oder t-Butyl) umgesetzt. PLEB wurde durch Hydroborierung von Lithium-tetravinylborat mit $BH_3 \cdot$ THF hergestellt, wohingegen PESB durch Hydroborierung von Tetravinylsilan mit $BH_3 \cdot S(CH_3)_2$ synthetisiert wurde.

Die amorphe Struktur all dieser Polymere wurde durch Pulverdiffraktometrie nachgewiesen und die strukturellen Eigenschaften dann mittels FT-IR und Festkörper-NMR Spektroskopie näher untersucht. Die chemische Zusammensetzung der Polymere wurde durch Elementaranalysen bestimmt. Die thermischen Eigenschaften wurden mittels DTA/TG/MS -Analysen und die Ionenleitfähigkeit dieser Polyelektrolyte mit Hilfe der Impedanzspektroskopie untersucht.

Poly-Lithium-organylborylborate

Im Rahmen dieser Arbeit wurden neuartige feste Polyelektrolyte auf Alkylboranbasis, mit immobilisierten Anionen, verringertem Ioneneinfang und einer Lithiumionenüberführungszahl von nahe eins realisiert. Obwohl Poly-Lithium -tetrakis(ethylenboryl)borat (PLEB) selbst ein Polyelektrolyt ist, wurde es auch als Startmaterial für andere Poly-Lithium-organylborylborate eingesetzt. Den Ergebnissen der FT-IR-, Festkörper-NMR- und DTA/TG/MS- Analysen zufolge, enthält der wichtigste Strukturbaustein

von PLEB hauptsächlich Tetraethylenborat und über Wasserstoffbrückenbindungen
verknüpfte Boraneinheiten, welche über Ethylenbrücken miteinander verbunden sind.
In diesem dreidimensionalen Netzwerk wird die positive Ladung der Lithiumionen
durch Boratanionen ausgeglichen. Die Strukturen, die Ionenleitfähigkeit dieser Verbin-
dungen, sowie der Effekt des Temperns - in diesem Fall bei 275 °C - wurde untersucht.
Nach dem Tempern des PLEB Polymers bleiben die Hauptbausteine und deren Kon-
nektivität erhalten, wobei die Bildung einer geringen Zahl an Vinylgruppen beobachtet
wurde. Die Aktivierungsenergie der Ionenleitung war für das getemperte Polymer
(70 kJ mol^{-1}) geringer als für ungetemperte Proben (145 kJ mol^{-1}). Die durch das
Tempern induzierte Vernetzung verändert die Struktur des Polymers was zu einer Er-
höhung der Ladungsträgerkonzentration führt. Die meisten Salze und lineare oder
vernetzte Netzwerke, die in der Literatur beschrieben werden, weisen Kationentrans-
ferzahlen zwischen 0.3 und 0.5 auf. Im Gegensatz dazu beträgt t_+ von Poly-Lithium-
tetrakis(ethylenboryl)borat, einem reinen Lithiumionenleiter, 1.0(2) bei 137 °C.

Der Einbau von Phenyllithium in das PLEB Polymer zur Bildung von Poly-Lithium-
tetrakis(triethylenphenylboryl)borat (PLEPB) führt zu einer Erhöhung der Ionenleit-
fähigkeit (3 x 10^{-7} S cm^{-1} für PLEB und 2.2 x 10^{-6} S cm^{-1} für PLEPB bei 80 °C),
sowohl des unbehandelten als auch des getemperten PLEB Polymers, eine signifikante
Verbesserung der Aktivierungs-energien (145 kJ mol^{-1} für PLEB und 146 kJ mol^{-1}
für PLEPB) wird hierbei nicht beobachtet. Zusätzlich zum Hauptbaustein des PLEB
Polymers, wurde durch Kombination der Ergebnisse ein neuartiger Baustein identi-
fiziert der aus vierfach koordinerten Boratbaueinheiten bestehend aus drei Ethylen-
und einem Phenylliganden aufgebaut ist.

Darüberhinaus wurde auch der Einbau von Methyllithium in PLEB untersucht
(Poly-Lithium-tetrakis(triethylenmethylboryl)borat, PLEMB). Die größte Ionenleit-
fähigkeit für diese Art von Polyelektrolyten wurde bei getempertem PLEMB erhalten,
sie beträgt 3.2 x 10^{-5} S cm^{-1}. In allen Fällen verringert Tempern die Aktivierungsen-
ergie.

Poly-Lithium-tris(tetraethylensilyl)organylborate

Analog der Synthese von Polyelektrolyten auf Basis von Poly-Lithium-(tetrakisethylen-
boryl)borate wurden verschiedene lithiumionenleitende Polyelektrolyte durch Umset-
zung von Poly-tris(tetraethylensilyl)boran (PESB) Polymer mit Phenyl-, n-Butyl- und
t-Butyllithium dargestellt (Poly-Lithium-tris(tetraethylensilyl)phenylborat (PLESPB),
Poly-Lithium-tris(tetraethylensilyl)n-butylborat (PLESnBB) bzw. Poly-Lithium-tris-
(tetraethylensilyl)t-butylborat (PLEStBB)). Verglichen mit den Polyelektrolyten auf

Basis von Poly-Lithium-tetrakis(ethylenboryl)borate weisen alle auf Poly-tris(tetraet-hylensilyl)boran Basierenden Polyelektrolyte eine geringere Ionenleitfähigkeit auf. Dies rührt wahrscheinlich von einer Vergrößerung der Sprungdistanz und einer Abnahme der Ladungsträgerkonzentration der Lithiumionen durch den Einbau von Tetraalkylsilan-gruppen zwischen den Boratanionen innerhalb des Polymernetzwerks her.

Alkali Fluorooxoborat

Lithium Fluorooxoborat, LiB_6O_9F

Zur Darstellung von kristallinem LiB_6O_6F wurde eine Festkörperreaktion mit LiF und B_2O_3 bei 400 °C durchgeführt. In dieser Arbeit ist es erstmals gelungen, eine Einkristallstruktur eines Alkali-Fluorooxoborates erfolgreich zu lösen. LiB_6O_6F kristal-lisiert in der orthorhombischen Raumgruppe $Pna2_1$ mit dem Gitterparametern $a = 7.6555(1)$ Å, $b = 8.5318(1)$ Å und $c = 10.7894(2)$ Å. Die Struktur von LiB_6O_6F ent-hält ein Paar von Boroxin-Ringen, die über ein Sauerstoffatom miteinander verknüpft sind. Außerdem ist das Fluorid-Ion an eines der beiden Boroxinringe gebunden. Die Fluorooxoboratanionen binden zweidimensional gewölbte Schichten, in denen das Lithi-um zwischen den einzelnen Lagen eingebettet ist.

In DTA/TG/MS Untersuchungen (Argonatmosphäre) zeigt LiB_6O_6F beim Aufheiz-en bis 470 °C keinen erkennbaren Massenverlust, erst beim Erhitzen auf 1000 °C wird ein Massenverlust von 8 % beobachtet.

Die Aktivierungenergie für die Ionenleitung beträgt 160 kJ mol^{-1} und wurde aus der Impedanzspektroskopie bestimmt. Die Lithiumionen-Leitfähigkeit beträgt 6.6×10^{-9} S cm^{-1} bei 400 °C. Durch diese Ergebnisse kann die Verbindung in die Klasse der Festkörperelektrolyten eingestuft werden.

Natrium Fluorooxoborat, $Na_3B_3O_3F_6$

$Na_3B_3O_3F_6$ wurde bei der Reaktion von H_3BO_3 and $NaBF_4$ bei 350 °C erhalten. Die Verbindung stellt neben LiB_6O_6F die einzige Struktur dar, die aus Fluorooxoboratanio-nen und Alkaliionen gebildet wird. Auserdem ist es die erste bekannte Kristallstruktur, deren anionische Trimere ausschließlich aus BO_2F_2 Tetraedern aufgebaut sind. In der Struktur sind die einzelnen Tetraeder zu $B_3O_6F_6{}^{3-}$-Anionen kondensiert. $Na_3B_3O_3F_6$

kristallisiert in der monoklinen Raumgruppe $C2/c$ mit den Gitternparametern $a =$ 11.866(7) Å, $b = 6.901(4)$ Å, $c = 9.367(6)$ Å, $\beta = 113.724(9)°$. Bor ist in den BO_2F_2 Tetraedern direkt an zwei Fluoratome koordiniert. Die grundlegende Baueinheit der Kristallstruktur ist der oben genannte sechsgliedrige Hexafluorotriborat-Ring mit der Zusammensetzung $B_3O_6F_6{}^{3-}$. Die $B_3O_6F_6{}^{3-}$-Anionen bilden Schichten mit Natrium-Kationen in den Zwischenräumen. $Na_3B_3O_3F_6$ wurde mittels Röntgenstrukturanalyse, DTA/TG/MS-Messungen, FT-IR, Raman- und Impedanzspektroskopie untersucht und charakterisiert. In Gleichstromleitfähigkeits messungen ergab sich bei einer Temperatur von 55 °C ein Wert von $t_+ = 1$. Der Anteil der elektronischen Leitfähigkeit wurde bei einer Temperatur von 287 °C mit $t_{el} = 0.0016$ bestimmt. Hieraus ergibt sich, das $Na_3B_3O_3F_6$ ein reiner Natrium-Ionenleiter ist. Die Ionenleitfähigkeit beträgt 3.6 x $10^{-3}\,S\,cm^{-1}$ bei 350 °C. Die Aktivierungsenergie der Ionenleitfähigkeit beträgt 107 kJ mol^{-1} zwischen 200 und 350 °C. Diese Ergebnisse bestätigen, dass es sich bei $Na_3B_3O_3F_6$ um einen schnellen Ionenleiter handelt.

Kalium Fluorooxoborat, $K_3B_3O_3F_6$

Kristallines $K_3B_3O_3F_6$ wurde in einer Festkörperreaktion aus wasserfreiem KBO_2 und KBF_4 bei 400 °C dargestellt. Basierend auf der vollständigen Charakterisierung von $Na_3B_3O_3F_6$, konnte durch die Übereinstimmung der Schwingungsspektren der beiden analogen Alkali-Fluorooxoborate die Struktur von $K_3B_3O_3F_6$ hergeleitet werden. Anhand der Untersuchungen konnte eindeutig bewiesen werden, dass $K_3B_3O_3F_6$ ebenfalls aus sechs-gliedrigen Hexafluorotriborat Ringen $B_3O_3F_6{}^{3-}$ aufgebaut wird. Wie in der analogen Natriumverbindung ist jedes Boratom von zwei Fluor- und zwei Sauerstoffatomen tetraedrisch koordiniert. Ebenso kann $K_3B_3O_3F_6$ als schnelles Ionenleiter klassifiziert werden. Die Ionenleitfähigkeit beträgt 1.2 x 10^{-4} S cm^{-1} bei 350 °C und gleichzeitig vernachlässigbarem elektronischem Beitrag.

List of Figure

List of Figures

List of Tables

List of Tables

References

[1] M. B. Armand. Polymer Electrolytes. *Annu. Rev. Mater. Sci.*, 16:245–261, 1986.

[2] Y. Katoa, M. Watanabe, K. Sanuia and N. Ogata. Ionic Transport Number of Network PEO Electrolytes. *Solid State Ionics*, 40-41:632–636, 1990.

[3] T. Mizumo, K. Sakamato, N. Matsumi and H. Ohno. Facile Preparation of Anion Trapping Polymer Electrolytes by Reaction Between 9-Borabicyclo[3.3.1]nonane (9-BBN) and Poly(propylene oxide). *Chem. Lett.*, 33(4):396–397, 2004.

[4] W. Xu, M. D. Williams and C. A. Angell. Novel Polyanionic Solid Electrolytes with Weak Coulomb Traps and Controllable Caps and Spacers. *Chem. Mater.*, 14(1):401–409, 2002.

[5] X. G. Sun, W. Xu, S. S. Zhang and C. A. Angell. Polyanionic Electrolytes with High Alkali Ion Conductivity. *J. Phys.:Condens. Matter.*, 13(36), 2001.

[6] W. Xu and C. A. Angell. Preparation and Characterization of Novel "polyMOB" Polyanionic Solid Electrolytes with Weak Coulomb Traps. *Solid State Ionics*, 147:295–301, 2002.

[7] M. Doyle, T. F. Fuller and J. Newman. The Importance of the Lithium Ion Transference Number in Lithium/Polymer Cells. *Electrochim. Acta*, 39(13):2073–2081, 1994.

[8] L. Dominquez and W. H. Meyer. Solid Polyelectrolytes. *Solid State Ionics*, 28-30:941–949, 1988.

[9] Z. Florjanczyk, W. Bzducha, W. Wieczorek, E. Z. Monikowska, W. Krawiec and S. H. Chung. Highly Conducting Lithium Polyelectrolytes Based on Maleic Anhydride Styrene Copolymers. *J. Phys. Chem. B*, 10243):8409–8416, 1998.

[10] M. Jansen. Volume Effect or Paddle-Wheel Mechanism-Fast Alkali-Metal Ionic Conduction in Solids with Rotationally Disordered Complex Anions. *Angew. Chem. Int. Ed. Engl.*, 30(12):1547–1558, 1991.

[11] K. Funke. Jump Relaxation in Solid Electrolytes. *Prog. Solid State Chem.*, 22(2):111–195, 1993.

[12] Y.-F. Y. Yao and J. T. Kummer. Ion Exchange Properties of and Rates of Ionic Diffusion in Beta-Alumina. *J. Inorg. Nucl. Chem.*, 29(9):2453–2466, 1967.

[13] H. Y.-P. Hong. Crystal-Structure and Ionic-Conductivity of $Li_{14}Zn(GeO_4)_4$ and Other New Li^+ Superionic Conductors. *Mater. Res. Bull.*, 13(2):117–124, 1978.

[14] P. Becker. A Contribution to Borate Crystal Chemistry:Rules for the Occurrence of Polyborate Anion Types. *Z. Kristallogr.*, 216(10):523–533, 2001.

[15] G. Yuan and D. Xue. Crystal Chemistry of Borates:The Classification and Algebraic Description by Topological Type of Fundamental Building Blocks. *Acta Crystallogr., Sect. B:Struct. Sci.*, 63:353–362, 2007.

[16] P. C. Burns, J. D. Grice and F. C. Hawthorne. Borate Minerals. I. Polyhedral Clusters and Fundamental Building Block. *Can. Mineral.*, 33:1131–1151, 1995.

[17] W. Schlenk and H. Thal. Metal-Ketyls, a Great Class of Compounds with Three Valent Carbon II . *Ber. Dtsch. Chem. Ges.*, 46:2840–2854, 1913.

[18] NETZSCH Proteus. *Thermal Analysis, Ver. 4.2.*, 2002.

[19] NETZSCH. *Software Package SW/STA/652.72-2, Ver. 3.6.*, 1999.

[20] Varian Australia Pty. Ltd. *Vista Pro CCD Simultaneous ICP-OES, Ver. 4.0*, 1997-2000.

[21] O. Buresch and H. G. Schnering. A New Teflon Liner for the Digestion of Small Samples with Acids in the Pressure System Berghof-Da-I. *Fresenius Z. Anal. Chem.*, 319(4):418–420, 1984.

[22] Stoe and Cie. *WinXPOW Software Pocket Stoe Stadi P, Ver. 1.1*, 1999.

[23] ICSD. *Inorganic Crystal Structure Database*, FIZ, Karlsruhe.

[24] ICDD-JCDPS. *Joint Commitee on Powder Standards*, Swartmore, USA.

[25] G. M. Sheldrick. *SHELXS-97 Program to Solve Crystal Structures*, 1997.

[26] G. M. Sheldrick. *SHELXL-97 Program to Refine Crystal Structures*, 1997.

[27] L. J. Farrugia. WinGX Suite for Small-Molecule Single-Crystal Crystallography. *J. Appl. Crystallogr.*, 32:837–838, 1999.

[28] Bruker Analytic. *XWin-NMR Ver. 2.5*, 1998.

[29] Bruker Analytic. *XWin-PLOT Ver. 2.6.0*, 1998.

[30] Mathworks. *MatLab, Ver. 7*, 2005.

[31] J. D. van Beek. matNMR:A Flexible Toolbox for Processing, Analyzing and Visualizing Magnetic Resonance Data in Matlab. *J. Magn. Reson.*, 187:19–26, 2007.

[32] S. Hediger, B. H. Meier and R. R. Ernst. Adiabatic Passage Hartmann-Hahn Cross Polarization in NMR Under Magic Angle Sample Spinning. *Chem. Phys. Lett.*, 240:449–456, 1995.

[33] L. Frydman and J. S. Harwood. Isotropic Spectra of Half-Integer Quadrupolar Spins from Bidimensional Magic-Angle Spinning NMR. *J. Am. Chem. Soc.*, 117:5367–5368, 1995.

[34] J. P. Amoureux, C. Fernandez and S. Steuernagel. Z Filtering in MQMAS NMR. *J. Magn. Reson., Ser. A*, 123:116–118, 1996.

[35] J. R. Macdonald and W. B. Johnson. Fundamentals of Impedance Spectroscopy. In J. R. Macdonald, editor, *Impedance Spectroscopy, Emphasizing Solid Materials and Systems.* Wiley-Interscience, New York, 1987.

[36] J. R. MacDonald. Impedance Spectroscopy and its Use in Analyzing the Steady-State AC Response of Solid and Liquid Electrolytes. *J. Electroanal. Chem.*, 223(1-2):25–50, 1987.

[37] J. E. Bauerle. Study of Solid Electrolyte Polarization by a Complex Admittance Method. *J. Phys. Chem. Solids*, 30:2657–2670, 1969.

[38] J. Randles. Kinetics of Rapid Electrode Reactions. *Faraday Discuss. Soc.*, 1:11–19, 1947.

[39] S. P. Jiang, J. G. Love and S. P. S. Badwal. Electrochemical Techniques in Studies of Solid Ionic Conductors. *Key Eng. Mater.*, 125-126:81–132, 1997.

[40] W. Scheider. Theory of Frequency Dispersion of Electrode Polarization-Topology of Networks with Fractional Power Frequency-Dependence. *J. Phys. Chem.*, 79(2):127–136, 1975.

[41] J. F. McCann and S. P. S. Badwall. Equivalent-Circuit Analysis of the Impedance Response of Semiconductor Electrolyte Counter-Electrode Cells. *J. Electrochem. Soc.*, 129(3):551–559, 1982.

[42] J. Bates, J. C. Wang and Y. T. Chu. Impedance of Metal-Solid Electrolyte Interfaces. *Solid State Ionics*, 18-19:1045–1049, 1986.

[43] A. Jonscher. Universal Dielectric Response. *Nature*, 267(5613):673–679, 1977.

[44] A. R. West. *Solid State Chemistry and its Applications*, page 452. John Wiley & Sons, Chichester, 1984.

[45] J. T. S. Irvine, D. C. Sinclair and A. R. West. Electroceramics: Characterization by Impedance Spectroscopy. *Adv. Mater.*, 2, 1990.

[46] Novocontrol GmbH. *WinDeta, Ver. 4.5*, 1995-2003.

[47] U. Kohler. PhD thesis, Universität Hannover, Germany, 1987.

[48] Novocontrol GmbH. *WinFit, Ver. 2.9*, 1996.

[49] BioLogic. *EC Lab, Ver. 8.3*, 2004.

[50] Crystal-Impact. *Diamond, Ver. 3.0b*, Bonn, Germany, 1997-2005.

[51] P. Mcgeehin and A. Hooper. Fast Ion Conduction Materials. *J. Mater. Sci.*, 12(1):1–27, 1977.

[52] H. Tuller and P. K. Moon. Fast Ion Conductors-Future-Trends. *Mater. Sci. Eng., B*, 1(2):171–191, 1988.

[53] P. Knauth and H. L. Tuller. Solid-State Ionics:Roots, Status, and Future Prospects. *J. Am. Ceram. Soc.*, 85(7):1654–1680, 2002.

[54] C. Tubandt and E. Lorenz. Molecular State and Electrical Conductivity of Crystallised Salts. *Z. Phys. Chem.*, 87(5):513–542, 1914.

[55] B. B. Owens and G. R. Argue. High-Conductivity Solid Electrolytes-MAg_4I_5. *Science*, 157(3786):308–310, 1967.

[56] J. B. Bates, J. C. Wang and N. J. Dudney. Solid Electrolytes-the Beta Aluminas. *Phys. Today*, 35(7):46–53, 1982.

[57] B. E. Fenton, J. M. Parker and P. V. Wright. Complexes of Alkali Metal Ions with Poly(ethylene oxide). *Polymer*, 14(11):589–589, 1973.

[58] M. B. Armand, J. M. Chabagno and M. J. Duclot. Poly-Ethers as Solid Electrolytes. In P. Vashishta, J. N. Mundy and G. K. Shenoy, editor, *Fast Ion Transport in Solids. Electrodes and Electrolytes*, pages 131–136. North Holland, Amsterdam, 1979.

[59] J. Y. Song, Y. Y. Wang and C. C. Wan. Review of Gel-Type Polymer Electrolytes for Lithium-Ion Batteries. *J. Power Sources*, 77(2):183–197, 1999.

[60] F. B. Dias, L. Plomp and J. B. J. Veldhuis. Trends in Polymer Electrolytes for Secondary Lithium Batteries. *J. Power Sources*, 88(2):169–191, 2000.

[61] J. M. Tarascon and M. Armand. Issues and Challenges Facing Rechargeable Lithium Batteries. *Nature*, 414(6861):359–367, 2001.

[62] A. Patil, V. Patila, D. W. Shina, J.-W. Choia, D.-S. Paika and S.-J. Yoon. Issue and Challenges Facing Rechargeable Thin Film Lithium Batteries. *Mater. Res. Bull.*, 43(8-9):1913–1942, 2008.

[63] B. Scrosati. Lithium Polymer Electrolytes. In W. A. van Schalkwijk and B. Scrosati, editor, *Advances in Lithium-Ion Batteries*, page 251. Kluwer Academic/Plenum, New York, 2002.

[64] M. Gauthier, A. Belanger, B. Kapfer, G. Vassort and M. Armand. Polymer Electrolyte Lithium Batteries. In J. R. MacCallum and C. A. Vincent, editor, *Polymer Electrolyte Reviews-2*, page 285. Elsevier, New York, 1989.

[65] K. Murata, S. Izuchi and Y. Yoshihisa. An Overview of the Research and Development of Solid Polymer Electrolyte Batteries. *Electrochim. Acta*, 45(8-9):1501–1508, 2000.

[66] P. V. Wright. Polymer Electrolytes-the Early Days. *Electrochim. Acta*, 43(10-11):1137–1143, 1998.

[67] Y. Okamato and M. G. Mc Lin. Ionically Conductive Polymers. In K. Natada, T. Kitayama and O. Vogl, editor, *Macromolecular Design of Polymeric Materials*, page 573. Marcel Dekker, New York, 1997.

[68] W. H. Meyer. Polymer Electrolytes for Lithium-Ion Batteries. *Adv. Mater.*, 10(6):941–949, 1998.

[69] A. G. Einset and G. E. Wnek. Polymer Electrolyte Review. In Z. A. Munshi, editor, *Handbook of Solid State Batteries and Capacitors*, page 289. World Scientific, Singapore, 1999.

[70] D. G. Fauteux and M. F. van Buren. Solid Polymer Electolytes. In J. C. Salamone, editor, *Polymer Materials Encyclopedia*, volume 10, page 7791. CRC Press, New York, 1996.

[71] M. Kumar and S. S. Sekhon. Ionic Conductance Behaviour of Plasticized Polymer Electrolytes Containing Different Plasticizers. *Ionics*, 8(3-4):223–233, 2002.

[72] A. M. Stephan and K. S. Nahm. Review on Composite Polymer Electrolytes for Lithium Batteries. *Polymer*, 47:5952–5964, 2006.

[73] V. Afanasev and A. G. Grechin. Chemical Modification of the Electrolytes for Lithium Batteries. *Russ. Chem. Rev.*, 71(9):775–787, 2002.

[74] R. C. Agrawal and G. P. Pande. Solid Polymer Electrolytes:Materials Designing and All-Solid-State Battery Applications:an Overview. *J. Phys. D:Appl. Phys.*, 41(22):1–18, 2008.

[75] I. I. Olsena, R. Koksbanga and E. Skou. Transference Number Measurements on a Hybrid Polymer Electrolyte. *Electrochim. Acta*, 40(11):1701–1706, 1995.

[76] C. Julien and G. A. Nazri. Polymer Electrolytes. In H. L. Tuller, editor, *Solid State Batteries:Materials Design and Optimization*, page 347. Kluwer Academic, Boston, MA, 1994.

[77] M. Watanabe, M. Itoh, K. Sanui and N. Ogata. Carrier Transport and Generation Processes in Polymer Electrolytes Based on Poly(ethylene oxide) Networks. *Macromolecules*, 20(3):569–573, 1987.

[78] G. Petersen, P. Jacobsson and L. M. Torell. A Raman Study of Ion Polymer and Ion Interactions in Low Molecular Weight Polyether $LiCF_3SO_3$ Complexes. *Electrochim. Acta*, 37(9):1495–1497, 1992.

[79] D. Fauteux, A. Massucco, M. McLin, M. Van Buren and J. Shi. Lithium Polymer Electrolyte Rechargeable Battery. *Electrochim. Acta*, 40(13-14):2185–2190, 1995.

[80] D. Baril, C. Michot and M. Armand. Electrochemistry of Liquids vs. Solids:Polymer Electrolytes. *Solid State Ionics*, 94(1-4):35–47, 1997.

[81] J. McBreen, H. S. Lee, X. Q. Yang and X. Sun. New Polymer and Liquid Electrolytes for Lithium Batteries. In S. Surampudi, R. A. Marsch, Z. Oguni and J. Prakash, editor, *Lithium Batteries:Proceedings of the International Symposium*, volume 99, pages 494–503. The Electrochemical Society Inc., New Jersey, 1999.

[82] C. A. Angell, C. Liu and E. Sanchez. Rubbery Solid Electrolytes with Dominant Cationic Transport and High Ambient Conductivity. *Nature*, 362(6416):137–139, 1993.

[83] K. Xu. Nonaqueous Liquid Electrolytes for Lithium Based Rechargeable Batteries. *Chem. Rev.*, 104:4303–4417, 2004.

[84] G. Fellade and Ph. Perche. Ion Conductive Macromolecular Gels and Membranes for Solid Lithium Cells. *J. Appl. Electrochem.*, 5:63–69, 1975.

[85] A. M. Stephan. Review on Gel Polymer Electrolytes for Lithium Batteries. *Eur. Polym. J.*, 42:21–42, 2006.

[86] C. S. Kim and S. M. Oh. Importance of Donor Number in Determining Solvating Ability of Polymers and Transport Properties in Gel-Type Polymer Electrolytes. *Electrochim. Acta*, 45(13):2101–2109, 2000.

[87] M. Wakihara. Recent Developments in Lithium Ion Batteries. *Mater. Sci. Eng., R*, 33(4):109–134, 2001.

[88] B. Scrosati. New Approaches to Developing Lithium Polymer Batteries. *Chem. Rec.*, 1(2):173–181, 2001.

[89] J. F. Synder, M. A. Ratner and D. F. Shriver. Polymer Electrolytes and Polyelectrolytes:Monte Carlo Simulations of Thermal Effects on Conduction. *Solid State Ionics*, 147:249–257, 2002.

[90] M. A. Ratner and D. F. Shriver. Ion Transport in Solvent-Free Polymers. *Chem. Rev.*, 88(1):109–124, 1988.

[91] N. Kobayashi, M. Uchiyama and E. Tsuchida. Poly[lithium methacrylate-co-oligo(oxyethylene)methacrylate] as a Solid Electrolyte with High Ionic-Conductivity. *Solid State Ionics*, 17(4):307–311, 1985.

[92] Y. Nakacho, A. Inubushi and Y. Tada. All Solid State Battery. *US Patent 5 183 716*, 1993.

[93] E. Tsuchida, N. Kobayashi and H. Ohno. Single-Ion Conduction in Poly[(oligo(oxyethylene)methacrylate)-co-(alkali-metal methacrylates). *Macromolecules*, 21(1):96–100, 1988.

[94] H. Tsutsumi, M. Yamamoto, M. Morita, Y. Matsuda, T. Nakamura and H. Asai. Novel Single and Double Ion Type Siloxane Polymeric Solid Electrolytes Prepared by Same Prepolymers. *Electrochim. Acta*, 37(7):1183–1186, 1992.

[95] S. Zhang, Z. Deng and G. Wan. Cationic Conductivity of Blend Complexes Composed of Poly[oligo(oxyethylene)methacrylate] and the Alkali-Metal Salts of Poly(sulfoalkyl methacrylate). *Polym. J.*, 23(2):73–78, 1991.

[96] D. Benrabah, S. Sylla, J. Y. Sanchez and M. Armand. Cationic Conductivity in Poly(oxyethylene oxide) Networks. *J. Power Sources*, 54:456–460, 1995.

[97] D. Benrabah, S. Sylla, F. Alloin, J. Y. Sanchez and M. Armand. Perfluorosulfonate-Polyether Based Single Ion Conductors. *Electrochim. Acta*, 40(13-14):2259, 1995.

[98] T. Fujinami, A. Tokimune, M. A. Mehta, G. C. Rawsky and D. F. Shriver. Siloxyaluminate Polymers with High Li^+ Ion Conductivity. *Chem. Mater.*, 9:2236–2239, 1997.

[99] F. M. Gray. *Solid Polymer Electrolytes:Fundamentals and Technological Applications*. The Royal Society of Chemistry, Cambridge, 1997.

[100] C. Bertier, W. Gorecki, M. Minier, M. B. Armand, J. M. Chabagno and P. Rigaud. Microscopic Investigation of Ionic Conductivity in Alkali Metal Salt-Poly(ethylene oxide) Adducts. *Solid State Ionics*, 11:91–95, 1983.

[101] D. F. Shriver and P. G. Bruce. Polymer Electrolytes I. In P. G. Bruce, editor, *Solid State Electrochemistry*, page 95. Cambridge University Press, Cambridge, 1995.

[102] B. L. Papke, M. A. Ratner and D. F. Shriver. Conformation and Ion-Transport Models for the Structure and Ionic Conductivity in Complexes of Polyethers with Alkali Metal Salts. *J. Electrochem. Soc.*, 129:1694–1701, 1982.

[103] Y. G. Andreev and P. G. Bruce. Polymer Electrolyte Structure and its Implications. *Electrochim. Acta*, 45(8-9):1417–1423, 2000.

[104] Z. Gadjourova, Y. G. Andreev, D. P. Tunstall and P. G. Bruce. Ionic Conductivity in Crystalline Polymer Electrolytes. *Nature*, 412(6846):520–523, 2001.

[105] M. A. Ratner. Aspects of the Theoretical Treatment of Polymer Solid Electrolytes. In J. R. MacCallum and C. A. Vincent, editor, *Polymer Electrolyte Reviews-1*, page 173. Elsevier, London, 1987.

[106] W. V. Gool. Fast Ion Conduction. *Annu. Rev. Mater. Sci.*, 4:311–335, 1974.

[107] G. C. Farrington and J. L. Briant. Fast Ionic Transport in Solids. *Science*, 204(4400):1371–1379, 1979.

[108] S. Chandra. *Superionic Solids:Principles and Applications*, page 225. North Holland, Amsterdam, 1981.

[109] H. Sato. Solid Elecrolytes. In S. Geller, editor, *Topics in Applied Physics*. Springer-Verlag, Berlin, 1977.

[110] C. Richard and A. Catlow. Atomistic Mechanisms of Ionic Transport in Fast-Ion Conductors. *J. Chem. Soc., Faraday Trans.*, 86(8):1167–1176, 1990.

[111] J. B. Goodenough. Review Lecture:Fast Ionic Conduction in Solids. *Proc. R. Soc. London, Ser. A*, 393(1805):215–234, 1984.

[112] J. R. Manning. Diffusion Kinetics for Atoms in Crystals. *Am. J. Phys.*, 36(10):922–923, 1968.

[113] P. Padma Kumar and S. Yashonath. Ion Conduction in the Solid State. *J. Chem. Sci.*, 118(1):135–154, 2006.

[114] R. A. Huggins. Crystal Structures and Fast Ionic Conduction. In P. Hagenmuller and W. van Gool, editor, *Solid Elecrolytes:General Principles, Characterization, Materials, Applications*, page 27. Academic Press, London, 1978.

[115] M. S. Whittingham and R. A. Huggins. Measurement of Sodium Ion Transport in Beta Alumina Using Reversible Solid Electrodes. *J. Chem Phys.*, 54(1):414–416, 1971.

[116] B. Dunn, G. C Farrington and J. O. Thomas. Frontiers in β''-Alumina Research. *MRS Bulletin*, 14(9):22–30, 1989.

[117] J. B. Bates, J. C. Wang and N. J. Dudney. Solid Electrolytes-The Beta Aluminas. *Phys. Today*, 35(7):46–53, 1982.

[118] C. R. Peters, M. Bettman, J. W. Moore and M. D. Glick. Refinement of the Structure of Sodium beta Alumina. *Acta Crystallogr., Sect. B:Struct. Sci*, 27(9):1826–1834, 1971.

[119] J. B. Goodenough, H. Y. P. Hong and J. A. Kafalas. Fast Na^+-Ion Transport in Skeleton Structures. *Mater. Res. Bull.*, 11(2):203–220, 1976.

[120] H.Y-P. Hong. Crystal Structures and Crystal Chemistry in the System $Na_{1+x}Zr_2Si_xP_{3-x}O_{12}$. *Mater. Res. Bull.*, 11(2):173–182, 1976.

[121] U. Alpen, A. Rabenau and G. H. Talat. Ionic Conductivity in Li_3N Single Crystals. *Appl. Phys. Lett.*, 30(12):621–623, 1977.

[122] B. A. Boukamp and R. A. Huggins. Lithium Ion Conductivity in Lithium Nitride. *Phys. Lett. A*, 58(4):231–233, 1976.

[123] R. A. Huggins. Recent Results on Lithium Ion Conductors. *Electrochim. Acta*, 22(7):773–781, 1977.

[124] L. Strock. The Crystal Structure of High Temperature Iodine Silver alpha-AgI. *Z. Phys. Chem. B:Chem. E.*, 25(5/6):441–459, 1934.

[125] M. A. Ratner and D. F. Shriver. Polymer Ionics. *MRS Bulletin*, September:39–51, 1989.

[126] F. M. Gray. *Polymer Electrolytes*. The Royal Society of Chemistry, Cambridge, 1997.

[127] S. Takeoka, H. Ohno and E. Tsuchida. Recent Advancement of Ion-Conductive Polymers. *Polym. Adv. Technol.*, 4:53–73, 1993.

[128] K. Onishi, M. Matsumoto, Y. Nakacho and K. Shigehara. Synthesis of Aluminate Polymer Complexes as Single-Ionic Solid Electrolytes. *Chem. Mater.*, 8:469–472, 1996.

[129] D. P. Siska and D.F. Shriver. Enhanced Ion Mobility in Aluminosilicate/Polysiloxane Network Polyelectrolytes. *Mater. Res. Soc. Symp. Proc.*, 575:131–136, 2000.

[130] S. W. Ryu, P. E. Trapa, S. C. Olugebefola, J. A. Gonzalez-Leon, D. R. Sadoway and A. M. Mayes. Effect of Counter Ion Placement on Conductivity in Single-Ion Conducting Block Copolymer Electrolytes. *J. Electrochem. Soc.*, 152:A158–A163, 2005.

[131] Y. Nishihara, M. Miyazaki, Y. Tomita, Y. Kadono and K. Takagi. Synthesis and Ion Conductive Characteristics of Inorganic-Organic Hybrid Polymers Bearing a Tetraarylpentaborate Unit. *J. Polym. Sci., Part A:Polym. Chem.*, 46(23):7913–7918, 2008.

[132] K. Xu and C. A. Angell. Synthesis and Characterization of Lithium Sulfonates as Components of Molten Salt Electrolytes. *Electrochim. Acta*, 40(13-14):2401–2403, 1995.

[133] J. F. Snyder, M. A. Ratner and D. F. Shriver. Optimizing the Design of Polyelectrolytes Using Monte Carlo Simulations. *J. Electrochem. Soc.*, 148:A858–A863, 2001.

[134] S. Takeoka, K. Horiuchi, S. Yamagata and E. Tsuchida. Sodium Ion Conduction of Perfluorosulfonate Ionomer/Poly(oxyethylene) Composite Films. *Macromolecules*, 24(8):2003–2006, 1991.

[135] T. Aoki, A. Konno and T. Fujinami. Lithium Ion Conductivity of Blend Polymer Electrolytes Based on Borate Polymers Containing Fluoroalkane Dicarboxylate and Poly(ethylene oxide). *Electrochim. Acta*, 50(2-3):301–304, 2004.

[136] D. J. Banister, G. R. Davies, I. M. Ward and J. E. Mc Intyre. Ionic Conductivities for Poly(ethylene oxide) Complexes with Lithium Salts of Monobasic and Dibasic Acids and Blends of Poly(ethylene oxide) with Lithium Salts of Anionic Polymers. *Polymer*, 25(9):1291–1296, 1984.

[137] G. B. Zhou, I. M. Khan and J. Smid. Cation Transport Polymer Electrolytes. Siloxane Comb Polymers with Pendant Oligooxyethylene Chains and Sulphonate Groups. *Polym. Commun.*, 30(2):52–55, 1989.

[138] H. Ohno and K. Ito. Copolymerization of Methacrylic Acid Alkali Metal Salts and Polyether-containing Monomers in Solid Polymer Electrolytes. *Polym. Adv. Technol*, 2(2):97–101, 1991.

[139] W. Xu, K. S. Siow, Z. Gao and S. Y. Lee. Novel Alternating Comblike Copolymer Electrolytes with Single Lithium Ionic Conduction. *Chem. Mater.*, 10(7):1951–1957, 1998.

[140] H. T. Kim and J. K. Park. Poly(oligo-oxyethylene methacrylate-co-alkali metal acrylamidocaproate) as a Single Ion Conductor. *Polym. Bull.*, 36(4):427–433, 1996.

[141] E. Tsuchida, H. Ohno, N. Kobayashi and H. Ishizaka. Poly[(ω-carboxy)oligo(oxyethylene) methacrylate] as a New Type of Polymeric Solid Electrolyte for Alkali-Metal Ion Transport. *Macromolecules*, 22(4):1771–1775, 1989.

[142] S. Takeoka, Y. Maeda, H. Ohno and E Tsuchida. Synthesis, Polymerization and Cation Conductive Properties of (ω-carboxy)-oligo (oxyethylene) Methacrylate. *Polym. Adv. Technol.*, 1:201–205, 1990.

[143] R. Dupon, B. L. Papke, M. A. Ratner, D. H. Whitmore and D. F. Shriver. Influence of Ion Pairing on Cation Transport in the Polymer Electrolytes Formed by Poly(ethylene oxide) with Sodium Tetrafluoroborate and Sodium Tetrahydroborate. *J. Am. Chem. Soc*, 104(23):6247–6251, 1982.

[144] L. C. Hardy and D. F. Shriver. Chloride Ion Conductivity in a Plasticized Quaternary Ammonium Polymer. *Macromolecules*, 17(4):975–977, 1984.

[145] Y. Okamoto, T. F. Yeh, H. S. Lee and T. A. Skotheim. Design of Alkaline Metal Ion Conducting Polymer Electrolytes. *J. Polym. Sci., Part A:Polym. Chem.*, 31(10):2573–2581, 1993.

[146] L. C. Hardy and D. F. Shriver. Preparation and Electrical Response of Solid Polymer Electrolytes with Only One Mobile Species. *J. Am. Chem. Soc*, 107(13):3823–3828, 1985.

[147] S. C. Narang and S. C. Ventura. Single-Ion Conducting Solid Polymer Electrolytes. *US Patent 5 548 055*, 1996.

[148] S. C. Narang and S. C. Ventura. Batteries Containing Single-Ion Conducting Solid Polymer Electrolytes. *US Patent 5 633 098*, 1997.

[149] E. A. Rietman and M. L. Kaplan. Single-Ion Conductivity in Comblike Polymers. *J. Polym. Sci., Part C:Polym. Lett.*, 28(6):187–191, 1990.

[150] T. Fujinami. Design and Applications of Boron Compounds for High Performance Polymer Electrolytes. In B. V. R. Chowdari, M. A. Careem, M. A. K. L. Dissanayake, R. M. G. Rajapakse, V. A. Seneviratne, editor, *Advanced Materials for Emerging Technologies:Proceedings of the 10th Asian Conference on Solid State Ionics*, pages 449–458. World Scientific Publishing, Singapore, 2006.

[151] Y. Kato, K. Suwa, H. Ikuta, Y. Uchimoto, M. Wakihara, S. Yokoyama, T. Yabe and M. Yamamoto. Influence of Lewis Acidic Borate Ester Groups on Lithium Ionic Conduction in Polymer Electrolytes. *J. Mater. Chem.*, 13(2):280–285, 2003.

[152] M. A. Mehta, T. Fujinami, S. Inoue, K. Matsushita, T. Miwa and T. Inoue. The Use of Boroxine Rings for the Development of High Performance Polymer Electrolytes. *Electrochim. Acta*, 45(8-9):1175–1180, 2000.

[153] M. A. Mehta and T. Fujinami. Novel Inorganic-Organic Polymer Electrolytes-Preparation and Properties. *Solid State Ionics*, 113-115:187–192, 1998.

[154] M. A. Mehta, T. Fujinami and T. Inoue. Boroxine Ring Containing Polymer Electrolytes. *J. Power Sources*, 81-82:724–728, 1999.

[155] N. Matsumi, K. Sugai and H. Ohno. Ion Conductive Characteristics of Alkylborane Type and Boric Ester Type Polymer Electrolytes Derived from Mesitylborane. *Macromolecules*, 36(7):2321–2326, 2003.

[156] N. Matsumi, K. Sugai and H. Ohno. Selective Ion Transport in Organoboron Polymer Electrolytes Bearing a Mesitylboron Unit. *Macromolecules*, 35(15):5731–5733, 2002.

[157] N. Matsumi, T. Mizumo and H. Ohno. Preparation of Comb-Like Organoboron Polymer Electrolyte Without Generation of Salt. *Chem. Lett.*, 33(4):372–373, 2004.

[158] J. F. Le Nest, A. Gandini, H. Cheradame and J. P. Cohen Addad. Cationic Transport Features of Ionomeric Polymer Networks. *Polymer Comm.*, 28(11):302–305, 1987.

[159] H. Ohno and K. Ito. Poly(ethylene oxide)s having Carboxylate Groups on the Chain End. *Polymer*, 36:891–893, 1995.

[160] K. Ito and H. Ohno. Ionic Conductivity of Poly(ethylene oxide) having Charges on the Chain End. *Solid State Ionics*, 79:300–305, 1995.

[161] G. B. Zhou, I. M. Khan and J. Smid. Solvent-Free Cation-Conducting Polysiloxane Electrolytes with Pendant Oligo(oxyethylene) and Sulfonate Groups. *Macromolecules*, 26(9):2202–2208, 1993.

[162] S. Ganapathiappan, K. Chen and D. F. Shriver. A New Class of Cation Conductors:Polyphosphazene Sulfonates. *Macromolecules*, 21(7):2299–2301, 1988.

[163] S. Ganapathiappan, K. Chen and D. F. Shriver. Synthesis, Characterization and Electrical Response of Phosphazene Polyelectrolytes. *J. Am. Chem. Soc*, 111(11):4091–4095, 1989.

[164] K. Ito, N. Nishina and H. Ohno. High Lithium Ionic Conductivity of Poly(ethylene oxide)s Having Sulfonate Groups on their Chain Ends. *J. Mater. Chem.*, 7(8):1357–1362, 1997.

[165] Y. G. Lee, C. H. Kim, J. K. Park and D. Y. Seung. Lithium Sulfonated Styrene Oligomer (LiSSO) as a New Class of Lithium Salt for Polymer Electrolytes. *Polym. Bull.*, 47(2):167–174, 2001.

[166] J. F. Snyder, M. A. Ratner and D. F. Shriver. Ion Conductivity of Comb Polysiloxane Polyelectrolytes Containing Oligoether and Perfluoroether Sidechains. *J. Electrochem. Soc.*, 150:A1090–A1094, 2003.

[167] M. C. Lonergan, M. A. Ratner and D. F. Shriver. Cryptand Addition to Polyelectrolytes:A Means of Conductivity Enhancement and a Probe of Ionic Interactions. *J. Am. Chem. Soc*, 117(8):2344–2350, 1995.

[168] T. Fujinami, M. A. Mehta, K. Sugie and K. Mori. Molecular Design of Inorganic-Organic Hybrid Polyelectrolytes to Enhance Lithium Ion Conductivity. *Electrochim. Acta*, 45(8-9):1181–1186, 2000.

[169] P. Chetri, N. N. Dass and N. S. Sarma. Conductivity Measurement of Poly(vinyl borate) and its Lithium Derivative in Solid State. *Mater. Sci. Eng., B*, 139(2-3):261–264, 2007.

[170] P. Chetri, N. Sarma and N. N. Dass. Preparation, Characterization and Conductivity Measurement of Poly(vinyl borate) and its Sodium Derivative. *J. Polym. Mater.*, 14:165–170, 1997.

[171] N. S. Sarma, P. Chetri and N. N. Dass. Synthesis, Characterization and Conductivity Measurement of Poly(vinyl borate) and its Potassium Derivative. *J. Polym. Mater.*, 15(1):23–26, 1998.

[172] N. S. Sarma and N. N. Dass. Measurement of Ionic Conductivity of Some Electrolytes, Polyelectrolytes and Complexes in Solid State. *Indian J. Pure Appl. Phys.*, 37(4):321–324, 1999.

[173] T. Aoki, A. Konno and T. Fujinami. Li-Ion Conductivity of Aluminate and Borate Complex Polymers Containing Fluoroalkane Dicarboxylate. *J. Electrochem. Soc.*, 151:A887–A890, 2004.

[174] X. G. Sun and C. A. Angell. "Acid-in-Chain" versus "Base-in-Chain" Anionic Polymer Electrolytes for Electrochemical Devices. *Electrochim. Acta*, 46(10-11):1467–1473, 2001.

[175] K. E. Doan, M. A. Ratner and D. F. Shriver. Synthesis and Electrical Response of Single-Ion Conducting Network Polymers Based on Sodium Poly(tetraalkoxyaluminates). *Chem. Mater.*, 3:418–423, 1991.

[176] O. K. Onishi, M. Matsumoto and K. Shigehara. Lithium Batteries Composed of Aluminate Polymer Complexes as Single-Ion Conductive Solid Electrolytes. *J. Power Sources*, 92(1-2):120–123, 2001.

[177] K. Matsushita, Y. Shimazaki, M. A. Mehta and T. Fujinami. Synthesis and Characterization of Aluminate Polymer Electrolytes and their Blends with Poly(ether)s. *Solid State Ionics*, 133:295–301, 2000.

[178] K. Onishi, M. Matsumoto and K. Shigehara. Thioaluminate Polymer Complexes as Single-Ionic Solid Electrolytes. *Chem. Mater.*, 10:927–931, 1998.

[179] G. C. Rawsky, T. Fujinami and D. F. Shriver. Aluminosilicate/Poly(ethylene glycol) Copolymers:A New Class of Polyelectrolytes. *Chem. Mater.*, 6:2208–2209, 1994.

[180] N. Matsumi, K. Sugai, K. Sakamoto, T. Mizumo and H. Ohno. Direct Synthesis of Poly(lithium organoborate)s and their Ion Conductive Properties. *Macromolecules*, 38(12):4951–4954, 2005.

[181] K. E. Doan, S. D. Druger, D. F. Shriver, M. A. Ratner and A. Nitzan. Coulomb Trapping Effects in Polymer Solid Electrolytes:A Simulation Study of Stoichiometry Dependence. *Mol. Cryst. Liq. Crys.*, 160(1):311–319, 1988.

[182] S. Zhang, Z. Chang, K. Xu and C. A. Angell. Molecular and Anionic Polymer and Oligomer Systems with Microdecoupled Conductivities. *Electrochim. Acta*, 45(8-9):1229–1236, 2000.

[183] W. Xu, X. G. Sun and C. A. Angell. Anion-Trapping and Polyanion Electrolytes Based on Acid-in-Chain Borate Polymers. *Electrochim. Acta*, 48(14-16):2255–2266, 2003.

[184] M. Pompetzki. PhD thesis, Rheinischen Friedrich-Wilhelms-Universität Bonn, Germany, 2003.

[185] L. Hildebrandt. PhD thesis, Universität Stuttgart, Germany, 2006.

[186] D. Seyferth and M. A. Weiner. The Preparation of Organolithium Compounds by the Transmetalation Reaction:I. Vinyllithium. *J. Am. Chem. Soc.*, 83:3583–3586, 1961.

[187] W. Bauer and C. Griesinger. Vinyllithium:Dynamic Behavior in Tetrahydrofuran Solution and Comprehensive Analysis of NMR Spin-Spin Coupling Constants. *J. Am. Chem. Soc.*, 115:10871–10882, 1993.

[188] R. J. Thompson and J. C. Davis. Electronegativity Effects on ^{11}B Chemical Shifts in Tetrahedral BX_4^- Ions. *Inorg. Chem.*, 4:1464–1467, 1965.

[189] H. J. Becher and F. Bramsiepe. Schwingungsspektren und Kraftkonstanten von Bortrimethyl und Rubidiumtetramethylboranat. *Spectrochim. Acta*, 35 A:53–57, 1979.

[190] W. Biffar, H. Nöth and D. Sedlak. Chemistry of Boron 130:The Reaction of Organo-Lithium Compounds with Borane Donors-Preparation and Isolation of Lithium Monoorganotrihydroborates. *Organometallics*, 2(5):579–585, 1983.

[191] B. E. Smith, B. D. James and R. M. Peachey. Hydrogen-Deuterium Exchange between MBH_4 and MBD_4 (M = Li, Na)-Isotope Effects on ^{1}H and ^{11}B NMR-Spectra of BH_nD_{4-n} Anions and a Discussion of Exchange-Reactions in Some Covalent Tetrahydroborate Systems. *Inorg. Chem.*, 16(8):2057–2062, 1977.

[192] J. B. Leach, C. B. Ungermann and T. P. Onak. Proton Magnetic Resonance Studies on Methyl and Chloro Substituted Diboranes. *J. Magn. Reson.*, 6(1):74–83, 1972.

[193] J. K. Jeon, Q. D. Nghiem, D. P. Kim and J. Lee . Olefin Hydroboration of Borazine with Vinylsilanes as Precursors of Si-B-C-N Ceramics. *J. Organomet. Chem.*, 689:2311–2318, 2004.

[194] P. M. Blonsky, D. F. Shriver, P. Austin and H. R. Allock. Complex Formation and Ionic Conductivity of Polyphosphazene Solid Electrolytes. *Solid State Ionics*, 18-19:258–264, 1986.

[195] A. Abragam. In J. Birman, S. F. Edwards, R. H. Friend, C. H. L. Smith, M. Rees, D. Sherrington and G. Vaneziano, editor, *Principles of Nuclear Magnetism*, pages 455–456. Clarendon Press, Oxford, 1996.

[196] S. G. Bishop and P. J. Bray. NMR Studies of Diffusion in Glassy and Crystalline Lithium Borates. *J. Chem. Phys.*, 48:1709–1717, 1968.

[197] H. A. Every, F. Zhou, M. Forsyth and D. R. MacFarlane. Lithium Ion Mobility in Poly(vinyl alcohol) Based Polymer Electrolytes as Determined by ^{7}Li NMR Spectroscopy. *Electrochim. Acta*, 43(10-11):1465–1469, 1998.

[198] G. Cakmak, A. Verhoeven and M. Jansen. Synthesis and Characterization of Solid Single Ion Conductors Based on Poly[lithium tetrakis(ethyleneboryl)borate]. *J. Mater. Chem.*, 19:4310–4318, 2009.

[199] G. Sokrates. *Infrared and Raman Characteristic Group Frequencies*. John Wiley&Sons, Chichester, 2001.

[200] B. Schrader. Organic Substances. In B. Schrader, editor, *Infrared and Raman Spectroscopy*, page 189. VCH Publishers, Weinheim, 1985.

[201] A. Haoudi-Mazzah, A. Mazzah, J. Gnado and P. Dhamelincourt. Vibrational Study of Eight-Membered Zirconium- and Boron-Containing Siloxane Rings. *J. Raman Spectrosc.*, 27(6):451–455, 1996.

[202] M. R. Hansen, T. Vosegaard, H. J. Jakobsen and J. Skibsted. [11]B Chemical Shift Anisotropies in Borates from [11]B MAS, MQMAS, and Single-Crystal NMR Spectroscopy. *J. Phys. Chem. A*, 108:586–594, 2004.

[203] M. Weinmann, T. W. Kamphowe, P. Fischer and F. Aldinger. Tris(hydridosilyethyl)boranes:Highly Reactive Synthons for Polymeric Silicon Compounds. *J. Organomet. Chem.*, 592:115–127, 1999.

[204] L. Delmulle and G. Vanderkelen. NMR Study (^{1}H, ^{13}C and [29]Si) of $(CH_3)_{4-x}$ $Si(CH=CH_2)_x$ Compounds where x= 0, 1, 2, 3, 4. *J. Mol. Struct.*, 66:309–314, 1980.

[205] T. P. Onak, H. Landesman, R. E. Williams and I. Shapiro. The [11]B Nuclear Magnetic Resonance Chemical Shifts and Spin Coupling Values for Various Compounds. *J. Phys. Chem.*, 63(9):1533–1535, 1959.

[206] H. Nöth and H. Vahrenkamp. Kernresonanzuntersuchungen an Bor-Verbindungen, I. [11]B Kernresonanzspektren von Boranen mit Substituenten aus der ersten Achterperiode des Periodensystems. *Chem. Ber.*, 99(3):1049–1067, 1966.

[207] A. A. Pronkin, V. N. Naraev, I. V. Murin and I. A. Sokolov. Concentration Dependence of Electric Conductivity for Fluorine-Containing Sodium Borate Glasses. *Glass Phys. Chem.*, 26(3), 2000.

[208] I. G. Ryss. The Trimeric Difluoro-Orthoborates of Sodium and Potassium. *Dokl. Akad. Nauk SSSR*, 97, 1954.

[209] L. Maya. Identification of Polyborate and Fluoropolyborate Ions in Solution by Raman Spectroscopy. *Inorg. Chem.*, 15(9):2179–2184, 1976.

[210] L. Maya. Crystalline Compounds and Glasses in System B_2O_3-NaF-NaBF$_4$. *J. Am. Ceram. Soc.*, 60(7-8):323–328, 1977.

[211] N. N. Babich, B. F. Dmitruk and G. N. Novitskaya. The Synthesis and Study of Sodium Hexafluorotriborate. *Russ. J. Inorg. Chem.*, 37(7):729–731, 1992.

[212] I. G. Ryss and L. P. Bogdanova. Potassium Hexa Fluoroboron-Oxolate $K_3[B_3O_3F_6]$ and Potassium Hydroxopenta Fluoroboron-Oxolate $K_3[B_3O_3F_5OH]$. *Russ. J. Inorg. Chem*, 4(8):831, 1959.

[213] A. A. Andriiko, N. I. Parkhomenko and A. N. Antishko. KF-$K_3B_3O_3F_6$ System. *Russ. J. Inorg. Chem.*, 33:410–413, 1988.

[214] M. V. Akhamanova and G. E. Kurilchikova. Infrared Absorption Spectra of Hydroyfluoroboric Complexes of Potassium and Sodium. *Opt. Spectrosc.*, 8(4):264–267, 1960.

[215] C. Rodellas, S. Garcia-Blanco and A. Vegas. Crystal Structure Refinement of Jeremejevite ($Al_6B_5F_3O_{15}$). *Z. Kristallogr.*, 165(1-4):255–260, 1983.

[216] Bruker Suite. *Ver. 2008/3*, Bruker AXS, Inc., Madison, USA, 2007.

[217] G. M. Sheldrick. *SADABS-Bruker AXS Area Detector Scaling and Absorption, Ver. 2007/4*, 2007.

[218] G. M. Sheldrick. A Short History of SHELX. *Acta Crystallogr., Sect. A:Found. Crystallogr.*, 64:112–122, 2008.

[219] A. A. Coelho. *TOPAS-Graphics Based Profile and Structure Analysis Software, Ver. 3.0*, 2005.

[220] A. LeBail, H. Duroy and J. L. Fourquet. Ab-initio Structure Determination of $LiSbWO_6$ by X-ray Powder Diffraction. *Mater. Res. Bull.*, 23:447–452, 1988.

[221] H. Koenig and R. Hoppe. On Borates of Alkaline Metals II. On the Knowledge of LiB_3O_5. *Z. Anorg. Allg. Chem.*, 439(2):71–79, 1978.

[222] J. Krogh-Moe. Interpretation of the Infra-red Spectra of Boron Oxide and Alkali Borate Glasses. *Phys. Chem. Glasses*, 6(2):46–54, 1965.

[223] J. D. Grice, P. C. Burns and F. C. Hawthorne. Borate Minerals. II. A Hierarchy of Structures Based Upon the Borate Fundamental Building Block. *Can. Mineral.*, 37:731–762, 1999.

[224] M. Wenger and T. Armbruster. Crystal Chemistry of Lithium:Oxygen Coordination and Bonding. *Eur. J. Mineral.*, 3:387–399, 1991.

[225] L. Li, G. Li, Y. Wang, F. Liao and J. Lin. Bismuth Borates:One-Dimensional Borate Chains and Nonlinear Optical Properties. *Chem. Mater.*, 17(16):4174–4180, 2005.

[226] G. Xiong, G. Lan, H. Wang and C. Huang. Infrared Reflectance and Raman Spectra of Lithium Triborate Single Crystal. *J. Raman Spectrosc.*, 24:785–789, 1993.

[227] E. I. Kamitsos and G. D. Chryssikos. Borate Glass Structure by Raman and Infrared Spectroscopies. *J. Mol. Struct.*, 247:1–16, 1991.

[228] E. I. Kamitsos, A. P. Patsis, M. A. Karakassides and G. D. Chryssikos. Infrared Reflectance Spectra of Lithium Borate Glasses. *J. Non-Cryst. Solids*, 126:52–67, 1990.

[229] G. D. Chryssikos, E. I. Kamitsos, A. P. Patsis, M. S. Bitsis and M. A. Karakassides. The Devitrification of Lithium Metaborate:Polymorphism and Glass Formation. *J. Non-Cryst. Solids*, 126(1-2):42–51, 1990.

[230] T. Alekel and D. A. Keszler. The Pyroborate Fluoride $Ba_5(B_2O_5)F_2$. *J. Solid State Chem.*, 106(2):310–316, 1993.

[231] H. Muller-Bunz and T. Schleid. Two Fluoride Borates of Gadolinium: $Gd_2F_3[BO_3]$ and $Gd_3F_3[BO_3]_2$. *Z. Anorg. Allg. Chem.*, 628:2750–2756, 2002.

[232] D. Chakraburtty. The Structure of $BaBOF_3$. *Acta Crystallogr.*, 10(3):199–200, 1957.

[233] M. J. R. Clark and H. Lynton. The Existence of Salts of the Oxyfluoroborate Ion $[BF_3O]^{2-}$. *Can. J. Chem.*, 47:2943–2946, 1969.

[234] Y.-X. Huang, G. Schäfer, H. Borrmann, J.-T. Zhao and R. Kniep. $(C_2H_{10}N_2)[BPO_4F_2]$-Structural Relations between $[BPO_4F_2]^{2-}$ and $[Si_2O_6]^{4-}$. *Z. Anorg. Allg. Chem.*, 629(1):3–5, 2003.

[235] J. H. Von Barner, K. B. Andersen and R. W. Berg. Vibrational Spectroscopic Study on Fluorooxoborate Formation in Fluoride Melts:Indications of B_2OF_6 and $B_3O_3F_6$. *J. Mol. Liq.*, 83:141–151, 1999.

[236] G. Cakmak, J. Nuss and M. Jansen. LiB_6O_9F, the First Lithium Fluorooxoborate-Crystal Structure and Ionic Conductivity. *Z. Anorg. Allg. Chem.*, 635(4-5):631–636, 2009.

[237] Yu. F. Shepelev, R. S. Bubnova, S. K. Filatov, N. A. Sennova and N. A. Pilneva. LiB_3O_5 Crystal Structure at 20, 227, and 377 °C. *J. Solid State Chem.*, 178:2987–2997, 2005.

[238] M. Marezio, H. A. Plettinger and W. H. Zachariasen. The Bond Lengths in the Sodium Metaborate Structure. *Acta Crystallogr.*, 16:594–595, 1963.

[239] G. Brunton. Refinement of the Structure of $NaBF_4$. *Acta Crystallogr., Sect. B:Struct. Sci.*, 24(12):1703–1704, 1968.

[240] E. V. Sokolova, K. Yu. Egorov-Tismenko, S. V. Kargal'tsev, V. A. Klyakhin and V. S. Urnsov. Refinement of the Crystal Structure of Synthetic Fluorian Jeremejevite $Al_6(BO_3)_5F_3$. *Vestn. Mosk. Univ. Geol.*, 3:82–84, 1987.

[241] H. D. Fischer, W. J. Lehmann and I. Shapiro. Trifluoroboroxine: Preparation, Infrared Spectrum and Structure. *J. Phys. Chem.*, 65:1166–1168, 1961.

[242] A. Hooper. Fast Ionic Conductors. *Contemp. Phys.*, 19:147–168, 1978.

[243] G. C. Farrington and J. L. Briant. Fast Ionic Transport in Solids. *Science*, 204(4400):1371–1379, 1979.

[244] H. Bonadeo and E. Silberman. The Vibrational Spectra of Sodium, Potassium and Ammonium Fluoroborates. *Spectrochim. Acta Part A*, 26:2337–2343, 1970.

[245] T. W. Bril. PhD thesis, Eindhoven Technical University, Holland, 1976.

Part IV

Appendixes

Ionic conductivity data for as-synthesized PLEB polymer

Diameter: 0.06 cm   Thickness: 0.215 cm
        (2nd cycle)

T /K	R_1/Ω	Q_1	n_1	C_1 /F	log (σT)	log (σ)
384.15	2.32E6	6.54E-11	0.7648	4.4E-12	-3.90	-6.485
384.15	2.47E6	6.59E-11	0.7635	4.4E-12	-3.93	-6.512
382.15	2.79E6	6.11E-11	0.7671	4.4E-12	-3.98	-6.565
382.15	2.47E6	6.01E-11	0.7707	4.4E-12	-3.93	-6.512
383.15	2.44E6	6.53E-11	0.7653	4.5E-12	-3.92	-6.506
383.15	2.57E6	6.58E-11	0.7641	4.5E-12	-3.95	-6.529
382.15	2.75E6	6.61E-11	0.7628	4.5E-12	-3.98	-6.558
381.15	3.00E6	6.69E-11	0.7604	4.6E-12	-4.01	-6.596
381.15	3.30E6	6.70E-11	0.7589	4.6E-12	-4.06	-6.638
380.15	3.68E6	6.72E-11	0.7566	4.6E-12	-4.11	-6.685
379.15	4.12E6	6.60E-11	0.7561	4.7E-12	-4.16	-6.734
378.15	4.65E6	6.64E-11	0.7533	4.7E-12	-4.21	-6.787
376.15	5.25E6	6.46E-11	0.7531	4.7E-12	-4.26	-6.839
375.15	5.89E6	6.35E-11	0.7523	4.7E-12	-4.31	-6.889
374.15	6.62E6	6.33E-11	0.7502	4.8E-12	-4.37	-6.940
373.15	7.46E6	6.24E-11	0.7489	4.8E-12	-4.42	-6.992
372.15	8.45E6	6.14E-11	0.7479	4.8E-12	-4.47	-7.046
371.15	9.61E6	6.10E-11	0.7457	4.8E-12	-4.53	-7.102
370.15	1.09E7	6.03E-11	0.7437	4.8E-12	-4.59	-7.158
369.15	1.25E7	5.88E-11	0.7434	4.9E-12	-4.65	-7.214
368.15	1.45E7	5.92E-11	0.7395	4.9E-12	-4.71	-7.280
367.15	1.67E7	5.68E-11	0.7398	4.9E-12	-4.78	-7.341
366.15	1.93E7	5.54E-11	0.7387	4.9E-12	-4.84	-7.404
365.15	2.23E7	5.41E-11	0.7370	4.9E-12	-4.91	-7.468
363.15	2.59E7	5.34E-11	0.7346	5.0E-12	-4.97	-7.532
362.15	2.99E7	5.30E-11	0.7314	5.0E-12	-5.04	-7.595
361.15	3.45E7	5.02E-11	0.7332	5.0E-12	-5.10	-7.657
360.15	3.98E7	4.69E-11	0.7361	4.9E-12	-5.16	-7.719
359.15	4.61E7	4.52E-11	0.7362	4.9E-12	-5.23	-7.783
358.15	5.40E7	4.60E-11	0.7300	5.0E-12	-5.30	-7.851
357.15	6.28E7	4.23E-11	0.7341	4.9E-12	-5.36	-7.917
356.15	7.27E7	4.35E-11	0.7273	5.0E-12	-5.43	-7.981
355.15	8.57E7	4.35E-11	0.7236	5.1E-12	-5.50	-8.052
354.15	9.88E7	3.57E-11	0.7405	4.9E-12	-5.56	-8.114
353.15	1.16E8	4.07E-11	0.7205	5.1E-12	-5.64	-8.183
352.15	1.34E8	3.15E-11	0.7449	4.8E-12	-5.70	-8.245
351.15	1.56E8	3.14E-11	0.7388	4.8E-12	-5.77	-8.313
350.15	1.87E8	3.67E-11	0.7153	5.1E-12	-5.85	-8.390
349.15	2.12E8	3.18E-11	0.7300	5.0E-12	-5.90	-8.445
348.15	2.51E8	2.95E-11	0.7310	4.9E-12	-5.98	-8.519
346.15	3.41E8	2.87E-11	0.7273	5.1E-12	-6.11	-8.652
346.15	3.98E8	3.12E-11	0.7082	5.1E-12	-6.18	-8.718
345.15	4.53E8	2.45E-11	0.7346	4.8E-12	-6.24	-8.775
344.15	5.32E8	2.81E-11	0.7225	5.6E-12	-6.31	-8.845
343.15	6.11E8	2.51E-11	0.7231	5.1E-12	-6.37	-8.905
342.15	6.95E8	2.44E-11	0.7227	5.1E-12	-6.43	-8.961
340.15	1.09E9	2.24E-11	0.7233	5.4E-12	-6.62	-9.155
339.15	1.24E9	2.05E-11	0.7273	5.2E-12	-6.68	-9.212
338.15	1.61E9	1.72E-11	0.7535	5.3E-12	-6.80	-9.325
332.15	4.85E9	1.12E-11	0.7766	4.9E-12	-7.28	-9.804
331.15	6.38E9	1.05E-11	0.7733	4.8E-12	-7.40	-9.923
329.15	9.22E9	1.40E-11	0.7114	6.1E-12	-7.57	-10.084

Ionic conductivity data for annealed PLEB polymer

Diameter: 0.6 cm   Thickness: 0.075 cm

(2nd cycle)

T /K	R$_1$/Ω	Q$_1$	n$_1$	C$_1$ /F	log (σT)	log (σ)
551.15	1.44E5	1.48E-10	0.7902	8.5E-12	-2.99	-5.735
549.15	1.62E5	1.55E-10	0.7856	8.6E-12	-3.05	-5.787
548.15	1.55E5	1.29E-10	0.7978	8.3E-12	-3.03	-5.768
549.15	1.45E5	1.36E-10	0.7950	8.3E-12	-3.00	-5.738
551.15	1.42E5	1.43E-10	0.7917	8.4E-12	-2.99	-5.727
551.15	1.46E5	1.51E-10	0.7881	8.4E-12	-3.00	-5.739
550.15	1.54E5	1.54E-10	0.7861	8.5E-12	-3.02	-5.765
548.15	1.66E5	1.50E-10	0.7867	8.5E-12	-3.06	-5.797
547.15	1.64E5	1.37E-10	0.7929	8.3E-12	-3.05	-5.791
547.15	1.71E5	1.50E-10	0.7863	8.4E-12	-3.07	-5.808
545.15	1.84E5	1.54E-10	0.7837	8.5E-12	-3.10	-5.841
543.15	2.02E5	1.53E-10	0.7827	8.6E-12	-3.15	-5.881
540.15	2.02E5	1.34E-10	0.7911	8.4E-12	-3.15	-5.882
540.15	2.00E5	1.39E-10	0.7892	8.4E-12	-3.15	-5.878
540.15	2.06E5	1.44E-10	0.7865	8.5E-12	-3.16	-5.891
539.15	2.18E5	1.45E-10	0.7853	8.5E-12	-3.18	-5.916
538.15	2.36E5	1.45E-10	0.7843	8.6E-12	-3.22	-5.949
535.15	2.58E5	1.42E-10	0.7843	8.6E-12	-3.26	-5.988
533.15	2.64E5	1.42E-10	0.7843	8.6E-12	-3.27	-5.998
531.15	2.87E5	1.39E-10	0.7846	8.6E-12	-3.31	-6.034
529.15	3.11E5	1.38E-10	0.7842	8.6E-12	-3.35	-6.069
527.15	3.39E5	1.35E-10	0.7846	8.6E-12	-3.38	-6.106
525.15	3.39E5	1.25E-10	0.7895	8.5E-12	-3.39	-6.107
524.15	3.53E5	1.31E-10	0.7859	8.6E-12	-3.40	-6.124
523.15	3.80E5	1.32E-10	0.7847	8.7E-12	-3.44	-6.157
518.15	4.52E5	1.26E-10	0.7857	8.7E-12	-3.52	-6.231
516.15	4.52E5	1.23E-10	0.7871	8.7E-12	-3.52	-6.232
515.15	4.66E5	1.25E-10	0.7857	8.7E-12	-3.53	-6.245
514.15	4.93E5	1.26E-10	0.7844	8.8E-12	-3.56	-6.269
513.15	5.33E5	1.26E-10	0.7841	8.9E-12	-3.59	-6.303
510.15	5.87E5	1.18E-10	0.7870	8.8E-12	-3.64	-6.345
508.15	6.04E5	1.22E-10	0.7846	8.9E-12	-3.65	-6.357
507.15	6.43E5	1.24E-10	0.7830	9.0E-12	-3.68	-6.385
505.15	6.95E5	1.24E-10	0.7822	9.1E-12	-3.71	-6.418
503.15	7.58E5	1.21E-10	0.7831	9.2E-12	-3.75	-6.456
501.15	7.93E5	1.16E-10	0.7848	9.1E-12	-3.78	-6.476
500.15	7.84E5	1.17E-10	0.7846	9.1E-12	-3.77	-6.471
499.15	8.13E5	1.17E-10	0.7842	9.2E-12	-3.79	-6.486
498.15	8.85E5	1.20E-10	0.7818	9.3E-12	-3.83	-6.523
496.15	9.61E5	1.19E-10	0.7814	9.4E-12	-3.86	-6.559
491.15	1.10E6	1.14E-10	0.7829	9.4E-12	-3.93	-6.619
490.15	1.10E6	1.13E-10	0.7837	9.4E-12	-3.93	-6.618
490.15	1.12E6	1.14E-10	0.7825	9.4E-12	-3.93	-6.624
489.15	1.16E6	1.14E-10	0.7823	9.5E-12	-3.95	-6.640
488.15	1.24E6	1.14E-10	0.7823	9.7E-12	-3.98	-6.669
483.15	1.52E6	1.11E-10	0.7806	9.7E-12	-4.07	-6.759
482.15	1.52E6	1.09E-10	0.7817	9.6E-12	-4.08	-6.759
481.15	1.54E6	1.10E-10	0.7814	9.7E-12	-4.08	-6.763
481.15	1.59E6	1.11E-10	0.7801	9.7E-12	-4.10	-6.778
480.15	1.69E6	1.12E-10	0.7793	9.8E-12	-4.12	-6.804
478.15	1.82E6	1.11E-10	0.7791	9.9E-12	-4.16	-6.836
474.15	2.12E6	1.06E-10	0.7794	9.9E-12	-4.23	-6.902
473.15	2.15E6	1.05E-10	0.7798	9.9E-12	-4.23	-6.909
472.15	2.20E6	1.06E-10	0.7794	9.9E-12	-4.25	-6.920
471.15	2.31E6	1.06E-10	0.7789	1.0E-11	-4.27	-6.941
470.15	2.47E6	1.02E-10	0.7819	1.0E-11	-4.30	-6.970
467.15	2.78E6	1.04E-10	0.7777	1.0E-11	-4.35	-7.020
466.15	2.87E6	1.02E-10	0.7782	1.0E-11	-4.37	-7.034
465.15	2.95E6	1.01E-10	0.7783	1.0E-11	-4.38	-7.046
464.15	3.09E6	1.02E-10	0.7775	1.0E-11	-4.40	-7.066
462.15	3.29E6	1.02E-10	0.7766	1.0E-11	-4.43	-7.093
461.15	3.57E6	1.02E-10	0.7748	1.0E-11	-4.47	-7.130
459.15	3.69E6	9.92E-11	0.7765	1.0E-11	-4.48	-7.143
458.15	3.93E6	9.98E-11	0.7754	1.0E-11	-4.51	-7.171
456.15	4.18E6	9.95E-11	0.7748	1.0E-11	-4.54	-7.197
455.15	4.48E6	9.93E-11	0.7741	1.0E-11	-4.57	-7.228
451.15	5.25E6	9.72E-11	0.7730	1.0E-11	-4.64	-7.297
450.15	5.37E6	9.67E-11	0.7729	1.0E-11	-4.65	-7.307
449.15	5.55E6	9.63E-11	0.7729	1.1E-11	-4.67	-7.320
448.15	5.84E6	9.65E-11	0.7722	1.1E-11	-4.69	-7.343
447.15	6.27E6	9.76E-11	0.7701	1.1E-11	-4.72	-7.374
445.15	6.78E6	9.74E-11	0.7693	1.1E-11	-4.76	-7.407
444.15	7.38E6	9.60E-11	0.7691	1.1E-11	-4.80	-7.444
442.15	7.71E6	9.23E-11	0.7720	1.1E-11	-4.82	-7.463
440.15	8.18E6	9.35E-11	0.7697	1.1E-11	-4.85	-7.489

439.15	8.65E6	9.41E-11	0.7682	1.1E-11	-4.87	-7.513
438.15	9.23E6	9.38E-11	0.7678	1.1E-11	-4.90	-7.541
437.15	1.00E7	9.36E-11	0.7663	1.1E-11	-4.94	-7.578
435.15	1.01E7	8.88E-11	0.7711	1.1E-11	-4.94	-7.581
434.15	1.07E7	9.34E-11	0.7653	1.1E-11	-4.97	-7.607
433.15	1.14E7	9.32E-11	0.7644	1.1E-11	-5.00	-7.635
432.15	1.23E7	9.28E-11	0.7639	1.1E-11	-5.03	-7.666
430.15	1.33E7	9.11E-11	0.7644	1.2E-11	-5.07	-7.700
427.15	1.61E7	8.93E-11	0.7624	1.2E-11	-5.15	-7.782
425.15	1.67E7	8.95E-11	0.7611	1.2E-11	-5.17	-7.800
424.15	1.75E7	8.74E-11	0.7631	1.2E-11	-5.19	-7.819
423.15	1.92E7	9.00E-11	0.7580	1.2E-11	-5.23	-7.861
421.15	2.08E7	8.66E-11	0.7604	1.2E-11	-5.27	-7.893
419.15	2.27E7	8.62E-11	0.7590	1.2E-11	-5.31	-7.932
416.15	2.66E7	8.21E-11	0.7602	1.2E-11	-5.38	-8.002
415.15	2.78E7	8.21E-11	0.7595	1.2E-11	-5.40	-8.021
414.15	2.93E7	8.51E-11	0.7542	1.2E-11	-5.43	-8.042
413.15	3.07E7	7.95E-11	0.7605	1.2E-11	-5.45	-8.064
411.15	3.36E7	8.39E-11	0.7525	1.2E-11	-5.49	-8.103
410.15	3.64E7	8.39E-11	0.7513	1.2E-11	-5.52	-8.137
408.15	3.94E7	8.12E-11	0.7523	1.2E-11	-5.56	-8.172
407.15	4.38E7	8.24E-11	0.7493	1.3E-11	-5.61	-8.218
405.15	4.69E7	7.78E-11	0.7527	1.2E-11	-5.64	-8.248
403.15	4.96E7	8.00E-11	0.7491	1.3E-11	-5.67	-8.272
402.15	5.35E7	7.73E-11	0.7516	1.3E-11	-5.70	-8.305
395.15	7.73E7	7.11E-11	0.7518	1.3E-11	-5.87	-8.465
394.15	8.34E7	7.23E-11	0.7478	1.3E-11	-5.90	-8.497
391.15	9.60E7	6.73E-11	0.7516	1.3E-11	-5.97	-8.559
390.15	1.04E8	6.88E-11	0.7468	1.3E-11	-6.00	-8.593
388.15	1.14E8	6.89E-11	0.7422	1.3E-11	-6.04	-8.633
387.15	1.24E8	6.95E-11	0.7383	1.3E-11	-6.08	-8.669
384.15	1.47E8	6.81E-11	0.7427	1.4E-11	-6.16	-8.743
382.15	1.61E8	6.70E-11	0.7375	1.3E-11	-6.20	-8.782
380.15	1.79E8	6.55E-11	0.7423	1.4E-11	-6.25	-8.830
379.15	1.94E8	6.57E-11	0.7327	1.3E-11	-6.29	-8.865
377.15	2.08E8	5.95E-11	0.7504	1.4E-11	-6.32	-8.894
376.15	2.24E8	5.85E-11	0.7449	1.3E-11	-6.35	-8.927
375.15	2.43E8	6.33E-11	0.7332	1.4E-11	-6.39	-8.961
373.15	2.64E8	5.99E-11	0.7342	1.3E-11	-6.43	-8.997
372.15	2.84E8	5.80E-11	0.7364	1.3E-11	-6.46	-9.029
371.15	3.11E8	6.38E-11	0.7226	1.4E-11	-6.50	-9.069
369.15	3.39E8	5.17E-11	0.7568	1.4E-11	-6.54	-9.107
368.15	3.71E8	6.31E-11	0.7203	1.5E-11	-6.58	-9.146
367.15	3.97E8	6.08E-11	0.7250	1.5E-11	-6.61	-9.176
365.15	4.32E8	5.65E-11	0.7299	1.4E-11	-6.65	-9.212
364.15	4.63E8	5.36E-11	0.7312	1.4E-11	-6.68	-9.242
362.15	5.32E8	5.12E-11	0.7312	1.4E-11	-6.74	-9.302
360.15	5.79E8	5.38E-11	0.7284	1.5E-11	-6.78	-9.339
359.15	6.21E8	5.22E-11	0.7284	1.5E-11	-6.81	-9.370
358.15	6.79E8	5.34E-11	0.7197	1.5E-11	-6.85	-9.408
357.15	7.44E8	5.04E-11	0.7326	1.5E-11	-6.89	-9.448
353.15	8.96E8	4.40E-11	0.7431	1.4E-11	-6.98	-9.529
348.15	1.29E9	4.53E-11	0.7164	1.5E-11	-7.15	-9.688
347.15	1.41E9	4.67E-11	0.7211	1.6E-11	-7.18	-9.725
346.15	1.47E9	4.06E-11	0.7396	1.5E-11	-7.20	-9.743
345.15	1.55E9	4.31E-11	0.7239	1.5E-11	-7.23	-9.766
343.15	1.84E9	3.74E-11	0.7415	1.5E-11	-7.31	-9.842
340.15	2.23E9	3.93E-11	0.7352	1.6E-11	-7.39	-9.925
339.15	2.54E9	4.05E-11	0.7208	1.7E-11	-7.45	-9.982
336.15	3.22E9	4.11E-11	0.7081	1.8E-11	-7.56	-10.084
334.15	3.71E9	3.79E-11	0.7117	1.7E-11	-7.62	-10.145
330.15	4.56E9	3.30E-11	0.7225	1.6E-11	-7.72	-10.236
329.15	5.45E9	3.55E-11	0.7037	1.8E-11	-7.80	-10.313
327.15	6.43E9	3.23E-11	0.7097	1.7E-11	-7.87	-10.385
322.15	8.97E9	2.72E-11	0.7276	1.6E-11	-8.02	-10.529
318.15	1.21E10	2.61E-11	0.7235	1.7E-11	-8.16	-10.658
316.15	1.43E10	2.70E-11	0.6990	1.8E-11	-8.23	-10.732
314.15	1.58E10	2.07E-11	0.7665	1.5E-11	-8.28	-10.775
313.15	1.68E10	2.13E-11	0.7449	1.5E-11	-8.31	-10.802
312.15	1.99E10	2.05E-11	0.7380	1.5E-11	-8.38	-10.876
311.15	1.97E10	2.18E-11	0.7371	1.6E-11	-8.38	-10.871
308.15	2.42E10	1.90E-11	0.7569	1.5E-11	-8.47	-10.961
307.15	2.54E10	1.55E-11	0.7615	1.2E-11	-8.49	-10.981
306.15	2.87E10	1.74E-11	0.7607	1.4E-11	-8.55	-11.034
304.15	3.27E10	1.60E-11	0.7570	1.3E-11	-8.61	-11.090
303.15	4.49E10	1.73E-11	0.7463	1.6E-11	-8.75	-11.229

Ionic conductivity data for as-synthesized PLEPB polymer

Diameter: 0.6 cm   Thickness: 0.08 cm
    (2nd cycle)

T /K	R_1/Ω	Q_1	n_1	C_1 /F	$\log(\sigma T)$	$\log(\sigma)$
381.15	1.33E5	3.19E-10	0.8095	3.0E-11	-3.09	-5.672
382.15	1.26E5	3.33E-10	0.8070	3.0E-11	-3.07	-5.650
382.15	1.24E5	3.48E-10	0.8042	3.0E-11	-3.06	-5.640
383.15	1.24E5	3.59E-10	0.8018	3.0E-11	-3.06	-5.642
383.15	1.28E5	3.67E-10	0.7999	3.0E-11	-3.07	-5.655
382.15	1.34E5	3.72E-10	0.7983	3.0E-11	-3.09	-5.675
382.15	1.42E5	3.78E-10	0.7963	3.1E-11	-3.12	-5.702
381.15	1.66E5	3.73E-10	0.7951	3.1E-11	-3.19	-5.769
380.15	1.81E5	3.70E-10	0.7944	3.1E-11	-3.23	-5.807
379.15	1.99E5	3.66E-10	0.7938	3.1E-11	-3.27	-5.848
378.15	2.20E5	3.64E-10	0.7927	3.1E-11	-3.31	-5.891
377.15	2.44E5	3.58E-10	0.7924	3.1E-11	-3.36	-5.935
376.15	2.70E5	3.53E-10	0.7920	3.1E-11	-3.41	-5.980
374.15	3.01E5	3.47E-10	0.7914	3.1E-11	-3.45	-6.027
373.15	3.36E5	3.41E-10	0.7910	3.1E-11	-3.50	-6.074
372.15	3.75E5	3.35E-10	0.7906	3.1E-11	-3.55	-6.122
371.15	4.20E5	3.28E-10	0.7903	3.1E-11	-3.60	-6.171
370.15	4.70E5	3.22E-10	0.7897	3.1E-11	-3.65	-6.221
369.15	5.28E5	3.15E-10	0.7895	3.1E-11	-3.70	-6.271
368.15	5.93E5	3.09E-10	0.7892	3.1E-11	-3.76	-6.321
367.15	6.67E5	3.02E-10	0.7890	3.1E-11	-3.81	-6.372
366.15	7.49E5	2.94E-10	0.7889	3.1E-11	-3.86	-6.423
365.15	8.43E5	2.88E-10	0.7885	3.1E-11	-3.91	-6.474
363.15	9.49E5	2.81E-10	0.7887	3.1E-11	-3.97	-6.525
362.15	1.07E6	2.73E-10	0.7888	3.1E-11	-4.02	-6.577
361.15	1.20E6	2.67E-10	0.7885	3.1E-11	-4.07	-6.629
360.15	1.35E6	2.60E-10	0.7889	3.1E-11	-4.12	-6.680
359.15	1.52E6	2.52E-10	0.7893	3.1E-11	-4.18	-6.731
358.15	1.72E6	2.45E-10	0.7895	3.1E-11	-4.23	-6.784
357.15	1.94E6	2.39E-10	0.7896	3.1E-11	-4.28	-6.836
356.15	2.18E6	2.32E-10	0.7901	3.1E-11	-4.34	-6.888
355.15	2.47E6	2.30E-10	0.7887	3.1E-11	-4.39	-6.941
354.15	2.79E6	2.21E-10	0.7902	3.1E-11	-4.44	-6.994
353.15	3.54E6	2.09E-10	0.7905	3.1E-11	-4.55	-7.098
352.15	4.00E6	2.06E-10	0.7893	3.1E-11	-4.60	-7.151
351.15	4.51E6	2.02E-10	0.7887	3.1E-11	-4.66	-7.202
350.15	5.07E6	1.96E-10	0.7892	3.1E-11	-4.71	-7.254
349.15	5.73E6	1.94E-10	0.7877	3.1E-11	-4.76	-7.307
348.15	6.47E6	1.90E-10	0.7868	3.1E-11	-4.82	-7.359
347.15	8.25E6	1.81E-10	0.7865	3.1E-11	-4.92	-7.465
346.15	9.30E6	1.77E-10	0.7859	3.1E-11	-4.98	-7.517
345.15	1.05E7	1.73E-10	0.7855	3.1E-11	-5.03	-7.570
344.15	1.33E7	1.63E-10	0.7861	3.1E-11	-5.14	-7.673
343.15	1.51E7	1.56E-10	0.7881	3.1E-11	-5.19	-7.727
342.15	1.70E7	1.52E-10	0.7881	3.1E-11	-5.24	-7.778
341.15	1.92E7	1.46E-10	0.7902	3.1E-11	-5.30	-7.831
340.15	2.16E7	1.45E-10	0.7880	3.1E-11	-5.35	-7.883
340.15	2.44E7	1.42E-10	0.7880	3.1E-11	-5.40	-7.935
339.15	2.74E7	1.38E-10	0.7880	3.1E-11	-5.46	-7.986
338.15	3.52E7	1.35E-10	0.7827	3.1E-11	-5.57	-8.095
337.15	3.96E7	1.28E-10	0.7866	3.1E-11	-5.62	-8.146
336.15	4.46E7	1.27E-10	0.7844	3.1E-11	-5.67	-8.198
335.15	5.68E7	1.18E-10	0.7879	3.1E-11	-5.78	-8.302
334.15	6.41E7	1.17E-10	0.7860	3.1E-11	-5.83	-8.355
333.15	8.20E7	1.11E-10	0.7859	3.1E-11	-5.94	-8.462
332.15	9.21E7	9.93E-11	0.7960	3.0E-11	-5.99	-8.513
331.15	1.16E8	1.01E-10	0.7901	3.1E-11	-6.09	-8.614
330.15	1.47E8	9.35E-11	0.7895	3.0E-11	-6.20	-8.715
329.15	1.82E8	8.84E-11	0.7937	3.0E-11	-6.29	-8.809
328.15	2.05E8	8.55E-11	0.7925	3.0E-11	-6.34	-8.861
327.15	2.55E8	8.35E-11	0.7899	3.0E-11	-6.44	-8.955
326.15	3.16E8	7.70E-11	0.8008	3.1E-11	-6.53	-9.048
325.15	3.91E8	7.28E-11	0.7967	2.9E-11	-6.63	-9.141
324.15	4.35E8	6.94E-11	0.8025	2.9E-11	-6.68	-9.187
323.15	5.34E8	6.58E-11	0.8068	3.0E-11	-6.77	-9.276
322.15	8.10E8	6.17E-11	0.8089	3.0E-11	-6.95	-9.457
321.15	9.76E8	6.17E-11	0.7962	3.0E-11	-7.03	-9.538
320.15	1.18E9	5.77E-11	0.8072	3.0E-11	-7.12	-9.621
319.15	1.44E9	5.86E-11	0.7901	3.0E-11	-7.20	-9.707
318.15	1.73E9	5.34E-11	0.8069	3.0E-11	-7.28	-9.785
317.15	2.37E9	4.40E-11	0.8380	2.8E-11	-7.42	-9.923
316.15	2.76E9	4.59E-11	0.8186	2.9E-11	-7.49	-9.990
315.15	3.35E9	3.54E-11	0.8599	2.5E-11	-7.57	-10.073
314.15	4.33E9	3.42E-11	0.8611	2.5E-11	-7.69	-10.185
313.15	6.05E9	3.69E-11	0.8527	2.8E-11	-7.83	-10.330

312.15	8.03E9	3.05E-11	0.8532	2.4E-11	-7.96	-10.453
311.15	9.01E9	3.16E-11	0.8714	2.6E-11	-8.01	-10.503
311.15	1.08E10	3.31E-11	0.8452	2.7E-11	-8.09	-10.580
310.15	1.24E10	2.85E-11	0.8964	2.5E-11	-8.15	-10.642
309.15	1.44E10	2.48E-11	0.9384	2.3E-11	-8.22	-10.706
308.15	2.04E10	2.65E-11	0.8823	2.4E-11	-8.37	-10.858
307.15	2.59E10	2.58E-11	0.8631	2.4E-11	-8.47	-10.963

Ionic conductivity data for annealed PLEPB polymer

Diameter: 0.6 cm   Thickness: 0:155 cm

(2nd cycle)

T /K	R_1/Ω	Q_1	n_1	C_1 /F	$\log (\sigma T)$	$\log (\sigma)$
550.15	1.33E5	1.27E-10	0.7718	4.9E-12	-2.64	-5.384
550.15	1.43E5	1.38E-10	0.7658	5.0E-12	-2.68	-5.416
548.15	1.51E5	1.23E-10	0.7725	5.0E-12	-2.70	-5.439
548.15	1.40E5	1.14E-10	0.7778	4.9E-12	-2.67	-5.407
549.15	1.32E5	1.18E-10	0.7761	4.9E-12	-2.64	-5.382
550.15	1.32E5	1.26E-10	0.7720	4.9E-12	-2.64	-5.383
550.15	1.42E5	1.33E-10	0.7682	5.0E-12	-2.67	-5.413
548.15	1.58E5	1.40E-10	0.7640	5.1E-12	-2.72	-5.459
546.15	1.58E5	1.21E-10	0.7732	5.0E-12	-2.72	-5.458
546.15	1.53E5	1.20E-10	0.7740	4.9E-12	-2.71	-5.444
546.15	1.54E5	1.25E-10	0.7710	5.0E-12	-2.71	-5.450
545.15	1.67E5	1.35E-10	0.7659	5.1E-12	-2.75	-5.483
544.15	1.86E5	1.43E-10	0.7623	5.3E-12	-2.79	-5.530
541.15	2.08E5	1.37E-10	0.7640	5.4E-12	-2.85	-5.579
539.15	2.07E5	1.18E-10	0.7738	5.3E-12	-2.85	-5.577
537.15	2.31E5	1.29E-10	0.7683	5.6E-12	-2.89	-5.625
535.15	2.58E5	1.31E-10	0.7676	5.8E-12	-2.94	-5.673
533.15	2.73E5	1.19E-10	0.7721	5.7E-12	-2.97	-5.697
532.15	2.66E5	1.17E-10	0.7738	5.6E-12	-2.96	-5.686
532.15	2.65E5	1.13E-10	0.7762	5.6E-12	-2.96	-5.685
531.15	2.81E5	1.15E-10	0.7751	5.8E-12	-2.98	-5.709
530.15	3.06E5	1.12E-10	0.7784	6.0E-12	-3.02	-5.747
527.15	3.41E5	1.09E-10	0.7806	6.2E-12	-3.07	-5.794
525.15	3.62E5	1.03E-10	0.7831	6.1E-12	-3.10	-5.820
524.15	3.56E5	9.96E-11	0.7851	6.0E-12	-3.09	-5.812
524.15	3.54E5	9.16E-11	0.7917	6.0E-12	-3.09	-5.811
523.15	3.80E5	9.06E-11	0.7937	6.3E-12	-3.12	-5.840
521.15	4.16E5	8.74E-11	0.7976	6.5E-12	-3.16	-5.880
519.15	4.61E5	8.50E-11	0.8005	6.8E-12	-3.21	-5.924
517.15	4.78E5	8.92E-11	0.7950	6.7E-12	-3.23	-5.940
516.15	4.70E5	8.26E-11	0.8007	6.6E-12	-3.22	-5.933
516.15	4.80E5	7.86E-11	0.8048	6.7E-12	-3.23	-5.942
515.15	5.04E5	7.31E-11	0.8129	7.0E-12	-3.25	-5.964
513.15	5.36E5	6.12E-11	0.8305	7.4E-12	-3.28	-5.990
511.15	6.09E5	7.21E-11	0.8157	7.5E-12	-3.34	-6.046
509.15	6.07E5	7.07E-11	0.8163	7.3E-12	-3.34	-6.045
509.15	5.99E5	6.83E-11	0.8190	7.3E-12	-3.33	-6.039
509.15	6.11E5	6.37E-11	0.8251	7.4E-12	-3.34	-6.047
507.15	6.62E5	6.86E-11	0.8206	7.7E-12	-3.38	-6.082
506.15	7.21E5	6.61E-11	0.8259	8.1E-12	-3.41	-6.119
503.15	8.08E5	6.90E-11	0.8222	8.3E-12	-3.47	-6.169
501.15	8.56E5	6.95E-11	0.8189	8.1E-12	-3.49	-6.194
500.15	8.72E5	6.31E-11	0.8273	8.1E-12	-3.50	-6.202
499.15	9.25E5	6.44E-11	0.8280	8.5E-12	-3.53	-6.227
497.15	1.00E6	6.30E-11	0.8318	8.9E-12	-3.56	-6.261
495.15	1.11E6	6.67E-11	0.8264	9.0E-12	-3.61	-6.307
493.15	1.14E6	6.54E-11	0.8266	8.9E-12	-3.63	-6.320
492.15	1.16E6	6.33E-11	0.8292	8.9E-12	-3.64	-6.327
491.15	1.22E6	6.36E-11	0.8297	9.1E-12	-3.66	-6.348
490.15	1.32E6	6.35E-11	0.8311	9.4E-12	-3.69	-6.380
488.15	1.45E6	6.73E-11	0.8245	9.4E-12	-3.73	-6.422
487.15	1.47E6	6.41E-11	0.8286	9.4E-12	-3.74	-6.427
486.15	1.47E6	6.19E-11	0.8319	9.4E-12	-3.74	-6.430
485.15	1.54E6	6.24E-11	0.8315	9.6E-12	-3.76	-6.447
484.15	1.65E6	6.28E-11	0.8318	9.8E-12	-3.79	-6.478
481.15	1.95E6	6.81E-11	0.8214	9.8E-12	-3.87	-6.551
479.15	2.04E6	6.69E-11	0.8229	9.8E-12	-3.89	-6.570

478.15	2.19E6	6.78E-11	0.8221	1.0E-11	-3.92	-6.601
474.15	2.69E6	7.11E-11	0.8137	1.0E-11	-4.01	-6.691
472.15	2.80E6	7.01E-11	0.8140	1.0E-11	-4.03	-6.708
471.15	2.94E6	6.90E-11	0.8154	1.0E-11	-4.06	-6.729
468.15	3.45E6	7.33E-11	0.8056	9.9E-12	-4.13	-6.798
466.15	3.56E6	7.13E-11	0.8075	9.9E-12	-4.14	-6.812
465.15	3.73E6	7.01E-11	0.8086	1.0E-11	-4.17	-6.833
464.15	3.98E6	6.91E-11	0.8095	1.0E-11	-4.19	-6.861
462.15	4.42E6	7.34E-11	0.8007	1.0E-11	-4.24	-6.907
461.15	4.61E6	7.35E-11	0.7991	9.9E-12	-4.26	-6.925
460.15	4.79E6	7.21E-11	0.8004	9.9E-12	-4.28	-6.941
459.15	5.18E6	7.83E-11	0.7918	1.0E-11	-4.31	-6.975
457.15	5.80E6	8.11E-11	0.7852	1.0E-11	-4.36	-7.025
455.15	6.06E6	7.67E-11	0.7893	9.9E-12	-4.39	-7.044
454.15	6.34E6	7.54E-11	0.7893	9.8E-12	-4.41	-7.063
453.15	6.80E6	8.07E-11	0.7817	9.9E-12	-4.44	-7.093
451.15	7.32E6	8.32E-11	0.7784	1.0E-11	-4.47	-7.126
450.15	8.10E6	8.36E-11	0.7739	9.9E-12	-4.52	-7.170
448.15	8.45E6	8.24E-11	0.7740	9.9E-12	-4.54	-7.188
447.15	8.77E6	8.13E-11	0.7747	9.9E-12	-4.55	-7.204
446.15	9.35E6	8.11E-11	0.7736	9.9E-12	-4.58	-7.232
445.15	1.03E7	7.80E-11	0.7738	9.7E-12	-4.62	-7.273
443.15	1.12E7	7.88E-11	0.7706	9.7E-12	-4.66	-7.311
441.15	1.19E7	7.60E-11	0.7727	9.7E-12	-4.69	-7.335
440.15	1.25E7	7.86E-11	0.7681	9.7E-12	-4.72	-7.359
439.15	1.35E7	7.88E-11	0.7667	9.8E-12	-4.75	-7.392
437.15	1.46E7	7.53E-11	0.7684	9.7E-12	-4.78	-7.426
436.15	1.50E7	7.97E-11	0.7611	9.6E-12	-4.80	-7.437
436.15	1.48E7	7.70E-11	0.7654	9.7E-12	-4.79	-7.432
435.15	1.53E7	7.46E-11	0.7675	9.6E-12	-4.81	-7.447
434.15	1.68E7	7.77E-11	0.7594	9.5E-12	-4.85	-7.487
433.15	1.82E7	7.88E-11	0.7573	9.7E-12	-4.88	-7.521
432.15	2.04E7	7.66E-11	0.7559	9.5E-12	-4.93	-7.570
428.15	2.36E7	6.82E-11	0.7654	9.5E-12	-5.00	-7.634
426.15	2.54E7	7.21E-11	0.7561	9.4E-12	-5.04	-7.666
425.15	2.68E7	7.33E-11	0.7539	9.6E-12	-5.06	-7.689
424.15	2.95E7	7.12E-11	0.7523	9.3E-12	-5.10	-7.731
422.15	3.25E7	6.94E-11	0.7528	9.4E-12	-5.15	-7.773
418.15	3.93E7	6.21E-11	0.7598	9.3E-12	-5.23	-7.855
416.15	4.12E7	6.05E-11	0.7619	9.3E-12	-5.26	-7.876
415.15	4.55E7	6.18E-11	0.7541	9.1E-12	-5.30	-7.919
414.15	4.95E7	6.23E-11	0.7501	9.1E-12	-5.34	-7.956
412.15	5.25E7	6.31E-11	0.7491	9.3E-12	-5.37	-7.982
408.15	6.46E7	5.79E-11	0.7511	9.1E-12	-5.46	-8.071
407.15	6.79E7	5.64E-11	0.7543	9.2E-12	-5.48	-8.093
405.15	7.22E7	5.03E-11	0.7645	8.9E-12	-5.51	-8.120
404.15	7.79E7	4.72E-11	0.7710	8.9E-12	-5.55	-8.153
402.15	9.43E7	6.30E-11	0.7292	9.4E-12	-5.63	-8.235
401.15	9.91E7	6.52E-11	0.7245	9.6E-12	-5.65	-8.257
399.15	1.20E8	6.04E-11	0.7216	9.0E-12	-5.74	-8.339
397.15	1.26E8	6.13E-11	0.7215	9.4E-12	-5.76	-8.362
395.15	1.31E8	5.55E-11	0.7268	8.7E-12	-5.78	-8.377
394.15	1.41E8	5.57E-11	0.7260	8.9E-12	-5.81	-8.409
392.15	1.43E8	3.18E-11	0.8022	8.4E-12	-5.82	-8.416
390.15	1.62E8	3.37E-11	0.7817	7.9E-12	-5.88	-8.470
389.15	2.09E8	6.42E-11	0.6917	9.4E-12	-5.99	-8.581
387.15	2.05E8	5.81E-11	0.7027	8.9E-12	-5.99	-8.573
385.15	2.27E8	5.51E-11	0.7096	9.2E-12	-6.03	-8.617
384.15	2.15E8	2.66E-11	0.8120	8.1E-12	-6.01	-8.594
383.15	2.67E8	4.88E-11	0.7114	8.4E-12	-6.10	-8.687
381.15	3.08E8	5.70E-11	0.6857	8.9E-12	-6.17	-8.749
380.15	3.33E8	5.52E-11	0.6950	9.6E-12	-6.20	-8.783
378.15	3.65E8	5.15E-11	0.6910	8.7E-12	-6.25	-8.824
377.15	4.05E8	5.59E-11	0.6771	9.2E-12	-6.29	-8.869
375.15	4.15E8	4.29E-11	0.7124	8.4E-12	-6.30	-8.879
374.15	4.92E8	4.82E-11	0.6851	8.6E-12	-6.38	-8.953
372.15	5.18E8	4.48E-11	0.6929	8.5E-12	-6.40	-8.975
371.15	5.92E8	4.41E-11	0.6912	8.7E-12	-6.46	-9.034
369.15	6.44E8	4.61E-11	0.6838	9.1E-12	-6.50	-9.070
368.15	6.46E8	3.88E-11	0.7273	9.7E-12	-6.51	-9.071
366.15	6.27E8	2.76E-11	0.7970	9.8E-12	-6.49	-9.058
365.15	9.88E8	5.79E-11	0.6365	1.1E-11	-6.69	-9.256
363.15	1.05E9	5.54E-11	0.6359	1.1E-11	-6.72	-9.281
359.15	1.35E9	4.87E-11	0.6322	1.0E-11	-6.84	-9.392
358.15	1.41E9	3.70E-11	0.6890	9.8E-12	-6.86	-9.412
355.15	1.73E9	4.58E-11	0.6261	1.0E-11	-6.95	-9.498
354.15	1.82E9	3.33E-11	0.6824	9.0E-12	-6.97	-9.520
353.15	1.98E9	3.17E-11	0.7139	1.0E-11	-7.01	-9.557
352.15	2.02E9	2.79E-11	0.7058	8.4E-12	-7.02	-9.566
351.15	2.19E9	3.36E-11	0.6819	1.0E-11	-7.06	-9.602
350.15	2.59E9	2.91E-11	0.7031	9.8E-12	-7.13	-9.674
348.15	2.86E9	3.41E-11	0.6518	9.8E-12	-7.18	-9.718
347.15	2.92E9	2.76E-11	0.7055	9.7E-12	-7.19	-9.726
346.15	3.29E9	2.40E-11	0.7277	9.3E-12	-7.24	-9.779
344.15	3.35E9	2.38E-11	0.7361	9.6E-12	-7.25	-9.786
343.15	3.39E9	1.97E-11	0.7506	8.0E-12	-7.26	-9.791
341.15	4.74E9	3.25E-11	0.6116	9.9E-12	-7.40	-9.937

340.15	4.22E9	1.64E-11	0.7759	7.6E-12	-7.35	-9.886
339.15	4.51E9	2.03E-11	0.7308	8.4E-12	-7.39	-9.915
338.15	4.76E9	2.05E-11	0.7337	8.8E-12	-7.41	-9.938
334.15	7.45E9	2.26E-11	0.6704	9.4E-12	-7.61	-10.133
331.15	7.80E9	1.76E-11	0.7462	8.9E-12	-7.63	-10.153
331.15	1.10E10	2.07E-11	0.7099	1.1E-11	-7.78	-10.304
329.15	9.58E9	1.42E-11	0.7607	7.6E-12	-7.73	-10.243
328.15	9.84E9	1.84E-11	0.7000	8.8E-12	-7.74	-10.254
326.15	1.54E10	1.90E-11	0.7090	1.2E-11	-7.94	-10.449
325.15	1.27E10	1.68E-11	0.7245	9.3E-12	-7.85	-10.364
319.15	2.61E10	1.61E-11	0.7200	1.2E-11	-8.17	-10.677
318.15	2.74E10	1.67E-11	0.6540	1.1E-11	-8.20	-10.698
317.15	2.39E10	1.17E-11	0.8475	9.3E-12	-8.14	-10.639
315.15	2.80E10	1.15E-11	0.7252	7.5E-12	-8.21	-10.709
314.15	3.21E10	1.56E-11	0.7150	1.2E-11	-8.27	-10.767
313.15	4.87E10	1.85E-11	0.6694	1.8E-11	-8.45	-10.949
313.15	5.54E10	1.45E-11	0.6522	1.3E-11	-8.51	-11.005
312.15	2.95E10	1.19E-11	0.7585	8.6E-12	-8.24	-10.731
312.15	3.20E10	8.57E-12	0.8603	6.9E-12	-8.27	-10.767
310.15	3.36E10	9.20E-12	0.8697	7.7E-12	-8.30	-10.788
309.15	4.40E10	8.25E-12	0.7652	6.0E-12	-8.41	-10.904
308.15	3.11E10	5.09E-12	0.9634	4.7E-12	-8.27	-10.754
307.15	3.75E10	8.45E-12	0.8564	7.0E-12	-8.35	-10.835

Ionic conductivity data for as-synthesized PLEMB polymer

Diameter: 0.6 cm   Thickness: 0.15 cm

     (2nd cycle)

T /K	R_1/Ω	Q_1	n_1	C_1 /F	log (σT)	log (σ)
423.15	1.32E7	1.08E-10	0.7026	6.8E-12	-4.77	-7.397
423.15	1.40E7	1.09E-10	0.6996	6.7E-12	-4.79	-7.421
422.15	1.54E7	9.53E-11	0.7067	6.4E-12	-4.84	-7.462
422.15	1.44E7	9.22E-11	0.7107	6.2E-12	-4.81	-7.435
422.15	1.37E7	9.55E-11	0.7081	6.2E-12	-4.79	-7.413
423.15	1.35E7	9.64E-11	0.7070	6.1E-12	-4.78	-7.406
423.15	1.37E7	9.50E-11	0.7069	6.1E-12	-4.79	-7.414
423.15	1.44E7	9.31E-11	0.7065	6.0E-12	-4.81	-7.435
423.15	1.57E7	9.22E-11	0.7041	5.9E-12	-4.84	-7.470
422.15	1.72E7	8.51E-11	0.7085	5.8E-12	-4.88	-7.510
421.15	1.95E7	8.34E-11	0.7065	5.8E-12	-4.94	-7.565
420.15	2.21E7	8.16E-11	0.7042	5.7E-12	-5.00	-7.620
419.15	2.48E7	7.64E-11	0.7069	5.7E-12	-5.05	-7.669
417.15	2.82E7	6.73E-11	0.7144	5.5E-12	-5.11	-7.726
416.15	3.29E7	7.03E-11	0.7055	5.6E-12	-5.17	-7.792
414.15	3.71E7	6.09E-11	0.7158	5.4E-12	-5.23	-7.844
413.15	4.34E7	6.05E-11	0.7116	5.4E-12	-5.30	-7.913
411.15	5.00E7	5.61E-11	0.7143	5.3E-12	-5.36	-7.975
409.15	5.88E7	5.29E-11	0.7151	5.3E-12	-5.43	-8.044
408.15	6.81E7	5.33E-11	0.7099	5.4E-12	-5.50	-8.108
406.15	8.07E7	5.13E-11	0.7075	5.3E-12	-5.57	-8.182
404.15	9.19E7	4.81E-11	0.7101	5.3E-12	-5.63	-8.239
403.15	1.09E8	4.81E-11	0.7068	5.5E-12	-5.71	-8.312
401.15	1.26E8	4.30E-11	0.7134	5.3E-12	-5.77	-8.377
398.15	1.71E8	4.30E-11	0.7047	5.5E-12	-5.91	-8.509
397.15	1.95E8	4.01E-11	0.7030	5.2E-12	-5.97	-8.565
394.15	2.71E8	4.10E-11	0.6934	5.6E-12	-6.11	-8.708
392.15	3.06E8	3.15E-11	0.7160	5.0E-12	-6.17	-8.761
391.15	3.53E8	3.21E-11	0.7046	4.9E-12	-6.23	-8.823
390.15	4.07E8	2.65E-11	0.7218	4.6E-12	-6.29	-8.885
386.15	6.29E8	2.78E-11	0.7085	5.3E-12	-6.49	-9.074
383.15	8.22E8	2.48E-11	0.7053	4.9E-12	-6.61	-9.190
382.15	9.58E8	2.47E-11	0.7102	5.3E-12	-6.67	-9.257
380.15	1.07E9	1.91E-11	0.7295	4.5E-12	-6.73	-9.305
379.15	1.27E9	2.40E-11	0.7007	5.4E-12	-6.80	-9.380
378.15	1.48E9	2.40E-11	0.6769	4.9E-12	-6.87	-9.446
377.15	1.65E9	1.64E-11	0.7141	3.9E-12	-6.92	-9.492
376.15	1.82E9	1.26E-11	0.7981	4.9E-12	-6.96	-9.535
374.15	2.10E9	1.59E-11	0.7311	4.6E-12	-7.03	-9.598
367.15	5.37E9	1.16E-11	0.7480	4.6E-12	-7.44	-10.005
356.15	2.34E10	6.98E-12	0.7868	4.3E-12	-8.09	-10.644
347.15	6.31E10	4.70E-12	0.8419	3.7E-12	-8.53	-11.075
343.15	1.56E11	4.15E-12	0.7711	3.6E-12	-8.93	-11.469

Ionic conductivity data for annealed PLEMB polymer

Diameter: 0.6 cm   Thickness: 0.03 cm

    (2nd cycle)

T /K	R_1/Ω	Q_1	n_1	C_1 /F	log (σT)	log (σ)
627.15	2.98E3	6.10E-12	0.9998	6.1E-12	-1.65	-4.449
626.15	3.17E3	7.37E-12	0.9888	6.0E-12	-1.68	-4.475
625.15	2.99E3	4.74E-12	1.0142	6.1E-12	-1.65	-4.450
626.15	3.02E3	6.53E-12	0.9958	6.1E-12	-1.66	-4.455
625.15	3.21E3	7.86E-12	0.9851	6.0E-12	-1.69	-4.481
623.15	3.30E3	6.45E-12	0.9963	6.0E-12	-1.70	-4.493
624.15	3.10E3	5.40E-12	1.0066	6.1E-12	-1.67	-4.465
626.15	2.98E3	5.82E-12	1.0024	6.1E-12	-1.65	-4.449
626.15	3.02E3	6.73E-12	0.9940	6.1E-12	-1.66	-4.454
625.15	3.18E3	7.90E-12	0.9848	6.0E-12	-1.68	-4.477
624.15	3.20E3	6.17E-12	0.9989	6.1E-12	-1.68	-4.480
625.15	3.07E3	5.94E-12	1.0012	6.1E-12	-1.66	-4.461
626.15	3.04E3	6.66E-12	0.9946	6.1E-12	-1.66	-4.457
625.15	3.16E3	7.75E-12	0.9858	6.0E-12	-1.68	-4.473
623.15	3.37E3	8.93E-12	0.9776	6.0E-12	-1.71	-4.501
621.15	3.58E3	9.07E-12	0.9764	6.0E-12	-1.73	-4.528
620.15	3.50E3	7.63E-12	0.9863	6.0E-12	-1.73	-4.519
621.15	3.48E3	8.63E-12	0.9793	6.0E-12	-1.72	-4.515
619.15	3.68E3	1.02E-11	0.9695	6.0E-12	-1.75	-4.540
617.15	3.95E3	1.20E-11	0.9602	5.9E-12	-1.78	-4.571
615.15	4.13E3	1.07E-11	0.9666	5.9E-12	-1.80	-4.591
613.15	4.41E3	1.51E-11	0.9466	5.9E-12	-1.83	-4.619
611.15	4.83E3	1.93E-11	0.9325	6.0E-12	-1.87	-4.659
609.15	4.80E3	1.45E-11	0.9488	6.0E-12	-1.87	-4.656
608.15	4.99E3	1.80E-11	0.9362	6.0E-12	-1.89	-4.672
607.15	5.42E3	2.29E-11	0.9223	6.0E-12	-1.92	-4.708
604.15	5.94E3	2.37E-11	0.9200	6.0E-12	-1.97	-4.748
603.15	6.03E3	1.71E-11	0.9388	6.0E-12	-1.97	-4.755
602.15	6.58E3	5.39E-11	0.8722	6.1E-12	-2.01	-4.793
600.15	7.06E3	5.46E-11	0.8709	6.1E-12	-2.04	-4.823
598.15	7.69E3	5.99E-11	0.8649	6.1E-12	-2.08	-4.860
596.15	7.77E3	4.36E-11	0.8830	6.1E-12	-2.09	-4.865
595.15	8.05E3	5.67E-11	0.8675	6.1E-12	-2.11	-4.880
593.15	8.67E3	6.37E-11	0.8601	6.1E-12	-2.14	-4.912
590.15	9.36E3	6.29E-11	0.8603	6.1E-12	-2.17	-4.946
589.15	9.49E3	6.17E-11	0.8613	6.1E-12	-2.18	-4.951
588.15	9.96E3	6.80E-11	0.8552	6.1E-12	-2.20	-4.973
586.15	1.07E4	7.80E-11	0.8466	6.2E-12	-2.24	-5.004
583.15	1.11E4	7.36E-11	0.8497	6.2E-12	-2.26	-5.021
582.15	1.17E4	8.13E-11	0.8434	6.2E-12	-2.28	-5.044
580.15	1.26E4	8.72E-11	0.8387	6.2E-12	-2.31	-5.073
577.15	1.35E4	8.57E-11	0.8390	6.2E-12	-2.34	-5.103
576.15	1.35E4	8.06E-11	0.8426	6.2E-12	-2.34	-5.103
575.15	1.41E4	8.83E-11	0.8368	6.2E-12	-2.36	-5.122
573.15	1.51E4	9.38E-11	0.8326	6.2E-12	-2.39	-5.152
570.15	1.64E4	8.85E-11	0.8351	6.2E-12	-2.43	-5.188
569.15	1.63E4	7.71E-11	0.8434	6.2E-12	-2.43	-5.186
568.15	1.70E4	9.16E-11	0.8328	6.2E-12	-2.45	-5.204
566.15	1.79E4	9.56E-11	0.8297	6.3E-12	-2.48	-5.228
564.15	1.93E4	1.03E-10	0.8247	6.3E-12	-2.51	-5.259
562.15	2.00E4	8.67E-11	0.8344	6.2E-12	-2.53	-5.276
561.15	2.02E4	9.22E-11	0.8306	6.3E-12	-2.53	-5.279
560.15	2.10E4	9.66E-11	0.8274	6.3E-12	-2.55	-5.296
558.15	2.23E4	9.98E-11	0.8249	6.3E-12	-2.58	-5.322
556.15	2.39E4	1.02E-10	0.8227	6.3E-12	-2.61	-5.353
554.15	2.45E4	8.53E-11	0.8333	6.2E-12	-2.62	-5.363
553.15	2.51E4	9.43E-11	0.8270	6.3E-12	-2.63	-5.373
552.15	2.61E4	9.70E-11	0.8249	6.3E-12	-2.65	-5.392
550.15	2.77E4	9.96E-11	0.8227	6.3E-12	-2.68	-5.416
548.15	2.95E4	1.00E-10	0.8216	6.3E-12	-2.70	-5.444
546.15	3.00E4	9.14E-11	0.8271	6.3E-12	-2.71	-5.451
545.15	3.09E4	9.45E-11	0.8248	6.3E-12	-2.73	-5.464
544.15	3.24E4	9.82E-11	0.8220	6.3E-12	-2.75	-5.484
542.15	3.44E4	1.01E-10	0.8197	6.4E-12	-2.78	-5.511
540.15	3.69E4	9.15E-11	0.8250	6.3E-12	-2.81	-5.541
539.15	3.66E4	9.17E-11	0.8249	6.3E-12	-2.81	-5.537
538.15	3.76E4	9.46E-11	0.8228	6.3E-12	-2.82	-5.549
537.15	3.92E4	9.66E-11	0.8210	6.4E-12	-2.84	-5.568
536.15	4.17E4	9.83E-11	0.8193	6.4E-12	-2.86	-5.594
534.15	4.44E4	9.59E-11	0.8202	6.4E-12	-2.89	-5.621
531.15	4.67E4	9.00E-11	0.8236	6.4E-12	-2.92	-5.644
530.15	4.72E4	8.95E-11	0.8238	6.4E-12	-2.92	-5.648
529.15	4.83E4	9.13E-11	0.8224	6.4E-12	-2.93	-5.658
528.15	5.04E4	9.32E-11	0.8207	6.4E-12	-2.95	-5.677
527.15	5.38E4	9.50E-11	0.8188	6.4E-12	-2.98	-5.705

525.15	5.73E4	9.24E-11	0.8198	6.4E-12	-3.01	-5.733
523.15	5.86E4	8.40E-11	0.8256	6.4E-12	-3.02	-5.742
522.15	5.90E4	8.58E-11	0.8242	6.4E-12	-3.03	-5.745
521.15	6.08E4	8.76E-11	0.8226	6.4E-12	-3.04	-5.758
520.15	6.35E4	8.79E-11	0.8219	6.4E-12	-3.06	-5.777
519.15	6.73E4	8.81E-11	0.8212	6.4E-12	-3.09	-5.802
517.15	7.21E4	9.25E-11	0.8174	6.5E-12	-3.12	-5.832
515.15	7.41E4	8.05E-11	0.8260	6.4E-12	-3.13	-5.844
514.15	7.41E4	8.01E-11	0.8264	6.4E-12	-3.13	-5.844
513.15	7.67E4	8.27E-11	0.8239	6.4E-12	-3.15	-5.859
512.15	8.01E4	8.25E-11	0.8236	6.4E-12	-3.17	-5.878
511.15	8.47E4	8.18E-11	0.8236	6.4E-12	-3.19	-5.902
509.15	8.97E4	7.78E-11	0.8263	6.4E-12	-3.22	-5.927
507.15	9.44E4	7.56E-11	0.8276	6.4E-12	-3.24	-5.949
506.15	9.63E4	7.56E-11	0.8274	6.4E-12	-3.25	-5.958
505.15	9.97E4	7.62E-11	0.8266	6.4E-12	-3.27	-5.973
504.15	1.05E5	7.60E-11	0.8263	6.4E-12	-3.29	-5.994
502.15	1.11E5	7.50E-11	0.8266	6.4E-12	-3.32	-6.020
500.15	1.19E5	7.77E-11	0.8236	6.5E-12	-3.35	-6.050
498.15	1.25E5	6.98E-11	0.8301	6.4E-12	-3.37	-6.071
497.15	1.26E5	6.82E-11	0.8316	6.4E-12	-3.38	-6.074
496.15	1.27E5	6.87E-11	0.8311	6.4E-12	-3.38	-6.078
496.15	1.30E5	6.92E-11	0.8304	6.4E-12	-3.39	-6.088
495.15	1.35E5	6.94E-11	0.8298	6.5E-12	-3.41	-6.105
494.15	1.42E5	6.85E-11	0.8302	6.5E-12	-3.43	-6.127
492.15	1.51E5	6.76E-11	0.8306	6.5E-12	-3.46	-6.152
490.15	1.61E5	6.61E-11	0.8313	6.5E-12	-3.49	-6.180
488.15	1.66E5	6.39E-11	0.8332	6.5E-12	-3.51	-6.195
487.15	1.72E5	6.35E-11	0.8334	6.5E-12	-3.52	-6.210
486.15	1.78E5	6.34E-11	0.8332	6.5E-12	-3.54	-6.225
485.15	1.87E5	6.37E-11	0.8325	6.5E-12	-3.56	-6.247
483.15	1.97E5	6.04E-11	0.8356	6.5E-12	-3.58	-6.269
482.15	2.08E5	6.06E-11	0.8348	6.5E-12	-3.61	-6.293
480.15	2.15E5	5.98E-11	0.8354	6.5E-12	-3.63	-6.307
479.15	2.21E5	5.99E-11	0.8350	6.5E-12	-3.64	-6.319
478.15	2.31E5	5.95E-11	0.8351	6.5E-12	-3.66	-6.337
477.15	2.43E5	5.89E-11	0.8353	6.5E-12	-3.68	-6.359
475.15	2.57E5	5.83E-11	0.8355	6.5E-12	-3.71	-6.385
474.15	2.73E5	5.72E-11	0.8363	6.5E-12	-3.74	-6.411
472.15	2.82E5	5.62E-11	0.8371	6.5E-12	-3.75	-6.424
471.15	2.89E5	5.60E-11	0.8371	6.6E-12	-3.76	-6.435
470.15	2.99E5	5.58E-11	0.8371	6.6E-12	-3.78	-6.449
469.15	3.12E5	5.55E-11	0.8370	6.6E-12	-3.80	-6.469
468.15	3.29E5	5.51E-11	0.8371	6.6E-12	-3.82	-6.491
466.15	3.49E5	5.45E-11	0.8373	6.6E-12	-3.85	-6.516
465.15	3.59E5	5.37E-11	0.8380	6.6E-12	-3.86	-6.530
464.15	3.68E5	5.34E-11	0.8382	6.6E-12	-3.87	-6.540
463.15	3.79E5	5.33E-11	0.8381	6.6E-12	-3.89	-6.553
462.15	3.98E5	5.29E-11	0.8383	6.6E-12	-3.91	-6.574
461.15	4.22E5	5.19E-11	0.8391	6.6E-12	-3.94	-6.599
459.15	4.59E5	5.13E-11	0.8390	6.6E-12	-3.97	-6.636
457.15	4.79E5	5.09E-11	0.8392	6.6E-12	-3.99	-6.655
455.15	5.00E5	5.06E-11	0.8392	6.7E-12	-4.02	-6.673
454.15	5.22E5	5.00E-11	0.8396	6.7E-12	-4.03	-6.692
453.15	5.50E5	4.96E-11	0.8396	6.7E-12	-4.06	-6.715
451.15	5.82E5	4.88E-11	0.8403	6.7E-12	-4.09	-6.739
450.15	6.12E5	4.83E-11	0.8405	6.7E-12	-4.11	-6.761
449.15	6.36E5	4.78E-11	0.8410	6.7E-12	-4.13	-6.778
448.15	6.64E5	4.73E-11	0.8412	6.7E-12	-4.15	-6.797
446.15	6.99E5	4.69E-11	0.8414	6.7E-12	-4.17	-6.819
445.15	7.37E5	4.63E-11	0.8418	6.7E-12	-4.19	-6.842
444.15	7.68E5	4.58E-11	0.8421	6.7E-12	-4.21	-6.859
442.15	8.01E5	4.52E-11	0.8428	6.7E-12	-4.23	-6.878
440.15	8.64E5	2.82E-11	0.8779	6.4E-12	-4.27	-6.911
438.15	9.04E5	2.86E-11	0.8766	6.5E-12	-4.29	-6.930
437.15	9.51E5	2.91E-11	0.8747	6.5E-12	-4.31	-6.952
436.15	9.84E5	2.99E-11	0.8723	6.5E-12	-4.33	-6.967
435.15	1.03E6	3.23E-11	0.8660	6.5E-12	-4.35	-6.986
434.15	1.07E6	3.33E-11	0.8633	6.6E-12	-4.37	-7.003
433.15	1.12E6	3.52E-11	0.8582	6.6E-12	-4.39	-7.025
432.15	1.19E6	3.70E-11	0.8538	6.6E-12	-4.41	-7.050
431.15	1.28E6	4.08E-11	0.8451	6.7E-12	-4.45	-7.081
430.15	1.37E6	4.04E-11	0.8451	6.7E-12	-4.48	-7.109
428.15	1.46E6	4.55E-11	0.8349	6.8E-12	-4.51	-7.139
427.15	1.51E6	4.47E-11	0.8358	6.8E-12	-4.52	-7.154
426.15	1.58E6	4.67E-11	0.8317	6.8E-12	-4.54	-7.174
425.15	1.68E6	5.19E-11	0.8223	6.9E-12	-4.57	-7.200
424.15	1.78E6	5.33E-11	0.8193	6.9E-12	-4.60	-7.226
422.15	1.90E6	5.64E-11	0.8137	7.0E-12	-4.63	-7.254
421.15	2.05E6	6.34E-11	0.8031	7.1E-12	-4.66	-7.287
419.15	2.09E6	3.89E-11	0.8432	6.7E-12	-4.67	-7.294
418.15	2.33E6	6.20E-11	0.8028	7.1E-12	-4.72	-7.342
416.15	2.47E6	6.67E-11	0.7959	7.1E-12	-4.75	-7.367
415.15	2.60E6	6.87E-11	0.7926	7.2E-12	-4.77	-7.390
414.15	2.78E6	7.60E-11	0.7831	7.3E-12	-4.80	-7.418
413.15	2.95E6	7.58E-11	0.7823	7.3E-12	-4.83	-7.444
411.15	3.14E6	7.51E-11	0.7822	7.3E-12	-4.86	-7.471

410.15	3.38E6	7.99E-11	0.7756	7.4E-12	-4.89	-7.503
408.15	3.52E6	5.94E-11	0.8002	7.2E-12	-4.91	-7.521
407.15	3.87E6	7.91E-11	0.7742	7.5E-12	-4.95	-7.562
405.15	4.10E6	7.89E-11	0.7735	7.5E-12	-4.98	-7.587
404.15	4.36E6	8.36E-11	0.7674	7.6E-12	-5.01	-7.614
403.15	4.61E6	8.19E-11	0.7682	7.6E-12	-5.03	-7.638
401.15	4.90E6	8.13E-11	0.7677	7.6E-12	-5.06	-7.665
400.15	5.23E6	8.19E-11	0.7658	7.6E-12	-5.09	-7.693
399.15	5.59E6	8.24E-11	0.7640	7.7E-12	-5.12	-7.721
397.15	5.95E6	8.19E-11	0.7633	7.7E-12	-5.15	-7.749
396.15	6.36E6	8.25E-11	0.7614	7.7E-12	-5.18	-7.778
394.15	6.79E6	8.40E-11	0.7584	7.8E-12	-5.21	-7.806
393.15	7.23E6	8.02E-11	0.7613	7.7E-12	-5.24	-7.834
392.15	7.78E6	8.19E-11	0.7577	7.8E-12	-5.27	-7.865
390.15	8.43E6	7.91E-11	0.7591	7.8E-12	-5.31	-7.900
388.15	9.19E6	7.84E-11	0.7580	7.8E-12	-5.35	-7.938
387.15	9.72E6	7.48E-11	0.7611	7.7E-12	-5.37	-7.962
385.15	1.03E7	7.23E-11	0.7628	7.7E-12	-5.40	-7.987
384.15	1.10E7	7.32E-11	0.7600	7.7E-12	-5.43	-8.016
384.15	1.10E7	7.32E-11	0.7600	7.7E-12	-5.43	-8.016
383.15	1.17E7	6.94E-11	0.7637	7.7E-12	-5.46	-8.041
382.15	1.23E7	6.67E-11	0.7662	7.6E-12	-5.48	-8.065
380.15	1.30E7	6.40E-11	0.7687	7.6E-12	-5.51	-8.089
379.15	1.38E7	6.27E-11	0.7691	7.5E-12	-5.54	-8.114
378.15	1.47E7	6.32E-11	0.7668	7.6E-12	-5.56	-8.141
377.15	1.55E7	5.79E-11	0.7741	7.5E-12	-5.59	-8.164
376.15	1.65E7	6.10E-11	0.7678	7.6E-12	-5.62	-8.191
375.15	1.75E7	5.92E-11	0.7692	7.5E-12	-5.64	-8.217
373.15	1.85E7	5.67E-11	0.7720	7.5E-12	-5.67	-8.241
372.15	1.98E7	5.64E-11	0.7706	7.4E-12	-5.70	-8.271
370.15	2.19E7	5.29E-11	0.7755	7.5E-12	-5.75	-8.315
369.15	2.30E7	5.13E-11	0.7768	7.4E-12	-5.77	-8.336
368.15	2.40E7	4.71E-11	0.7848	7.3E-12	-5.79	-8.354
367.15	2.57E7	5.11E-11	0.7753	7.5E-12	-5.82	-8.384
366.15	2.66E7	4.64E-11	0.7842	7.3E-12	-5.84	-8.399
365.15	2.79E7	4.40E-11	0.7891	7.3E-12	-5.86	-8.420
364.15	2.92E7	4.30E-11	0.7905	7.3E-12	-5.88	-8.440
363.15	3.07E7	4.20E-11	0.7919	7.3E-12	-5.90	-8.461
362.15	3.23E7	4.13E-11	0.7931	7.3E-12	-5.92	-8.483
361.15	3.37E7	3.82E-11	0.7995	7.2E-12	-5.94	-8.502
360.15	3.58E7	3.69E-11	0.8025	7.2E-12	-5.97	-8.528
359.15	3.72E7	3.65E-11	0.8025	7.2E-12	-5.99	-8.545
358.15	3.88E7	3.60E-11	0.8042	7.3E-12	-6.01	-8.563
357.15	4.12E7	3.50E-11	0.8047	7.2E-12	-6.04	-8.589
356.15	4.39E7	3.52E-11	0.8029	7.2E-12	-6.06	-8.616
355.15	4.58E7	3.55E-11	0.8025	7.3E-12	-6.08	-8.635
355.15	4.80E7	3.46E-11	0.8041	7.3E-12	-6.10	-8.655
354.15	4.98E7	3.12E-11	0.8141	7.1E-12	-6.12	-8.671
353.15	5.14E7	3.00E-11	0.8184	7.1E-12	-6.14	-8.685
352.15	5.66E7	3.06E-11	0.8144	7.2E-12	-6.18	-8.727
351.15	6.00E7	3.18E-11	0.8099	7.3E-12	-6.21	-8.752
350.15	6.17E7	3.28E-11	0.8057	7.4E-12	-6.22	-8.765
349.15	6.78E7	2.87E-11	0.8200	7.3E-12	-6.26	-8.806
348.15	6.97E7	2.57E-11	0.8296	7.0E-12	-6.28	-8.817
347.15	7.26E7	2.77E-11	0.8210	7.2E-12	-6.29	-8.835
346.15	7.61E7	2.79E-11	0.8198	7.2E-12	-6.32	-8.856
345.15	7.99E7	2.67E-11	0.8259	7.3E-12	-6.34	-8.877
345.15	8.22E7	2.29E-11	0.8408	7.0E-12	-6.35	-8.889
344.15	8.84E7	2.45E-11	0.8305	7.0E-12	-6.38	-8.921
343.15	9.12E7	2.29E-11	0.8408	7.1E-12	-6.40	-8.934
342.15	9.59E7	2.74E-11	0.8212	7.5E-12	-6.42	-8.956
341.15	1.01E8	2.11E-11	0.8466	6.9E-12	-6.44	-8.977
340.15	1.08E8	2.43E-11	0.8298	7.2E-12	-6.48	-9.008
339.15	1.16E8	2.43E-11	0.8294	7.3E-12	-6.51	-9.040
338.15	1.23E8	2.19E-11	0.8395	7.1E-12	-6.54	-9.066
337.15	1.26E8	2.07E-11	0.8453	7.0E-12	-6.55	-9.075
336.15	1.37E8	2.13E-11	0.8447	7.3E-12	-6.58	-9.110
335.15	1.45E8	1.71E-11	0.8695	7.0E-12	-6.61	-9.136
334.15	1.56E8	2.09E-11	0.8459	7.4E-12	-6.64	-9.168
333.15	1.64E8	1.72E-11	0.8698	7.2E-12	-6.67	-9.190
332.15	1.72E8	1.86E-11	0.8596	7.3E-12	-6.69	-9.210
331.15	1.86E8	1.91E-11	0.8534	7.2E-12	-6.72	-9.243
330.15	1.95E8	2.13E-11	0.8341	7.2E-12	-6.75	-9.265
329.15	2.14E8	1.79E-11	0.8525	6.8E-12	-6.79	-9.306
328.15	2.28E8	1.90E-11	0.8454	7.0E-12	-6.82	-9.331
327.15	2.35E8	1.81E-11	0.8573	7.3E-12	-6.83	-9.345
326.15	2.62E8	2.25E-11	0.8271	7.7E-12	-6.88	-9.392
325.15	2.69E8	1.92E-11	0.8411	7.1E-12	-6.89	-9.404
324.15	2.87E8	1.91E-11	0.8415	7.2E-12	-6.92	-9.432
323.15	2.99E8	1.89E-11	0.8436	7.2E-12	-6.94	-9.450
322.15	3.25E8	1.87E-11	0.8534	7.8E-12	-6.98	-9.486
321.15	3.40E8	1.69E-11	0.8526	6.9E-12	-7.00	-9.506
320.15	3.45E8	1.71E-11	0.8614	7.5E-12	-7.01	-9.513
319.15	3.88E8	1.64E-11	0.8607	7.2E-12	-7.06	-9.563
318.15	4.46E8	1.90E-11	0.8309	7.2E-12	-7.12	-9.623
317.15	4.62E8	1.88E-11	0.8388	7.6E-12	-7.14	-9.639
316.15	5.00E8	1.90E-11	0.8452	8.1E-12	-7.17	-9.673

315.15	5.40E8	1.94E-11	0.8283	7.5E-12	-7.21	-9.707
314.15	5.89E8	1.61E-11	0.8467	6.9E-12	-7.25	-9.745
313.15	6.12E8	1.62E-11	0.8519	7.3E-12	-7.27	-9.761
312.15	6.48E8	1.65E-11	0.8530	7.6E-12	-7.29	-9.786
311.15	6.68E8	1.29E-11	0.8869	7.0E-12	-7.31	-9.799
310.15	7.42E8	1.57E-11	0.8504	7.2E-12	-7.35	-9.845
309.15	8.49E8	1.66E-11	0.8381	7.3E-12	-7.41	-9.903
308.15	9.65E8	1.71E-11	0.8342	7.6E-12	-7.47	-9.959

Ionic conductivity data for PLESPB polymer

Diameter: 0.6 cm   Thickness: 0.09 cm

$(2^{nd}$ cycle)

T /K	R_1/Ω	Q_1	n_1	C_1 /F	log (σT)	log (σ)
372.15	1.103E11	3.03E-12	1.0052	3.0E-12	-8.97	-11.540
376.15	7.681E10	2.39E-12	1.1540	3.0E-12	-8.81	-11.383
379.15	6.368E10	2.16E-12	1.0576	2.4E-12	-8.72	-11.301
381.15	5.865E10	2.63E-12	1.0400	2.8E-12	-8.68	-11.265
384.15	6.668E10	4.75E-12	0.9215	4.3E-12	-8.74	-11.321
385.15	5.974E10	3.25E-12	1.0891	3.7E-12	-8.69	-11.273
393.15	5.903E10	6.46E-12	0.7390	4.6E-12	-8.67	-11.268
395.15	3.433E10	5.79E-12	0.8716	4.6E-12	-8.44	-11.033
395.15	2.668E10	3.12E-12	1.2393	5.0E-12	-8.33	-10.923
395.15	3.836E10	4.57E-12	0.9042	3.8E-12	-8.48	-11.081
397.15	6.857E10	2.04E-11	0.5735	2.6E-11	-8.73	-11.333
399.15	2.727E10	8.54E-12	0.7617	5.4E-12	-8.33	-10.933
404.15	2.009E10	6.97E-12	0.8118	4.4E-12	-8.19	-10.800
404.15	2.292E10	1.07E-11	0.7698	7.1E-12	-8.25	-10.857
405.15	3.335E10	1.57E-11	0.5721	9.7E-12	-8.41	-11.020
405.15	1.749E10	6.28E-12	0.8452	4.2E-12	-8.13	-10.740
407.15	1.084E10	5.32E-12	0.9367	4.4E-12	-7.92	-10.532
409.15	2.232E10	2.48E-11	0.6269	1.7E-11	-8.23	-10.846
413.15	1.132E10	1.12E-11	0.7875	6.4E-12	-7.93	-10.551
411.15	1.472E10	1.17E-11	0.7456	6.5E-12	-8.05	-10.665
411.15	1.738E10	1.20E-11	0.7441	7.0E-12	-8.12	-10.737
413.15	1.221E10	6.56E-12	0.8844	4.7E-12	-7.97	-10.584

Ionic conductivity data for PLEStBB polymer

Diameter: 0.6 cm   Thickness: 0.35 cm

$(2^{nd}$ cycle)

T /K	R_1/Ω	Q_1	n_1	C_1 /F	log (σT)	log (σ)
473.15	1.10E9	5.60E-12	0.8036	1.6E-12	-6.27	-8.949
474.15	9.64E8	1.66E-12	0.9022	8.3E-13	-6.22	-8.892
473.15	1.16E9	3.23E-12	0.8798	1.5E-12	-6.30	-8.973
470.15	1.29E9	4.57E-12	0.8257	1.5E-12	-6.35	-9.018
468.15	1.40E9	7.25E-12	0.7563	1.6E-12	-6.38	-9.052
466.15	1.40E9	3.22E-12	0.8256	1.0E-12	-6.39	-9.054
465.15	1.54E9	3.37E-12	0.8530	1.4E-12	-6.43	-9.093
461.15	1.89E9	8.08E-12	0.7182	1.6E-12	-6.52	-9.183
460.15	1.78E9	2.71E-12	0.8769	1.3E-12	-6.49	-9.158
459.15	2.05E9	3.59E-12	0.8580	1.6E-12	-6.56	-9.219
456.15	2.31E9	2.31E-12	1.0272	2.7E-12	-6.61	-9.270
454.15	2.52E9	2.10E-12	0.9515	1.6E-12	-6.65	-9.309
453.15	2.62E9	4.29E-12	0.7768	1.2E-12	-6.67	-9.326
447.15	3.30E9	3.66E-12	0.8444	1.6E-12	-6.78	-9.426
434.15	6.15E9	1.85E-12	1.0364	2.2E-12	-7.06	-9.697
430.15	9.48E9	1.09E-11	0.6923	3.9E-12	-7.25	-9.884
428.15	8.28E9	2.53E-12	0.8082	1.0E-12	-7.19	-9.826
422.15	1.21E10	2.58E-12	0.9835	2.4E-12	-7.37	-9.991
415.15	1.56E10	2.27E-12	1.0032	2.3E-12	-7.48	-10.099

Ionic conductivity data for PLESnBB polymer

Diameter: 0.6 cm   Thickness: 0.26 cm

(2nd cycle)

T /K	R_1/Ω	Q_1	n_1	C_1 /F	log (σT)	log (σ)
456.15	8.71E8	2.25E-11	0.7494	6.0E-12	-6.19	-8.854
454.15	9.30E8	2.00E-11	0.7629	5.8E-12	-6.22	-8.882
454.15	1.10E9	2.33E-11	0.7118	5.3E-12	-6.30	-8.954
453.15	1.25E9	1.59E-11	0.7994	5.9E-12	-6.35	-9.011
451.15	1.67E9	2.23E-11	0.7144	6.0E-12	-6.48	-9.135
447.15	2.53E9	1.77E-11	0.7078	4.9E-12	-6.67	-9.317
446.15	2.51E9	1.28E-11	0.8172	6.0E-12	-6.66	-9.312
445.15	2.92E9	6.60E-12	0.9431	5.2E-12	-6.73	-9.379
444.15	3.42E9	1.31E-11	0.8063	6.2E-12	-6.80	-9.448
443.15	4.41E9	1.33E-11	0.8196	7.1E-12	-6.91	-9.558
439.15	6.10E9	6.77E-12	0.8794	4.4E-12	-7.06	-9.699
437.15	8.23E9	9.58E-12	0.8436	6.0E-12	-7.19	-9.829
435.15	1.33E10	1.01E-11	0.8428	7.0E-12	-7.40	-10.037
432.15	1.48E10	7.88E-12	0.8756	5.8E-12	-7.45	-10.084
430.15	2.12E10	8.36E-12	0.8847	6.7E-12	-7.61	-10.240
423.15	4.76E10	8.14E-12	0.8412	6.8E-12	-7.96	-10.591
420.15	7.19E10	6.52E-12	0.8839	5.9E-12	-8.15	-10.770
419.15	7.16E10	6.74E-12	0.8691	6.0E-12	-8.15	-10.768
412.15	6.55E10	3.17E-12	1.0322	3.3E-12	-8.11	-10.730

Ionic conductivity data for LiB$_6$O$_9$F

Diameter: 0.6 cm   Thickness: 0.115 cm

(2nd cycle)

T /K	R_1/Ω	Q_1	n_1	C_1 /F	log (σT)	log (σ)
679.15	6.66E7	5.10E-11	0.7337	6.5E-12	-5.38	-8.214
678.15	5.10E7	5.44E-11	0.7443	7.2E-12	-5.27	-8.098
676.15	8.19E7	3.12E-11	0.7845	6.0E-12	-5.47	-8.304
674.15	6.16E7	3.49E-11	0.7912	6.9E-12	-5.35	-8.180
671.15	1.18E8	5.12E-11	0.7165	6.8E-12	-5.63	-8.461
663.15	9.34E7	3.80E-11	0.7706	7.1E-12	-5.54	-8.361
665.15	1.41E8	3.89E-11	0.7526	7.0E-12	-5.72	-8.540
656.15	1.53E8	3.01E-11	0.7782	6.5E-12	-5.76	-8.575
656.15	2.05E8	4.35E-11	0.7385	8.2E-12	-5.89	-8.703
649.15	3.05E8	4.97E-11	0.6917	7.7E-12	-6.06	-8.875
647.15	2.32E8	1.66E-11	0.8506	6.3E-12	-5.94	-8.755
634.15	4.52E8	3.72E-11	0.7456	9.2E-12	-6.24	-9.046
636.15	5.47E8	2.57E-11	0.7679	7.1E-12	-6.32	-9.128
629.15	7.59E8	3.03E-11	0.7308	7.6E-12	-6.47	-9.271
627.15	8.22E8	5.00E-11	0.6539	9.2E-12	-6.51	-9.306
625.15	1.26E9	2.69E-11	0.7652	9.5E-12	-6.69	-9.491
616.15	1.19E9	3.18E-11	0.6995	7.8E-12	-6.68	-9.468
618.15	1.47E9	2.58E-11	0.7474	8.5E-12	-6.77	-9.559
603.15	2.43E9	2.73E-11	0.7054	8.8E-12	-7.00	-9.776
596.15	3.44E9	1.55E-11	0.8230	8.3E-12	-7.15	-9.928
594.15	5.27E9	1.87E-11	0.7273	7.9E-12	-7.34	-10.112
586.15	5.95E9	1.24E-11	0.8426	7.6E-12	-7.40	-10.165
582.15	6.54E9	1.93E-11	0.7076	8.2E-12	-7.44	-10.206
575.15	1.44E10	1.44E-11	0.8140	1.0E-11	-7.79	-10.548
568.15	1.08E10	1.21E-11	0.8690	8.9E-12	-7.67	-10.425
570.15	1.65E10	1.18E-11	0.8143	8.1E-12	-7.85	-10.609
555.15	2.33E10	1.10E-11	0.8737	9.1E-12	-8.01	-10.758
554.15	3.18E10	1.26E-11	0.8064	1.0E-11	-8.15	-10.892
549.15	4.69E10	1.31E-11	0.7939	1.2E-11	-8.32	-11.062
543.15	5.02E10	1.32E-11	0.7321	1.1E-11	-8.36	-11.091

Ionic conductivity data for $Na_3B_3O_3F_6$ (with gold electrodes)

Diameter: 0.6 cm   Thickness: 0.2 cm

$(2^{nd}$ cycle)

T /K	R_1/Ω	Q_1	n_1	C_1 /F	log (σT)	log (σ)
624.15	1.66E2	6.23E-9	0.5901	4.3E-13	0.43	-2.369
626.15	1.62E2	6.23E-9	0.5901	4.3E-13	0.44	-2.360
624.15	1.48E2	6.23E-9	0.5901	4.0E-13	0.47	-2.322
625.15	1.62E2	6.23E-9	0.5901	4.3E-13	0.44	-2.359
624.15	1.77E2	6.23E-9	0.5901	4.5E-13	0.40	-2.397
620.15	2.00E2	6.23E-9	0.5901	4.9E-13	0.34	-2.451
620.15	1.96E2	6.23E-9	0.5901	4.9E-13	0.35	-2.442
620.15	2.06E2	6.23E-9	0.5901	5.0E-13	0.33	-2.463
613.15	2.45E2	6.23E-9	0.5901	5.7E-13	0.25	-2.539
613.15	2.48E2	6.23E-9	0.5901	5.7E-13	0.24	-2.546
610.15	2.77E2	6.23E-9	0.5901	6.2E-13	0.19	-2.592
607.15	2.87E2	6.23E-9	0.5901	6.3E-13	0.18	-2.608
607.15	2.94E2	6.23E-9	0.5901	6.4E-13	0.16	-2.619
603.15	3.55E2	6.23E-9	0.5901	7.3E-13	0.08	-2.701
602.15	3.57E2	6.23E-9	0.5901	7.4E-13	0.08	-2.703
600.15	3.81E2	6.23E-9	0.5901	7.7E-13	0.05	-2.732
597.15	4.34E2	6.23E-9	0.5901	8.4E-13	-0.01	-2.787
596.15	4.28E2	6.23E-9	0.5901	8.4E-13	-0.01	-2.782
595.15	4.77E2	6.23E-9	0.5901	9.0E-13	-0.05	-2.829
590.15	5.04E2	6.23E-9	0.5901	9.4E-13	-0.08	-2.853
588.15	5.93E2	6.23E-9	0.5901	1.0E-12	-0.15	-2.923
584.15	6.53E2	6.23E-9	0.5901	1.1E-12	-0.20	-2.965
584.15	6.56E2	6.23E-9	0.5901	1.1E-12	-0.20	-2.967
582.15	7.21E2	6.23E-9	0.5901	1.2E-12	-0.24	-3.008
578.15	8.04E2	6.23E-9	0.5901	1.3E-12	-0.29	-3.055
578.15	7.89E2	6.23E-9	0.5901	1.3E-12	-0.29	-3.048
577.15	8.04E2	6.23E-9	0.5901	1.3E-12	-0.29	-3.055
573.15	9.69E2	6.23E-9	0.5901	1.5E-12	-0.38	-3.137
571.15	1.01E3	6.23E-9	0.5901	1.5E-12	-0.40	-3.153
570.15	1.06E3	6.23E-9	0.5901	1.6E-12	-0.42	-3.177
567.15	1.23E3	6.23E-9	0.5901	1.7E-12	-0.49	-3.241
566.15	1.21E3	6.23E-9	0.5901	1.7E-12	-0.48	-3.233
565.15	1.29E3	6.23E-9	0.5901	1.8E-12	-0.51	-3.261
562.15	1.52E3	6.23E-9	0.5901	2.0E-12	-0.58	-3.333
559.15	1.56E3	1.41E-9	0.6736	2.6E-12	-0.60	-3.343
559.15	1.55E3	1.30E-9	0.6745	2.3E-12	-0.59	-3.340
556.15	1.99E3	5.30E-9	0.6012	2.6E-12	-0.70	-3.449
552.15	2.00E3	2.76E-9	0.6324	2.4E-12	-0.71	-3.452
550.15	2.27E3	3.13E-9	0.6273	2.7E-12	-0.77	-3.507
547.15	2.40E3	9.43E-10	0.6866	2.5E-12	-0.79	-3.530
546.15	2.41E3	5.64E-10	0.7180	2.8E-12	-0.79	-3.532
546.15	2.57E3	9.47E-10	0.6905	2.9E-12	-0.82	-3.560
543.15	3.28E3	3.21E-9	0.6233	3.2E-12	-0.93	-3.666
539.15	3.45E3	1.27E-9	0.6684	2.8E-12	-0.96	-3.688
538.15	3.57E3	7.82E-10	0.6966	3.0E-12	-0.97	-3.703
536.15	4.15E3	9.10E-10	0.6877	3.1E-12	-1.04	-3.768
533.15	4.66E3	5.95E-10	0.7083	3.1E-12	-1.09	-3.818
531.15	4.81E3	4.55E-10	0.7230	3.1E-12	-1.11	-3.833
529.15	5.97E3	1.17E-9	0.6688	3.3E-12	-1.20	-3.926
524.15	6.28E3	1.32E-10	0.7865	3.0E-12	-1.23	-3.948
524.15	6.68E3	4.62E-10	0.7175	3.1E-12	-1.26	-3.975
520.15	8.81E3	6.28E-10	0.6966	3.2E-12	-1.38	-4.095
516.15	9.81E3	1.01E-10	0.7957	2.9E-12	-1.43	-4.142
514.15	1.10E4	3.08E-10	0.7323	3.1E-12	-1.48	-4.190
511.15	1.46E4	6.80E-11	0.6839	3.3E-12	-1.61	-4.315
504.15	1.92E4	1.78E-10	0.7543	2.9E-12	-1.73	-4.434
500.15	2.12E4	6.44E-11	0.8102	2.7E-12	-1.78	-4.478
499.15	2.51E4	1.48E-10	0.7608	2.9E-12	-1.85	-4.551
495.15	2.84E4	5.75E-11	0.8128	2.7E-12	-1.91	-4.604
494.15	2.94E4	7.13E-11	0.7999	2.7E-12	-1.92	-4.619
493.15	3.30E4	1.16E-10	0.7700	2.8E-12	-1.98	-4.669
491.15	3.80E4	1.18E-10	0.7670	2.8E-12	-2.04	-4.730
489.15	4.18E4	6.17E-11	0.8036	2.7E-12	-2.08	-4.772
488.15	4.42E4	9.54E-11	0.7773	2.8E-12	-2.11	-4.796
487.15	5.19E4	1.43E-10	0.7515	2.9E-12	-2.18	-4.866
484.15	6.28E4	1.48E-10	0.7464	2.9E-12	-2.26	-4.948
481.15	7.21E4	9.07E-11	0.7733	2.7E-12	-2.33	-5.008
479.15	8.37E4	1.50E-10	0.7412	2.9E-12	-2.39	-5.073
476.15	1.04E5	1.56E-10	0.7351	2.9E-12	-2.49	-5.169
473.15	1.14E5	8.46E-11	0.7709	2.7E-12	-2.53	-5.207
471.15	1.25E5	1.03E-10	0.7577	2.8E-12	-2.57	-5.246
470.15	1.38E5	1.03E-10	0.7558	2.8E-12	-2.62	-5.291
468.15	1.61E5	9.03E-11	0.7618	2.8E-12	-2.69	-5.358
466.15	1.82E5	1.10E-10	0.7477	2.9E-12	-2.74	-5.411
463.15	2.11E5	1.10E-10	0.7455	2.9E-12	-2.81	-5.474

461.15	2.30E5	7.06E-11	0.7721	2.7E-12	-2.85	-5.513
460.15	2.52E5	9.72E-11	0.7504	2.8E-12	-2.89	-5.552
457.15	3.10E5	1.03E-10	0.7434	2.9E-12	-2.98	-5.641
453.15	3.65E5	8.29E-11	0.7548	2.8E-12	-3.06	-5.713
450.15	4.30E5	7.14E-11	0.7622	2.8E-12	-3.13	-5.784
447.15	4.82E5	6.23E-11	0.7694	2.7E-12	-3.18	-5.834
445.15	5.30E5	6.71E-11	0.7632	2.8E-12	-3.23	-5.875
443.15	5.88E5	5.54E-11	0.7745	2.7E-12	-3.27	-5.920
442.15	6.67E5	7.84E-11	0.7492	2.9E-12	-3.33	-5.975
438.15	7.48E5	5.62E-11	0.7697	2.8E-12	-3.38	-6.024
437.15	8.24E5	5.42E-11	0.7711	2.8E-12	-3.43	-6.066
435.15	8.97E5	5.05E-11	0.7748	2.8E-12	-3.46	-6.103
433.15	9.49E5	4.86E-11	0.7767	2.8E-12	-3.49	-6.128
432.15	1.07E6	7.03E-11	0.7495	2.9E-12	-3.55	-6.181
429.15	1.22E6	5.24E-11	0.7679	2.8E-12	-3.60	-6.236
427.15	1.31E6	4.92E-11	0.7714	2.8E-12	-3.64	-6.267
425.15	1.42E6	5.11E-11	0.7675	2.8E-12	-3.67	-6.302
423.15	1.61E6	5.76E-11	0.7572	2.9E-12	-3.73	-6.358
422.15	1.77E6	5.40E-11	0.7603	2.9E-12	-3.77	-6.398
419.15	1.99E6	5.40E-11	0.7584	2.9E-12	-3.83	-6.449
416.15	2.23E6	5.11E-11	0.7604	2.9E-12	-3.88	-6.498
414.15	2.46E6	4.38E-11	0.7701	2.9E-12	-3.92	-6.542
412.15	2.70E6	5.13E-11	0.7565	2.9E-12	-3.97	-6.582
410.15	3.18E6	5.06E-11	0.7544	2.9E-12	-4.04	-6.652
407.15	3.63E6	4.02E-11	0.7694	2.8E-12	-4.10	-6.710
405.15	3.89E6	4.02E-11	0.7679	2.8E-12	-4.13	-6.740
403.15	4.19E6	3.89E-11	0.7689	2.8E-12	-4.17	-6.772
401.15	5.00E6	4.25E-11	0.7585	2.9E-12	-4.25	-6.850
398.15	5.84E6	4.02E-11	0.7595	2.9E-12	-4.32	-6.917
394.15	6.80E6	3.75E-11	0.7620	2.8E-12	-4.39	-6.983
391.15	7.81E6	3.89E-11	0.7562	2.9E-12	-4.45	-7.043
389.15	8.69E6	3.67E-11	0.7590	2.8E-12	-4.50	-7.089
387.15	9.77E6	3.40E-11	0.7629	2.8E-12	-4.55	-7.140
385.15	1.15E7	3.96E-11	0.7473	2.9E-12	-4.63	-7.211
381.15	1.33E7	3.48E-11	0.7556	2.9E-12	-4.69	-7.276
379.15	1.50E7	3.05E-11	0.7647	2.9E-12	-4.75	-7.326
377.15	1.67E7	3.19E-11	0.7588	2.9E-12	-4.80	-7.373
375.15	1.89E7	3.17E-11	0.7571	2.9E-12	-4.85	-7.427
372.15	2.06E7	2.79E-11	0.7671	2.9E-12	-4.89	-7.465
370.15	2.51E7	2.88E-11	0.7605	3.0E-12	-4.98	-7.551
367.15	2.91E7	2.66E-11	0.7640	2.9E-12	-5.05	-7.614
365.15	3.18E7	2.77E-11	0.7604	3.0E-12	-5.09	-7.652
362.15	3.89E7	2.61E-11	0.7601	3.0E-12	-5.18	-7.740
359.15	4.65E7	2.71E-11	0.7512	3.0E-12	-5.26	-7.818
357.15	5.16E7	2.71E-11	0.7491	3.0E-12	-5.31	-7.863
355.15	5.67E7	2.48E-11	0.7535	2.9E-12	-5.35	-7.904
354.15	6.66E7	2.29E-11	0.7573	2.9E-12	-5.42	-7.974
351.15	7.53E7	2.26E-11	0.7546	2.8E-12	-5.48	-8.027
349.15	8.21E7	1.79E-11	0.7771	2.8E-12	-5.52	-8.065
347.15	9.10E7	1.91E-11	0.7691	2.8E-12	-5.57	-8.109
346.15	1.02E8	2.22E-11	0.7536	3.0E-12	-5.62	-8.158
344.15	1.15E8	1.80E-11	0.7679	2.8E-12	-5.67	-8.210
342.15	1.31E8	2.64E-11	0.7275	3.2E-12	-5.73	-8.267
341.15	1.52E8	2.23E-11	0.7439	3.1E-12	-5.80	-8.332
339.15	1.62E8	1.62E-11	0.7737	2.9E-12	-5.83	-8.360
338.15	1.89E8	2.58E-11	0.7179	3.2E-12	-5.90	-8.426
336.15	2.01E8	2.78E-11	0.7050	3.2E-12	-5.93	-8.453
335.15	2.04E8	1.18E-11	0.8087	2.8E-12	-5.93	-8.460
333.15	2.46E8	1.68E-11	0.7550	2.8E-12	-6.02	-8.542
331.15	3.04E8	2.64E-11	0.7095	3.7E-12	-6.11	-8.634
329.15	3.18E8	2.76E-11	0.6976	3.5E-12	-6.13	-8.652
328.15	2.86E8	6.05E-12	0.8811	2.6E-12	-6.09	-8.606
327.15	3.85E8	3.80E-11	0.6502	3.9E-12	-6.22	-8.735
326.15	4.17E8	1.88E-11	0.7398	3.4E-12	-6.26	-8.770
325.15	4.68E8	1.68E-11	0.7541	3.5E-12	-6.31	-8.820
323.15	5.00E8	2.42E-11	0.6861	3.2E-12	-6.34	-8.849
322.15	5.57E8	2.16E-11	0.7177	3.8E-12	-6.39	-8.897
321.15	6.00E8	2.58E-11	0.6593	3.0E-12	-6.42	-8.929
320.15	6.25E8	1.28E-11	0.7514	2.6E-12	-6.44	-8.946
319.15	7.00E8	1.41E-11	0.7853	4.0E-12	-6.49	-8.995
318.15	7.49E8	1.46E-11	0.7324	2.8E-12	-6.52	-9.025
317.15	8.36E8	2.04E-11	0.7071	3.8E-12	-6.57	-9.073
316.15	8.19E8	4.91E-12	0.8323	1.6E-12	-6.56	-9.064
315.15	8.95E8	1.52E-11	0.7569	3.8E-12	-6.60	-9.102
315.15	9.88E8	2.15E-11	0.6798	3.5E-12	-6.65	-9.145
314.15	1.03E9	2.11E-11	0.6869	3.7E-12	-6.67	-9.165
313.15	1.14E9	2.44E-11	0.6464	3.4E-12	-6.71	-9.208
312.15	1.17E9	2.45E-11	0.6430	3.4E-12	-6.72	-9.219
311.15	1.32E9	2.60E-11	0.6676	4.8E-12	-6.78	-9.270
310.15	1.38E9	1.33E-11	0.7984	4.9E-12	-6.80	-9.291
309.15	1.53E9	2.25E-11	0.6590	3.9E-12	-6.85	-9.336
308.15	1.58E9	1.23E-11	0.7963	4.5E-12	-6.86	-9.350
307.15	1.85E9	2.65E-11	0.6218	4.2E-12	-6.93	-9.418
306.15	1.90E9	2.49E-11	0.6011	3.3E-12	-6.94	-9.429
305.15	1.96E9	1.36E-11	0.7514	4.1E-12	-6.96	-9.442
305.15	2.27E9	2.74E-11	0.6114	4.7E-12	-7.02	-9.507
305.15	2.13E9	1.86E-11	0.6980	4.6E-12	-6.99	-9.479

304.15	2.12E9	1.15E-11	0.7578	3.5E-12	-6.99	-9.477
303.15	1.77E9	1.15E-11	0.7373	2.9E-12	-6.92	-9.398

Ionic conductivity data for $Na_3B_3O_3F_6$ (with sodium electrodes)

Diameter: 0.6 cm   Thickness: 0.2 cm

(2nd cycle)

T /K	R_1/Ω	Q_1	n_1	C_1 /F	log (σT)	log (σ)
351.15	4.53E7	1.80E-11	0.7852	2.6E-12	-5.26	-7.806
351.15	4.64E7	1.99E-11	0.7752	2.6E-12	-5.27	-7.816
351.15	4.78E7	2.12E-11	0.7691	2.7E-12	-5.28	-7.830
350.15	5.02E7	2.11E-11	0.7689	2.7E-12	-5.31	-7.851
350.15	5.26E7	2.24E-11	0.7623	2.7E-12	-5.33	-7.871
349.15	5.52E7	2.28E-11	0.7579	2.7E-12	-5.35	-7.892
348.15	5.82E7	1.93E-11	0.7735	2.6E-12	-5.37	-7.916
347.15	6.20E7	2.00E-11	0.7676	2.6E-12	-5.40	-7.943
346.15	6.55E7	2.46E-11	0.7461	2.8E-12	-5.43	-7.966
345.15	6.86E7	2.16E-11	0.7567	2.7E-12	-5.45	-7.987
344.15	7.24E7	1.88E-11	0.7688	2.6E-12	-5.47	-8.010
343.15	7.68E7	2.39E-11	0.7443	2.8E-12	-5.50	-8.036
342.15	8.20E7	2.54E-11	0.7386	2.9E-12	-5.53	-8.064
341.15	8.55E7	1.74E-11	0.7727	2.6E-12	-5.55	-8.082
341.15	9.04E7	2.55E-11	0.7336	2.8E-12	-5.57	-8.106
340.15	9.72E7	2.24E-11	0.7476	2.8E-12	-5.61	-8.138
339.15	1.01E8	2.04E-11	0.7551	2.7E-12	-5.62	-8.155
338.15	1.05E8	1.62E-11	0.7749	2.5E-12	-5.64	-8.173
337.15	1.12E8	2.26E-11	0.7387	2.7E-12	-5.67	-8.200
336.15	1.17E8	1.56E-11	0.7771	2.5E-12	-5.69	-8.220
336.15	1.25E8	1.79E-11	0.7662	2.8E-12	-5.72	-8.247
335.15	1.31E8	1.62E-11	0.7717	2.6E-12	-5.74	-8.266
334.15	1.36E8	2.02E-11	0.7493	2.8E-12	-5.76	-8.285
333.15	1.43E8	1.72E-11	0.7596	2.6E-12	-5.78	-8.305
332.15	1.57E8	1.84E-11	0.7557	2.8E-12	-5.83	-8.347
331.15	1.67E8	2.11E-11	0.7386	2.9E-12	-5.85	-8.372
330.15	1.77E8	1.77E-11	0.7605	2.9E-12	-5.88	-8.398
330.15	1.83E8	3.11E-11	0.6978	3.3E-12	-5.89	-8.412
329.15	1.86E8	1.99E-11	0.7359	2.7E-12	-5.90	-8.420
328.15	2.07E8	2.38E-11	0.7145	2.8E-12	-5.95	-8.465
327.15	2.25E8	1.57E-11	0.7637	2.7E-12	-5.99	-8.502
326.15	2.30E8	2.64E-11	0.6977	2.9E-12	-6.00	-8.513
325.15	2.48E8	1.93E-11	0.7339	2.8E-12	-6.03	-8.545
324.15	2.65E8	2.24E-11	0.7074	2.7E-12	-6.06	-8.574
323.15	2.84E8	1.94E-11	0.7252	2.7E-12	-6.09	-8.603
322.15	3.07E8	2.58E-11	0.6978	3.2E-12	-6.13	-8.637
321.15	3.27E8	2.20E-11	0.7192	3.2E-12	-6.16	-8.665
320.15	3.47E8	2.79E-11	0.6893	3.5E-12	-6.19	-8.691
319.15	3.72E8	2.66E-11	0.6948	3.5E-12	-6.22	-8.721
318.15	4.13E8	2.58E-11	0.7051	3.9E-12	-6.26	-8.766
317.15	4.40E8	6.82E-12	0.8700	2.9E-12	-6.29	-8.794
316.15	4.48E8	2.62E-11	0.6802	3.2E-12	-6.30	-8.801
315.15	4.81E8	2.00E-11	0.7214	3.3E-12	-6.33	-8.833
314.15	5.14E8	1.84E-11	0.7270	3.2E-12	-6.36	-8.861
313.15	5.66E8	1.85E-11	0.7262	3.3E-12	-6.41	-8.903
312.15	6.05E8	1.65E-11	0.7416	3.3E-12	-6.44	-8.932
311.15	6.51E8	2.09E-11	0.7125	3.7E-12	-6.47	-8.964
310.15	6.98E8	2.09E-11	0.7025	3.5E-12	-6.50	-8.994
309.15	7.44E8	2.10E-11	0.6809	3.0E-12	-6.53	-9.022
309.15	7.61E8	2.39E-11	0.6672	3.2E-12	-6.54	-9.032
308.15	8.31E8	2.05E-11	0.6930	3.4E-12	-6.58	-9.070
307.15	9.02E8	1.01E-11	0.8102	3.4E-12	-6.62	-9.106
306.15	9.91E8	1.59E-11	0.7391	3.7E-12	-6.66	-9.147
305.15	1.03E9	2.75E-11	0.6482	4.0E-12	-6.68	-9.164
305.15	1.08E9	2.23E-11	0.6823	3.9E-12	-6.70	-9.183
304.15	1.11E9	1.38E-11	0.7714	4.0E-12	-6.71	-9.195

Ionic conductivity data for $K_3B_3O_3F_6$

Diameter: 0.6 cm   Thickness: 0.09 cm

   (2nd cycle)

T /K	R_1/Ω	Q_1	n_1	C_1 /F	log (σT)	log (σ)
632.15	2.51E3	1.32E-11	0.9437	4.7E-12	-1.10	-3.897
631.15	2.61E3	1.32E-11	0.9437	4.8E-12	-1.11	-3.914
628.15	2.86E3	1.32E-11	0.9437	4.8E-12	-1.16	-3.953
624.15	2.83E3	1.32E-11	0.9437	4.8E-12	-1.15	-3.949
628.15	2.61E3	1.32E-11	0.9437	4.8E-12	-1.12	-3.913
631.15	2.66E3	1.32E-11	0.9437	4.8E-12	-1.12	-3.922
628.15	2.86E3	1.32E-11	0.9437	4.8E-12	-1.16	-3.953
625.15	2.81E3	1.32E-11	0.9437	4.8E-12	-1.15	-3.946
629.15	2.71E3	1.32E-11	0.9437	4.8E-12	-1.13	-3.930
626.15	2.94E3	1.32E-11	0.9437	4.8E-12	-1.17	-3.965
622.15	3.10E3	1.32E-11	0.9437	4.8E-12	-1.20	-3.989
618.15	3.12E3	1.32E-11	0.9437	4.8E-12	-1.20	-3.992
619.15	2.97E3	1.32E-11	0.9437	4.8E-12	-1.18	-3.971
620.15	3.11E3	1.32E-11	0.9437	4.8E-12	-1.20	-3.989
617.15	3.26E3	1.32E-11	0.9437	4.8E-12	-1.22	-4.011
613.15	3.47E3	1.32E-11	0.9437	4.8E-12	-1.25	-4.037
609.15	3.63E3	1.32E-11	0.9437	4.8E-12	-1.27	-4.057
608.15	3.49E3	1.32E-11	0.9437	4.8E-12	-1.26	-4.039
611.15	3.35E3	1.32E-11	0.9437	4.8E-12	-1.24	-4.022
610.15	3.61E3	1.32E-11	0.9437	4.8E-12	-1.27	-4.055
606.15	3.84E3	1.32E-11	0.9437	4.9E-12	-1.30	-4.081
601.15	4.11E3	1.32E-11	0.9437	4.9E-12	-1.33	-4.111
596.15	4.17E3	1.32E-11	0.9437	4.9E-12	-1.34	-4.117
598.15	3.93E3	1.32E-11	0.9437	4.9E-12	-1.31	-4.092
599.15	3.97E3	1.32E-11	0.9437	4.9E-12	-1.32	-4.095
598.15	4.11E3	1.32E-11	0.9437	4.9E-12	-1.33	-4.111
595.15	4.37E3	1.32E-11	0.9437	4.9E-12	-1.36	-4.137
590.15	4.73E3	1.32E-11	0.9437	4.9E-12	-1.40	-4.172
586.15	4.60E3	1.32E-11	0.9437	4.9E-12	-1.39	-4.160
588.15	4.62E3	1.32E-11	0.9437	4.9E-12	-1.39	-4.162
588.15	4.73E3	1.32E-11	0.9437	4.9E-12	-1.40	-4.172
586.15	4.93E3	1.32E-11	0.9437	4.9E-12	-1.42	-4.190
583.15	5.23E3	1.32E-11	0.9437	5.0E-12	-1.45	-4.215
579.15	5.66E3	1.32E-11	0.9437	5.0E-12	-1.49	-4.250
575.15	5.93E3	1.32E-11	0.9437	5.0E-12	-1.51	-4.270
574.15	5.73E3	1.32E-11	0.9437	5.0E-12	-1.50	-4.255
576.15	5.49E3	1.32E-11	0.9437	5.0E-12	-1.48	-4.237
577.15	5.51E3	1.32E-11	0.9437	5.0E-12	-1.48	-4.238
576.15	5.67E3	1.32E-11	0.9437	5.0E-12	-1.49	-4.251
574.15	5.97E3	1.32E-11	0.9437	5.0E-12	-1.51	-4.273
571.15	6.25E3	1.32E-11	0.9437	5.0E-12	-1.54	-4.293
568.15	6.66E3	1.32E-11	0.9437	5.0E-12	-1.57	-4.321
564.15	7.16E3	1.32E-11	0.9437	5.0E-12	-1.60	-4.352
560.15	7.37E3	1.32E-11	0.9437	5.1E-12	-1.62	-4.365
561.15	7.03E3	1.32E-11	0.9437	5.0E-12	-1.60	-4.344
563.15	6.91E3	1.32E-11	0.9437	5.0E-12	-1.59	-4.337
562.15	7.04E3	1.32E-11	0.9437	5.0E-12	-1.59	-4.344
561.15	7.34E3	1.32E-11	0.9437	5.1E-12	-1.61	-4.363
558.15	7.76E3	1.32E-11	0.9437	5.1E-12	-1.64	-4.387
555.15	8.30E3	1.32E-11	0.9437	5.1E-12	-1.67	-4.416
551.15	7.44E3	1.20E-12	1.0807	4.8E-12	-1.63	-4.369
547.15	8.97E3	1.64E-12	1.0569	4.3E-12	-1.71	-4.450
549.15	7.71E3	1.32E-12	1.0720	4.6E-12	-1.64	-4.384
552.15	7.14E3	1.23E-12	1.0787	4.8E-12	-1.61	-4.351
550.15	7.36E3	9.56E-13	1.0961	5.0E-12	-1.62	-4.364
548.15	7.40E3	7.35E-13	1.1148	5.2E-12	-1.63	-4.366
545.15	1.12E4	2.33E-12	1.0390	4.5E-12	-1.81	-4.545
536.15	1.98E4	4.67E-12	0.9995	4.6E-12	-2.07	-4.795
529.15	4.37E4	9.73E-12	0.9474	4.3E-12	-2.41	-5.137
532.15	4.25E4	8.74E-12	0.9541	4.3E-12	-2.40	-5.126
533.15	4.53E4	8.19E-12	0.9592	4.4E-12	-2.43	-5.153
532.15	5.08E4	6.95E-12	0.9719	4.5E-12	-2.48	-5.203
530.15	6.11E4	7.03E-12	0.9729	4.7E-12	-2.56	-5.283
527.15	8.28E4	7.18E-12	0.9705	4.6E-12	-2.69	-5.415
524.15	1.27E5	1.03E-11	0.9437	4.6E-12	-2.88	-5.603
520.15	1.83E5	1.07E-11	0.9341	4.2E-12	-3.04	-5.760
516.15	1.98E5	5.30E-12	0.9904	4.6E-12	-3.08	-5.795
513.15	2.16E5	3.92E-12	1.0184	5.1E-12	-3.12	-5.831
511.15	3.47E5	9.29E-12	0.9416	4.2E-12	-3.33	-6.037
512.15	2.92E5	5.70E-12	0.9822	4.5E-12	-3.25	-5.962
510.15	3.63E5	4.13E-12	1.0160	5.1E-12	-3.35	-6.057
508.15	4.88E5	4.07E-12	1.0128	4.8E-12	-3.48	-6.185
506.15	5.01E5	2.64E-12	1.0530	5.2E-12	-3.49	-6.197
503.15	6.99E5	3.01E-12	1.0330	4.6E-12	-3.64	-6.342
501.15	7.61E5	2.04E-12	1.0663	4.7E-12	-3.68	-6.379

499.15	9.75E5	3.09E-12	1.0350	4.8E-12	-3.79	-6.486
494.15	1.82E6	6.33E-12	0.9610	4.0E-12	-4.06	-6.757
495.15	1.67E6	6.20E-12	0.9767	4.7E-12	-4.03	-6.721
494.15	1.93E6	5.13E-12	0.9933	4.7E-12	-4.09	-6.783
493.15	2.11E6	5.78E-12	0.9838	4.8E-12	-4.13	-6.821
490.15	2.45E6	3.65E-12	1.0246	4.8E-12	-4.20	-6.886
488.15	3.05E6	5.77E-12	0.9793	4.6E-12	-4.29	-6.982
486.15	2.89E6	3.45E-12	1.0344	5.1E-12	-4.27	-6.957
483.15	4.64E6	5.89E-12	0.9773	4.6E-12	-4.48	-7.164
481.15	6.42E6	7.55E-12	0.9496	4.5E-12	-4.62	-7.305
478.15	8.19E6	6.69E-12	0.9695	4.9E-12	-4.73	-7.410
476.15	8.60E6	6.69E-12	0.9695	4.9E-12	-4.75	-7.432
474.15	1.62E7	3.11E-11	0.8087	5.2E-12	-5.03	-7.707
471.15	1.64E7	9.90E-12	0.9123	4.3E-12	-5.04	-7.711
469.15	2.28E7	8.17E-12	0.9534	5.4E-12	-5.18	-7.856
466.15	1.90E7	1.16E-11	0.9025	4.7E-12	-5.11	-7.777
464.15	2.10E7	1.16E-11	0.9025	4.7E-12	-5.15	-7.818
462.15	3.93E7	5.21E-12	0.9573	3.6E-12	-5.43	-8.092
457.15	4.51E7	4.16E-12	1.0330	5.5E-12	-5.49	-8.151
453.15	5.82E7	4.16E-12	1.0330	5.4E-12	-5.61	-8.262
451.15	5.33E7	4.16E-12	1.0330	5.4E-12	-5.57	-8.224
449.15	6.79E7	4.16E-12	1.0330	5.4E-12	-5.68	-8.329
447.15	9.31E7	4.16E-12	1.0330	5.3E-12	-5.82	-8.466
445.15	1.49E8	4.16E-12	1.0330	5.3E-12	-6.02	-8.671
440.15	1.33E8	4.16E-12	1.0330	5.3E-12	-5.98	-8.620
437.15	2.11E8	2.90E-12	1.0162	3.3E-12	-6.18	-8.822
436.15	1.49E8	4.17E-12	1.0324	5.3E-12	-6.03	-8.671
442.15	1.75E8	1.88E-11	0.7993	4.5E-12	-6.09	-8.740
440.15	2.94E8	1.88E-11	0.7993	5.1E-12	-6.32	-8.966
438.15	3.86E8	2.11E-11	0.8595	9.6E-12	-6.44	-9.084
431.15	4.10E8	1.01E-11	0.8601	4.1E-12	-6.48	-9.110
429.15	5.02E8	2.11E-11	0.8595	1.0E-11	-6.57	-9.198
427.15	7.23E8	3.76E-12	1.3690	1.8E-11	-6.73	-9.356
425.15	8.74E8	7.79E-12	0.9967	7.7E-12	-6.81	-9.439
423.15	7.11E8	1.93E-12	1.2460	7.1E-12	-6.72	-9.349
421.15	8.29E8	5.44E-12	1.1110	9.3E-12	-6.79	-9.416
419.15	1.18E9	1.85E-11	0.8289	8.4E-12	-6.95	-9.570
415.15	1.12E9	4.13E-11	0.6484	7.8E-12	-6.93	-9.546
397.15	3.54E10	1.54E-11	0.7128	1.2E-11	-8.45	-11.047
394.15	5.71E10	1.61E-11	0.7169	1.6E-11	-8.66	-11.254
393.15	4.65E10	1.36E-11	0.7036	1.1E-11	-8.57	-11.165
391.15	3.02E10	1.22E-11	0.7109	8.1E-12	-8.39	-10.977
385.15	6.10E10	9.25E-12	0.7393	7.6E-12	-8.70	-11.283
385.15	1.21E11	1.26E-11	0.6316	1.6E-11	-8.99	-11.579
384.15	5.22E10	8.66E-12	0.7858	7.0E-12	-8.63	-11.215
382.15	3.72E10	3.48E-12	1.1078	4.3E-12	-8.49	-11.067
380.15	3.26E11	7.87E-12	0.7698	1.0E-11	-9.43	-12.010
376.15	8.14E10	6.82E-12	0.8265	6.0E-12	-8.83	-11.408
375.15	6.78E10	5.97E-12	0.8907	5.3E-12	-8.75	-11.328

8   List of Abbreviation

ac: Alternating Current

C: Capacitance

CPE: Constant Phase Element

DSC: Differential Scanning Calorimetry

DTA: Differential Thermal Calorimetry

dc: Direct Current

E: Potential

E_a: Activation Energy

IR: Infrared Spectroscopy

I: current

MS: Mass Sspectroscopy

NMR: Nuclear Magnetic Resonance

PSD: Position Sensitive Detector

R: Resistance

RF: Radio Frequency

RT: Room Temperature

t: Time

t_{el}: Electonic transport number

t_+: Cationic transport number

T: Temperature

THF: Tetrahydrofuran

TG: Thermal Gravimetry

Q: Constant phase element

Z: Impedance

|Z|: Impedance modulus

$\mathbf{Z}_{im}$ and Z ": Imaginary impedance

$\mathbf{Z}_{re}$ and Z': Real impedance

Ω: Ohm

S: Siemens

σ : Conductivity

ω : Radial frequency

θ : Phase shift

Å: Angstrom

K: Kelvin

ν: stretching vibration

δ: deformation vibration

ρ: rocking vibration

γ: wagging vibration

w: weak

m: medium

s: strong

vs: very strong

PLEB: poly[lithium tetrakis(ethyleneboryl)borate]

PLEPB: poly[lithium tetrakis(triethylenephenylborylborate)]

PLEMB: poly[lithium tetrakis(triethylenemethylborylborate)]

PESB: poly[tris(tetraethylenesilyl)borane]

PLESPB: poly[lithium tris(tetraethylenesilyl)phenylborate]

PLESnBB: poly[lithium tris(tetraethylenesilyl)n-butylborate]

PLEStBB: poly[lithium tris(tetraethylenesilyl)t-butylborate]

9 Curriculum Vitae

Personal

Name	Güliz Cakmak
Maiden Name	Otabatmaz
Date of Birth	16.10.1978
Place of Birth	Ankara/Türkiye
Marital Status	Married

Education

09/1995 — 06/1999	Bachelor Degrees in Chemistry, Department of Chemistry, Middle East Technical University, Ankara, Türkiye.
09/1999 — 07/2002	Master of Science in Chemistry, Department of Chemistry, Middle East Technical University, Ankara, Türkiye
Title of the Thesis:	Synthesis and Characterization of Polyaniline/Polypyrrole Conductive Films
08/2004 — 07/2009	Ph.D. research in the group of Prof. Dr. Dr. h.c. Martin Jansen, Max-Planck-Institute for Solid State Research, Stuttgart, Germany, and Ph.D. Degree from the Department of Chemistry, University of Stuttgart, Stuttgart, Germany.
Title of the Thesis:	Synthesis and Characterization of Ion Conducting Solid Polyelectrolytes and Alkali Fluorooxoborates

List of Publications

Scientific Publications

1. G. Cakmak, Z. Küçükyavuz, S. Küçükyavuz, Flexible and Conducting Composites of Polypyrrole and Poly(dimethylsiloxane), *Journal of Applied Polymer Science*, **93**(2)**,** 2004, pp:736−741.

2. G. Cakmak, Z. Küçükyavuz, S. Küçükyavuz and H. Çakmak, Mechanical, Electrical and Thermal Properties of Carbon Fiber Reinforced Poly(dimethylsiloxane)/ Polypyrrole Composites, *Composites Part A: Applied Science and Manufacturing*, **35**(4), 2004, pp:417−421.

3. G. Cakmak, Z. Küçükyavuz, S. Küçükyavuz, Conductive Copolymers of Polyaniline, Polypyrrole and Poly(dimethylsiloxane), *Synthetic Metals*, **151**(1), 2005, pp:10−18.

4. D. Pitzschke, J. Curda, G. Cakmak, M. Jansen, $Ag_9I_3(SeO_4)_2(IO_3)_2$ − Synthesis, Crystal Structure and Ionic Conductivity, *Zeitschrift für Anorganische and Allgemeine Chemie (ZAAC)*, **634** (11), 2008, pp:1907 −1910.

5. D. Pitzschke, J. Curda, G. Cakmak, M. Jansen, $Ag_4I_2SeO_4$ and Ag_3ITeO_4 −Two New Silver Solid Electrolytes, *Zeitschrift für Anorganische and Allgemeine Chemie (ZAAC)*, **634** (6−7), 2008, pp:1071−1076.

6. G. Cakmak, A. Verhoeven, M. Jansen, Synthesis and Characterization of Single Solid Ion Conductors Based on Poly[lithium tetrakis(ethylene boryl)borate], *Journal of Materials Chemistry*, **19**(25), 2009, pp:4310− 4318.

7. G. Cakmak, J. Nuss, M. Jansen, LiB_6O_9F, the First Lithium Fluorooxoborate − Crystal Structure and Ionic Conductivity, *Zeitschrift für Anorganische and Allgemeine Chemie (ZAAC)*, **635**(4−5), 2009, pp:631−636.

8. G. Cakmak, M. Jansen, Synthesis and Characterization of Solid Ion Conductors Based on Poly[lithium tetrakis(triethyleneorganylboryl)borate], *in preperation*.

9. G. Cakmak, M. Jansen, Synthesis, Crystal Structure and Ionic Conductivity of $Na_3B_3O_3F_6$, *in preperation*.

10. G. Cakmak, M. Jansen, Synthesis, Characterization and Ionic Conductivity of $K_3B_3O_3F_6$, *in preperation*.

Meetings & Proceedings:

1. G. Cakmak, J. Nuss, M. Jansen, Synthesis of Novel Alkali Metal Ion Conducting Materials, Gordon Research Conference on Solid State Chemistry — New Frontiers in Materials Synthesis and Characterization, September 2009, Oxford, United Kingdom.

2. G. Cakmak, J. Nuss, M. Jansen, Crystal Structures and Ionic Conductivities of the First Alkali Fluorooxoborates, ECSSC XIIth European Conference on Solid State Chemistry, EM004, pp:336, September 2009, Münster, Germany.

3. G. Cakmak, A.Verhoeven, M. Jansen, Synthesis and Characterization of a Novel Organoborate Polyelectrolyte, 6th International Conference on Inorganic Materials, P1-26, September 2008, Dresden, Germany.

4. Kronacher Impedancedays, Kloster Banz, April 2005, workshop organized by Zahner Company.

5. Z. Küçükyavuz, S. Küçükyavuz, G. Çakmak, Synthesis and characterization of polypyrrole and polydimethylsiloxane composites, Abstracts of Papers, 228th National Meeting of the American Chemical Society, **228**(2), 2004, pp:U468, Philadelphia, USA.

6. G. Cakmak, Z. Küçükyavuz, S. Küçükyavuz, Polidimetilsiloksan ve Polipirolün İletken ve Esnek Kompozitleri, XVIIth National Chemistry Symposium, September 2003, pp:742, Istanbul, Turkey.

7. G. Otabatmaz, Z. Küçükyavuz, S. Küçükyavuz, Conducting Composites of Polyaniline, Polymer Processing Society—2001 Regional Meeting, October 2001, pp:471, Antalya, Turkey (also a member of Organization Committee).

8. G. Otabatmaz, Z. Küçükyavuz, S. Küçükyavuz, Polianilinin İletken Kompozitleri, XVth National Chemistry Symposium, September 2001, P43, Istanbul, Turkey.

Explanation

Hiermit versichere ich an Eides statt, dass ich diese Dissertation unter Verwendung der angegebenen Hilfsmittel selbstständig angefertigt und bisher noch keinen Promotionversuch unternommen habe.

Stuttgart, den

Güliz Cakmak